nature chemistry

Article

https://doi.org/10.1038/s41557-023-01275-1

Optical control of ultrafast structural dynamics in a fluorescent protein

Received: 11 November 2021

Accepted: 12 June 2023

Published online: 10 August 2023

Check for updates

Christopher D. M. Hutchison[1,16], James M. Baxter[1,16], Ann Fitzpatrick[2], Gabriel Dorlhiac[1], Alisia Fadini[1], Samuel Perrett[1], Karim Maghlaoui[1], Salomé Bodet Lefèvre[1], Violeta Cordon-Preciado[1], Josie L. Ferreira[1], Volha U. Chukhutsina[1], Douglas Garratt[3], Jonathan Barnard[3], Gediminas Galinis[3], Flo Glencross[1], Rhodri M. Morgan[1], Sian Stockton[1], Ben Taylor[1], Letong Yuan[1], Matthew G. Romei[4], Chi-Yun Lin[4], Jon P. Marangos[3], Marius Schmidt[5], Viktoria Chatrchyan[6], Tiago Buckup[6], Dmitry Morozov[7], Jaehyun Park[8,9], Sehan Park[8], Intae Eom[8], Minseok Kim[8], Dogeun Jang[8], Hyeongi Choi[8], HyoJung Hyun[8], Gisu Park[8], Eriko Nango[10,11], Rie Tanaka[10,12], Shigeki Owada[10,13], Kensuke Tono[10,13], Daniel P. DePonte[14], Sergio Carbajo[14], Matt Seaberg[14], Andrew Aquila[14], Sebastien Boutet[14], Anton Barty[15], So Iwata[10,12], Steven G. Boxer[4], Gerrit Groenhof[7] & Jasper J. van Thor[1] ✉

The photoisomerization reaction of a fluorescent protein chromophore occurs on the ultrafast timescale. The structural dynamics that result from femtosecond optical excitation have contributions from vibrational and electronic processes and from reaction dynamics that involve the crossing through a conical intersection. The creation and progression of the ultrafast structural dynamics strongly depends on optical and molecular parameters. When using X-ray crystallography as a probe of ultrafast dynamics, the origin of the observed nuclear motions is not known. Now, high-resolution pump–probe X-ray crystallography reveals complex sub-ångström, ultrafast motions and hydrogen-bonding rearrangements in the active site of a fluorescent protein. However, we demonstrate that the measured motions are not part of the photoisomerization reaction but instead arise from impulsively driven coherent vibrational processes in the electronic ground state. A coherent-control experiment using a two-colour and two-pulse optical excitation strongly amplifies the X-ray crystallographic difference density, while it fully depletes the photoisomerization process. A coherent control mechanism was tested and confirmed the wave packets assignment.

Photoisomerization of chromophores in fluorescent proteins (FPs)[1], bacteriorhodopsin[2,3] and photoreceptors, such as rhodopsin[4,5], phytochrome[6,7] or the photoactive yellow protein[8–12], involve specific excited-state bond rearrangements in addition to macromolecular reaction dynamics and non-adiabatic transitions at conical intersections. Biological photoisomerization is a representative example of non-adiabatic reaction dynamics that involves substantial nuclear reconfiguration. The class of reversibly photoswitchable FPs (rs-FPs) is of particular interest for understanding the origin of structural motions that are associated with the *cis*–*trans* and *trans*–*cis* photoisomerization

A full list of affiliations appears at the end of the paper. ✉e-mail: j.vanthor@imperial.ac.uk

https://doi.org/10.1038/s41557-023-01275-1

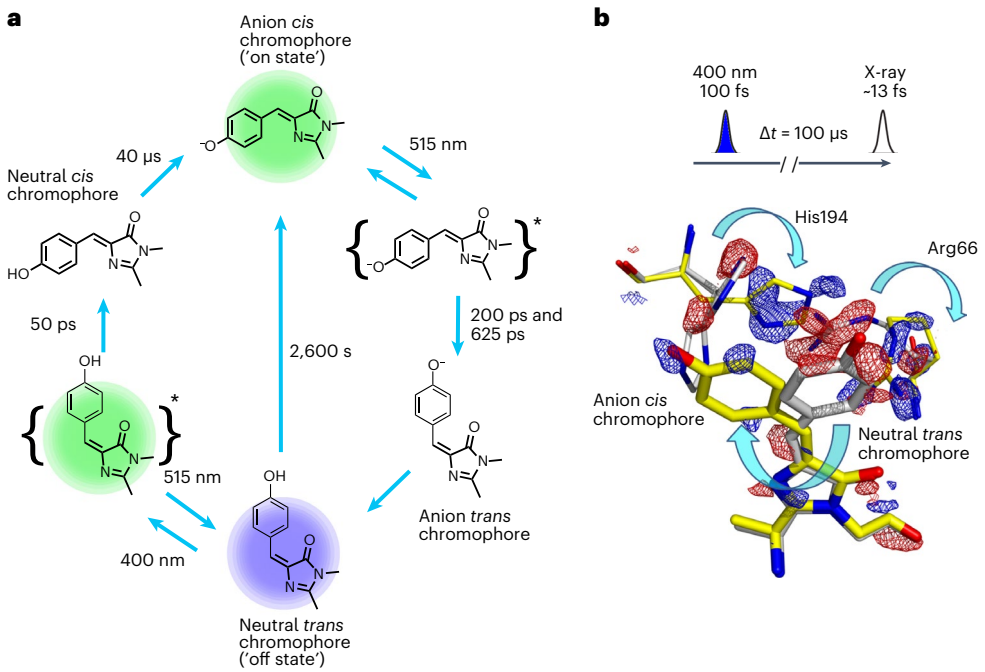

Fig. 1 | rsKiiro photocycle. a, General photocycle scheme of the reversible photoisomerization and proton-transfer reactions of rsKiiro. Light-induced transitions with 400-nm (blue) and 515-nm (green) wavelengths are indicated. **b**, Time-resolved crystallography measurement of *trans–cis* photoisomerization of the off state with a *trans* neutral chromophore using femtosecond excitation at a wavelength of 400 nm, conducted at PAL-XFEL. *Q*-weighted $F_{o(100\mu s)}-F_{o(Dark)}$ difference maps contoured at 3σ at a resolution of 1.5 Å and at a 100-µs delay show *trans–cis* photoisomerization and rearrangements of His194 and Arg66.

reactions of these biological chromophores. The photoisomerization reaction of rs-FPs includes incoherent excited-state barrier crossing[13]. These rs-FPs have therefore found widespread use in the fields of protein highlighting[14], optogenetics[15] and super-resolution microscopy[16]. The protein environment in rs-FPs controls the isomerization process through specific electrostatic interactions[13], and direct structural observations are therefore essential to understand how these interactions steer the ultrafast process.

Because photoisomerization occurs on the timescale of the excited-state (ES) lifetime, ultrafast time resolution is needed for direct structural observations. The non-adiabatic dynamics occur either coherently within the vibrational dephasing time[17] or incoherently through thermally driven barrier crossing within the excited-state lifetime[18]. In the latter case, excited-state motion may not contribute substantially to measurements made with short observation delays, because the product accumulates thermally by barrier crossing throughout the excited-state lifetime. The photoisomerization motion is therefore not directly captured in a pump–probe time series, which measures concentration changes instead if the process is incoherent. With the advent of X-ray free-electron laser (XFEL) sources, recording time-resolved X-ray crystallographic structures of such ultrafast photochemical processes has become a reality[12,19–22]. Successful time-resolved crystallography studies have used the pump–probe approach, and the light-induced X-ray crystallographic difference densities have been assigned to reactions and excited-state processes. However, the relationship between ultrafast nuclear dynamics that are measured in real space directly from crystallographic coordinates and the outcome of the non-adiabatic dynamics is not yet established. This is because there remain fundamental open questions regarding the correct physical assignment and interpretation of the observed ultrafast structural changes. First, analysis based on rate kinetics that quantifies concentration changes of static species is commonly applied to time-resolved observations, but this is not applicable if the time resolution is within vibrational dephasing. Second, although it is widely accepted in the field of Raman spectroscopy that both ground-state and excited-state motions contribute to the structural dynamics under conditions of ultrafast excitation[23–26], the extent of contributions from electronic ground-state motions has not yet been analysed for experimental time-resolved serial femtosecond crystallography (TR-SFX) results and has so far only been considered on a theoretical basis[26,27]. In this Article, to address these open questions, we demonstrate the use of optical control for analysis of the creation and evolution of coherence under conditions for ultrafast TR-SFX.

Based on the EosFP sequence[28], we developed a new reversibly photoswitching rs-FP, 'rsKiiro' (described in detail in Supplementary Discussion 10). Reversible photoswitching occurs between a bright fluorescent *cis* anionic *p*-hydroxybenzylideneimidazolinone (HBDI) chromophore (the 'on' state) and the non-fluorescent *trans* neutral (the 'off' state) (Fig. 1), as is also the case for the rs-FP 'Dronpa'[14]. Compared to Dronpa, rsKiiro has substantially improved structural ordering in the 'on' ground state as well as the 'off' photoproduct, allowing high-resolution X-ray crystallography of the photoreactions. In addition, rsKiiro was selected by screening variants for photoisomerization quantum yield, thermal recovery kinetics, complete photoconversion and full reversibility (Extended Data Figs. 1c and 2a and Supplementary Discussion 10). Illumination of the 'on' state with green light drives a *cis–trans* photoisomerization of the chromophore to produce a metastable non-fluorescent 'off' state with a neutral *trans* chromophore (Fig. 1a). The thermal-ground-state recovery of the 'on' state at ambient temperature is sufficiently slow for pump–probe TR-SFX, with $\tau_{rev} \approx 2{,}600$ s (Fig. 1), and reversible *trans–cis* photoisomerization driven by 400-nm illumination proceeds to completion with a quantum yield of ~0.2, enabling detection with a sufficient concentration of photoproduct (Fig. 1b). Transient visible (Extended Data Fig. 3) and mid-infrared (Extended Data Fig. 4) spectroscopy confirm the excited-state *trans–cis* photoisomerization with a pump-induced 12% yield in solution samples and crystals (Extended Data Fig. 2 and Supplementary Methods 6).

We conducted high-resolution ultrafast TR-SFX experiments of the 'off' state of rsKiiro under conditions designed to optically control

https://doi.org/10.1038/s41557-023-01275-1

Table 1 | LCLS LR23 PP and PDP crystallographic statistics for merged 0–1-ps delays

	Dark	400 nm, 0–1 ps	400–515 nm, 0–1 ps
Data collection			
Wavelength (eV)	9,486	9,486	9,486
Indexed patterns	35,030	47,590	39,754
Resolution limits (Å)	15.40–1.80 (1.864–1.800)[a]	15.40–1.80 (1.864–1.800)[a]	18.01–1.80 (1.864–1.800)[a]
	15.40–1.50 (1.554–1.500)[b]	15.40–1.50 (1.554–1.500)[b]	18.01–1.50 (1.554–1.500)[b]
	15.40–1.35 (1.398–1.350)[c]	15.40–1.35 (1.398–1.350)[c]	18.01–1.35 (1.398–1.350)[c]
No. of unique reflection indices	21,941[a]	21,941[a]	21,964[a]
	37,542[b]	37,542[b]	37,565[b]
	51,229[c]	51,229[c]	51,252[c]
No. of merged reflections	8,859,960 (583,183)[a]	9,663,635 (454,993)[a]	7,042,698 (265,101)[a]
	12,622,674 (790,070)[b]	11,562,142 (263,229)[b]	7,928,580 (96,156)[b]
	14,971,721 (647,523)[c]	11,990,599 (64,419)[c]	8,056,732 (13,369)[c]
Completeness (%)	100.00 (100.00)[a]	100.00 (100.00)[a]	99.96 (100.00)[a]
	100.00 (100.00)[b]	100.00 (100.00)[b]	99.98 (100.00)[b]
	100.00 (100.00)[c]	99.77 (97.73)[c]	96.67 (68.35)[c]
Signal to noise	8.568 (5.24)[a]	9.793 (5.65)[a]	8.272 (4.27)[a]
	6.328 (1.86)[b]	7.225 (2.36)[b]	5.790 (1.20)[b]
	4.843 (0.40)[c]	5.607 (0.61)[c]	4.566 (0.88)[c]
Wilson *b* factor (Å^2)	27.23[a]	13.84[a]	16.96[a]
	32.89[b]	16.13[b]	19.19[b]
	35.68[c]	16.60[c]	19.87[c]
R_{Split} (%)	9.27 (18.03)[a]	8.76 (16.90)[a]	9.83 (22.54)[a]
	9.51 (79.05)[b]	9.83 (40.27)[b]	11.19 (82.62)[b]
	9.68 (291.14)[c]	11.01 (142.12)[c]	12.19 (350.70)[c]
CC*	1.00 (0.98)[a]	1.00 (0.99)[a]	1.00 (0.98)[a]
	1.00 (0.61)[b]	1.00 (0.94)[b]	1.00 (0.82)[b]
	1.00 (0.07)[c]	1.00 (0.62)[c]	1.00 (N/A)[c]
$CC_{1/2}$	0.99 (0.94)[a]	0.99 (0.94)[a]	0.99 (0.91)[a]
	0.99 (0.23)[b]	0.99 (0.79)[b]	0.99 (0.51)[b]
	0.99 (0.00)[c]	0.99 (0.24)[c]	0.99 (0.05)[c]
Refinement			
Resolution (Å)	1.3/1.5	1.3/1.5	1.3/1.5
No. of reflections used (all/free)	51,401/35,668	51,120/35,645	47,319/35,676
Reflections used for *R*-free	2,754/1,828	2,671/1,851	2,460/1,833
R-factor	0.1836/0.1529	0.1922/0.1674	0.1984/0.1785
R-free	0.1901/0.1628	0.1946/0.1700	0.2055/0.1837
No. of non H atoms	2,074	2,074	2,074
Protein residues	216	216	216
Bonds (Å)	0.0288	0.0598	0.0589
Angles (°)	2.767	2.854	3.014

[a,b,c]Merged statistics for distinct resolution shells with resolution cut-off at (a) 1.80 Å, (b) 1.50 Å and (c) 1.35 Å. The values in parenthesis are given for the highest resolution shells.

vibrational coherence and population dynamics. Four experiments conducted at LCLS, PAL-XFEL and SACLA yielded a consistent and reproducible set of observations that revealed a fundamental new understanding of the origins of ultrafast structural dynamics in this photochromic rsKiiro FP. Two complementary sets of experiments were conducted, namely a pump–probe (PP) experiment and a two-pulse, two-colour pump–dump–probe (PDP) experiment, to control the excited- and ground-state motions.

Results and discussion

An ~100-fs pump interaction at 400 nm, close to resonance of the *trans* neutral chromophore (off state), creates an excited-state population with a lifetime of $\tau = 50$ ps in both solution and crystals (Fig. 1a and Extended Data Figs. 1a, 2 and 3d). A power density of 1,400 GW cm^{-2} (full-width at half-maximum, FWHM) was chosen for PP experiments to maximize the photoisomerization yield, based on optical measurements in crystals of anionic *cis* product absorption (Extended Data Fig. 2a).

https://doi.org/10.1038/s41557-023-01275-1

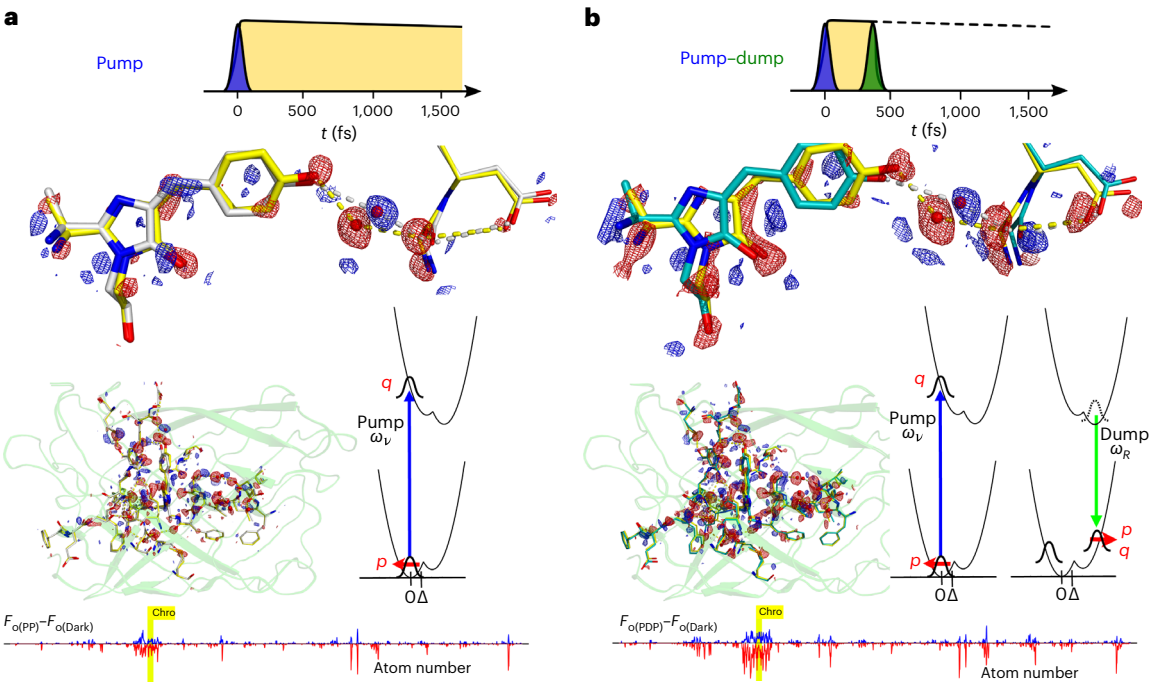

Fig. 2 | Optical control of structural dynamics in rsKiiro. a,**b**, Femtosecond time-resolved PP (**a**) and PDP (**b**) TR-SFX experiment for rsKiiro in the off state with a *trans* neutral chromophore. For this analysis, time-resolved data with delays between ~250 fs and 1.2 ps were merged, and *Q*-weighted $F_{o(PP)}-F_{o(Dark)}$ and $F_{o(PDP)}-F_{o(Dark)}$ maps are shown (red, -3σ, blue $+3\sigma$) at a resolution of 1.5 Å. Coordinates for the ground state are shown (yellow sticks; PDB 7QLM). Coordinates for the PP data (white sticks, **a**; PDB 7QLN) and PDP data (cyan sticks, **b**; PDB 7QLO) were refined from extrapolated structure factors and occupancy refinement. The creation of coherence in the PP and PDP conditions follows the density matrix theory of impulsive Raman spectroscopy applied to a double-well adiabatic potential. The initial Wigner coordinate and direction relative to the nuclear binding force (momentum, *p*; position, *q*) are indicated by arrows. Also shown are the sequentially integrated electron densities around each atom in the protein chain (bottom), with the atoms in the chromophore highlighted in yellow.

Under these conditions, a TR-SFX experiment shows that *trans*–*cis* photoisomerization is associated with short-range motions of His194 and Arg66 in the chromophore binding pocket (Fig. 1b). With the 100-µs PP delay, the formation of the on-state product has completed, which includes deprotonation of the phenolate chromophore (Fig. 1a). These observations match the static photoinduced differences between the on- and off-state crystal structures prepared with weak continuous-wave (c.w.) illumination (Supplementary Fig. 48).

Femtosecond TR-SFX experiments at LCLS achieved data at a resolution of 1.35 Å (Table 1), and timing tool measurements allowed binning of diffraction data into 150-fs-wide bins (Extended Data Figs. 5 and 6). The pump–probe observations up to 1-ps delay showed strong F_o-F_o difference electron-density features, up to 8.5σ, on the chromophore and on a hydrogen-bonded water and throughout the core of the protein (Fig. 2a and Extended Data Fig. 7). Coordinate refinement from extrapolated structure factors and occupancy refinement showed a small translational motion of the chromophore characterized by a 69-pm displacement of the phenolic oxygen. A 1.25-Å coordinate change of a nearby hydrogen-bonded water molecule modifies the O–O distance between the chromophore and water from 2.63 Å to 3.06 Å (Fig. 2a). A concomitant repositioning of the Gly155 backbone carbonyl changes its O–O distance to this water molecule from 2.77 Å to 2.84 Å. The larger distances in the femtosecond time-resolved structure suggest that the hydrogen bonding of the water molecule to both the chromophore and Gly155 is weakened. Other water molecules in the chromophore pocket and the side chains that primarily reside on the central helix undergo similar rearrangements (Fig. 2a). Separation of the ultrafast time-resolved PP data into bins of 150 fs showed complex dynamical changes of these difference-electron-density features throughout the protein, including those on the chromophore and hydrogen-bonding environment (Extended Data Fig. 5c). The dynamics are interpreted as a superposition of multiple impulsively driven modes that follow the displacement, rather than a single periodic motion. The displacements of protein, chromophore and water molecules, as shown in Fig. 2, were already detected in the early ~250–400-fs time bin. The time dependence of the dynamical modulation of difference features is limited by the ~4.4-THz experimental bandwidth, which is determined by the experimental pulse durations.

A two-pulse, two-colour PDP experiment was executed in which the delay between the pump (400 nm) and the Stokes (515 nm) 'dump' pulses was chosen to be 350 fs (Fig. 2b). Under these conditions, the electronic dephasing following the first interaction has completed, and coherent impulsive Raman processes are therefore not driven by the two-colour excitation[29]. At the chosen pump–dump delay of 350 fs, the Stokes 'dump' pulse selectively and fully depletes the S_1 excited state and generates a vibrationally excited electronic-ground-state population. The complete loss of the S_1 excited state in the PDP conditions is confirmed from spectrally resolved transient absorption (TA) spectroscopy in solution (Extended Data Fig. 3b–g) and the loss of photoisomerization product in crystals (Extended Data Fig. 2).

The PDP measurements were collected in an interleaved manner together with the PP data, and consistently showed significantly stronger but otherwise almost identical F_o-F_o electron-density differences as compared to the PP data (Fig. 2b). In addition to amplification of the light-induced differences, the time dependence of the dynamics was also modified when the dump pulse was included (Extended Data Fig. 5c). Structure refinement of the PDP data averaged to 1-ps delay resulted in coordinate changes very similar but with larger displacement compared to the PP data (Fig. 2b and Extended Data Fig. 7). These structural rearrangements suggest a double-well adiabatic potential in

https://doi.org/10.1038/s41557-023-01275-1

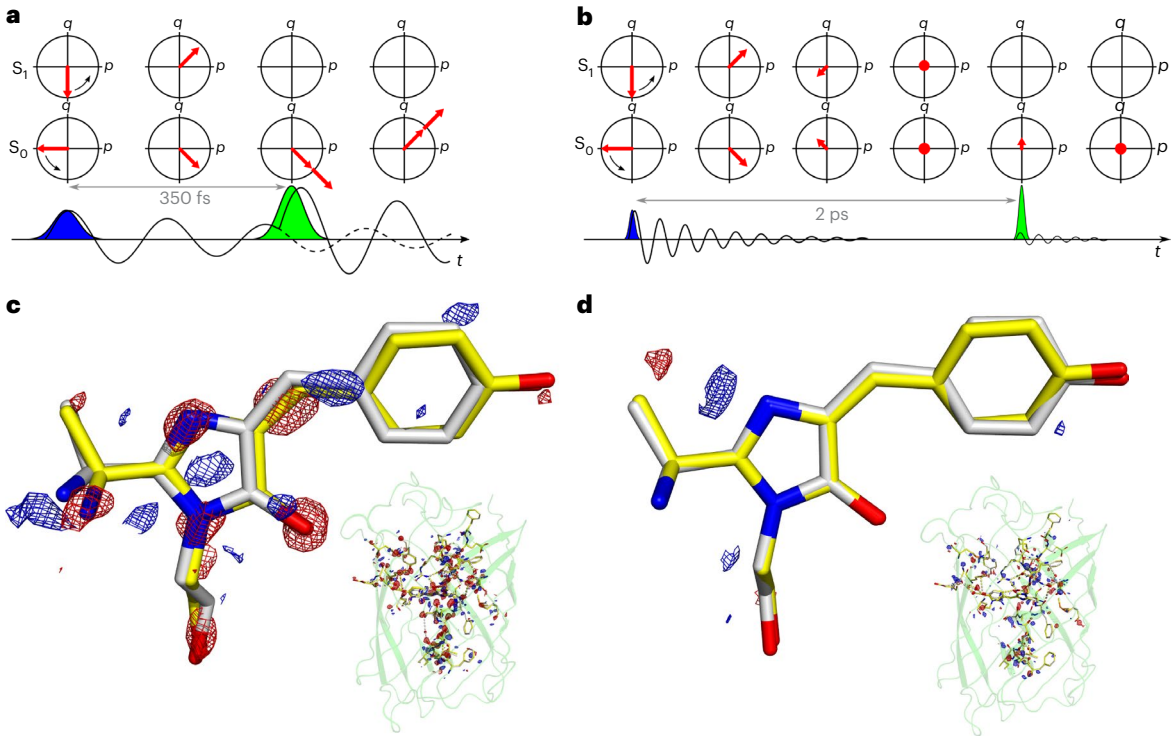

Fig. 3 | Amplification of structural motion requires the pump–dump delay to be within the vibrational dephasing time, not the excited-state lifetime. **a**,**b**, Vibrational-coherence transfer dominates the observed displacements on a femtosecond timescale for the PDP condition (**a**). A test for Tannor–Rice coherent dynamics moved the dump delay to 2 ps (**b**), after vibrational dephasing but well within the 50-ps excited-state lifetime. **c**,**d**, A comparison of the PDP experiment with a 350-fs dump time (**c**) conducted at SACLA reproduces the LCLS experiment in Fig. 2 in detail. F_o–F_o difference maps are shown at 3σ level and 1.5 Å resolution. Strong decay of the difference signals is observed when dumping at 2 ps after dephasing, as predicted by Tannor–Rice coherent control (**b**,**d**). A schematic representation of coherence in the ground state (S_0) and excited state (S_1) is shown in the Wigner phase-space representation as the evolution of momentum p and position q of the S_0 and S_1 wave packets (**a**,**b**). A full coherence simulation using a density-matrix calculation including Wigner transforms is presented in Fig. 4, Extended Data Fig. 8 and Supplementary Section 13.

both the electronic ground (S_0) and excited (S_1) states. The 1.25-Å coordinate change of the water seen in the PP and PDP differences (Fig. 2a,b), as well as the magnitude of other rearrangements, is too large to consider displacement for a single oscillator[27]. The double-well nature of the adiabatic potential of the S_1 state was experimentally confirmed from the temperature dependence of excited-state decay of the off state as well as the on state. In addition, structure-based thermodynamics modelling retrieved the barriers associated with the double-well potentials for the radiative and non-radiative transitions of the on and off states (Extended Data Fig. 1 and Supplementary Section 11). This is also in line with hybrid quantum mechanics/molecular mechanics (QM/MM) geometry optimizations of the protein in S_0 and S_1 (Extended Data Fig. 8 and Supplementary Section 12). The QM/MM simulations furthermore suggest that the relative energies of the minima of these double-well potentials interchange between the ground and excited states (Fig. 2).

We consider the premise that if a time-resolved signal contains both excited- and ground-state contributions, then, after selectively depleting S_1 by stimulated emission pumping, the signals belonging to the excited state should disappear and only the ground-state signals should remain. Here we observe the same structures in both PP and PDP experiments. However, the PDP data show stronger differences and a modified temporal dependence compared to the PP measurement after the Stokes 'dump' pulse was introduced, and there are no discernible signals that are depleted by stimulated emission pumping. This observation forms our primary motivation for assigning the structural changes observed in the PP conditions to dominating ground-state motion, which is unconnected to the photoisomerization reaction coordinate. This assignment shows that the ground-state nuclear coherence, which is impulsively driven[24,25], dominates the measured displacements. The excited-state coherence is not impulsively prepared; it is purely displacement-driven and insufficiently ordered, whereas the *cis* anionic chromophore product state is seen after full electronic and population decay and thermal proton transfer (Fig. 1). It is concluded that ground-state, rather than excited-state, motions dominate the ultrafast measurements, whereas the product state is only detected with longer waiting times (Fig. 1).

The direct correspondence between the structural changes observed in the PP and PDP experiments prompted further investigation into the electronic origin of the measured femtosecond motions. An ultrafast electronic TA study with 400-nm excitation of the neutral *trans* chromophore (off state) produces induced absorption at 440 nm and a broad stimulated emission spanning 460–600 nm. Including a Stokes 'dump' pulse at 515-nm wavelength and with FWHM power density of 2,800 GW cm^{-2} at either 350-fs or 2-ps delay after the pump fully depletes the stimulated-emission profile across the entire spectral width (Extended Data Fig. 3b–g). Strikingly, the Stokes 'dump' pulse reduces the induced absorption feature to approximately half the original amplitude, prompting assignment of the 440(+)-nm band to a combination of excited-state absorption and induced absorption of an electronic-ground-state intermediate. Fitting of this feature provides an ~4.5-ps time constant for its subsequent decay for samples in solution (Extended Data Fig. 3e,g).

Furthermore, ultrafast PDP optical measurements in crystal samples confirmed the complete depletion of photoisomerization (Extended Data Fig. 2d). A scan of the arrival time of the Stokes 'dump' pulse relative to the pump between negative time and the full

https://doi.org/10.1038/s41557-023-01275-1

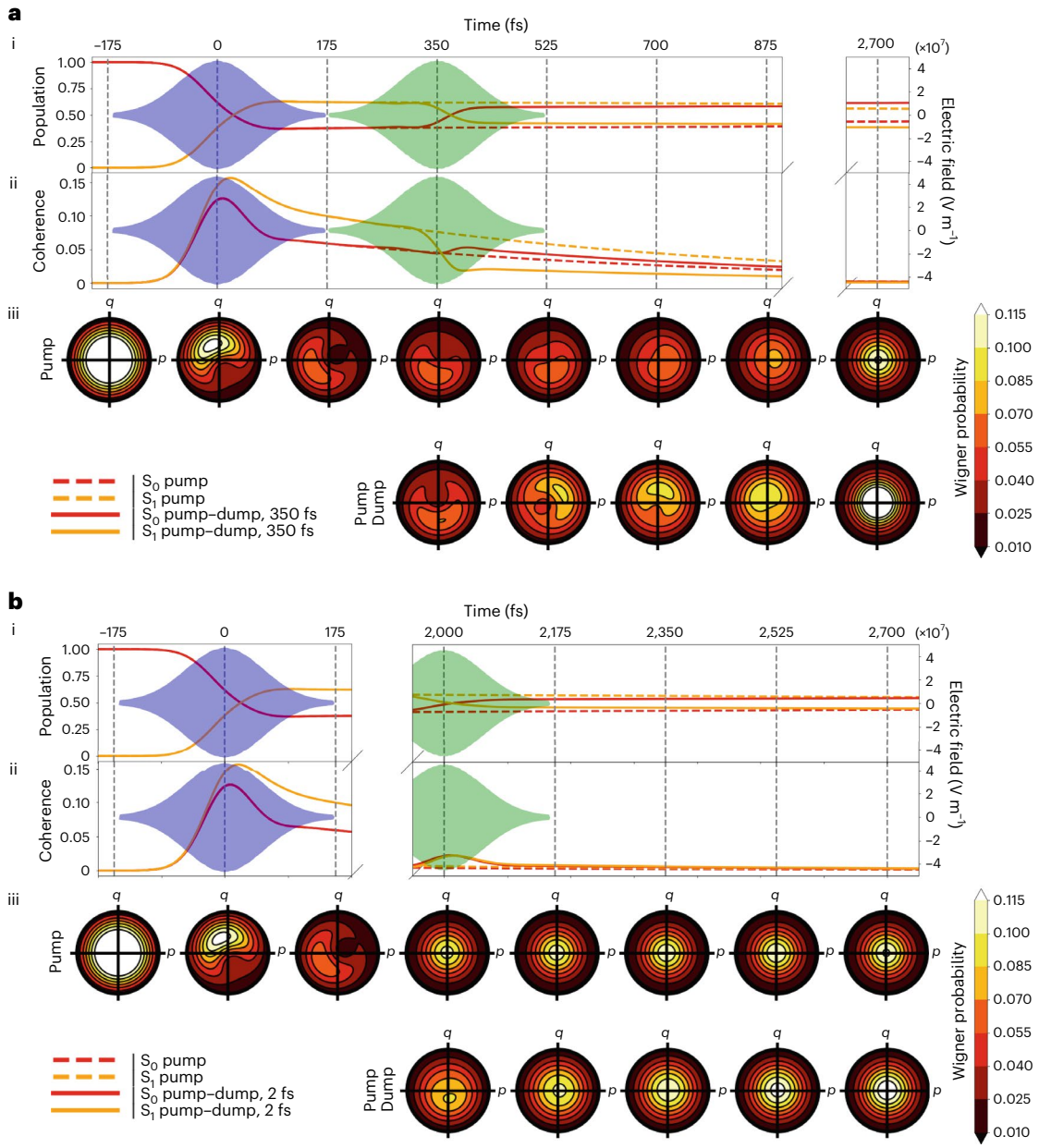

Fig. 4 | Density matrix calculations and resulting Wigner phase-space probability distributions for TR-SFX experimental conditions on rsKiiro using different pulse schemes. Calculations were performed using the parameters listed in Supplementary Table 11, which are representative of the TR-SFX conditions and use the methodology described in Supplementary Section 13. **a**,**b**, Comparison of the populations (**a**(i) and **b**(i)) and coherences (**a**(ii) and **b**(ii)) of the S_0 (red) and S_1 (yellow) electronic states over time, with the pump (dashed lines) and pump–dump (solid lines) schemes shown, for 350-fs pump–dump delay (**a**, corresponding to Figs. 2 and 3a) and 2-ps delay (**b**, corresponding to Fig. 3b). A coherence comparison is made between the pump and short 350-fs (**a**) and long 2-ps (**b**) pump–dump delays. The Wigner phase-space distributions of the S_0 ground state for all pulse schemes are shown in **a**(iii) and **b**(iii), with **a**(iii) showing an increase in asymmetry due to Tannor–Rice coherence transfer from excited to ground state after dump interaction within vibrational dephasing. In contrast, as expected, the longer 2-ps delay after vibrational dephasing in **b**(iii) shows minimal impact on the distribution, with a small generation of position (q) and no impulse momentum (p) transferred, but with population transfer after the dump interaction. The corresponding Wigner transformations for S_1 are shown in Supplementary Fig. 58 using surface representations.

excited-state decay showed the expected cross-correlation in the rise time of the action spectroscopy and was consistent with the 50-ps excited-state decay (Extended Data Figs. 1c and 2a). This is conclusive evidence that *trans–cis* photoisomerization proceeds from the S_1 singlet excited state via thermal barrier crossing, and is not a ground-state process as previously suggested[30]. The action spectroscopy additionally indicates that the isomerization is not vibrationally coherent as shown for rhodopsin[17], but proceeds incoherently throughout the excited-state decay.

In separate experiments at SACLA, a series of tests were performed to confirm the assignment of the ultrafast structural changes to ground-state coherent motions (Fig. 3 and Supplementary Section 5.3). First, for PP conditions, we followed the decay of the photoinduced signals by adjusting the pump–probe delay (Supplementary Fig. 38). A 3-ps pump–probe delay significantly decreased the photoinduced differences compared to the 1-ps delay. The 1-ps delay for the PP and PDP conditions reproduced the results from LCLS (Supplementary Fig. 40).

https://doi.org/10.1038/s41557-023-01275-1

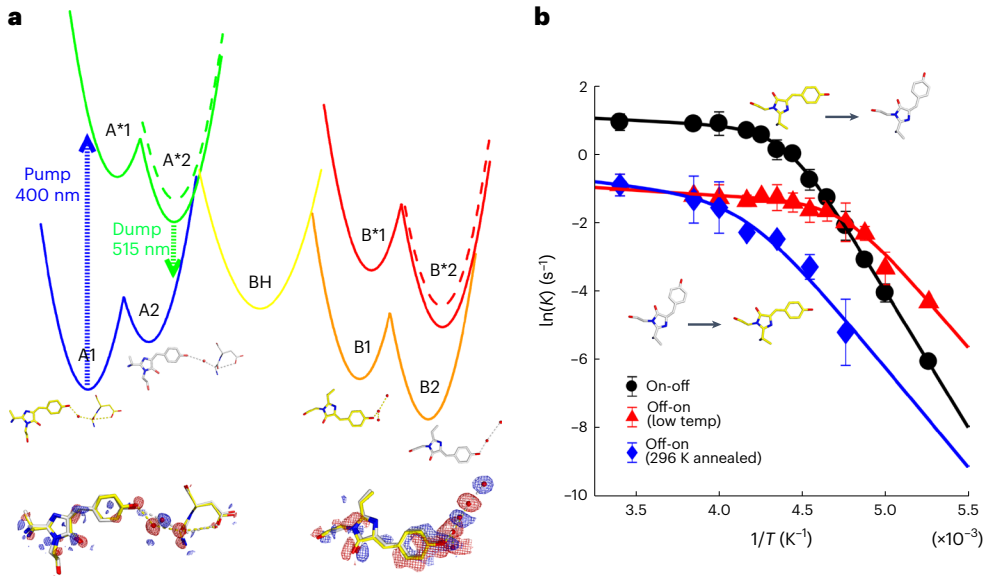

Fig. 5 | Temperature dependence of *trans*(A)–*cis*(B) and *cis*(B)–*trans*(A) photoisomerization kinetics. a, Potentials are shown as adiabatic states that contain the A1 (PDB 7QLM and 7QLJ) and A2 (PDB 7QLN and 7QLO) off-state and B1 (PDB 7QLK) and B2 (PDB 7QLL and 7QLI) on-state structures as shown. The protonated anionic BH state is a putative intermediate that connects the photocycle (Fig. 1). Cryo-trapping of the unrelaxed on state resolved the double-well structural features of the B1 and B2 on states (Supplementary Sections 9 and 11 provide crystallographic details and full thermodynamic modelling, respectively). **b**, Arrhenius plots for the on→off (black) and off→on (red, with low-temperature on→off pre-conversion; blue, with on→off pre-conversion at 296 K) kinetics under continuous illumination at 473 nm and 405 nm, respectively, showing convex behaviour in both directions. The off→on kinetics that included high-temperature annealing before conversion (blue) showed significantly reduced kinetics and shifting of the transition temperature to higher values. Both high- and low-temperature regions involved photoisomerization in both on→off and off→on directions, as shown from X-ray-crystal structural analysis (Supplementary Section 9). The error bars in **b** are the standard error.

Second, for PDP conditions, we tested the dump-induced amplification of ground-state motion as a function of vibrational-coherence decay. Data at 3 ps and 100 ps for the PDP condition at ~350-fs dump time confirmed the overall decay of the initial femtosecond motions (Supplementary Fig. 41). The decay is comparable to the ~4.5-ps lifetime of the induced absorption at 440 nm associated with the ground-state intermediate (Extended Data Fig. 3e,f).

Third, we proceeded with a test of vibrational wave-packet assignment based on coherent control methodology (Fig. 3). In the wave-packet picture, the nuclear motion is also expected to continue after electronic structure change in the Born–Oppenheimer approximation (Fig. 2b). Specifically, the impulse momentum of the wave packet present in the S_1 excited state may be transferred to the electronic ground state if the stimulated emission interaction occurs within the vibrational dephasing time, as shown by the Tannor–Rice scheme[27,31–33]. This coherence transfer adds to nuclear coherence that is created by the displacement, such that both impulse momentum p and position q are generated in the ground state after the dump interaction. This coherence furthermore adds to the ground-state coherence generated by the first pump pulse (Figs. 2–4). The initial excited-state coherence created by the pump pulse results only from displacement and is not impulsive, because the ground state is fully dephased before the arrival of the first pulse. Based on impulsive stimulated Raman spectroscopy measurements of vibrational dephasing of the neutral *cis* chromophore of green fluorescent protein (GFP[34–36]; which shows a typical ~1-ps time constant of decay[34–36]), we chose a 2-ps dump delay relative to the pump to take measurements that are representative of completed vibrational relaxation, but are still well within the 50-ps electronic population-decay time. Following the wave-packet assignment, we predict that the amplitude of momentum transfer by the dump pulse should decay in the delayed condition (2 ps; Fig. 3b). The comparison between the 350-fs and 2-ps dump times very clearly shows a full decay of the photoinduced differences, in line with the predictions from optimal coherent control theory (Fig. 3). This provides further evidence for the conclusion that the photoinduced displacements observed in the TR-SFX experiments are due to impulsive, coherent wave-packet motions on the electronic ground-state potential-energy surface rather than in the electronic excited state. The results of the tests that were performed thus confirm that the PP differences can also be confidently assigned to coherent wave-packet motion in the electronic ground state.

The creation and evolution of the impulse momentum p and position q of nuclear coherence in these experiments are depicted as wave packets in Fig. 2 and in the phase space in Figs. 3 and 4. The first pump interaction creates impulse momentum in the ground state in the direction of the nuclear binding force, and it creates position q in S_1 that is not impulsive[23–26]. Evolution of the coherences in S_0 and S_1 is depicted with the periodic interconversions of p and q according to their frequencies (Figs. 2–4) and their amplitude decays with the vibrational dephasing time. With the arrival of the dump pulse at 350 fs within the dephasing time, the wave-packet momentum is transferred from S_1 to S_0 and creates additional position q via the displacement (Figs. 2–4). When the dump pulse arrives at 2 ps, the vibrational coherence has decayed but the electronic excitation has not. In this case the dump pulse does not transfer momentum but only creates position (Figs. 3b and 4b).

We performed a non-perturbative density-matrix simulation that fully verified the coherence dynamics that were observed (Supplementary Table 11 and Supplementary Section 13). The electronic and nuclear wavefunctions are represented by the density matrix, and the pump and dump interactions are included according to the experimental frequencies and timings. The density matrix evolves under the Liouville–von Neumann equation, and the coherence and population progression and transfer are analysed using Wigner transforms. These can be separated for S_0 and S_1 to provide their momentum and position[37]. Specifically, the wave-packet dynamics are observed in the transfer and subsequent rotation of the two-dimensional surfaces in

phase space that represent the quasi-probabilistic distributions of position and momentum, which are equivalent to the schematic depiction in phase space shown at the top of Fig. 3. The rotation in phase space interconverts the impulse momentum and position and represents the vibrational coherence. Vibrational dephasing returns this surface to the centre of phase space, which represents the dephased populations in S_0 and S_1. The simulations are shown for the ground state in Fig. 4, and demonstrate the expected coherence evolution and transfer for the PP and PDP conditions as well as the dephasing conditions, with loss of momentum transfer that matches the diagrammatic representation shown in Fig. 3. Strikingly, the density-matrix simulation for the PDP condition doubles the magnitude of the ground-state coherence following the dump interaction (Fig. 4). This demonstrates the essential mechanism of amplification of ultrafast motion under conditions of PDP within the vibrational dephasing time.

The simulations lend strong support to the assignments for the PP and PDP crystallographic data, with the latter showing distinct amplification of motion. The wave-packet generation in these simulations can be readily extended to a double-well adiabatic potential that describes the time-resolved crystal structures (Fig. 2). The phase-space representation is particularly appropriate for representing and analysing the quantum dynamics, because it relates more directly to the real-space measurements of TR-SFX. The conclusions are furthermore fully consistent with the wave-packet description in Raman spectroscopy[23–25,31–33,38] and the wave-packet description of coherent control by Tannor et al.[31], Kosloff et al.[32], and Ruhman and Kosloff[33].

To derive the functional importance of the double-well adiabatic potential discovered in our ultrafast crystallography experiments, we combined the structural information with kinetics measurements and thermodynamics modelling. The double-well adiabatic nature of both the off and on states was additionally shown from the thermodynamic analysis of reversible photoisomerization as well as the excited-state decay. The temperature dependence of both *trans–cis* and *cis–trans* photoisomerization shows convex non-Arrhenius kinetics in which the transition temperature is additionally sensitive to structural annealing, which lowers the 'A*2' potential level (Fig. 5). Convex Arrhenius kinetics are conventionally analysed using parameters for double-well potentials. Modelling of the non-Arrhenius kinetics invoked an entropy–enthalpy compensation scheme and retrieved the relaxation parameters of the second energy level of the double-well potential (Figs. 2 and 5, A1*, A2*, Extended Data Fig. 1e,k and Supplementary Section 10.5). The detailed modelling uses the experimental separation of the radiative and non-radiative transitions, which show different barrier values (Extended Data Fig. 1f,l). Full thermodynamics treatment and theoretical considerations are provided in Supplementary Section 10. The reaction model that emerges is fully consistent with the time-resolved crystallography and also the QM/MM calculations. The barrier for internal conversion arises from viscosity dependence, which indicates that substantial reconfiguration is involved. Experimental evidence from the PDP yield in crystals and solutions furthermore supports that the non-adiabatic reaction dynamics proceed thermally throughout the 50-ps lifetime of the off state (Extended Data Fig. 2). The photoisomerization trajectory is therefore not directly observed in the time-resolved measurements because the photoproduct accumulates throughout the duration of the excited-state lifetime of 50 ps.

In conclusion, we have demonstrated a successful coherent control experiment with X-ray crystallographic observation. We show that ultrafast structural changes observed in TR-SFX of a reversibly photoswitchable fluorescent protein can be assigned with the application of optical control. The evidence illustrates that the data from conventional femtosecond PP measurements of the structural dynamics of the chromophore and protein are unrelated to the photoisomerization coordinate in our experiments. We present extensive experimental evidence that the PP and PDP data collected within the vibrational dephasing time in effect measured impulsively prepared electronic ground-state coherent wave-packet motion. The results are relevant to typical experimental conditions for TR-SFX that use a 50–100-fs optical pulse duration that limit the frequency of impulsively driven modes. Because the crystallographic differences are dominated by modes that have large displacement, increasing the experimental bandwidth will probably still contain such low-frequency modes[27]. Furthermore, the results clearly show that the commonly used technique of rate kinetics analysis, which is restricted to model concentration differences of static species, does not apply to the assignment of structural dynamics on the ultrafast timescale of vibrational dephasing that additionally have heterogeneous contributions. This report offers fundamental tools and methods for experimental execution and theoretical analysis of ultrafast crystallography. We emphasize the use of phase-space representation of the density matrix using the Wigner transform to visualize the coherent motions that are seen. The Wigner transform provides the evolution of nuclear position from explicit quantum dynamics simulations that use experimental conditions including coherent control and electronic and vibrational coherence. These methods are generally applicable, and their purpose is fully demonstrated with this example of ultrafast structural dynamics of a reversibly photoswitching fluorescent protein.

Online content

Any methods, additional references, Nature Portfolio reporting summaries, source data, extended data, supplementary information, acknowledgements, peer review information; details of author contributions and competing interests; and statements of data and code availability are available at https://doi.org/10.1038/s41557-023-01275-1.

References

1. Warren, M. M. et al. Ground-state proton transfer in the photoswitching reactions of the fluorescent protein Dronpa. *Nat. Commun.* **4**, 1461 (2013).
2. Du, M. & Fleming, G. R. Femtosecond time-resolved fluorescence spectroscopy of bacteriorhodopsin: direct observation of excited state dynamics in the primary step of the proton pump cycle. *Biophys. Chem.* **48**, 101–111 (1993).
3. Gai, F. Chemical dynamics in proteins: the photoisomerization of retinal in bacteriorhodopsin. *Science* **279**, 1886–1891 (1998).
4. Okada, T. et al. Functional role of internal water molecules in rhodopsin revealed by X-ray crystallography. *Proc. Natl Acad. Sci. USA* **99**, 5982–5987 (2002).
5. Polli, D. et al. Conical intersection dynamics of the primary photoisomerization event in vision. *Nature* **467**, 440–443 (2010).
6. Bischoff, M., Hermann, G., Rentsch, S. & Strehlow, D. Ultrashort processes of native phytochrome: femtosecond kinetics of the far-red-absorbing form Pfr. *J. Phys. Chem. A* **102**, 4399–4404 (1998).
7. Dasgupta, J., Frontiera, R. R., Taylor, K. C., Lagarias, J. C. & Mathies, R. A. Ultrafast excited-state isomerization in phytochrome revealed by femtosecond stimulated Raman spectroscopy. *Proc. Natl Acad. Sci. USA* **106**, 1784–1789 (2009).
8. Ihee, H. et al. Visualizing reaction pathways in photoactive yellow protein from nanoseconds to seconds. *Proc. Natl Acad. Sci. USA* **102**, 7145–7150 (2005).
9. Schmidt, M. et al. Protein energy landscapes determined by five-dimensional crystallography. *Acta Crystallogr. D Biol. Crystallogr.* **69**, 2534–2542 (2013).
10. Creelman, M., Kumauchi, M., Hoff, W. D. & Mathies, R. A. Chromophore dynamics in the PYP photocycle from femtosecond stimulated Raman spectroscopy. *J. Phys. Chem. B* **118**, 659–667 (2014).
11. Tenboer, J. et al. Time-resolved serial crystallography captures high-resolution intermediates of photoactive yellow protein. *Science* **346**, 1242–1246 (2014).

12. Pande, K. et al. Femtosecond structural dynamics drives the *trans*/*cis* isomerization in photoactive yellow protein. *Science* **352**, 725–729 (2016).
13. Romei, M. G., Lin, C. Y., Mathews, I. I. & Boxer, S. G. Electrostatic control of photoisomerization pathways in proteins. *Science* **367**, 76–79 (2020).
14. Ando, R., Mizuno, H. & Miyawaki, A. Regulated fast nucleocytoplasmic shuttling observed by reversible protein highlighting. *Science* **306**, 1370–1373 (2004).
15. Zhou, X. X., Chung, H. K., Lam, A. J. & Lin, M. Z. Optical control of protein activity by fluorescent protein domains. *Science* **338**, 810–814 (2012).
16. Dickson, R. M., Cubitt, A. B., Tsien, R. Y. & Moerner, W. E. On/off blinking and switching behaviour of single molecules of green fluorescent protein. *Nature* **388**, 355–358 (1997).
17. Wang, Q., Schoenlein, R., Peteanu, L., Mathies, R. & Shank, C. Vibrationally coherent photochemistry in the femtosecond primary event of vision. *Science* **266**, 422–424 (1994).
18. Chang, J., Romei, M. G. & Boxer, S. G. Structural evidence of photoisomerization pathways in fluorescent proteins. *J. Am. Chem. Soc.* **141**, 15504–15508 (2019).
19. Barends, T. R. M. et al. Direct observation of ultrafast collective motions in CO myoglobin upon ligand dissociation. *Science* **350**, 445–450 (2015).
20. Nogly, P. et al. Retinal isomerization in bacteriorhodopsin captured by a femtosecond X-ray laser. *Science* **361**, eaat0094 (2018).
21. Nass Kovacs, G. et al. Three-dimensional view of ultrafast dynamics in photoexcited bacteriorhodopsin. *Nat. Commun.* **10**, 3177 (2019).
22. Coquelle, N. et al. Chromophore twisting in the excited state of a photoswitchable fluorescent protein captured by time-resolved serial femtosecond crystallography. *Nat. Chem.* **10**, 31–37 (2018).
23. Mukamel, S. *Principles of Nonlinear Optical Spectroscopy* (Oxford Univ. Press, 1995).
24. Kumar, A. T. N., Rosca, F., Widom, A. & Champion, P. M. Investigations of ultrafast nuclear response induced by resonant and nonresonant laser pulses. *J. Chem. Phys.* **114**, 6795–6815 (2001).
25. Kumar, A. T. N., Rosca, F., Widom, A. & Champion, P. M. Investigations of amplitude and phase excitation profiles in femtosecond coherence spectroscopy. *J. Chem. Phys.* **114**, 701–724 (2001).
26. van Thor, J. J. Advances and opportunities in ultrafast X-ray crystallography and ultrafast structural optical crystallography of nuclear and electronic protein dynamics. *Struct. Dyn.* **6**, 050901 (2019).
27. Hutchison, C. D. M. & van Thor, J. J. Populations and coherence in femtosecond time resolved X-ray crystallography of the photoactive yellow protein. *Int. Rev. Phys. Chem.* **36**, 117–143 (2017).
28. Wiedenmann, J. et al. EosFP, a fluorescent marker protein with UV-inducible green-to-red fluorescence conversion. *Proc. Natl Acad. Sci. USA* **101**, 15905–15910 (2004).
29. Bardeen, C. J., Wang, Q. & Shank, C. V. Selective excitation of vibrational wave packet motion using chirped pulses. *Phys. Rev. Lett.* **75**, 3410–3413 (1995).
30. Laptenok, S. P. et al. Infrared spectroscopy reveals multi-step multi-timescale photoactivation in the photoconvertible protein archetype dronpa. *Nat. Chem.* **10**, 845–852 (2018).
31. Tannor, D. J., Kosloff, R. & Rice, S. A. Coherent pulse sequence induced control of selectivity of reactions: exact quantum mechanical calculations. *J. Chem. Phys.* **85**, 5805–5820 (1986).
32. Kosloff, R., Rice, S. A., Gaspard, P., Tersigni, S. & Tannor, D. J. Wavepacket dancing: achieving chemical selectivity by shaping light pulses. *Chem. Phys.* **139**, 201–220 (1989).
33. Ruhman, S. & Kosloff, R. Application of chirped ultrashort pulses for generating vibrational coherence: a computer simulation. *J. Opt. Soc. Am. B* **7**, 1748–1752 (1990).
34. Fang, C., Frontiera, R. R., Tran, R. & Mathies, R. A. Mapping GFP structure evolution during proton transfer with femtosecond Raman spectroscopy. *Nature* **462**, 200–204 (2009).
35. Fujisawa, T., Kuramochi, H., Takeuchi, S. & Tahara, T. Time-resolved impulsive Raman study of excited state structures of green fluorescent protein. In *Proc. Ultrafast Phenomena XIX* (Eds Yamanouchi, K. et al.) 539–542 (Springer, 2015); https://doi.org/10.1007/978-3-319-13242-6_132
36. Fujisawa, T., Kuramochi, H., Hosoi, H., Takeuchi, S. & Tahara, T. Role of coherent low-frequency motion in excited-state proton transfer of green fluorescent protein studied by time-resolved impulsive stimulated Raman spectroscopy. *J. Am. Chem. Soc.* **138**, 3942–3945 (2016).
37. Wigner, E. On the quantum correction for thermodynamic equilibrium. *Phys. Rev.* **40**, 749–759 (1932).
38. Hutchison, C. D. M. et al. X-ray free electron laser determination of crystal structures of dark and light states of a reversibly photoswitching fluorescent protein at room temperature. *Int. J. Mol. Sci.* **18**, 1918 (2017).

[1]Department of Life Sciences, Faculty of Natural Sciences, Imperial College London, London, UK. [2]Diamond Light Source Ltd, Harwell Science & Innovation Campus, Didcot, UK. [3]Quantum Optics and Laser Science Group, Blackett Laboratory, Imperial College London, London, UK. [4]Department of Chemistry, Stanford University, Stanford, CA, USA. [5]Physics Department, University of Wisconsin-Milwaukee, Milwaukee, WI, USA. [6]Physikalisch Chemisches Institut, Ruprecht-Karls Universität Heidelberg, Heidelberg, Germany. [7]Nanoscience Center and Department of Chemistry, University of Jyväskylä, Jyväskylä, Finland. [8]Pohang Accelerator Laboratory, POSTECH, Pohang, Republic of Korea. [9]Department of Chemical Engineering, POSTECH, Pohang, Republic of Korea. [10]RIKEN SPring-8 Center, Sayo, Hyogo, Japan. [11]Institute of Multidisciplinary Research for Advanced Materials, Tohoku University, Sendai, Miyagi, Japan. [12]Department of Cell Biology, Graduate School of Medicine, Kyoto University, Sakyo, Kyoto, Japan. [13]Japan Synchrotron Radiation Research Institute, Sayo, Hyogo, Japan. [14]Linac Coherent Light Source, Stanford Linear Accelerator Centre (SLAC), National Accelerator Laboratory, Menlo Park, CA, USA. [15]Center for Free-Electron Laser Science, Deutsches Elektronen-Synchrotron, Hamburg, Germany. [16]These authors contributed equally: Christopher D. M. Hutchison, James M. Baxter. ✉e-mail: j.vanthor@imperial.ac.uk

Methods

Protein expression and purification

Recombinant expression of the rsKiiro sequence cloned into pEGFP-N1 (Clontech), containing L62A and M159T mutations of the monomeric reversibly switchable mEos3 (ref. 39) construct based on the EosFP fluorescent protein from the stony coral *Lobophyllia hemprichii*[28], was carried out in *Escherichia coli* BL21(DE3). Large-scale fermentation was carried out using a 50-l culture of Terrific broth (48.2 g l^{-1}) (Sigma-Aldrich, T9179) containing 50 mg l^{-1} kanamycin and 10.1 g l^{-1} glycerol at 37 °C. When the culture reached an optical density at 600 nm (OD_{600}) of ~2, the bioreactor was cooled to 15 °C, and induction of expression was carried out by the addition of isopropyl β-D-1-thiogalactopyranoside (0.12 g l^{-1}; Sigma-Aldrich, CAS 367-93-1). Lysis was carried out using a buffer (50 mM Tris-HCl pH 8.0, 100 mM NaCl) per gram of wet cell mass including 0.1 mg ml^{-1} DNase I (Sigma-Aldrich, CAS 9003-98-9) and one tablet of EDTA-free protease inhibitors (Sigma-Aldrich) per 20 g of cell mass. The protein was purified using His-Pur Ni-NTA chromatography resin (Thermo Fisher Scientific) by elution in a single isocratic step with elution buffer (50 mM Tris-HCl, pH 8.0, 100 mM NaCl, 350 mM imidazole). The eluate was concentrated and exchanged into gel filtration buffer (50 mM Tris-HCl pH 8.0, 100 mM NaCl) and purified using an XK26/70 chromatography column (GE Lifesciences) packed with 300 ml of Superdex S75 gel filtration resin (GE Lifesciences). Fractions were concentrated to ~60 mg ml^{-1} and exchanged in final buffer (50 mM Tris-HCl pH 8.0, 50 mM NaCl) before storing at −20 °C.

Crystallization and sample preparation

Crystallization conditions were based on those previously described[38]. Micro-crystals were grown using the seeded batch method. Two different conditions were used—10 mg ml^{-1} protein concentration and 25% (wt/vol) PEG 3350 (Sigma-Aldrich, CAS 25322-68-3) and 15 mg ml^{-1} and 30% (wt/vol) PEG 3350—and both sets of conditions included 0.1 M Tris (Sigma-Aldrich, CAS 77-86-1) pH 8.5, 0.2 M lithium sulfate (Sigma-Aldrich, CAS 10377-48-7) and 1.5% (vol/vol) seed. Seed stocks were prepared using either condition and subsequently filtered with 50- and 30-µm CellTrics filters (Sysmex Partec). Crystallization was performed in 2-ml round-bottom Eppendorf tubes, and the addition of reagents followed the order 'buffer, precipitant, protein and seed' in a final 1-ml volume followed by gentle mixing. Needle-shaped micro-crystals with dimensions of ~3 × 5 × 10–100 µm matured after 24 h at 20 °C. To reduce issues with blockages during crystal injection, especially with the Gas Dynamic Virtual Nozzle (GDNV) during LCLS[40] injection, further size optimization was performed by breaking up the micro-crystals using glass beads (Supplementary Section 1 describes the procedure).

SFX sample injection

At LCLS CXI, micro-crystals were delivered into the interaction region using a GDVN[40] with 75-µm aperture, which was modified by removing the opaque coating surrounding the inner capillary to allow pre-illumination of the sample before injection. The flow rate was varied between 10 and 30 µl min^{-1} to maximize the hit rate and stability. At SACLA, a piezo-driven droplet-on-demand injector with an 80-µm nozzle (MICROJET, IJHDS-1000) was used. Approximately 300 µl of crystal slurry at 1×10^8 Xtal ml^{-1} was reverse-loaded through the jetting aperture to reduce the chance of blockages and crystal settling in the lines and reservoir. The piezo was driven with 110-V, 100-µs current pulses, which were slightly varied depending on the jetting behaviour. With optimization of the driving current pulse, jet position, jet timing and sample concentration, a hit rate of 50–80% was maintained for the majority of the data collection. This was greatly assisted by the synchronized live imaging of the droplets and almost live (few second delay) hit rate provided by the SACLA pipeline[41]. At PAL-XFEL, micro-crystal slurry was resuspended in monoolein (1-oleoyl-*rac*-glycerol, Sigma-Aldrich) in a 1:2 ratio of slurry (6.4×10^7 Xtal ml^{-1}) to monoolein, chosen for stable jetting and hit rate. The monoolein suspension was injected into the interaction region using a modified 100-µl syringe (Hamliton Gastight 1710 with 22-G style 3 needle), whose plunger was coupled to a second larger-diameter (5 mm) water syringe driven by a high-performance liquid chromatography pump. The water syringe was driven at 75.3 µl min^{-1}, corresponding to 6.42 µl min^{-1} in the Hamilton syringe, which in turn corresponds to an extrusion velocity of ~6 mm s^{-1} or ~200 µm per pulse at 30 Hz out of the 150-µm needle aperture. This high flow rate was necessary to ensure sufficient sample exchange between laser shots to prevent double exposure of sample due to the pump laser spot size of ~140 µm (FWHM) (see below) and possible 'light piping' up the continuous monoolein stream.

SFX data collection

This work includes data from four XFEL beamtimes, LCLS CXI LR23 (February 2018), SACLA BL3 EH2 2017B8008 (March 2018), 2019B8021 (November 2019) and PAL-XFEL 2020-2nd-NCI-007 (September 2020). A summary of the conditions and delays collected at each beamtime is provided in Extended Data Table 1.

At CXI, X-ray diffraction data were collected using the Cornell Stanford Pixel Area Detector (CS-PAD)[42] at a distance of 50.7 mm, determined through optimization of unit-cell distributions (Supplementary Figs. 1 and 2). LCLS was operated at 9.5 keV with ~1 mJ of X-ray energy. At SACLA, the MPCCD[43] detector was used, and the increased quantum efficiency of the phase III version of this detector allowed the SACLA to be operated at 10.5 keV, increasing the measurable resolution without significant reduction in signal to noise. The detector distance was determined to be 50.6 mm (Supplementary Figs. 3 and 4). Data were collected, interleaved pumped and unpumped with a ratio of 5:1, throughout the SACLA and LCLS beamtimes, and a comparison of 'only pre-illuminated' (that is, no femtosecond illumination) and interleaved unpumped datasets showed no significant differences, demonstrating that scatter from the pump or dump pulses did not impact subsequent shots. This allowed all dark data to be merged for creating difference maps. PP and PDP TR-SFX data were collected at picosecond and sub-picosecond delays, as well as dump only and negative delay controls. At PAL-XFEL, the MICOSS[44] sample chamber was used with a Rayonix MX225-HS detector in 4 × 4 binning mode to allow 30-Hz operation. The XFEL was operated at 12.4 keV with a bandwidth of 17.5 eV (r.m.s.) and pulse duration of 21.47 fs (FWHM), and the beam was attenuated to ~0.6 mJ as a compromise between X-ray flux and stable jetting. Due to the slower jetting speed of the viscous media injector, the interleaving pattern was set at 1:1 to more accurately characterize the pump scatter onto subsequent crystals.

TR-SFX optical excitation

At LCLS LR23, optical excitation pulses were provided by the on-site synchronized Ti:sapphire laser system. The 515-nm dump pulses were produced using an optical parametric amplifier (OPA) (TOPAS-Prime, Spectra Physics), and the remaining fundamental was taken after the final stage of the OPA and doubled using a 100-µm second-harmonic generation (SHG) beta-barium borate (BBO) nonlinear crystal (EKSMA Optics) to create the 400-nm pump pulses. Temporal delay between the two pulses was controlled using a motorized mirror inside the OPA. The pump and dump optical arms each had their own linear polarizer and $\lambda/2$ waveplate to allow independent control of polarization and pulse energy. The 'needle-like' nature of the crystals causes a tendency to align vertically out of the GDVN jet, and to reduce potential pumping suppression due to electric-field decomposition inside the crystals[45], both the pump- and dump-pulse polarizations were inclined at the same 45° to the jetting direction. Spatial overlap between the pulses and the X-rays was achieved using the fluorescence on a Ce:YAG scintillator screen, and this overlap was checked at the start and end of every shift. The final energy densities on the target of the pump and dump were 2 ± 0.1 mJ mm^{-2} and 4 ± 0.1 mJ mm^{-2}, respectively. Samples were

pre-illuminated using an array of five 10-W, 490-nm LEDs on a 1.5-m loop of tubing before injection. In addition, light from a single 3-W, 490-nm LED, installed outside the experimental chamber, was focused onto the transparent tip of the GDVN using a series of lenses. Course temporal overlap between the pump and dump pulses was obtained using a fast photodiode and oscilloscope. The final timing between the pump and dump pulses (~350 fs) and time zero with the XFEL was achieved by performing cross-correlations in a scintillator screen (Supplementary Fig. 6).

During SACLA 2017B8008 and 2019B8021, the optical pulses were provided by an onsite synchronized Ti:sapphire laser. The 515-nm pulses were generated by an OPA (HE-TOPAS), and for the 400-nm pulses a proportion of the fundamental was taken before the OPA and sent on a long optical delay to compensate the path inside the OPA, and then frequency-doubled using a 100-µm SHG BBO crystal. The pump–dump temporal delay was controlled by a motorized delay stage installed in the 515-nm arm. The samples were focused on the X-ray interaction region using a 300-mm lens, achieving the same energy densities as those used at LCLS. Pre-illumination was performed by illuminating the glass tip of the droplet injector with the unfocused beam (5 × 3 mm) of a 60-mW 488-nm c.w. diode laser. Both the power density and the pump–dump delay of ~500 fs, which is well within vibrational dephasing, matched the previous LCLS conditions, but frequency-resolved optical gating (FROG) characterization showed the pulse durations to be significantly shorter at 40 fs and 52 fs for the pump and dump, respectively (Supplementary Table 1).

Data processing

The rsKiiro crystals were indexed in space group $P2_12_12_1$, with $a = 39.44 \pm 0.05$, $b = 74.18 \pm 0.12$, $c = 78.83 \pm 0.12$, $\alpha = 90°$, $\beta = 90°$ and $\gamma = 90°$. Analysis of TR-SFX data at LCLS LR23 was performed using the Cheetah[46] and CrystFEL[47] software packages. Dark scans were taken approximately every 20–40 runs, which recorded images from the CS-PAD detectors in the absence of illumination to establish bad/damaged pixels, which were subsequently masked out before running indexing algorithms. The Cheetah package was used to perform hit finding. Before indexing and integration, nearly every run was manually masked to remove substantial shrouding caused by the shadow of the nozzle on the detected on images. The CrystFEL package was used to index and integrate the hits identified by Cheetah. Two indexing algorithms, DIRAX[48] and MOSFLM[49], were compared to identify which performed better, with both being fed the previously determined unit cell. The beam centre was monitored to account for any drift in the beam position relative to the input detector geometry file, with any offset being corrected. The detector distance was also refined in steps of 0.1, 0.05 and finally 0.01 and 0.001 mm by monitoring the detected distribution of unit cells from the output of the indexing algorithm until it narrowed and became symmetric (Supplementary Figs. 1 and 2). The optimized geometry yielded single narrow distributions with standard deviations of <0.5 Å for lattice axes and ~1° for the angles, while the unoptimized geometry showed deviations >1 Å in addition to showing a bimodal distribution for the *c* axis of the lattice. An L-test was also used in conjunction to monitor for crystal twinning, which appeared to be very high until the proper detector distance was determined. With unoptimized geometry, a twin fraction of 16–17% was observed, which improved to 6% upon optimization. This value remained slightly higher than expected, but was acceptable given a single set of narrow lattice distributions and appropriate *R*-factors. Although the detector was moved and replaced on a number of occasions, it was not found to be necessary to optimize the detector distance for each run individually, as a single optimized distance produced reasonable cell distributions and indexing results for the entire dataset. Indexing results were also found to be relatively insensitive to algorithm parameters such as integration radii or minimum signal-to-noise ratio requirements. For a number of runs, an electronic gain mask was used to avoid saturation of pixels at low resolution while maintaining sensitivity at high resolution. After indexing all runs with the optimized detector geometry, masked images and gain mask applied, the individual intensities were merged using the Monte Carlo method from the routine process_hkl included in CrystFEL, without consideration of a partiality model.

Data from SACLA 2019B were analysed in a manner similar to the data from LCLS with a number of minor differences. First, the nozzle in the SACLA experiment was sufficiently far away to avoid the shrouding issues from LCLS, and so no additional masking was needed beyond the removal of damaged pixels. Second, all SACLA data were collected in a single-gain mode, so no gain mask was included for the analysis. Finally, two additional indexing algorithms were tested for the analysis, TakeTwo[50] and XGANDALF[51]. The SACLA experiment had a particularly high hit rate (>60%), which typically means that recorded images contain diffraction patterns from multiple micro-crystals. These two algorithms were designed specifically for SFX experiments and a view to the indexing of multiple lattices per single image. For our dataset we found that XGANDALF performed the best, with an indexing rate of over 100% (that is, more than one lattice per image) for most runs. The same sensitivity to detector distance and systematic optimization was required (Supplementary Figs. 3 and 4).

At PAL-XFEL, Cheetah was only used for peak finding and for applying the beam-stop mask, not live hit-rate monitoring. Hit-finding parameters were initially optimized based on CrystFEL's indexing performance and manual inspection of laser off-condition images. The PAL-XFEL experiment used a commercial Rayonix MX225-HS detector. Unlike the detectors at SACLA and LCLS, this is a commercial detector, which has a pre-applied geometry correction and automatically subtracts a dark image, negating the need for manual hot/dark pixels masking in Cheetah. This meant that only the beam-centre and detector distance had to be optimized, not the geometry of individual detector panels. To maximize the merged data quality, two indexing programs, MOSFLM[49] and XGANDALF[51], were directly compared. XGANDALF was found to provide the best results, so it was selected as the indexing algorithm.

Crystallographic analysis

Bash scripts based on ref. 52 processed each light and dark bin to generate so-called *Q*-weighted electron difference density maps (maps based on Bayesian statistical analysis by Ursby and Bourgeois[53], and Terwilliger and Berendzen[54]), which were then interpreted by generating extrapolated electron density, for which 'light' coordinates were refined too. The PHENIX reflection conversion function, using the massage option, was used to convert intensities to structure factors[55]. Calculated structure factors from SFALL (CCP4i[56]) using the ground-state refinement model were combined with observed structure factors and combined into one file using CAD (CCP4i[56]). The observed structure factors were then scaled onto an absolute scale using anisotropic scaling in SCALEIT (CCP4i[56]), using a resolution cutoff at 1.5 Å for all experimental conditions. For coordinate refinement, relevant low- and high-resolution limits were applied depending on the experiment (maximum of 1.35, 1.44 and 1.42 Å at LCLS, SACLA and PAL-XFEL, respectively). The low-resolution limit was set between 20 and 30 Å. Difference structure factors were then weighted as described by Pandey et al.[52], and fast Fourier transform (CCP4i[56]) was used to convert the structure factors into a real-space map.

Extrapolated electron-density maps were generated, and extrapolated coordinates then refined to these maps. Difference structure factors, ΔF, were added in a linear combination in multiples of N_{EXT} to the calculated dark structure F_{Dark} to generate extrapolated structure factors, F_{EXT}. The negative electron density above the 3 r.m.s. level and a 7-Å radius around the chromophore were then integrated using published Fortran code[52]. The point where negative density started to build up was used to determine a characteristic N_{EXT} value, which was then used to generate the final extrapolated structure factors. Coordinates

were refined against the extrapolated structure factors using five cycles of rigid body refinement in REFMAC[57] and further real-space refinement using Coot[58] real-space refinement. The population transfer (PT) can be approximated from the N_{EXT} value as PT = 200/N_{EXT}.

Crystallographic statistics are shown in Table 1 and Extended Data Table 2 for LCLS, Supplementary Tables 4 and 5 for SACLA and Supplementary Table 6 for PAL-XFEL.

Solution steady-state spectroscopy

The highly fluorescent 'on' state of rsKiiro, corresponding to the *cis* conformation of the chromophore, has a characteristic absorption peak at 486 nm with a calculated absorption coefficient of 117,500 M^{-1} cm^{-1}. When illuminated within this band, it photoswitches to a metastable 'off' state with the *trans* conformation, with peak absorption at 388 nm (44,000 M^{-1} cm^{-1}) and highly reduced fluorescence (Extended Data Fig. 1b). The UV–vis solution spectra of the on and off states, collected with a spectrophotometer (Agilent 8453), are provided in Extended Data Fig. 1a. Extinction coefficients were calculated from the amino-acid aromatic ring absorption at 280 nm relative to the parent molecule (Skylan-NS[59]). Once converted, the off state thermally recovers to the on state with a time constant of ~40 min at 293 K. The thermal recovery rates were measured as a function of temperature (284–323 K) using a water feed cuvette holder coupled to a water bath (Julabo F12). Excited-state barrier heights (E_a) were determined by fitting of the Arrhenius equation:

$$\frac{1}{\tau} = \mathscr{A}_1 + \mathscr{A}_2 e^{-\frac{E_a}{RT}}$$

where $\mathscr{A}_1$ and $\mathscr{A}_2$ are temperature-independent constants, R is the gas constant, T is the temperature and τ is the inverse rate constant. A plot and fitting are shown in Extended Data Fig. 1c, where the fitting yields an energy barrier between the off and on states of 91 ± 5 kJ mol^{-1}.

Microsecond TA spectroscopy

TA spectroscopy was performed on solution samples of rsKiiro using a home-built device[60]. A 6-µl volume of 6 mg ml^{-1} rsKiiro solution was added to 50 µl of buffer to give an OD_{400} of ~0.2 with the 3-mm path length of the three-windowed quartz cuvette (Quartz SUPRASIL High Precision Cell, Hellma Analytics). The sample was pre-illuminated using an unfocused 15-mW, 473-nm, c.w. Transistor-transistor logic trigger laser for 10 ms at 20 Hz. A xenon pump lamp was filtered using a blue filter (FGB25 Thorlabs), resulting in ~150 µJ per flash in the 300–450 nm range, focused to a 3 × 1-mm elliptical spot inside the sample cuvette. The thermal recovery time constant of rsKiiro is ~40 min at 20 °C, so the sample was left with all three light sources flashing for 1 h to equilibrate before data collection. Approximately 4,000 PP spectra were collected at each delay. The time-resolved spectra are provided in Extended Data Fig. 3i. There is an increasing absorption at 486 nm with a time constant of 40 ± 10 µs, corresponding to formation of the *cis* anion (Extended Data Fig. 1a).

Femtosecond optical TA spectroscopy

Femtosecond TA spectroscopy of rsKiiro was performed using a previously described system[61]. The 400-nm pump pulses were generated by doubling the 100-fs fundamental at 800 nm (Hurricane, Spectra Physics) in a 100-µm-thick SHG-BBO device (EKSMA optics), and 515-nm dump pulses were generated using an OPA (OPA-C Spectra Physics). White-light probe pulses were generated using filamentation in a CaF_2 glass window.

A 20-µl solution sample of rsKiiro at 62 mg ml^{-1} was loading into a liquid cell (Harrick Scientific Products) between 1-mm (front) and 2-mm (back) sapphire windows (Crystran), using a 25.6-µm spacer corresponding to a peak absorption of ~0.3 at 380 nm when converted to the off state. The sample was continuously translated and illuminated using an unfocused 50-mW, 488-nm diode laser to convert the sample to the target off state. A second-order polynomial and linear interpolation was used to correct the majority inherent spectral chirp of the white-light probe. The Ultrafast Spectroscopy Modelling Toolbox[62] was used to globally fit the corrected TA datasets and recover the time-independent evolution associated difference spectra (EADS).

The weak pumping (7 GW cm^{-2}) PP transient absorption difference spectra of the off state with 400-nm pumping are shown in Extended Data Fig. 3d. Two sequential spectra with similar forms were recovered, with time constants of 7.6 ps and 50 ps. The negative signal observed at 385–400 nm is assigned to the ground-state bleach (GSB), the positive signal between 420 and 475 nm to excited-state absorption (ESA) and the negative signal at >480-nm to stimulated emission (SE). It is of particular note that there is no signal corresponding to the formation of the ground *cis* state at 490 nm within the maximum delay of the system (~2.5 ns). Temperature-controlled PP TA spectroscopy was performed using a home-built temperature-controlled liquid cell with a range of 10–50 °C and accuracy of 1 °C.

The addition of a 515-nm dump pulse after the 400-nm pump pulses causes substantial modification of the spectra. Comparison of temporal lineouts (Extended Data Fig. 3f) for the different regions for the first 50 ps and globally fitted spectra recovered after the dump pulse (Extended Data Fig. 3e) shows the remaining signal in the GSB and ESA exhibits a reduction in decay constant from ~8 ps to ~4.5 ps.

To analyse the effect of different short pump–dump delays, the PP delay was fixed to 1.5 ps and the pump–dump delay varied (Extended Data Fig. 3g). It can be seen that, for negative pump–dump delay, the TA signal is the same as that of the regular PP spectra, and the pump–dump delays of 150 fs, 275 fs and 400 fs are almost indistinguishable in the GSB and ESA signals.

To confirm that 515 nm is a suitable dumping wavelength and rule out the possibility of off-resonant pumping, PP TA measurements were performed using 515 nm as the pump. Extended Data Fig. 3h shows the dispersion-corrected lineouts for several pump–probe delays at two different energy densities, and it can be seen that a 0.007 mJ mm^{-2} 515-nm pulse (that is, sufficient to induce >0.1 OD TA differences in the on state) produces no measurable signals within the 0.1-mOD sensitivity of the instrument. A further order-of-magnitude increase in the energy density of the 515 nm pulse still did not produce any measurable signals.

Femtosecond infrared TA spectroscopy

Due to a weak optical signature associated with isomerization in the visible TA, mid-infrared femtosecond TA spectroscopy measurements were carried out on rsKiiro to look for vibrionic signatures. A 95 mg ml^{-1} rsKiiro solution in low-salt buffer (50 mM Tris-HCl, 100 mM NaCl at pH 8) was loaded into a 1-inch-diameter liquid cell, with two CaF_2 windows and 6-µm spacer giving a final OD of ~0.7 at 490 nm. Deuterated samples were made using the same buffers but with deuterated water at pD 8.4, and the normal protein solution was diluted at 500 µl of protein to 2 ml of deuterated buffer, reconcentrated and loaded into the liquid cell, giving a final OD_{490} of ~0.8.

To inform the ultrafast infrared measurements and assignments, steady-state Fourier-transform infrared (FTIR) spectra were collected using a Bruker ISF 66/S spectrometer. The samples were illuminated with a 100-mW 488-nm diode laser to collect both the on and off states. Comparison of the deuterated and non-deuterated spectra, as well as those of from Dronpa and GFP, informed the peak assignments shown in Extended Data Fig. 4c. The steady-state difference spectra of deuterated rsKiiro for off minus on states are shown in Extended Data Fig. 4a.

Femtosecond infrared TA difference spectra were collected over a temporal range of −40 ps to 2 ns between 1,800 and 1,500 cm^{-1} using a previously described system[63]. Samples were pre-illuminated with a 488-nm diode laser and optically pumped using 100-fs, 400-nm pulses at an energy density of 0.018 mJ mm^{-2}. The PP dataset was globally

fitted with a sequential model to produce EADS with time constants of 5.79 ps, 60.65 ps and a long-lived component (Extended Data Fig. 4b).

In the fast, 5.78-ps EADS spectra, we observe GSBs corresponding to the *trans* neutral at 1,689, 1,644 and 1,513 cm^{-1}, assigned to the C=O, C=C and phenol-3 bands. With induced absorption at 1,668 and 1,596 cm^{-1}, these are assigned to the rearrangement of the Arg66 asymmetric and symmetric $CN_3H_5^+$ modes, respectively, suggesting rearrangement of the Arg66 residue/hydrogen-bonding network—the first step in the photoreaction. It is also possible that the 1,668 cm^{-1} feature contains contributions from the C=O mode, as was seen in Dronpa[63]. The 60-ps EADS shows a new ESA at 1,632 cm^{-1}, corresponding to ν(C=C), which is indicative of a change in the methyl bridge dihedral angle; this is further supported by a new GSB at 1,618 cm^{-1} over the phenol-1 stretch of the *trans*-neutral chromophore. This combination leads us to conclude that isomerization must occur within the 50/60-ps time constant. However, the C=C peak does not correspond to the final position of the steady *cis* state (1,626 cm^{-1}), indicating an intermediate conformation relative to the final product. We note that cryo-trapping and macromolecular crystallography resolved a minor second chromophore conformation (Supplementary Fig. 50). The absorption strengths of the phenol-1 (1,576 cm^{-1}) and phenol-3 (1,497 cm^{-1}) peaks are linked to the protonation state, strongly absorbing in the anion but only weakly in the neutral. The complete absence of these peaks in all TA spectra (except 1 ms) supports the findings of the microsecond TA spectra (Extended Data Fig. 3i) whereby the protonation occurs on the microsecond timescale, as indicated in the photocycle scheme in Fig. 1a. Therefore, the time-resolved infrared measurements confirmed the *trans*–*cis* photoisomerization as well as the ~10% femtosecond flash yield that corresponds to the concentration measured by flash photolysis (see below) of the final product. Both the time-resolved visible TA and the time-resolved infrared measurements confirm the primary photoproduct of the off state to be the *cis* neutral chromophore, in agreement with the observed microsecond thermal deprotonation that generates the final deprotonated *cis* anion chromophore product (Fig. 1b).

Flash photolysis photoproduct yield determination

To maximize the photoactive population in the XFEL experiments, flash photolysis measurements were conducted in the home laboratory to determine the ideal pumping conditions. A thin-film crystalline sample of rsKiiro was prepared using a previously described method[64] at ODs between 0.2 and 0.5. For each measurement, the sample area was fully photoswitched forwards and then backwards using unfocused 473-nm and 400-nm c.w. laser illumination to measure the total photoswitchable population. The sample was fully switched to the off state and then exposed to a single 400-nm, 100-fs pump pulse to measure the photoconversion step, and then once again fully photocycled to measure the non-recoverable bleach. The process was repeated over a range of pulse energy densities at 100 fs (Extended Data Fig. 4a). A fresh sample region was used each time. A pump-pulse energy density of 2 mJ mm^{-2} was selected for XFEL experiments as this was the value that would produce a yield of >10% while keeping the irreversible bleach as small as possible. Using methods described in ref. 64, the photoproduct yield was fitted to recover the total effective nonlinear cross-section (Extended Data Fig. 4b,c). Analysis of the power density dependence provided values for the linear and nonlinear optical cross-sections (Extended Data Fig. 4b,c). Although excited-state absorption was not avoided, internal conversion followed Kasha's rule to produce a vibrationally excited S_1 population in addition to the S_1 population formed by linear photoexcitation.

To confirm the effect of dumping on the final photoproduct yield, flash photolysis measurements were conducted at a fixed pulse energies while the pump–dump delay was scanned. Extended Data Fig. 4d shows that the photoproduct yield is suppressed by illumination of the dump pulse after the pump pulse and that the form of the suppression follows the approximate shape of the cross-correlation of the two 100-fs pulses and the excited-state decay time constants obtained from TA (Extended Data Fig. 3d).

Data availability

The data that support the findings of this study are available on request from the corresponding author. The extensive data collection generated numerous raw data files. The results have been summarized in the main and supplementary figures and, due to the large number of raw data files, these are not provided with the Article, but are available from the corresponding author on request. Coordinates and structure factor amplitudes have been deposited to the PDB database. The rsKiiro *cis* structure at 290 K can be found at MX Data (PDB 7QLI). The rsKiiro *trans* structure with illumination at 290 K can be found at MX Data (PDB 7QLJ). The rsKiiro *cis* structure intermediate at 200 K can be found at MX Data (PDB 7QLK). The rsKiiro thermal annealing at 290 K of the 200 K *cis* intermediate can be found at MX Data (PDB 7QLL). The rsKiiro dark reference SFX coordinates for the *trans* off state are available at PDB 7QLM. The rsKiiro pump–probe picoseconds averaged coordinates are available at PDB 7QLN. The rsKiiro PDP picoseconds averaged coordinates are available at PDB 7QLO. Hydrogen-bonding configuration structures obtained from QM/MM (Extended Data Fig. 8) are available at https://doi.org/10.5281/zenodo.7887626.

Code availability

Computer codes for the density matrix calculations and Wigner transforms used for the results shown in Fig. 4 and Supplementary Figs. 54, 55, 56, 57, 58, 59, 60, 61, 62 and 63 are available at https://github.com/perrettsamuel/Wigner-Transform-of-Density-Matrix.

References

39. Zhang, M. et al. Rational design of true monomeric and bright photoactivatable fluorescent proteins. *Nat. Methods* **9**, 727–729 (2012).
40. DePonte, D. P. et al. Gas dynamic virtual nozzle for generation of microscopic droplet streams. *J. Phys. D Appl. Phys.* **41**, 195505 (2008).
41. Nakane, T. et al. Data processing pipeline for serial femtosecond crystallography at SACLA. *J. Appl. Crystallogr.* **49**, 1035–1041 (2016).
42. Herrmann, S. et al. CSPAD-140k: a versatile detector for LCLS experiments. *Nucl. Instruments Methods Phys. Res. A Accel. Spectrometers Detect. Assoc. Equip.* **718**, 550–553 (2013).
43. Kameshima, T. et al. Development of an X-ray pixel detector with multi-port charge-coupled device for X-ray free-electron laser experiments. *Rev. Sci. Instrum.* **85**, 033110 (2014).
44. Park, J., Kim, S., Kim, S. & Nam, K. H. Multifarious injection chamber for molecular structure study (MICOSS) system: development and application for serial femtosecond crystallography at Pohang Accelerator Laboratory X-ray Free-Electron Laser. *J. Synchrotron Radiat.* **25**, 323–328 (2018).
45. Hutchison, C. D. M. & van Thor, J. J. Optical control, selection and analysis of population dynamics in ultrafast protein X-ray crystallography. *Philos. Trans. R. Soc. A Math. Phys. Eng. Sci.* **377**, 20170474 (2019).
46. Barty, A. et al. Cheetah: software for high-throughput reduction and analysis of serial femtosecond X-ray diffraction data. *J. Appl. Crystallogr.* **47**, 1118–1131 (2014).
47. White, T. A. et al. CrystFEL: a software suite for snapshot serial crystallography. *J. Appl. Crystallogr.* **45**, 335–341 (2012).
48. Duisenberg, A. J. M. Indexing in single-crystal diffractometry with an obstinate list of reflections. *J. Appl. Crystallogr.* **25**, 92–96 (1992).
49. Battye, T. G. G., Kontogiannis, L., Johnson, O., Powell, H. R. & Leslie, A. G. W. iMOSFLM: a new graphical interface for diffraction-image processing with MOSFLM. *Acta Crystallogr. D Biol. Crystallogr.* **67**, 271–281 (2011).

50. Ginn, H. M. et al. TakeTwo: an indexing algorithm suited to still images with known crystal parameters. *Acta Crystallogr. D Struct. Biol.* **72**, 956–965 (2016).
51. Gevorkov, Y. et al. XGANDALF—extended gradient descent algorithm for lattice finding. *Acta Crystallogr. A Found. Adv.* **75**, 694–704 (2019).
52. Pandey, S. et al. Time-resolved serial femtosecond crystallography at the European XFEL. *Nat. Methods* **17**, 73–78 (2020).
53. Ursby, T. & Bourgeois, D. Improved estimation of structure-factor difference amplitudes from poorly accurate data. *Acta Crystallogr. A Found. Crystallogr.* **53**, 564–575 (1997).
54. Terwilliger, T. C. & Berendzen, J. Bayesian difference refinement. *Acta Crystallogr. D Biol. Crystallogr.* **52**, 1004–1011 (1996).
55. Adams, P. D. et al. PHENIX: a comprehensive Python-based system for macromolecular structure solution. *Acta Crystallogr. D Biol. Crystallogr.* **66**, 213–221 (2010).
56. Winn, M. D. et al. Overview of the CCP 4 suite and current developments. *Acta Crystallogr. D Biol. Crystallogr.* **67**, 235–242 (2011).
57. Murshudov, G. N. et al. REFMAC 5 for the refinement of macromolecular crystal structures. *Acta Crystallogr. D Biol. Crystallogr.* **67**, 355–367 (2011).
58. Emsley, P., Lohkamp, B., Scott, W. G. & Cowtan, K. Features and development of Coot. *Acta Crystallogr. D Biol. Crystallogr.* **66**, 486–501 (2010).
59. Zhang, X. et al. Highly photostable, reversibly photoswitchable fluorescent protein with high contrast ratio for live-cell superresolution microscopy. *Proc. Natl Acad. Sci. USA* **113**, 10364–10369 (2016).
60. Hutchison, C. D. M., Parker, S., Chukhutsina, V. U. & van Thor, J. J. Open hardware microsecond dispersive transient absorption spectrometer for linear optical response. *Photochem. Photobiol. Sci* **21**, 23–25 (2021).
61. Lincoln, C. N., Fitzpatrick, A. E. & van Thor, J. J. Photoisomerisation quantum yield and non-linear cross-sections with femtosecond excitation of the photoactive yellow protein. *Phys. Chem. Chem. Phys.* **14**, 15752–15764 (2012).
62. van Wilderen, L. J. G. W., Lincoln, C. N. & van Thor, J. J. Modelling multi-pulse population dynamics from ultrafast spectroscopy. *PLoS ONE* **6**, e17373 (2011).
63. Warren, M. M. et al. Ground-state proton transfer in the photoswitching reactions of the fluorescent protein Dronpa. *Nat. Commun.* **4**, 1461 (2013).
64. Hutchison, C. D. M. et al. Photocycle populations with femtosecond excitation of crystalline photoactive yellow protein. *Chem. Phys. Lett.* **654**, 63–71 (2016).

Acknowledgements

We thank T. Nakane for assistance with setting up the SFX data pipeline during SACLA XFEL beamtimes. The LCLS XFEL experiments were performed at the CXI end-station (proposal no. LR23), and use of the LCLS, SLAC National Accelerator Laboratory, is supported by the US Department of Energy, Office of Science, Office of Basic Energy Sciences under contract no. DE-AC02-76SF00515. SACLA XFEL experiments were performed at BL3 of SACLA with approval of the Japan Synchrotron Radiation Research Institute (JASRI; proposals nos. 2017B8008 and 2019B8032). PAL-XFEL experiments were performed at the NCI end-station of PAL-XFEL (proposal no. 2020-2nd-NCI-007) funded by the Ministry of Science and ICT of Korea, with additional support from the Global Science Experimental Data Hub Center (GSDC) for data computing and the Korea Research Environment Open NETwork (KREONET) for network service provided by the Korea Institute of Science and Technology Information (KISTI). J.J.v.T. acknowledges support by the Engineering and Physical Sciences Research Council (EPSRC; EP/M000192/1), the Biotechnology and Biological Sciences Research Council (BBSRC; BB/P00752X/1) and travel grant assistance from the UK XFEL HUB. G. Groenhof and D.M. acknowledge funding from the BioExcel CoE project funded by the European Union contracts H2020-INFRAEDI-02-2018-823830 and H2020-EINFRA-2015-1-675728, and the CSC-IT centre in Espoo for access to computing resources. This work is supported in part by NIH grant GM118044 (to S.G.B.). S.I. acknowledges support by Platform Project for Supporting Drug Discovery and Life Science Research (Basis for Supporting Innovative Drug Discovery and Life Science Research (BINDS)) from the Japan Agency for Medical Research and Development (AMED; grant no. JP21am0101070) and support by JSPS KAKENHI (JP19H05777). E.N. acknowledges support by JSPS KAKENHI (JP19H05781). V.U.C. was supported by an EMBO long-term fellowship (EMBO ALTF 244-2017) and has received funding from the European Union Horizon 2020 research and innovation programme under Marie Sklodowska-Curie grant agreement no. 839389.

Author contributions

J.J.v.T. conceptualized the study. C.D.M.H., J.M.B., S. Perrett, M.G.R., S.G.B., G. Groenhof and J.J.v.T. designed the methodology. C.D.M.H., J.M.B., A. Fitzpatrick, G.D., A. Fadini, K.M., S.B.L., V.C.-P., J.L.F., V.U.C., D.G., J.B., G. Galinis, F.G., R.M.M., S.S., B.T., L.Y., M.G.R., C.-Y.L., J.P., S. Park, I.E., M.K., D.J., H.C., H.H., G.P., E.N., R.T., S.O., K.T., D.P.D., S.C., M. Seaberg, A.A., S.B., A.B. and J.J.v.T. performed the experiments. C.D.M.H., J.M.B., S. Perrett, A. Fadini, G.D., M.G.R., C.-Y.L., D.M., G. Groenhof, M. Schmidt, V.C., T.B., S.G.B. and J.J.v.T. conducted analysis. J.J.v.T. wrote the manuscript. C.D.M.H., J.M.B., S. Perrett, A. Fadini, T.B., G.D., K.M., M.G.R., C.-Y.L., S.G.B. and G. Groenhof edited and reviewed the manuscript. J.P.M., S.I., G. Groenhof and J.J.v.T. acquired funding. J.J.v.T. provided overall supervision.

Competing interests

The authors declare no competing interests.

Additional information

Extended data is available for this paper at https://doi.org/10.1038/s41557-023-01275-1.

Supplementary information The online version contains supplementary material available at https://doi.org/10.1038/s41557-023-01275-1.

Correspondence and requests for materials should be addressed to Jasper J. van Thor.

Peer review information *Nature Chemistry* thanks the anonymous reviewers for their contribution to the peer review of this work.

https://doi.org/10.1038/s41557-023-01275-1

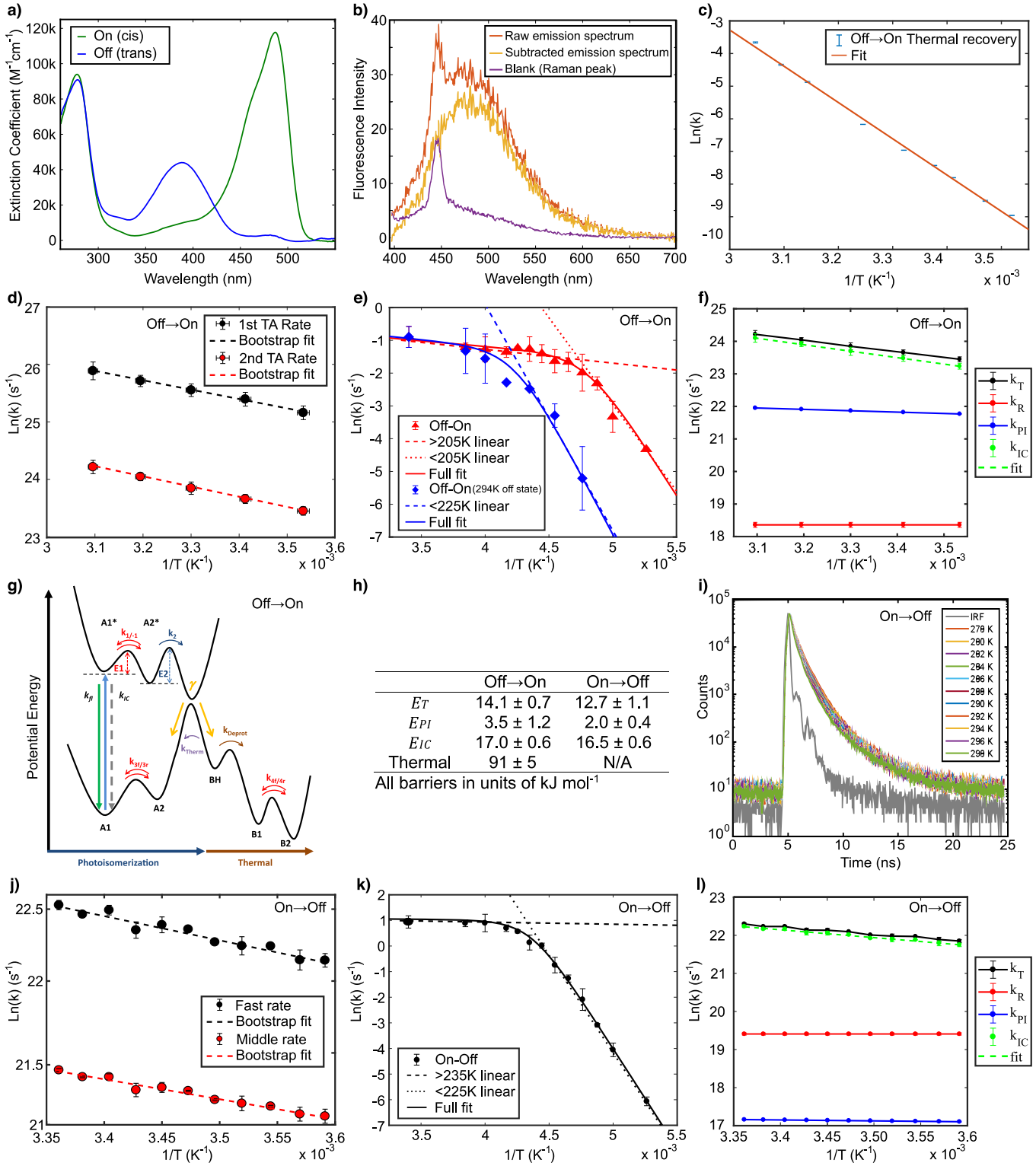

Extended Data Fig. 1 | Temperature dependence and energy barriers of rsKiiro photo-switching. a. Steady state UV -VIS spectra of the on (cis) and off (trans) state. **b**. Fluorescence emission spectra from the weakly fluorescent off state. **c**. Arrhenius plot of the off→on thermal recovery at temperature s ranging from 284-323 K fitting of the Arrhenius equation recovered an energy barrier of of 91± 5 kJ mol^{-1} between the states and an unscaled prefactor of $1.28\times10^{13\pm1}$ s^{-1}. **d**. Arrhenius plot of the temperature dependence of the two off→on PP TA time constants (Extended Data Fig. 3d), **e**. Arrhenius plot of the off→on photoswitching rate over a large range of cryo temperatures, where the preconversion to the off state was performed at cyro (red) and room temperature (blue). **f**. Bootstrap Arrhenius fitting of the total off→on rate (k_T) obtained from temperature dependence of the average TA rate which was used with the photoswitching scaled rate (k_{PI}) and radiative decay rate (k_R) to recover the internal conversion rate (k_{IC}) and barrier (E_{IC}). **g**. The proposed electronic structure model for the off→on reaction of rsKiiro. **h**. Summery table of electronic barriers recovered for rsKiiro photoswitching reactions. **i**. Time correlated single photon counting (TCSPC) decays for the on→off reaction of rsKiiro including the instrument response function (IRF). **j**. Arrhenius plots of the temperature dependence of the fast and middle rates recovered from TCSPC. **k & l** The same plots as e & f for the on→off reaction. A full description of all the fitting models and values are shown in section 11 of the supplementary materials. Error bars shown in **c-f** & **j-l** use SE.

https://doi.org/10.1038/s41557-023-01275-1

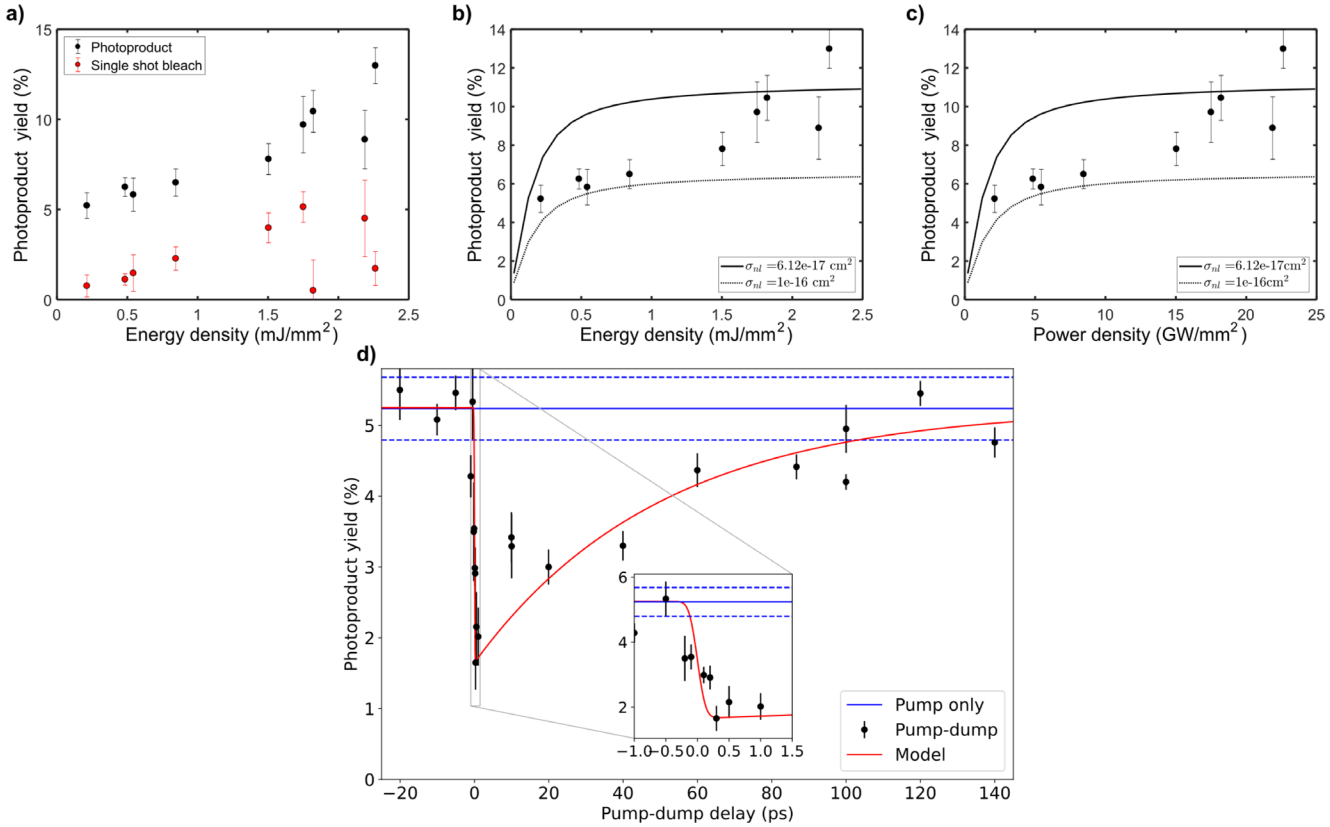

Extended Data Fig. 2 | Flash photolysis yields in crystalline rsKiiro with femtosecond pumping. a. Photoproduct yield and single shot bleach of rsKiiro prepared in the trans off state and pumped with 400 nm 100 femtosecond pulses over a range of energy densities. **b**. Fitting of total non-linear cross-section modelled with Z-scan theory using a quantum yield of 18.3% for the off→on reaction (section 6 of supplementary materials). **c**. Same fitting expressed against power density. **d**. Photoproduct yield in crystalline rsKiiro in the presence of a 515 nm dump pulse (black) as a function of pump-dump delay. The pump-probe yield (blue) and its error (blue dashed) are shown for reference, while the model (red) is the convolution of two 100 fs Gaussian pulses combined with the 50 ps exponential decay of the excited state lifetime obtained from transient absorption measurements. In **a-d** each measurement condition was repeated across numerous crystalline samples with absorptions ranging between 0.1-0.6 OD. Error bars shown use SE.

https://doi.org/10.1038/s41557-023-01275-1

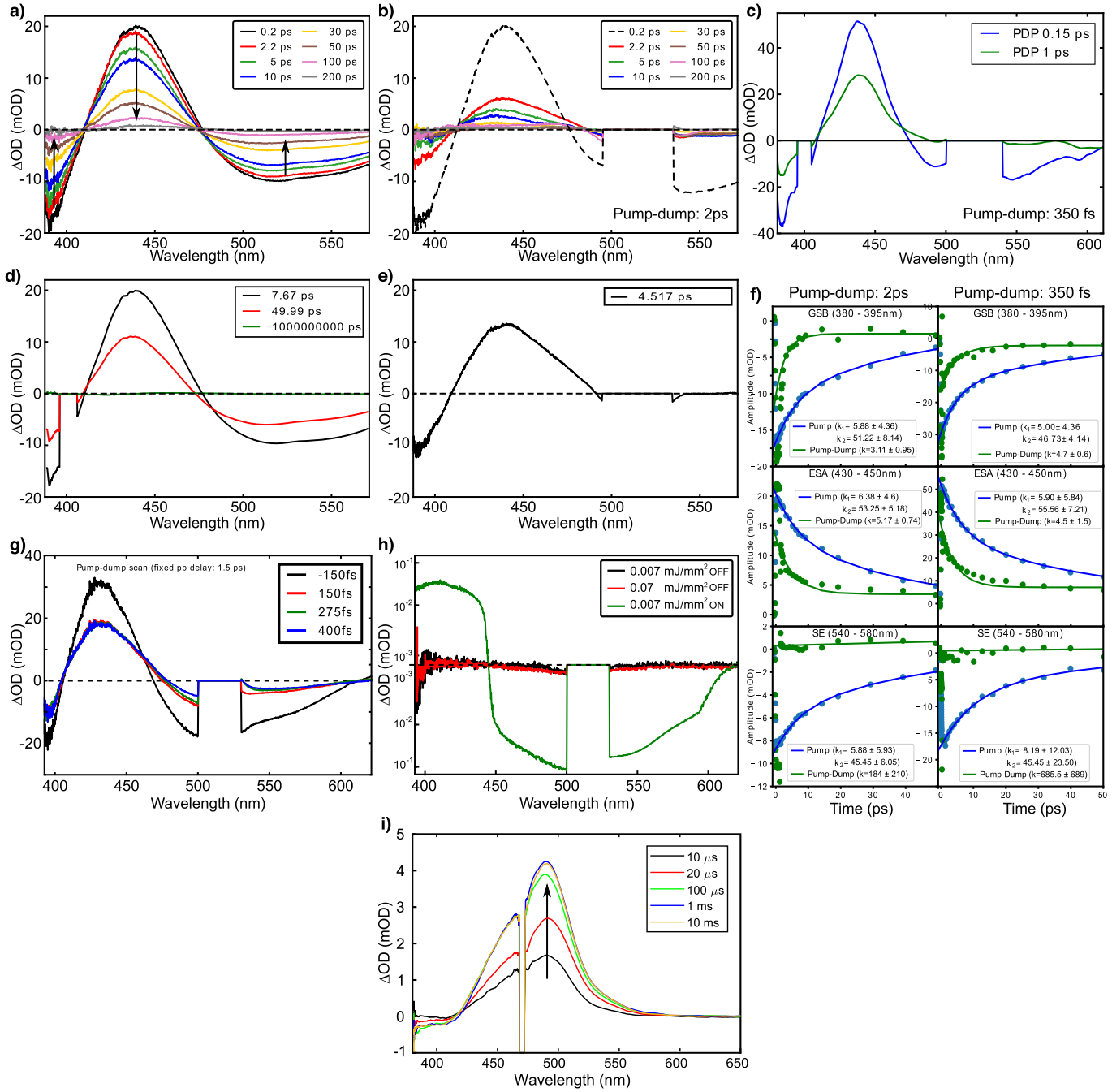

Extended Data Fig. 3 | Transient absorption spectroscopy of rsKiiro. **a**. PP transient absorption spectra showing GSB, ESA and SE at <410, 420-470 and 470-570 nm. **b**. PDP transient absorption spectroscopy for a 2 ps pump-dump delay, showing a ~50% reduction of the GSB and ESA and complete suppression of the SE. **c**. PDP TA spectra for pump-dump delay of 350 fs showing the same behaviour as the longer dump delay. **d**. Evolution Associated Difference Spectra (EADS) recovered from global fitting of PP TA spectra using a simple sequential model (A1*→A2*→A2/A1/BH)(Extended Data Figs. 1g and 8). **e**. Global fitting of the PDP TA spectra after the dump pulse recovered a single EADS corresponding to the A2 state. **f**. Lineout fits of the PP and PDP key spectra regions for 2 ps (left) and 350 fs (right) pump-dump delays, a bi-exponential was used for the PP fits with amplitude weighting and initial time constant taken from the global fitting. **g**. TA spectra for a fixed pump-probe delay of 1.5 ps while scanning the pump-dump delay. **h**. Dump only off-resonance pumping TA spectra with 510 nm femtosecond excitation of the 'off' state at fixed 1 ps pump probe delay ('off' spectra). Preillumination with 515 nm light prepares the pure off state and no TA signals are seen within the sensitivity of the instrument (black and red) while if the preillumination is not used and the ON state is present the weaker condition generates >100 mOD signals (Note: log vertical scale). This demonstrates that 515 nm dump pulse has sufficiently low cross section in the off state to not contribute to the signals seen in the absence of a pump-pulse. **i**. Microsecond transient absorption difference spectra of rsKiiro trans-cis reaction. The rise 488 nm peak corresponding to the cis-anion can be seen with a 40 ± 10 μs time constant. The break in the spectra at 473 nm corresponds to scatter of the pre-illumination laser.

https://doi.org/10.1038/s41557-023-01275-1

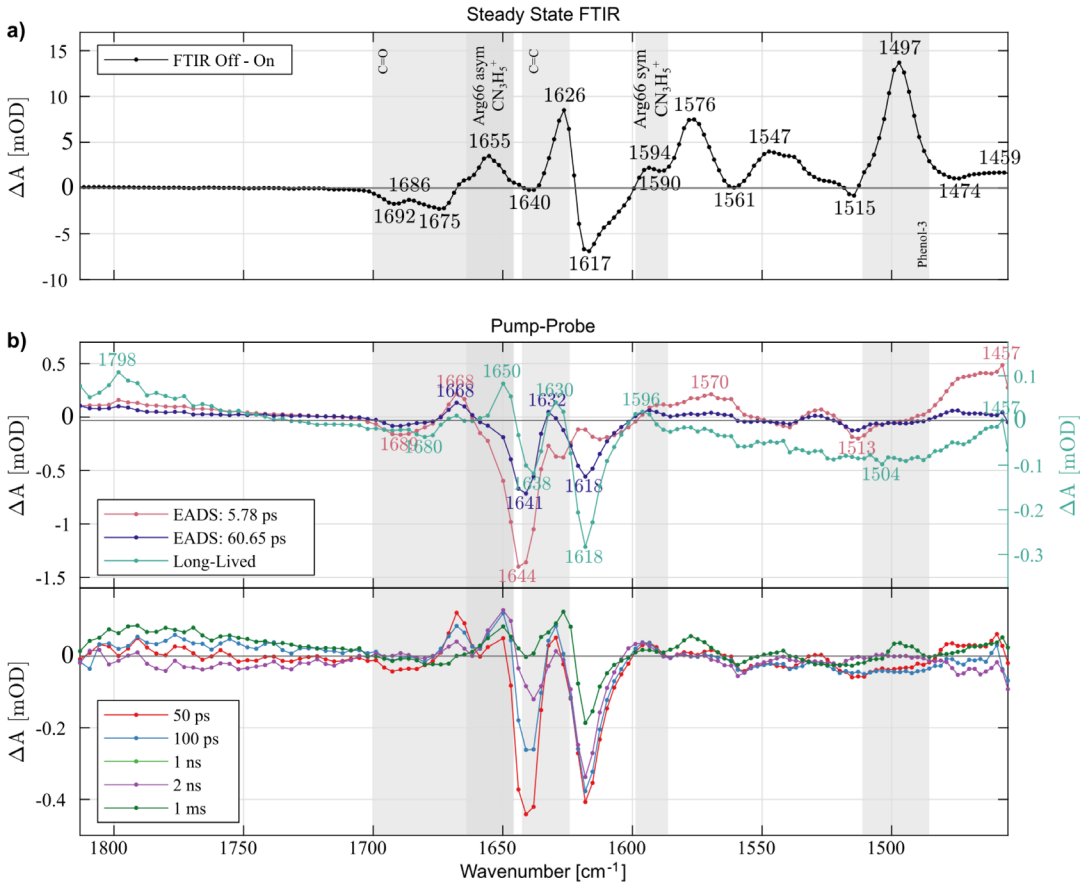

c)

Dominant Component	Dronpa pD 7.8 On	rsKiiro pD 8.4	rsKiiro pH 8 On	Dronpa pD 7.8 Off	rsKiiro pD 8.4 Off	rsKiiro pH 8 Off
C=O	1655	1655	1663	1688	1691/1675	1690/1676
Arg 66 asymmetric ($CN_3H_5^+$)	1655	1655	1649	-	-	-
C=C	1624	1626	1626	1644	1639	1643
Arg 66 symmetric ($CN_3H_5^+$)	1594	1594	1609	-	-	-
Phenol-1	1574	1576	1575	1615	1617	1617
Phenol-2	-	-	-	1600	-	-
C=N/C=C	1549	1547	1547	1561	1561	1561
Phenol-3	1497	1497	1497	1524	1515	1518
$^{13}C_5$	1350	-	-	1358	-	-
Phenol	1152	1152	1149	1177	1179	1177

Extended Data Fig. 4 | Femtosecond time resolved Infrared and FTIR spectroscopy of rsKiiro. a. steady state FTIR difference spectra of the off minus the on state of rsKiiro. Conversion to the off state was achieved by illuminating the sample with a 500 nm LED. **b**. TR-IR pump-probe measurements of the off state when pumped with 400 nm 100 fs pulses. The fitted EADS spectra are shown (top) and selected spectra at various pump-probe delays (bottom). Greyed out bands correspond to the labelled assignments. Note: For the on state there is overlap of the C = O and Arg66 asym $CN_3H_5^+$ in the 1645-1670 cm^{-1} region. **c**. Dronpa and rsKiiro on and off state FTIR peak assignments for ^2H and ^1H buffers. Dronpa assignments made by Warren et al. All values in units of cm^{-1}.

https://doi.org/10.1038/s41557-023-01275-1

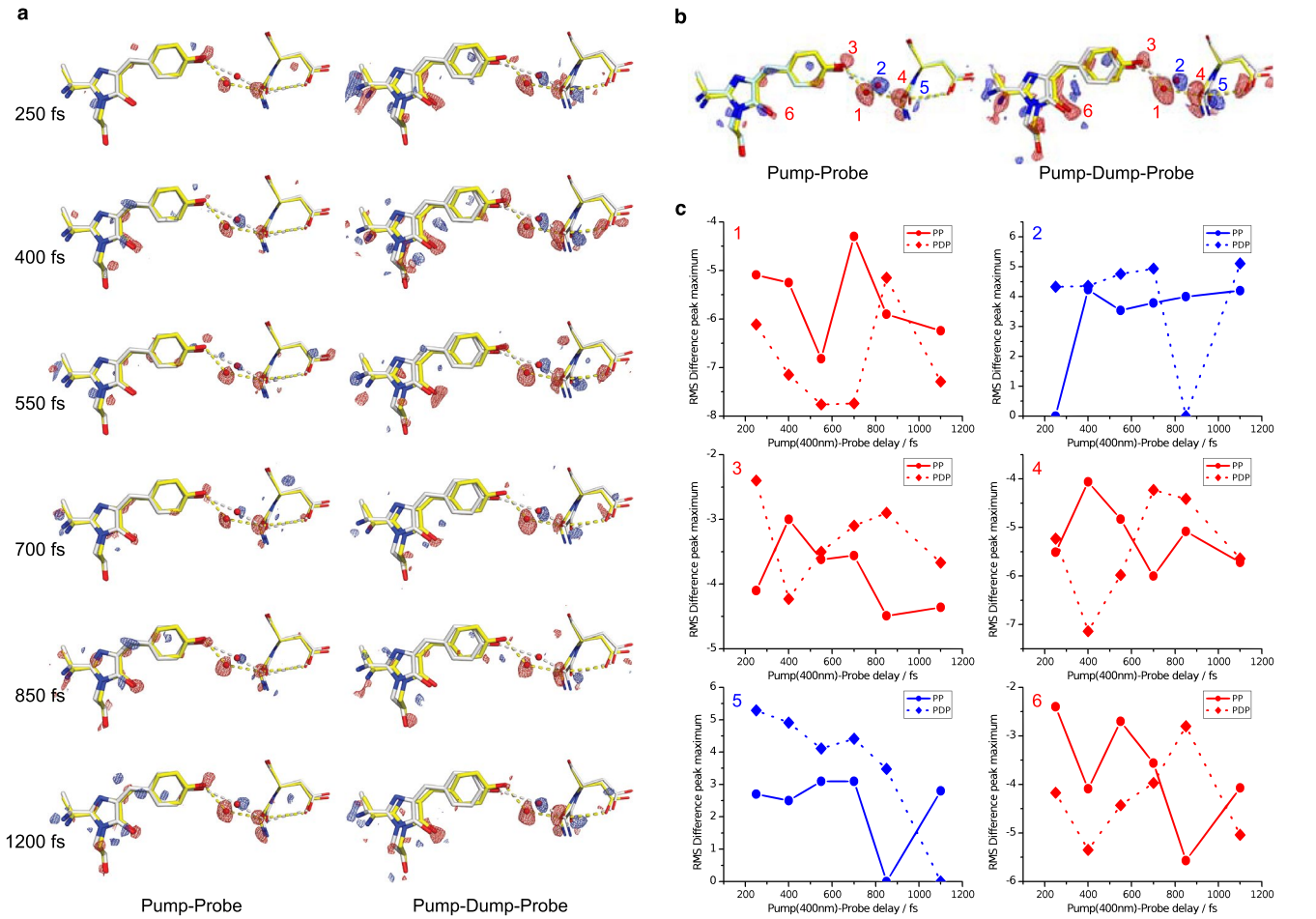

Extended Data Fig. 5 | Comparison of the PP vs PDP TR-SFX light induced differences in the rsKiiro chromophore region. a. Difference maps for the chromophore region, hydrogen bonded water and His194 for the femtosecond time bins for PP (Left) and PDP (right) data. The coordinates for ground state (yellow carbons) and the refined coordinates for light data after partiality refinement (grey carbons) are shown with electron density contoured at +3σ rms (blue) and -3σ rms (red). A 1.5 Å resolution cutoff was used. **b**. Same representation for the merged 0-1 ps PP delays with key difference peaks numbered. **c**. Difference density peak values at the locations shown in panel b. Plotted as a solid line (with dots) and a dashed line (with diamonds) for the PP and PDP respectively. Shown in blue for positive values of density, and in red for negative. The time dependence of difference features elsewhere in the protein (Fig. 1) showed a similar multi-mode character, but with different dependence for most features.

https://doi.org/10.1038/s41557-023-01275-1

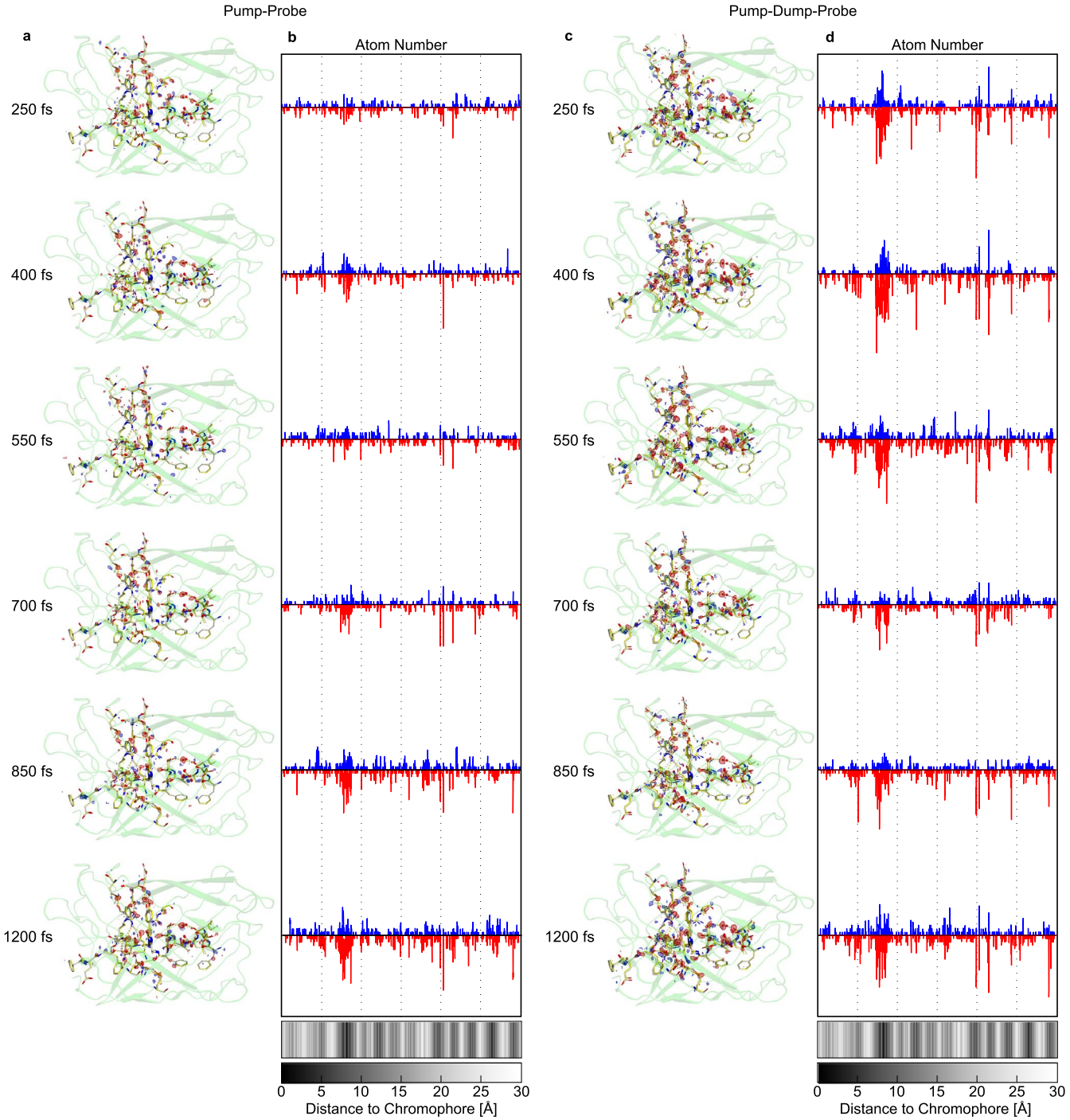

Extended Data Fig. 6 | Comparison of rsKiiro TR-SFX Pump-Probe vs Pump-Dump-Probe difference maps. a. Q-weighted difference electron density for each bin of the Pump-Probe (400 nm) on the left and of the Pump-Dump-Probe (400-515 nm) on the right. The secondary structure (green) of the ground state coordinates (yellow) are shown with electron density contoured at +3σ rms (blue) and -3σ rms (red). **b**. Integrated electron difference density above 3σ level within 2 Å of each sequential atom in the protein chain (in residue number order) for Pump-Probe data 3375set. Plotted for each time bin is the positive (blue) and negative (red) electron density, which are normalized with respect to all other time bins. Shown at the bottom is a greyscale bar indicating the distance from the center of the chromophore to the atom number[65] **c**. and **d**. The same analysis for the Pump-Dump-Probe case.

https://doi.org/10.1038/s41557-023-01275-1

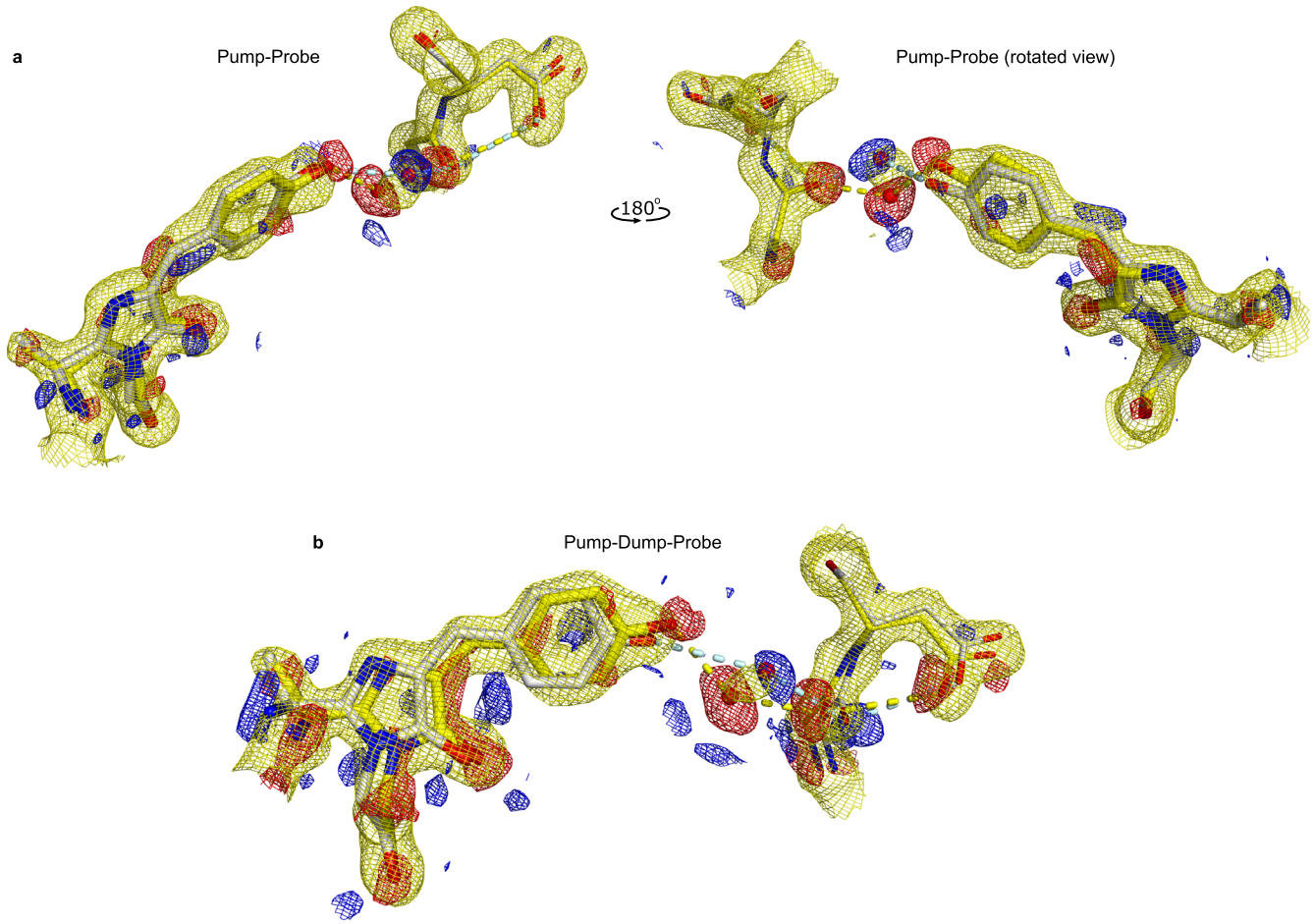

Extended Data Fig. 7 | Extrapolated maps and difference maps of merged 0-1 ps TR-SFX of rsKiiro with refined coordinates. a. Pump-probe illumination scheme. Map showing extrapolated F_o electron density for N_{EXT} = 13.6, contoured at 1.5 rms (yellow mesh) with the ground state (yellow) and extrapolated (grey) refined coordinates. Q-weighted difference electron density between the dark and 400 nm 0-1 ps is shown at 3 rms level with positive and negative signals in blue and red respectively. There is a 180° rotation between the left and right representations. **b**. Pump-Dump-Probe illumination scheme, with same representation except a value of N_{EXT} = 9 was chosen as it was closest to R-factor minimization occupancies of 21 % using the approximation: PT ~ 200/ N_{EXT} where PT is population transfer.

https://doi.org/10.1038/s41557-023-01275-1

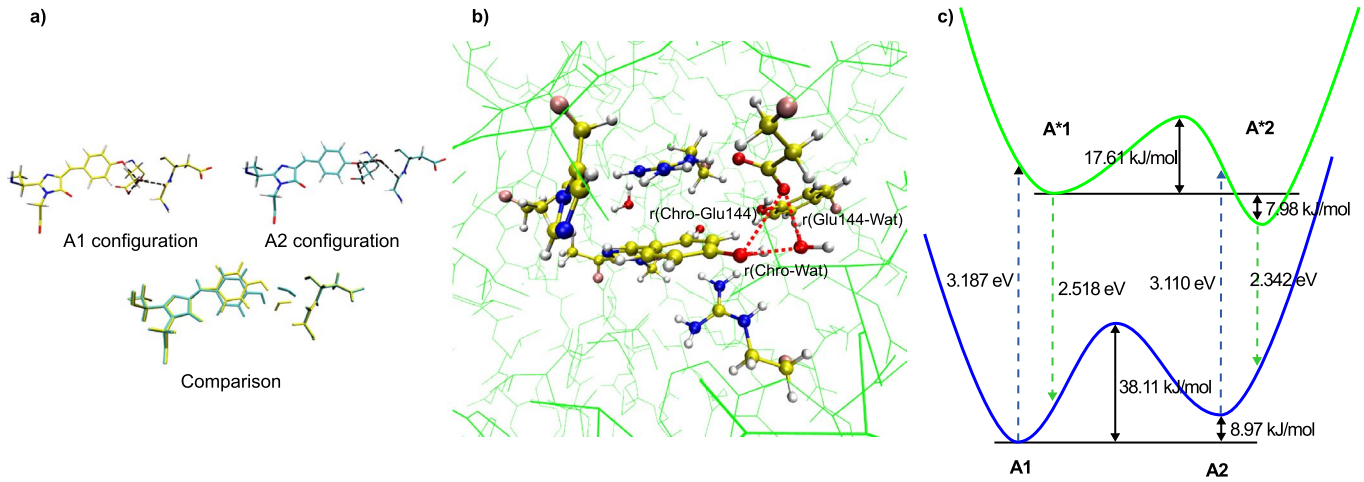

Extended Data Fig. 8 | Results of QM-MM calculations on rsKiiro. a. Hydrogen bonding configuration in state A1 (yellow), A2 (cyan) and an overlap of the two configurations. **b**. QM subsystem used for QM-MM calculations, shown with balls and sticks. Red dashed lines represent distances, used to search for transition state between A1 and A2 conformations. **c**. Energy diagram for optimized structure of A1 and A2 conformations from QM-MM calculations. These calculations are described in section 12 of the supplementary materials.

https://doi.org/10.1038/s41557-023-01275-1

Extended Data Table 1 | Summary of TR-SFX datasets collected during this work

Experiment	Conditions			
	Pump Probe	Pump Dump Probe	Dump Only	Dark
LCLS 2018 (LR23)	0 - 1 ps, 250 fs, 400 fs, 550 fs, 700 fs, 850 fs, 1100 fs, negative	0 - 1 ps*, 250 fs*, 400 fs*, 550 fs*, 700 fs*, 850 fs*, 1100 fs*, negative*	1 ps, negative	Dark
SACLA 2018 (2017B8008)	-	-	500 fs	Dark
SACLA 2019 (2019B8021)	550 fs, 3 ps, 100 ps, negative	550 fs**, 3 ps**, 100 ps**, 3 ps***, negative**	-	Dark
PAL-XFEL 2020 (2020-2nd-NCI-007)	1 ps, 100 μs, negative	-	-	Dark

pump-dump delay: *350 fs **500 fs ***2ps

https://doi.org/10.1038/s41557-023-01275-1

Extended Data Table 2 | LCLS LR23 TR-SFX PP & PDP crystallographic statistics for sub-ps time bins

	400nm -50fs-150fs	400nm 150fs-300fs	400nm 300fs-450fs	400nm 450fs-600fs	400nm 600fs-750fs	400nm 750fs-up	400nm Negative
Indexed Patterns:	6939	8851	8937	7082	6109	9672	674
Resolution Limits (Å)	15.38-1.80 (1.864-1.800)[1]	15.38-1.80 (1.864-1.800)[1]	15.38-1.80 (1.864-1.800)[1]	15.38-1.80 (1.864-1.800)[1]	15.40-1.80 (1.864-1.800)[1]	15.38-1.80 (1.864-1.800)[1]	14.60-1.80 (1.864-1.800)[1]
	15.38-1.50 (1.554-1.500)[2]	15.38-1.50 (1.554-1.500)[2]	15.38-1.50 (1.554-1.500)[2]	15.38-1.50 (1.554-1.500)[2]	15.40-1.50 (1.554-1.500)[2]	15.38-1.50 (1.554-1.500)[2]	14.60-1.50 (1.554-1.500)[2]
	15.38-1.35 (1.398-1.350)[3]	15.38-1.35 (1.398-1.350)[3]	15.38-1.35 (1.398-1.350)[3]	15.38-1.35 (1.398-1.350)[3]	15.40-1.35 (1.398-1.350)[3]	15.38-1.35 (1.398-1.350)[3]	14.60-1.41 (1.398-1.350)[3]
Number of Unique reflection indices:	21941[1]	21941[1]	21941[1]	21941[1]	21941[1]	21941[1]	21940[1]
	37542[2]	37542[2]	37542[2]	37542[2]	37542[2]	37542[2]	37541[2]
	51229[3]	51229[3]	51229[3]	51229[3]	51229[3]	51229[3]	51228[3]
No. Merged Reflections:	1411466(67442)[1]	1805581(85788)[1]	1854228(87736)[1]	1418718(66546)[1]	1230614(57712)[1]	1943189(89769)[1]	139031 (6484)[1]
	1704989(42954)[2]	2158555(48658)[2]	2221023(51247)[2]	1703429(39980)[2]	1472507(32758)[2]	2301688(47550)[2]	164828 (3137)[2]
	1775287 (9868)[3]	2238366(11858)[3]	2303118(11548)[3]	1767350 (8446)[3]	1523940 (6677)[3]	2372926 (8662)[3]	168886 (365)[3]
Completeness (%):	99.99 (100.00)[1]	100.00 (100.00)[1]	99.99 (100.00)[1]	100.00 (100.00)[1]	99.99 (100.00)[1]	100.00 (100.00)[1]	90.00 (77.23)[1]
	99.94 (99.65)[2]	99.97 (99.76)[2]	99.97 (99.76)[2]	99.91 (99.43)[2]	99.86 (98.80)[2]	99.97 (99.81)[2]	74.89 (33.61)[2]
	94.77 (57.49)[3]	95.83 (64.77)[3]	95.72 (62.66)[3]	94.08 (52.76)[3]	92.66 (44.74)[3]	94.50 (53.59)[3]	58.26 (3.46)[3]
Signal to noise:	3.903 (2.43)[1]	4.366 (2.59)[1]	4.417 (2.63)[1]	3.974 (2.43)[1]	3.691 (2.22)[1]	4.559 (2.70)[1]	2.098 (0.80)[1]
	2.902 (1.14)[2]	3.261 (1.17)[2]	3.295 (1.14)[2]	2.999 (1.14)[2]	2.761 (0.98)[2]	3.376 (1.10)[2]	2.221 (1.61)[2]
	2.696 (4.68)[3]	2.601 (-0.83)[3]	2.754 (0.69)[3]	2.486 (0.48)[3]	2.297 (0.52)[3]	2.748 (0.39)[3]	1.833 (0.48)[3]
Wilson b factor (Å^2):	12.78[1]	13.63[1]	13.71[1]	13.23[1]	13.82[1]	14.54[1]	10.30[1]
	15.25[2]	15.74[2]	15.92[2]	15.76[2]	16.18[2]	16.60[2]	12.30[2]
	16.21[3]	16.31[3]	16.74[3]	16.53[3]	16.80[3]	17.41[3]	13.32[3]
R_{Split} (%):	23.92 (45.92)[1]	20.62 (40.80)[1]	20.52 (39.65)[1]	23.38 (44.55)[1]	25.04 (46.72)[1]	19.56 (37.93)[1]	62.60 (94.66)[1]
	26.70 (95.74)[2]	23.14 (91.06)[2]	23.02 (88.59)[2]	25.94 (95.65)[2]	27.87 (109.07)[2]	21.89 (93.43)[2]	63.19 (114.60)[2]
	27.82 (259.45)[3]	24.29 (221.54)[3]	24.15 (217.17)[3]	26.93 (262.02)[3]	28.70 (251.11)[3]	22.95 (231.68)[3]	63.21 (N/A)[3]
CC*:	0.98 (0.86)[1]	0.98 (0.91)[1]	0.98 (0.91)[1]	0.98 (0.90)[1]	0.98 (0.89)[1]	0.99 (0.92)[1]	0.80 (0.50)[1]
	0.98 (0.70)[2]	0.99 (0.74)[2]	0.98 (0.75)[2]	0.98 (0.72)[2]	0.98 (0.67)[2]	0.99 (0.76)[2]	0.80 (0.77)[2]
	0.98 (0.23)[3]	0.99 (0.38)[3]	0.98 (0.48)[3]	0.98 (0.30)[3]	0.98 (0.46)[3]	0.99 (0.39)[3]	0.80 (N/A)[3]
$CC_{1/2}$:	0.91 (0.59)[1]	0.94 (0.70)[1]	0.93 (0.72)[1]	0.92 (0.67)[1]	0.91 (0.66)[1]	0.94 (0.74)[1]	0.47 (0.14)[1]
	0.92 (0.33)[2]	0.94 (0.38)[2]	0.94 (0.40)[2]	0.92 (0.35)[2]	0.92 (0.29)[2]	0.95 (0.41)[2]	0.48 (0.42)[2]
	0.92 (0.03)[3]	0.94 (0.08)[3]	0.94 (0.13)[3]	0.92 (0.05)[3]	0.92 (0.12)[3]	0.95 (0.08)[3]	0.48 (N/A)[3]

	400nm-515nm* -50fs-150fs	400nm-515nm* 150fs-300fs	400nm-515nm* 300fs-450fs	400nm-515nm* 450fs-600fs	400nm-515nm* 600fs-750fs	400nm-515nm* 750fs-up	400nm-515nm* Negative
Indexed Patterns:	4936	6965	7445	5549	5013	9846	284
Resolution Limits (Å)	15.40-1.80 (1.864-1.800)[1]	15.40-1.80 (1.864-1.800)[1]	15.40-1.80 (1.864-1.800)[1]	15.38-1.80 (1.864-1.800)[1]	15.40-1.80 (1.864-1.800)[1]	15.40-1.80 (1.864-1.800)[1]	15.11-1.81 (1.864-1.800)[1]
	15.40-1.50 (1.554-1.500)[2]	15.40-1.50 (1.554-1.500)[2]	15.40-1.50 (1.554-1.500)[2]	15.38-1.50 (1.554-1.500)[2]	15.40-1.50 (1.554-1.500)[2]	15.40-1.50 (1.554-1.500)[2]	15.11-1.6 1 (1.554-1.500)[2]
	15.40-1.38 (1.398-1.350)[3]	15.40-1.38 (1.398-1.350)[3]	15.40-1.38 (1.398-1.350)[3]	15.38-1.40 (1.398-1.350)[3]	15.40-1.39 (1.398-1.350)[3]	15.40-1.36 (1.398-1.350)[3]	15.11-1.61 (1.398-1.350)[3]
Number of Unique reflection indices:	21941[1]	21946[1]	21957[1]	21958[1]	21946[1]	21962[1]	21936[1]
	37542[2]	37547[2]	37558[2]	37559[2]	37547[2]	37563[2]	37537[2]
	51229[3]	51234[3]	51245[3]	51246[3]	51234[3]	51250[3]	51224[3]
No. Merged Reflections:	893288(34506)[1]	1232379(46402)[1]	1321858(49215)[1]	983632(37102)[1]	881928(33374)[1]	1729036(64348)[1]	43550(1078)[1]
	1008790(12766)[2]	1385663(16018)[2]	1485405(17502)[2]	1107532(12031)[2]	991780(11593)[2]	1945978(24248)[2]	46240(129)[2]
	1024201(1156)[3]	1405717(1427)[3]	1505921(1068)[3]	1119446(430)[3]	1003575(601)[3]	1975033(1784)[3]	46327(6)[3]
Completeness (%):	99.94 (99.86)[1]	99.97 (99.95)[1]	99.93 (99.95)[1]	99.88 (99.91)[1]	99.93 (99.81)[1]	99.91 (100.00)[1]	53.18 (20.90)[1]
	97.63 (83.83)[2]	98.69 (90.42)[2]	98.96 (92.60)[2]	97.52 (81.91)[2]	97.22 (80.65)[2]	99.56 (96.93)[2]	34.26 (1.69)[2]
	81.54 (10.20)[3]	84.07 (12.25)[3]	84.22 (9.41)[3]	79.44 (4.00)[3]	79.30 (5.47)[3]	86.82 (15.05)[3]	25.19 (0.06)[3]
Signal to noise:	3.169 (1.78)[1]	3.641 (1.96)[1]	3.721 (2.01)[1]	3.317 (1.82)[1]	3.097 (1.64)[1]	4.190 (2.24)[1]	2.943 (4.17)[1]
	2.480 (1.69)[2]	2.751 (2.26)[2]	2.681 (0.75)[2]	2.371 (0.77)[2]	2.505 (3.14)[2]	2.981 (0.74)[2]	3.108 (0.65)[2]
	2.293 (0.17)[3]	2.447 (-0.07)[3]	2.478 (1.92)[3]	2.216 (2.14)[3]	2.212 (0.72)[3]	2.587 (-0.48)[3]	3.102 (-3.33)[3]
Wilson b factor (Å^2):	16.26[1]	16.78[1]	16.77[1]	16.44[1]	16.72[1]	16.97[1]	15.17[1]
	18.60[2]	18.31[2]	19.26[2]	18.79[2]	18.66[2]	19.21[2]	16.91[2]
	19.64[3]	20.07[3]	19.11[3]	18.48[3]	20.17[3]	20.29[3]	11.82[3]
R_{Split} (%):	27.92 (60.83)[1]	23.86 (53.95)[1]	22.98 (52.12)[1]	26.59 (61.50)[1]	28.50 (66.46)[1]	20.46 (46.97)[1]	75.15 (89.99)[1]
	30.07 (158.53)[2]	26.15 (140.71)[2]	25.21 (147.71)[2]	28.71 (164.21)[2]	30.61 (158.01)[2]	22.84 (155.02)[2]	75.17 (N/A)[2]
	30.24 (163.15)[3]	26.36 (307.19)[3]	25.46 (263.64)[3]	28.80 (N/A)[3]	30.69 (244.85)[3]	23.24 (164.72)[3]	75.17 (N/A)[3]
CC*:	0.97 (0.85)[1]	0.98 (0.88)[1]	0.98 (0.87)[1]	0.97 (0.84)[1]	0.97 (0.82)[1]	0.98 (0.91)[1]	0.67 (0.31)[1]
	0.97 (0.60)[2]	0.98 (0.57)[2]	0.98 (0.69)[2]	0.98 (0.49)[2]	0.97 (0.65)[2]	0.99 (0.57)[2]	0.67 (N/A)[2]
	0.97 (N/A)[3]	0.98 (0.67)[3]	0.98 (0.32)[3]	0.98 (N/A)[3]	0.97 (N/A)[3]	0.99 (0.87)[3]	0.67 (N/A)[3]
$CC_{1/2}$:	0.90 (0.56)[1]	0.92 (0.63)[1]	0.93 (0.61)[1]	0.90 (0.54)[1]	0.89 (0.51)[1]	0.94 (0.70)[1]	0.29 (0.05)[1]
	0.90 (0.22)[2]	0.92 (0.19)[2]	0.93 (0.31)[2]	0.91 (0.14)[2]	0.90 (0.27)[2]	0.95 (0.19)[2]	0.29 (N/A)[2]
	0.90 (0.42)[3]	0.93 (0.28)[3]	0.93 (0.05)[3]	0.91 (N/A)[3]	0.90 (N/A)[3]	0.95 (0.60)[3]	0.29 (N/A)[3]

* Pump-dump delay of 350 fs [1,2,3] Represent merged statistics for distinct resolution shells, with a resolution cut-off at 1.80 Å (1), 1.50 Å (2) and 1.35 Å (3)
N/A is used for when statistical measurements for the highest resolution shell were unphysical

nature chemistry

Article

https://doi.org/10.1038/s41557-023-01275-1

Optical control of ultrafast structural dynamics in a fluorescent protein

In the format provided by the authors and unedited

nature chemistry

Article

https://doi.org/10.1038/s41557-023-01275-1

Optical control of ultrafast structural dynamics in a fluorescent protein

In the format provided by the authors and unedited

This PDF file includes:

Supplementary Methods

1. Micro crystal breaking with glass beads

To reduce issues with blockages during crystal injection particularly with the GDNV injection it was necessary to optimise the size distribution of the crystals, this was done by breaking up the microcrystals with glass beads.

1 mL of slurry in either 25% or 30% PEG 3350 condition was added to 0.5 mL of pre-rinsed glass beads of size <106 μm (Sigma-Aldrich) in a 2 mL round bottom Eppendorf tube before vortexing for 10 seconds at room temperature and keeping on ice for 1 minute. After a total of 15 breaking and cooling cycles, the mixture was spun down at 1000 x g for 10 s and the crystal-containing supernatant carefully pipetted away and poured in a 50 μm CellTrics filter (Sysmex Partec GmbH, Germany). The glass beads were then washed four times with 0.25 mL of 25% (or 30%) PEG 3350 in Tris and Lithium Sulfate buffer and spun down at 1000 x g and the supernatant loaded onto the 50 μm filter each time. The PEG 3350 concentration in the final filtered slurry was set as desired by changing that in the Tris and Lithium Sulfate buffer during the beads-washing step. The 2 mL filtered slurry was either left to settle at 20°C overnight or straight away loaded onto a 30 μm CellTrics filter. The crystal breakage procedure removed clumps and yielded a narrower crystal size range with maximum final crystal dimensions of the order of 3 x 5 x 30 μm.

Since crystals in slurries prepared with 25% PEG 3350 tended to settle in the reservoir and clog the injector tubing and GDVN injector, they were spun down at 1,000 x g for 10 s and exchanged in 30% PEG 3350 by adding a 32.5% PEG3350 buffer solution to the sedimented crystals in 2:1 ratio and adjusting the volume before measuring the crystal density.

2. SFX detector distance optimization

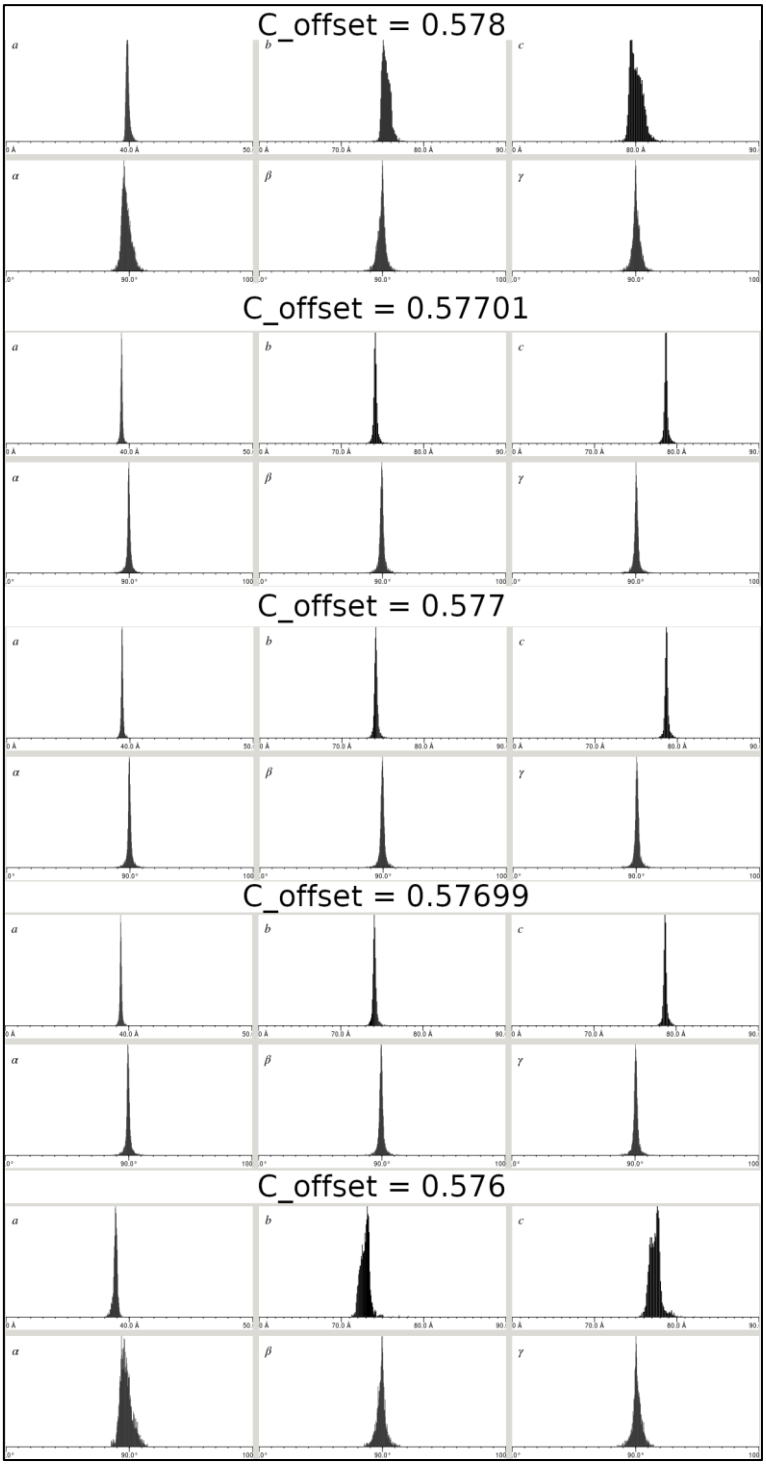

Supplementary Fig. 1 | Crystallographic unit cell optimization scan at LCLS LR23. The unit cell distribution data was highly sensitive to detector distance. Shown are the resulting distributions for the C_offset parameter values between 0.576 and 0.578.

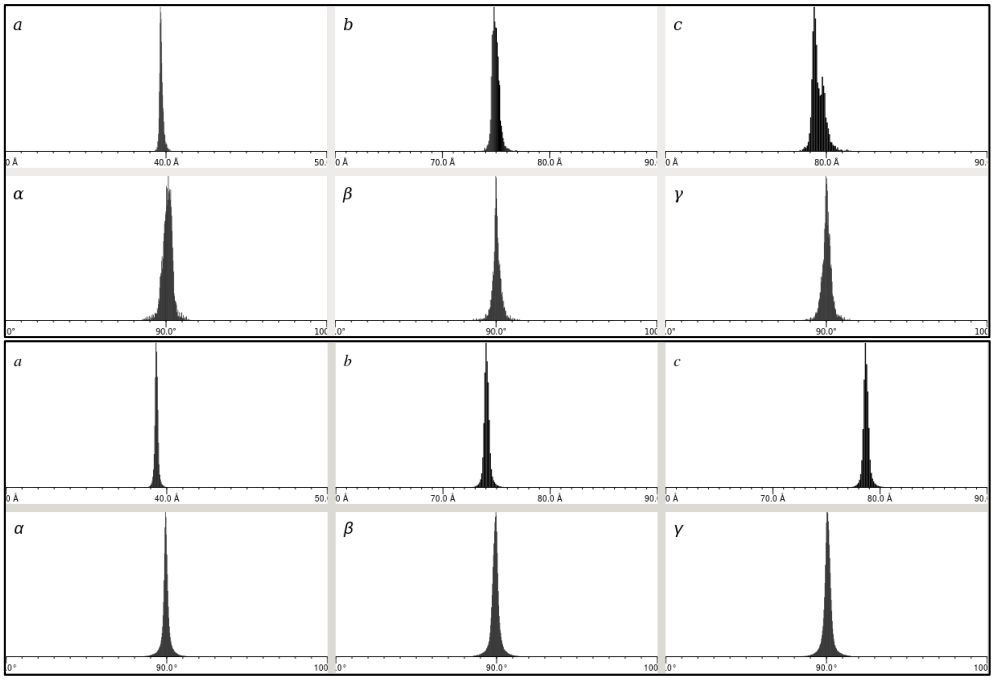

Supplementary Fig. 2 | Crystallographic unit cell optimization comparison at LCLS LR23. Comparison of the rsKiiro un-optimised (top) and optimized (bottom) unit cell distributions for LR23 beamtime.

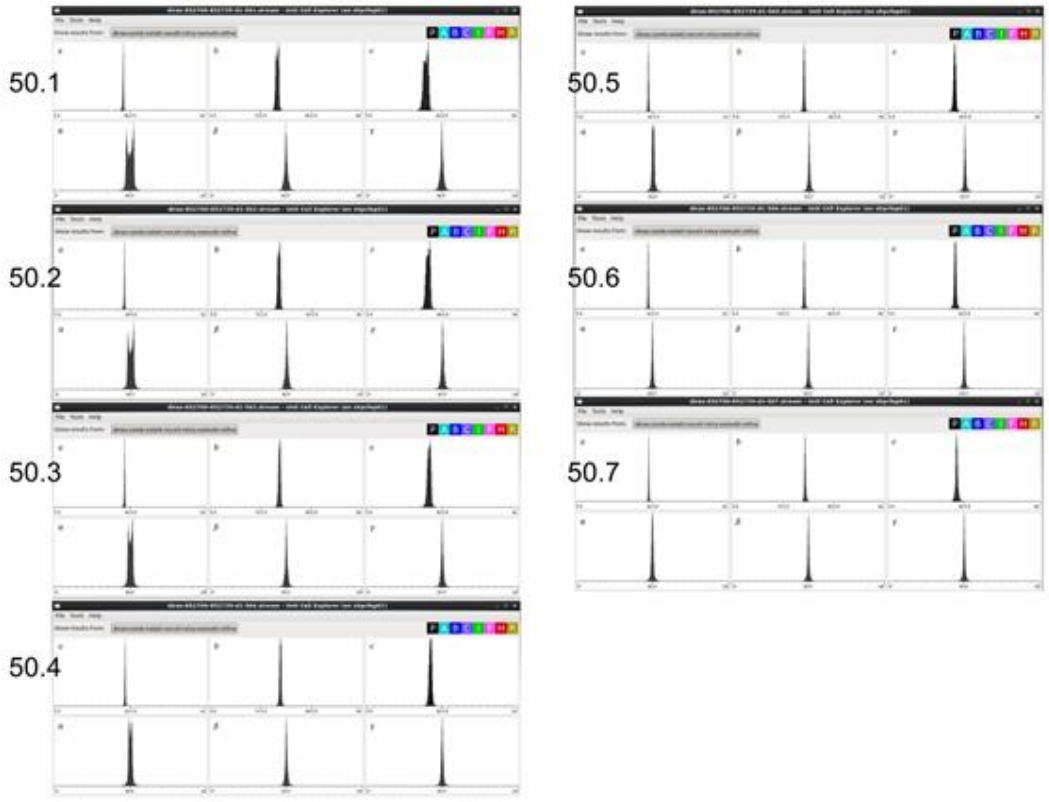

Supplementary Fig. 3 | Crystallographic unit cell optimization scan at SACLA 2019B8021. A systematic scan of the camera distance between 50.1 mm and 50.7 mm also revealed a very strong sensitivity of the cell distribution and splitting of primarily the c-dimension as well as the alpha angle. The narrowest distributions at 50.7 mm also led to the best L-test results with ~ 4% twin fraction calculated, and the optimum R-factors.

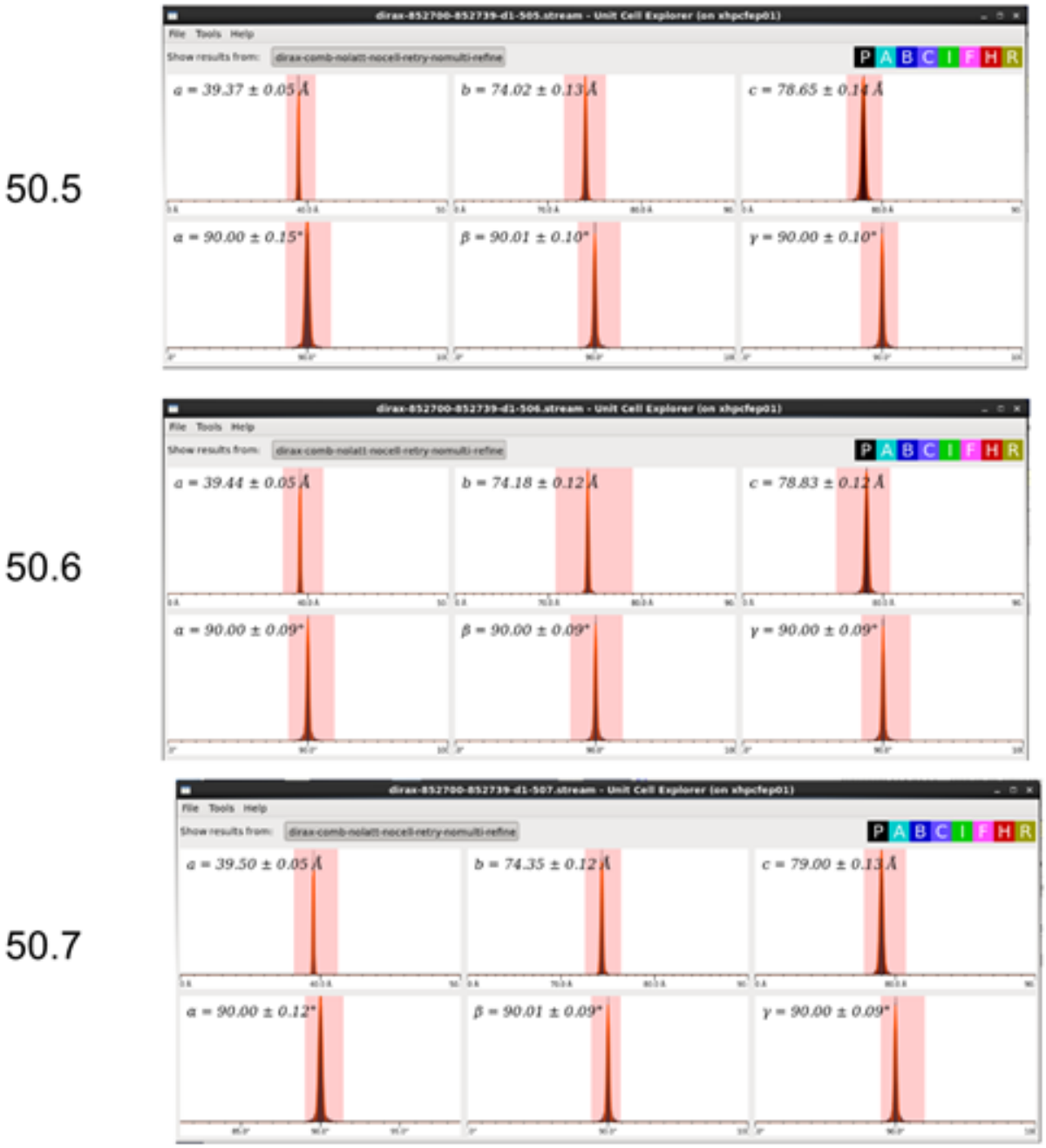

Supplementary Fig. 4 | Crystallographic unit cell optimization scan at SACLA 2019B8021,Values near 50.6 mm resulted in the narrowest distributions, loss of split cell parameters, and L-test calculation showed levels of potential twinning at or below 4%

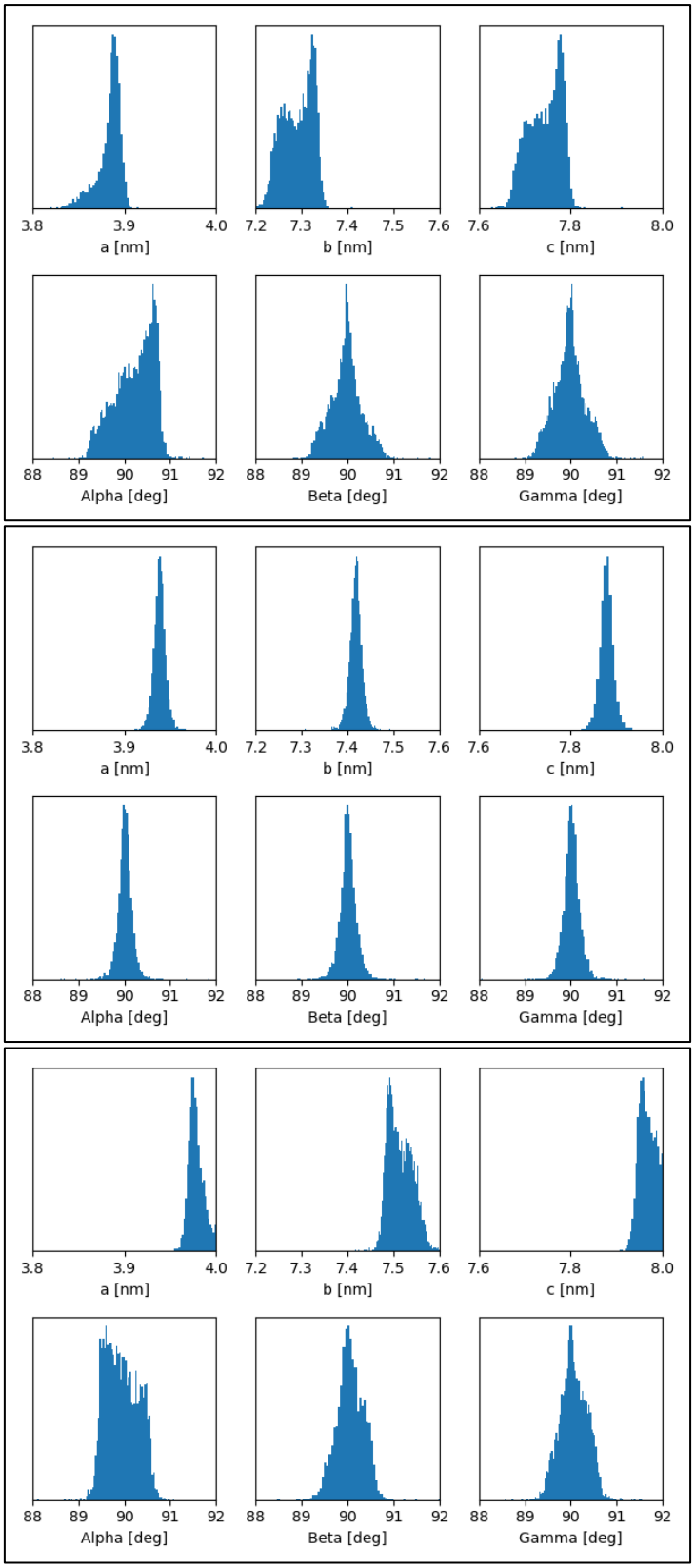

Supplementary Fig. 5 | Crystallographic unit cell optimization scan at PAL XFEL 2020-2nd-NCI-007. Histogram of unit cell distributions with different detector distances of 141.0, 142.9 and 144.5 mm for the top, middle, bottom figures respectively. For each detector distance the fitted cell dimensions were 39.36±0.06 Å, 74.15±0.13Å, 78.70±0.13 Å and angles of 90±0.13°, 90±0.15°, 90.02±0.19°.

3. Time zero determination by cross correlation.

At each of XFEL beamtimes the temporal delay between the X-rays and both the pump and dump optical pulses delay was measured using the standard cross-correlation technique exploiting the transient reflectivity [1] exhibited by semiconductors when exposed to hard X-rays. In each case a Ce:YAG scintillator screen that was used to achieve spatial overlap was used as the transient reflectivity medium, 20 μm thick at LCLS and 50 μm at SACLA. The XFEL beam was expanded by removing several lenses from the beryllium compound refractive lenses (CRL) stack to match the spot sizes of the optical beams to maximize the amplitude of the cross-correlation signal. The optical beam and X-rays were overlapped on the Ce:YAG screen and the transmission of the optical beam was measured using photodiode while the temporal delay between the two was scanned. With significant averaging a sigmoid-like change in transmission is seen roughly centred when the pulses are temporally overlapped. To improve the accuracy of the cross-correlation the output of each facility's timing tool was used to correct for the XFELs inherent temporal jitter (Supplementary Fig. 6). Finally the time corrected data was binned and fitted using the methods previous described in [2]. These cross correlations scans were made at the start of each beamtime and repeated multiple times throughout each data collection to check for slow temporal drift between the two optical arms and the X-rays. These measurements were also the most accurate way to set and confirm the relative delay between the pump and dump pulses at the interaction region which was ~350 fs at CXI LR23 and ~500 fs at 2019B8021 (Supplementary Fig. 6).

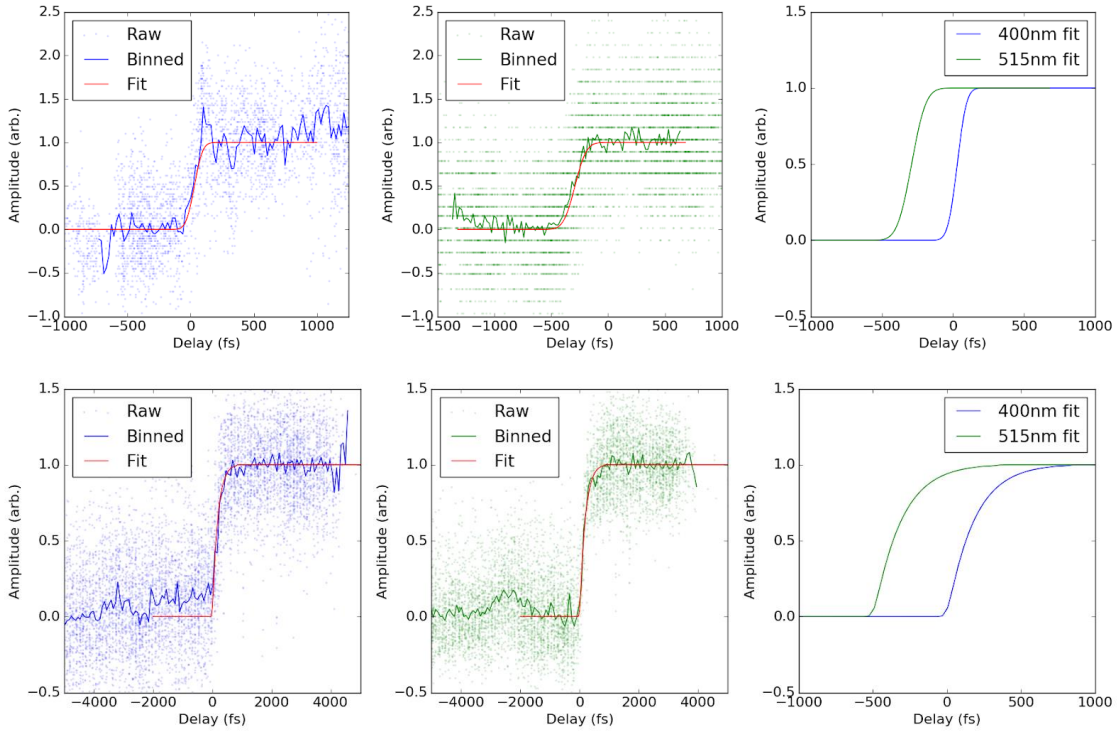

Supplementary Fig. 6 | TR-SFX cross correlation time zero determination. Shown for LCLS LR23 (top row) and SACLA 2019B8021 (bottom row). In the 400 nm pump (left column) and 515 nm dump (middle column) pulses, each show the raw photodiode signal after timing tool correction of the XFEL jitter was applied (dots), binned trace (line) and fitted sigmoid (red line). The fit was generated using the methods previous described[2]. The comparison of the fits (right column) shows the pump-dump delay. The delay at LR23 was determined to be ~350 fs while that at 2019B8021 was 500 fs. Note: the order of the optical pulses appears counter intuitive (i.e the 515 nm pulse appears first) in the cross-correlation measurement X-ray pulse is the “pump” and the optical pulse is the “probe” as opposed to the TR-SFX

experiment where the situation is reverse hence the temporal order of the optical pulses is effectively reversed when scanning the same optical delay stage.

4. Femtosecond Optical Pulse Characterization

To confirm spectral and temporal likeness of the optical excitation pulses provided by the onsite SACLA/LCLS lasers to those used for spectroscopic measurements in the homelab two compact homebuilt frequency resolved optical gating (FROG)[3] setups were deployed at the beamlines. A second harmonic generation based (SHG-FROG)[4] to characterize the 515 nm dump pulses and a cross correlation based (XFROG) for the 400 nm pump pulses. The more complicated XFROG was required for the 400 nm pulses due to the phase matching limitations of SHG non-linear crystals. Schematics of the two devices are shown in Supplementary Fig. 7. A type II 20 μm thick surface mounted BBO θ=29.2° (Newlight Photonics Inc.) was used for characterizing the 800 nm fundamental. A type II 20 μm thick surface mounted BBO (θ=55°) was used for SHG-FROG of the 515 nm and XFROG of the 400 nm, the phase matching angle of the crystal was adjusted in each case maximize the generated signal.

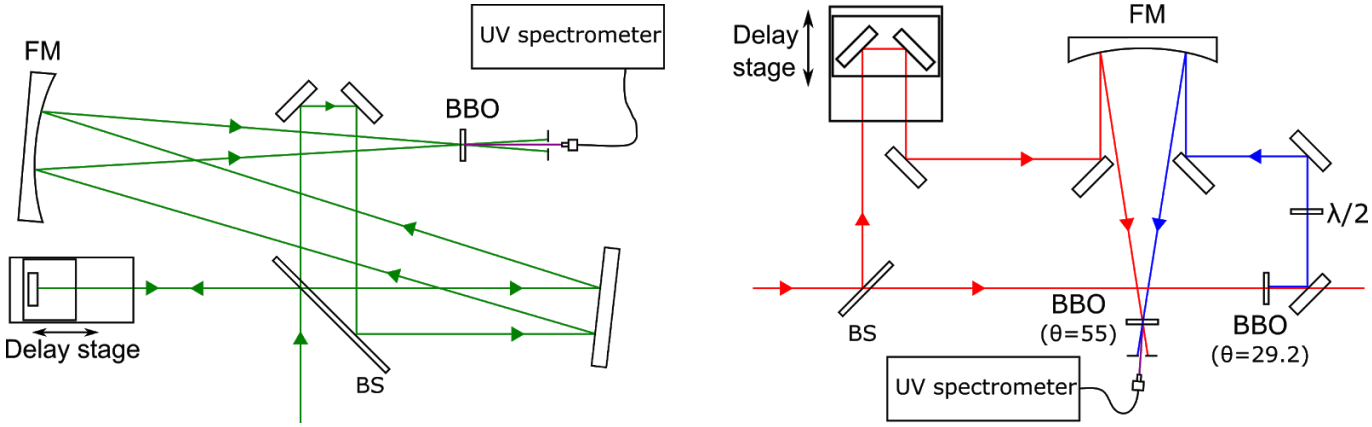

Supplementary Fig. 7 | FROG and XFROG schematics. SHG-FROG (left) and XFROG (right) used for pulse characterization during TR-SFX beamtimes. Where BS and FM are a pellicle beam splitter and f=200 mm focusing mirror. The SHG-FROG was used for both measurement of the 800 nm fundamental and 515 nm dump pulses by substituting the appropriate BBO crystal and spectrometer.

The results of the FROG retrieval for LR23 and 2019B8021 are shown in Supplementary Table. 1 and the individual fits are shown in Supplementary Fig. 8 - Supplementary Fig. 10. During LR23 difficulties with other parts of the experiment limited the time to perform FROG characterization as a result no signal was obtained from the XFROG therefore the 400 nm pump characteristics are estimated based on those obtained from the fundamental 800 nm measured after passing through the same 100 μm BBO used to generate the 400 nm pulses. At 2019B8021 the pulses are shorter than those used at LCLS this could help explain the reduced strength of signals in the SFX data[5]. In addition while an XFROG trace was obtained the retrieve a pulse width is far shorter than the fundamental used to generate it, we recognize that this is aphysical and more likely due to misalignment in the XFROG cropping the spectra.

In addition to the FROG characterisation of laser conditions at XFEL experiments, we have additionally measured and characterised the power density dependence of product formation. Analysis of the power density dependence provided values for the linear and non-linear optical cross sections (Extended Data Fig. 2b & c). While excited state absorption was not avoided, internal conversion followed Kasha's rule

to produce vibrationally excited S_1 population in addition to the S_1 population formed by linear photoexcitation.

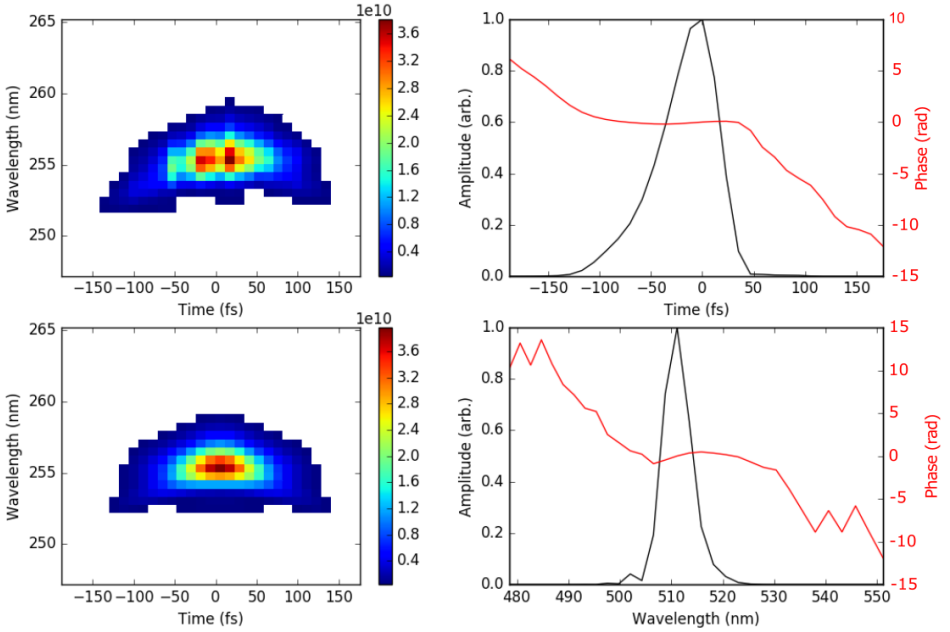

Supplementary Fig. 8 | LCLS LR23 515 nm dump FROG fitting. TOPAS output. SHG-FROG trace experiment (top left), reconstruction (bottom left), recovered pulse temporal profile (top right) and spectral profile (bottom right)

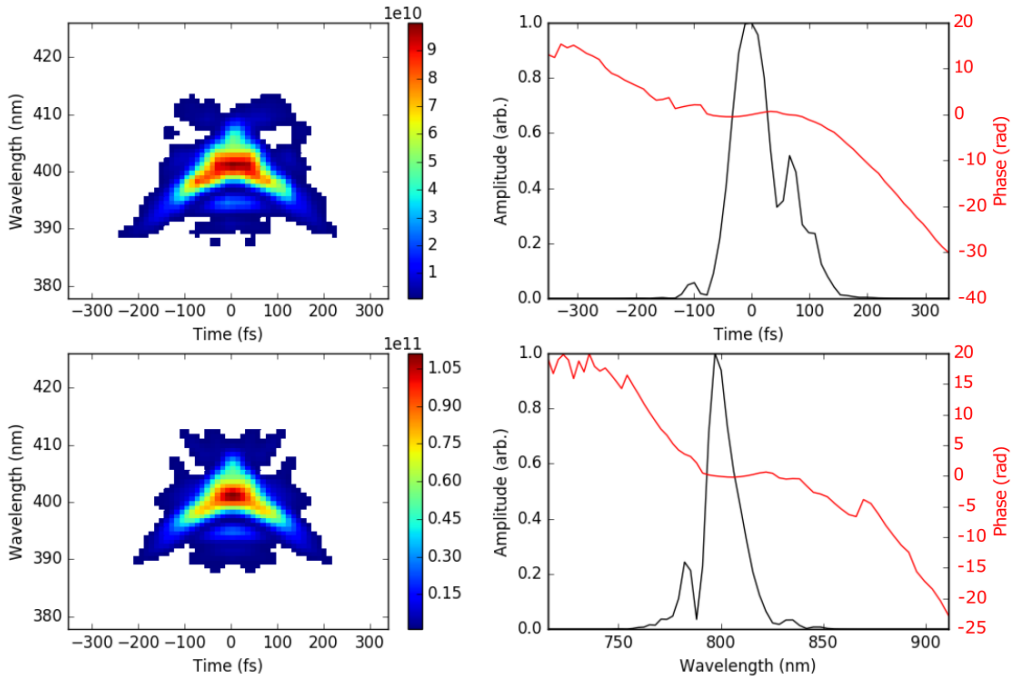

Supplementary Fig. 9 | LCLS CXI LR23 800 nm fundamental FROG fitting. SHG-FROG trace experiment (top left), reconstruction (bottom left), recovered pulse temporal profile (top right) and spectral profile (bottom right)

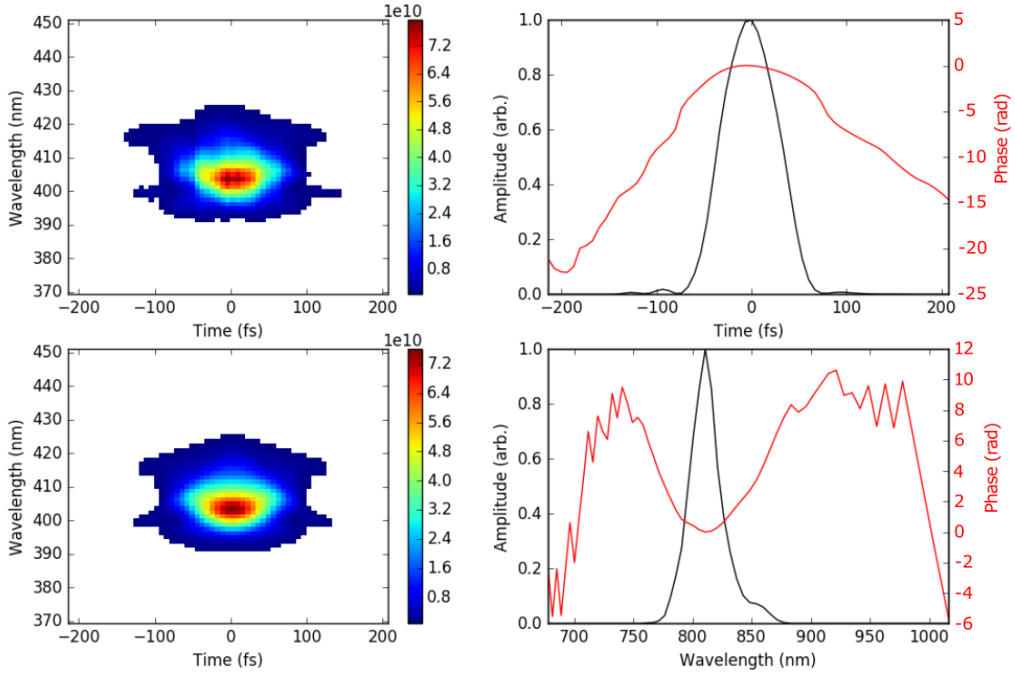

Supplementary Fig. 10 | SACLA 2019B8021 800 nm fundamental FROG fitting. SHG-FROG trace experiment (top left), reconstruction (bottom left), recovered pulse temporal profile (top right) and spectral profile (bottom right).

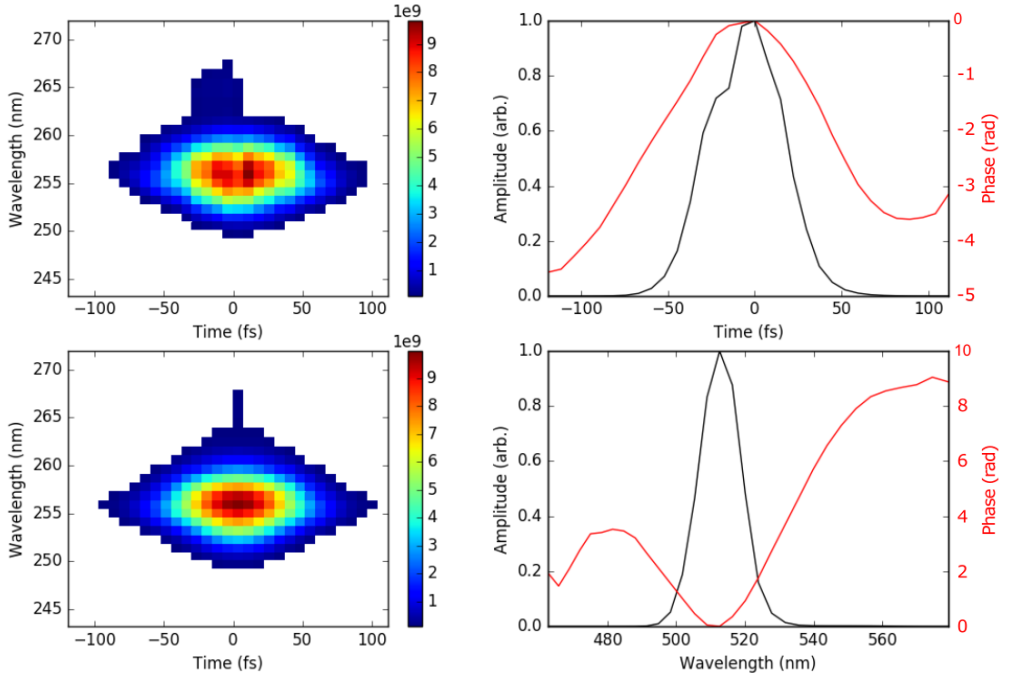

Supplementary Fig. 11 | SACLA 2019B8021 515 nm dump FROG fitting. Showing SHG-FROG trace experiment (top left), reconstruction (bottom left), recovered pulse temporal profile (top right) and spectral profile (bottom right).

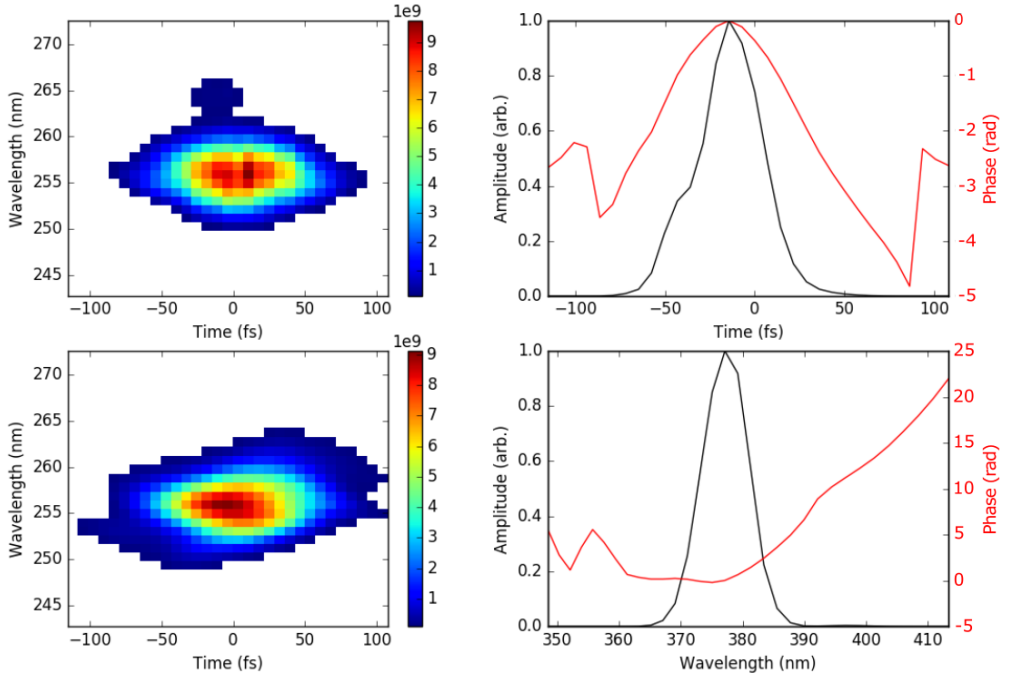

Supplementary Fig. 12 | SACLA 2019B8021 400 nm pump FROG fitting. Showing XFROG trace experiment (top left), reconstruction (bottom left), recovered pulse temporal profile (top right) and spectral profile (bottom right).

Supplementary Table. 1 | FROG fitting results. Results of SHG-FROG and XFROG pulse fitting for LCLS LR23 and SACLA 2019B8021 beamtimes.

	λ (nm)	Δλ (nm)	Δt (fs)	GDD (fs^2)	3rd Order (fs^3)
LCLS					
Fundamental (after BBO)	800	15.5	100 ± 15	554 ± 50	2944 ± 600
Pump	400	-	~100	-	-
Dump	515	6.8	71 ± 15	480 ± 40	2000 ± 400
SACLA					
Fundamental (after BBO)	800	27	72	262 ± 12	N/A
Pump	400	9	40	135 ± 15	N/A
Dump	515	14	52	355 ± 175	184 ± 20

5. TR-SFX datasets

A summary of all the different SFX datasets collected over the course of this study is shown in Extended Data Table 1.

5.1. LCLS CXI LR23

Figure 2 shows data from the LR23 experiment at LCLS beamline CXI. The Fourier shell Coefficient (FSC) and R-split for all merge laser off and dark data is shown in Supplementary Fig. 13. Estimation of the Dark (only preilluminated) occupancy is shown in Supplementary Fig. 29. N_{EXT} determination and occupancy refinement was performed on the combined 0-1 ps PP data (Supplementary Fig. 14 - Supplementary Fig. 15). The anisotropic ratio of the fully merged dark, PP and PDP is shown in Supplementary Table. 2. Using the output of the CXI timing tool the sub picosecond data was sorted into 150 fs wide bins. Occupancy refinement was performed for each of time bin for the PP (Supplementary Fig. 17 - Supplementary Fig. 22) and PDP (Supplementary Fig. 23 -Supplementary Fig. 28) datasets. The method used to determine occupancy for the pumped coordinates used here, is validated by scanning the occupancy of PDP coordinates for the dark unpumped data only. As expected, the addition of also small contributions of PDP coordinates increases the R-factor as expected, as shown in Supplementary Fig. 29.

Comparison of the PP and PDP bins shown in Extended Data Fig. 6, 7 and Supplementary Fig. 30. Supplementary Fig. 31 shows Pump-Probe and Pump-Dump-Probe Q-weighted Fo-Fo maps from the rsKiiro TR-SFX experiment. In the top row, Q-weighted Fo-Fo maps are shown for all of the collected PP, PDP, and dark data (as in Figure 2 of the main text). For the rows below, all datasets were split in two halves and Q-weighted Fo-Fo maps were recomputed for different combinations of the obtained structure factors. The amplification of signals in the Pump-Dump-Probe data compared to the Pump-Probe data is reproducibly shown across the different examples Supplementary Fig. 32 shows difference structure factor amplitudes for PP and PDP along with weighted assigned to each difference by Q-weighting. Crystallographic statistics are shown Extended Data Table 2 & 3.

Fo-Fo difference maps are calculated with the Q-weighted technique, and the weighted differences are used to calculated the extrapolated structure factors. With Q-weighting, the differences are found in the following way

$$WDF = w \times \Delta F$$

Where

$$\Delta \mathrm{F} = \left|\mathrm{F}_{\mathrm{obs_L}}\right| - \left|\mathrm{F}_{\mathrm{obs_D}}\right|$$

And

$$w = \left(1 + \frac{\sigma^2_{\Delta \mathrm{F}}}{\overline{\sigma^2_{\Delta \mathrm{F}}}} + \alpha \frac{|\Delta \mathrm{F}|^2}{\overline{|\Delta \mathrm{F}|^2}}\right)^{-1}$$

The scale factor α decreases the influence of structure factor differences that have very large magnitudes while maintaining what may be erroneously small uncertainties. In this work, a value of α= 1 was implemented as in Šrajer et al. (2001)[6]. Earlier work on Q-weighting by Ursby and Bourgeois (1997)[7] used a value of α= 0.

Extrapolated structure factors were calculated using the Q-weighted differences according to Pandey et al.(2020)[8] and Gorel, Schlichting, & Barends(2021)[9]

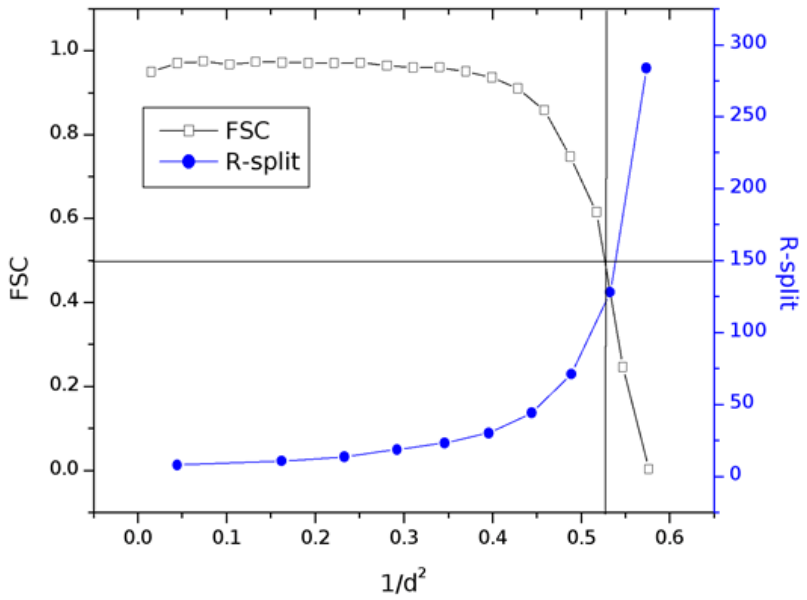

Supplementary Fig. 13 | LCLS LR23 FSC and R-Split for the all merged laser off, dark data. An FSC of 0.5 is chosen for a limiting 1.38 Å.

Supplementary Table. 2 | Anisotropic analysis by STARANISO[10] for merged 0-1 ps PP and PDP datasets.

Dataset	Anisotropic ratio	Diffraction limits of anisotropic ellipsoid (a*,b*,c*) [Å]
Dark	0.161	1.489, 1.400, 1.404
PP (400 nm)	0.141	1.489, 1.410, 1.404
PDP (400 and 515 nm)	0.140	1.572, 1.518, 1.498

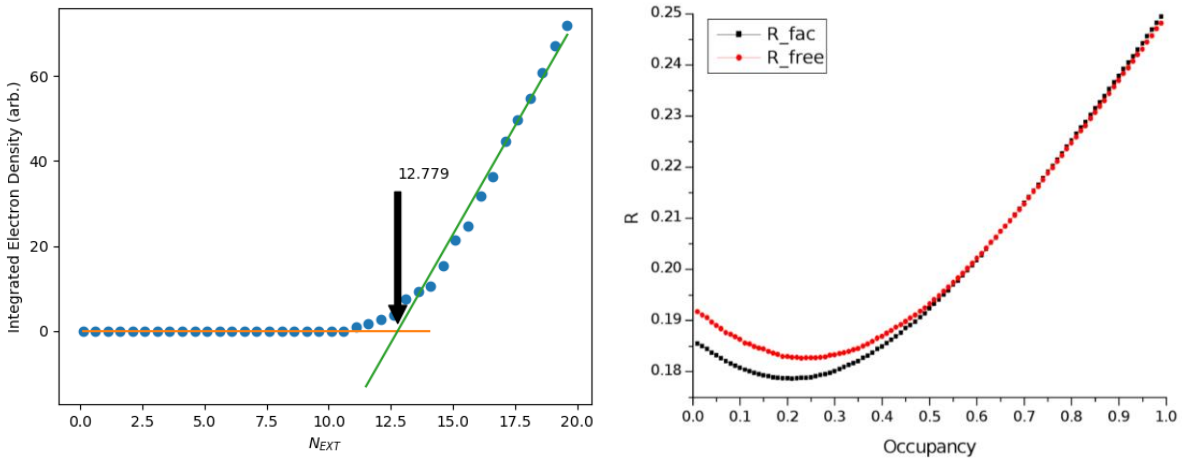

Supplementary Fig. 14 | LCLS LR23 PDP 400-515 nm merged 0-1 ps: Left: Extrapolated factor, N_{EXT}, determination through the intersection point of two linear fits to the magnitude of integrated negative electron density, shown as blue circles. Right: R_fac/R_free calculation for varied occupancy

of refined coordinates. Occupancy refers to the proportion of extrapolated coordinates (light) compared to ground state coordinates (dark). Both R_{fac} and R_{free} minimise at dark=0.79 and light=0.21.

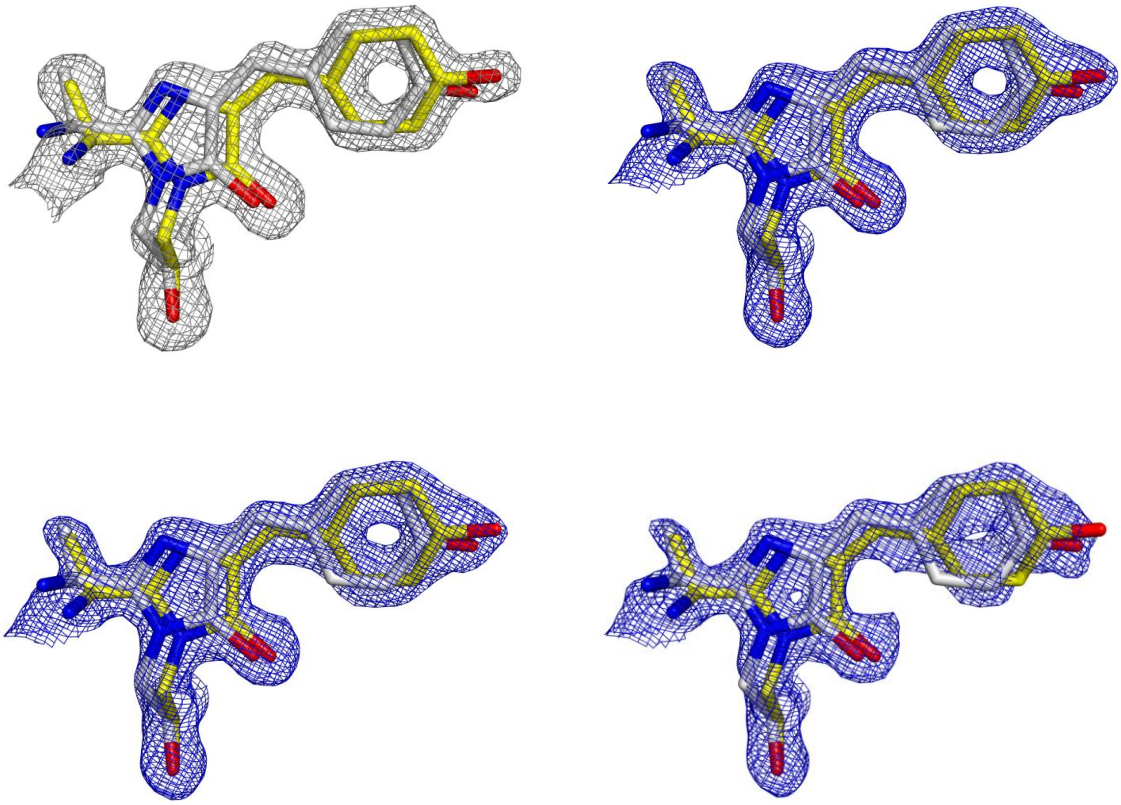

Supplementary Fig. 15 | LCLS LR23 PDP 400-515 nm merged 0-1 ps: Refined coordinates for the ground state (yellow) and the extrapolated map coordinates for PDP (grey). Top left: 2Fo -Fc electron density for at 1.5 rms contouring (white) for the 400 nm 0 - 1 ps bin with occupancy of 0.86 ground-state and 0.14 extrapolated. Top Right: F_o electron density for at 1.5 rms contouring (blue) for the extrapolated value of N_{EXT} = 5.1. Bottom Left: F_o electron density for at 1.5 rms contouring (blue) for the extrapolated value of N_{EXT} = 7.6. Bottom Right: F_o electron density for at 1.5 rms contouring (blue) for the extrapolated value of N_{EXT} = 12.6.

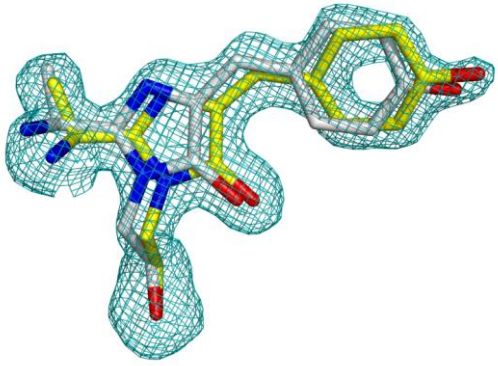

Supplementary Fig. 16 | LCLS LR23 PDP 400-515 nm merged 0-1 ps: Chromophore omitted Fo-Fc density contoured at +3σ level (teal) for 0.79:0.21 (ground:light) occupancy model. The coordinates refined to an extrapolated value of N_{EXT} = 9 are shown in yellow (Ground) and in grey (PDP).

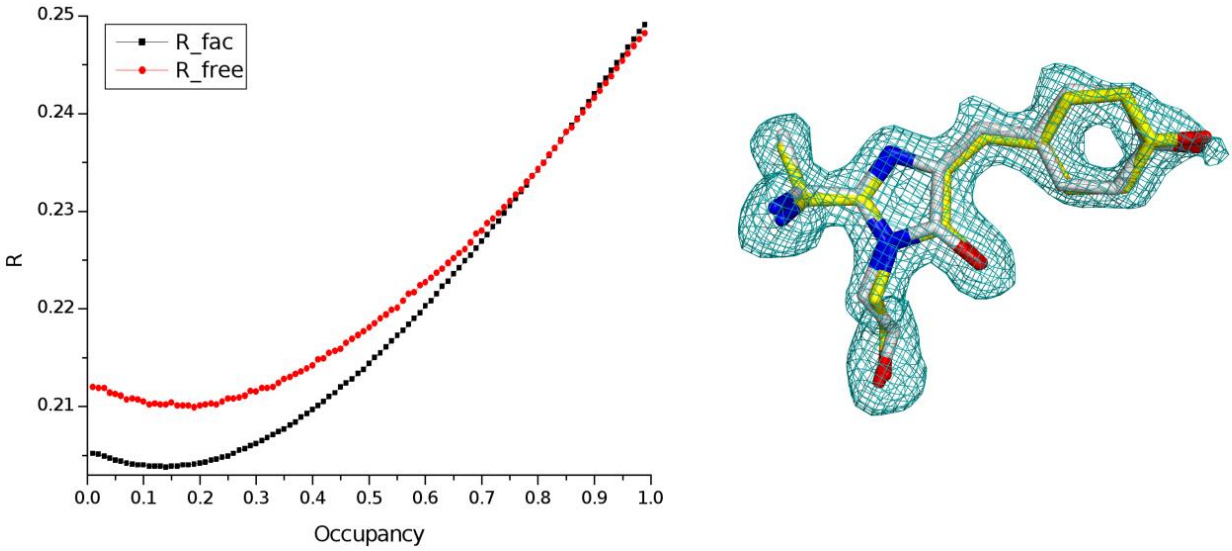

Supplementary Fig. 17 | LCLS LR23 PP 400 nm 250 fs. Left: R_{fac}/R_{free} calculation for varied occupancy of refined coordinates. Occupancy refers to the proportion of extrapolated coordinates (light) compared to ground state coordinates (dark). Both R_{fac} and R_{free} minimize at dark = 0.86 and light = 0.14. Right: Chromophore omitted F_o-F_c density contoured at +3σ level (teal) for 0.86:0.14 (ground:light) occupancy model. The coordinates refined to an extrapolated value of N_{EXT} = 8.6 are shown in grey (light) and ground state in yellow.

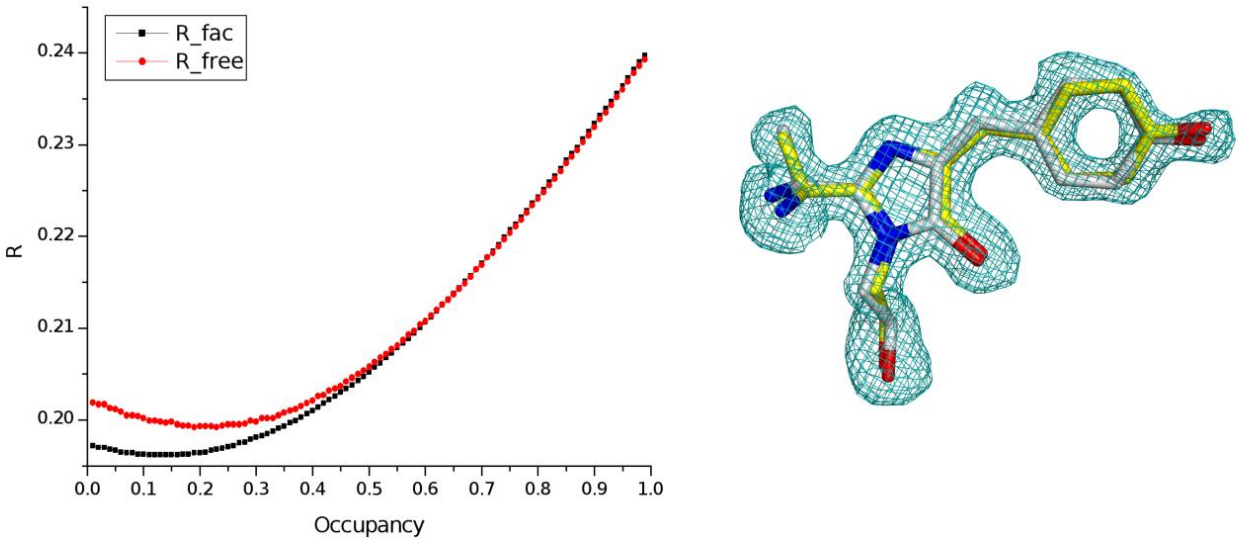

Supplementary Fig. 18 | LCLS LR23 PP 400 nm 400 fs. Left: R_{fac}/R_{free} calculation for varied occupancy of refined coordinates. Occupancy refers to the proportion of extrapolated coordinates (light) compared to ground state coordinates (dark). Both R_{fac} and R_{free} minimize at dark = 0.87 and light = 0.13. Right: Chromophore omitted F_o-F_c density contoured at +3σ level (teal) for 0.87:0.13 (ground:light) occupancy model. The coordinates refined to an extrapolated value of N_{EXT} = 8.6 are shown in grey (light) and ground state in yellow.

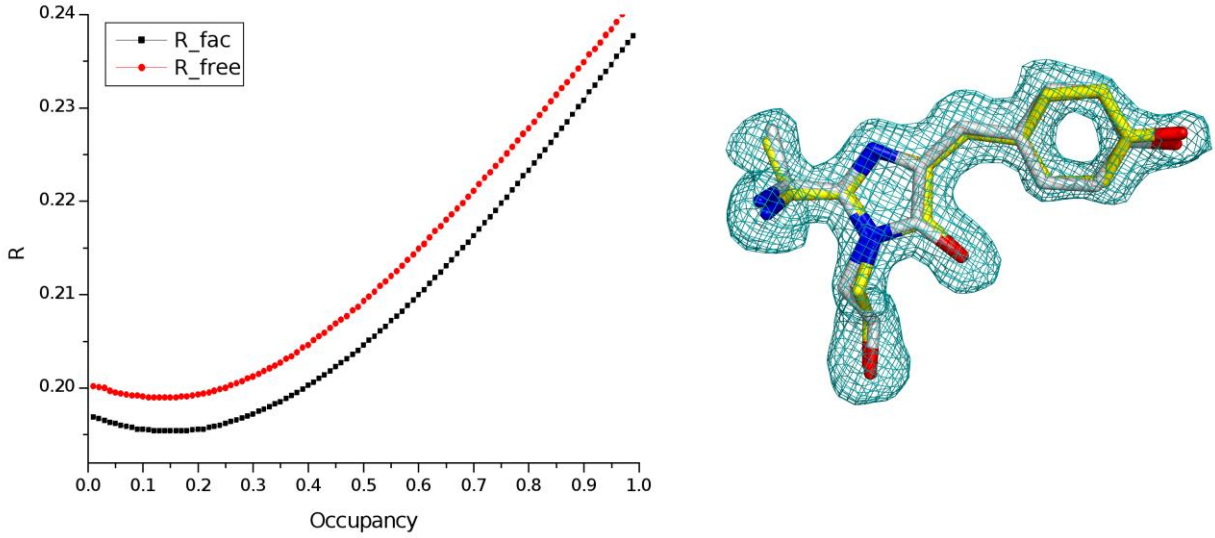

Supplementary Fig. 19 | LCLS LR23 PP 400 nm 550 fs. Left: R_{fac}/R_{free} calculation for varied occupancy of refined coordinates. Occupancy refers to the proportion of extrapolated coordinates (light) compared to ground state coordinates (dark). Both R_{fac} and R_{free} minimize at dark = 0.86 and light = 0.14. Right: Chromophore omitted F_o-F_c density contoured at +3σ level (teal) for 0.86:0.14 (ground:light) occupancy model. The coordinates refined to an extrapolated value of N_{EXT} = 8.6 are shown in grey (light) and ground state in yellow. R-free was calculated using 10% reflections

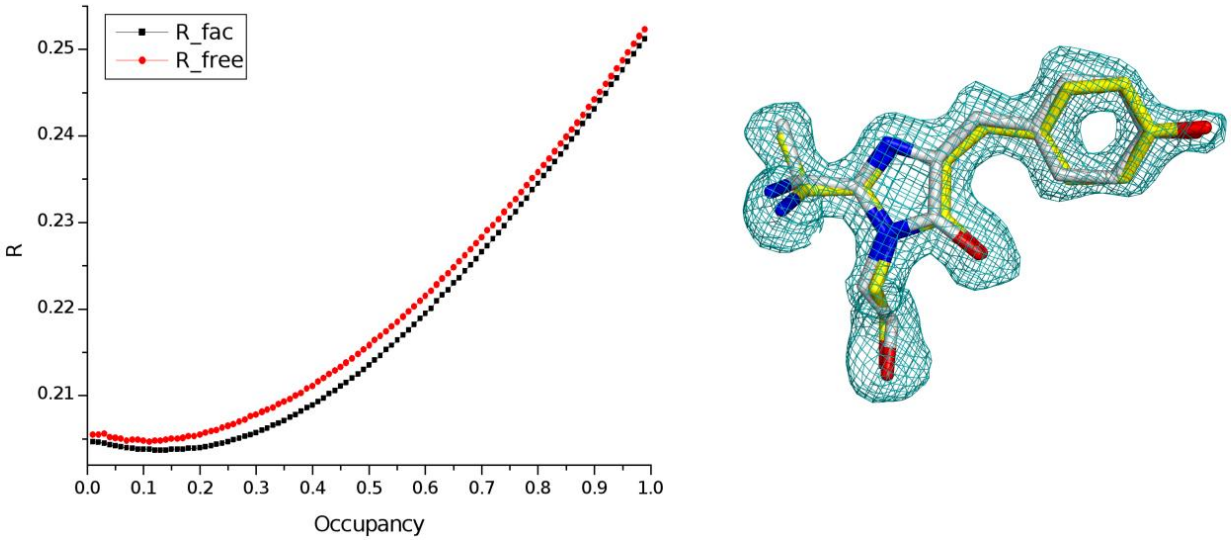

Supplementary Fig. 20 | LCLS LR23 PP 400 nm 700 fs. Left: R_{fac}/R_{free} calculation for varied occupancy of refined coordinates. Occupancy refers to the proportion of extrapolated coordinates (light) compared to ground state coordinates (dark). Both R_{fac} and R_{free} minimize at dark = 0.87 and light = 0.13. Right: Chromophore omitted F_o-F_c density contoured at +3σ level (teal) for 0.87:0.13 (ground:light) occupancy model. The coordinates refined to an extrapolated value of N_{EXT} = 8.6 are shown in grey (light) and ground state in yellow.

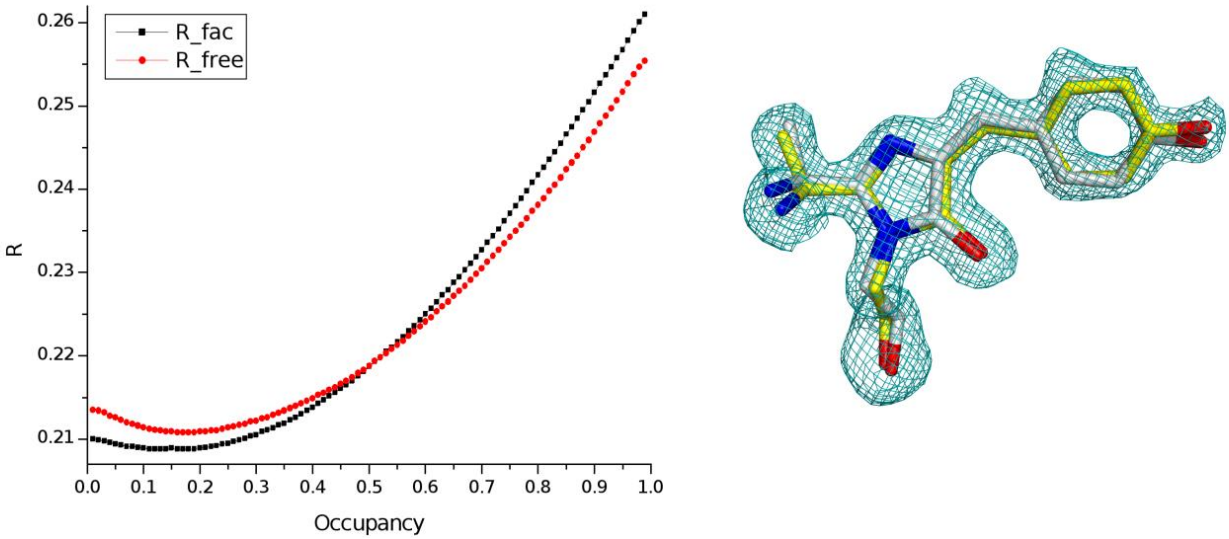

Supplementary Fig. 21 | LCLS LR23 PP 400 nm 850 fs. Left: R_{fac}/R_{free} calculation for varied occupancy of refined coordinates. Occupancy refers to the proportion of extrapolated coordinates (light) compared to ground state coordinates (dark). Both R_{fac} and R_{free} minimize at dark = 0.88 and light = 0.12. Right: Chromophore omitted F_o-F_c density contoured at +3σ level (teal) for 0.88:0.12 (ground:light) occupancy model. The coordinates refined to an extrapolated value of N_{EXT} = 8.6 are shown in grey (light) and ground state in yellow.

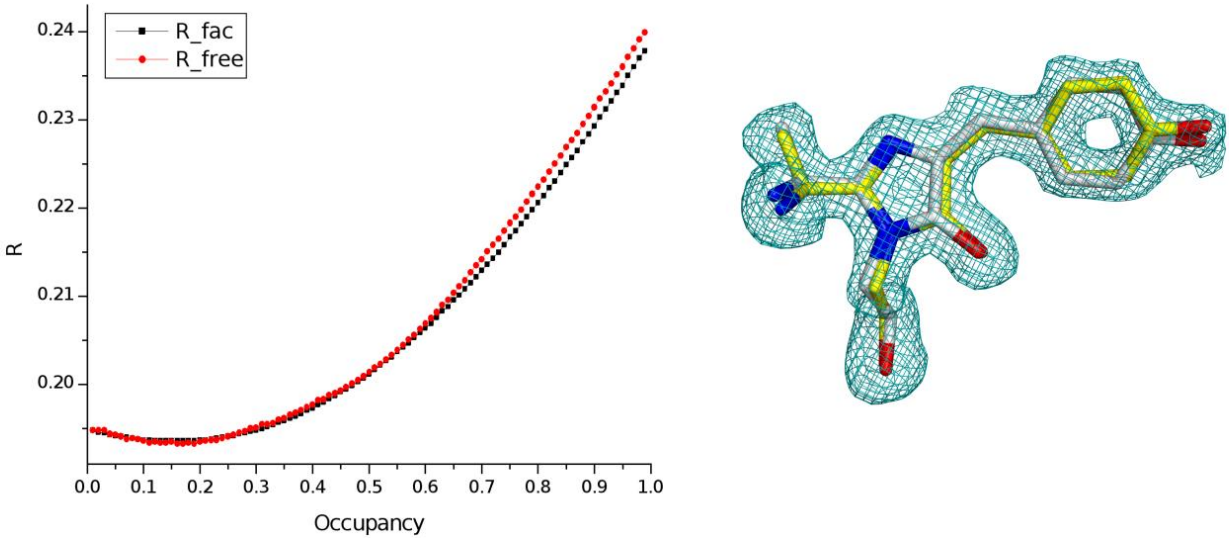

Supplementary Fig. 22 | LCLS LR23 PP 400 nm 1100 fs. Left: R_{fac}/R_{free} calculation for varied occupancy of refined coordinates. Occupancy refers to the proportion of extrapolated coordinates (light) compared to ground state coordinates (dark). Both R_{fac} and R_{free} minimize at dark = 0.83 and light = 0.17. Right: Chromophore omitted F_o-F_c density contoured at +3σ level (teal) for 0.83:0.17 (ground:light) occupancy model. The coordinates refined to an extrapolated value of N_{EXT} = 8.6 are shown in grey (light) and ground state in yellow.

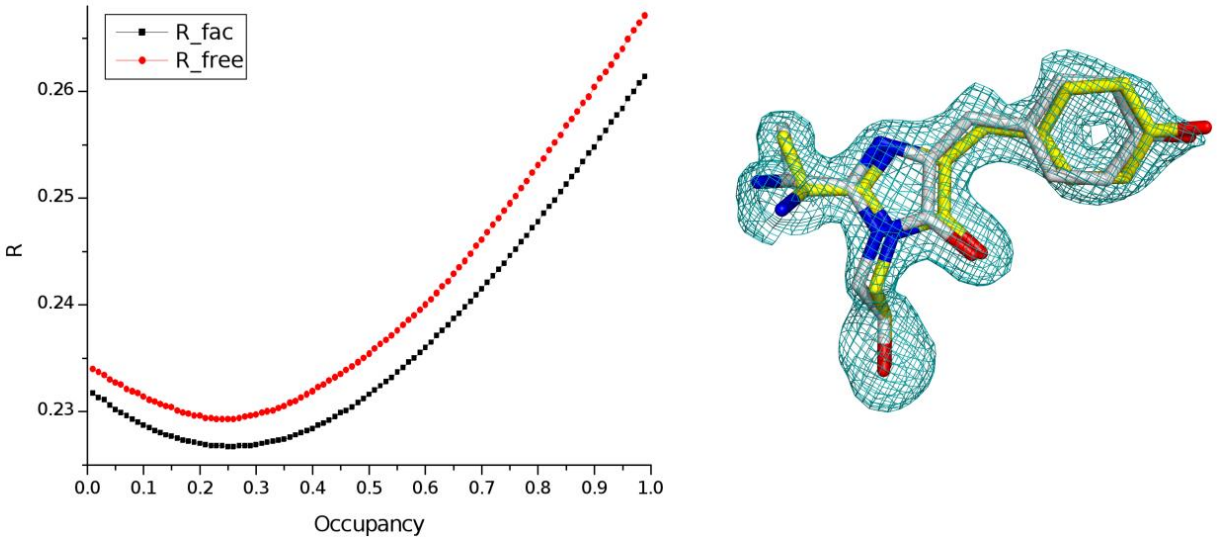

Supplementary Fig. 23 | LCLS LR23 PDP 400-515 nm 250 fs. Left: R_{fac}/R_{free} calculation for varied occupancy of refined coordinates. Occupancy refers to the proportion of extrapolated coordinates (light) compared to ground state coordinates (dark). Both R_{fac} and R_{free} minimize at dark = 0.75 and light = 0.25. Right: Chromophore omitted F_o-F_c density contoured at +3σ level (teal) for 0.75:0.25 (ground:light) occupancy model. The coordinates refined to an extrapolated value of N_{EXT} = 5.6 are shown in grey (light) and ground state in yellow.

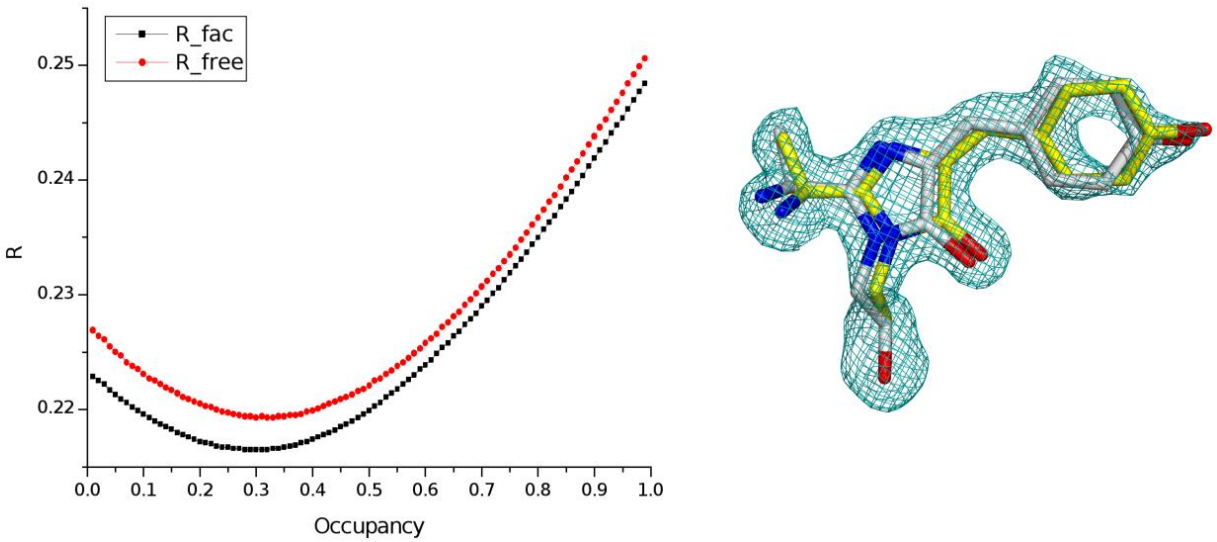

Supplementary Fig. 24 | LCLS LR23 PDP 400-515 nm 400 fs. Left: R_{fac}/R_{free} calculation for varied occupancy of refined coordinates. Occupancy refers to the proportion of extrapolated coordinates (light) compared to ground state coordinates (dark). Both R_{fac} and R_{free} minimize at dark = 0.70 and light = 0.30. Right: Chromophore omitted F_o-F_c density contoured at +3σ level (teal) for 0.70:0.30 (ground:light) occupancy model. The coordinates refined to an extrapolated value of N_{EXT} = 5.6 are shown in grey (light) and ground state in yellow.

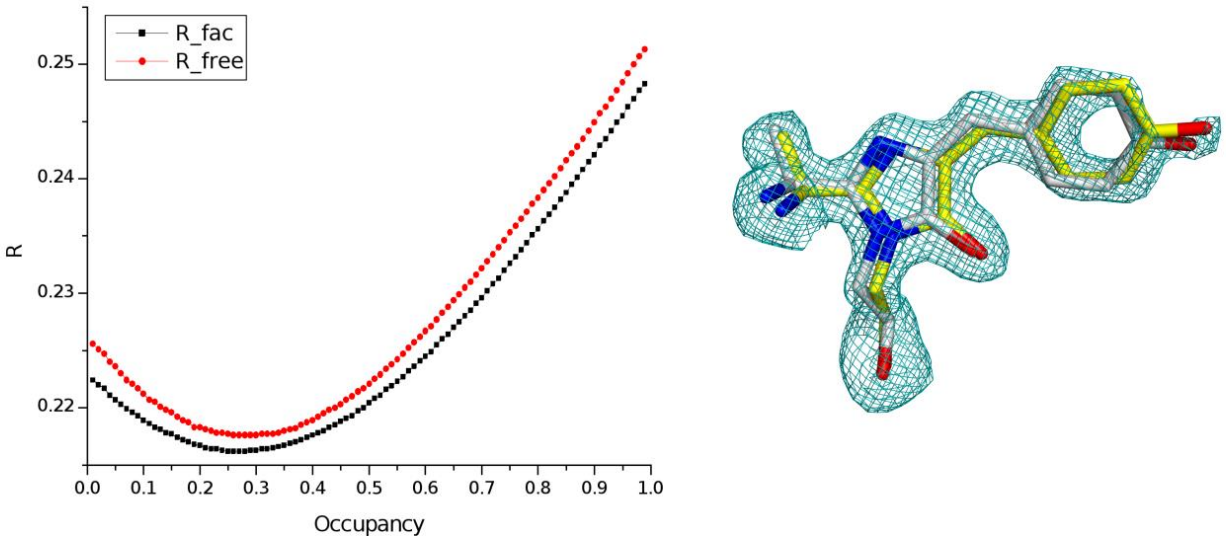

Supplementary Fig. 25 | LCLS LR23 PDP 400-515 nm 550 fs. Left: R_{fac}/R_{free} calculation for varied occupancy of refined coordinates. Occupancy refers to the proportion of extrapolated coordinates (light) compared to ground state coordinates (dark). Both R_{fac} and R_{free} minimize at dark = 0.84 and light = 0.16. Right: Chromophore omitted F_o-F_c density contoured at +3σ level (teal) for 0.84:0.16 (ground:light) occupancy model. The coordinates refined to an extrapolated value of N_{EXT} = 5.6 are shown in grey (light) and ground state in yellow.

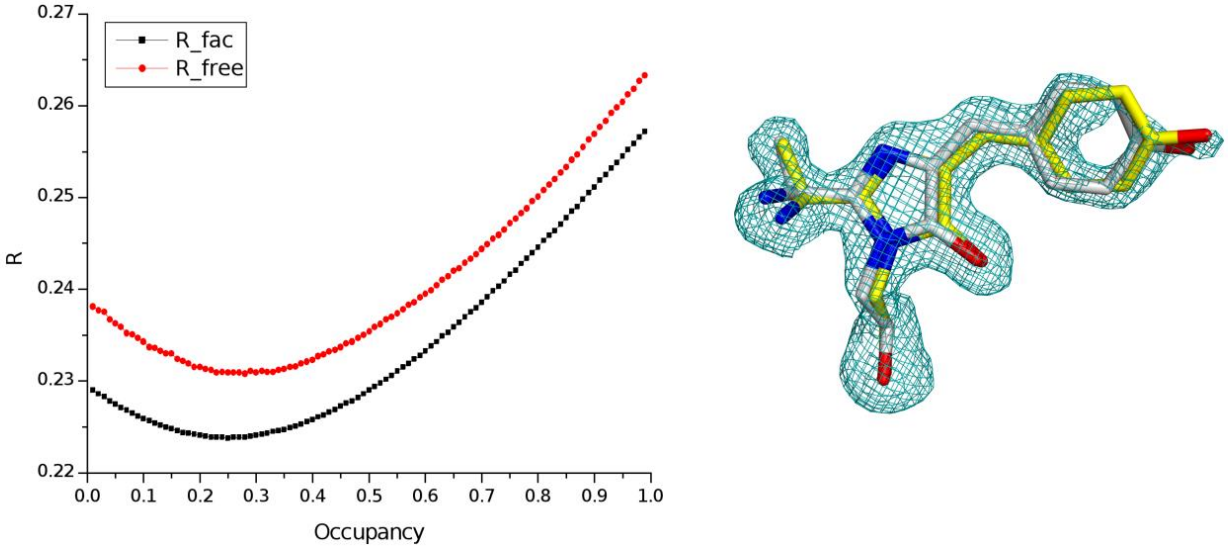

Supplementary Fig. 26 | LCLS LR23 PDP 400-515 nm 700 fs. Left: R_{fac}/R_{free} calculation for varied occupancy of refined coordinates. Occupancy refers to the proportion of extrapolated coordinates (light) compared to ground state coordinates (dark). Both R_{fac} and R_{free} minimize at dark = 0.75 and light = 0.25. Right: Chromophore omitted F_o-F_c density contoured at +3σ level (teal) for 0.75:0.25 (ground:light) occupancy model. The coordinates refined to an extrapolated value of N_{EXT} = 5.6 are shown in grey (light) and ground state in yellow.

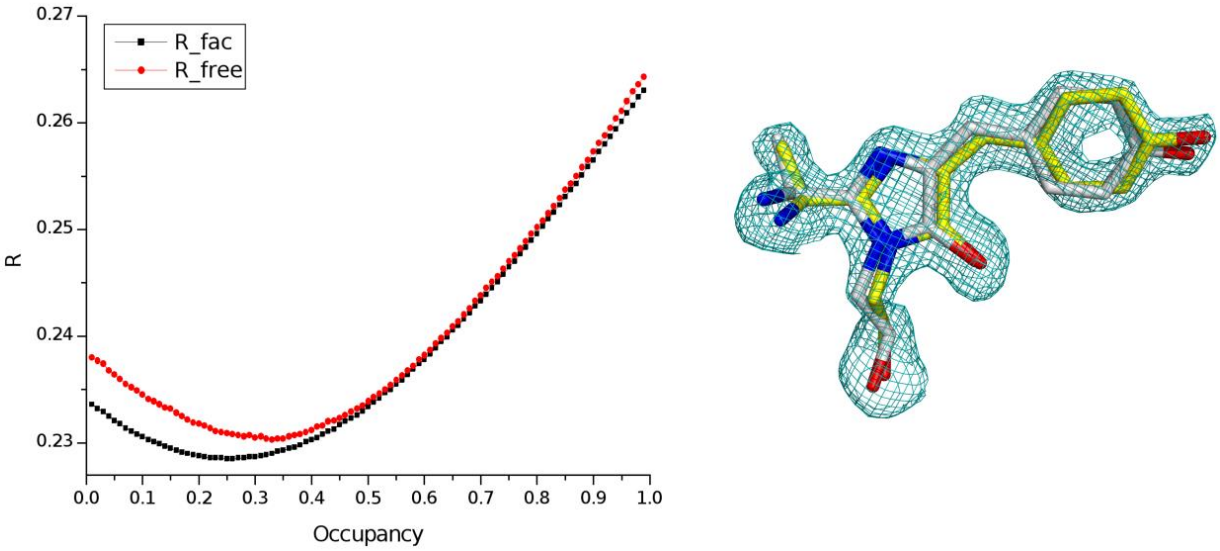

Supplementary Fig. 27 | LCLS LR23 PDP 400-515 nm 850 fs. Left: R_{fac}/R_{free} calculation for varied occupancy of refined coordinates. Occupancy refers to the proportion of extrapolated coordinates (light) compared to ground state coordinates (dark). Both R_{fac} and R_{free} minimise at dark = 0.75 and light = 0.25. Right: Chromophore omitted F_o-F_c density contoured at +3σ level (teal) for 0.75:0.25 (ground:light) occupancy model. The coordinates refined to an extrapolated value of N_{EXT} = 5.6 are shown in grey (light) and ground state in yellow.

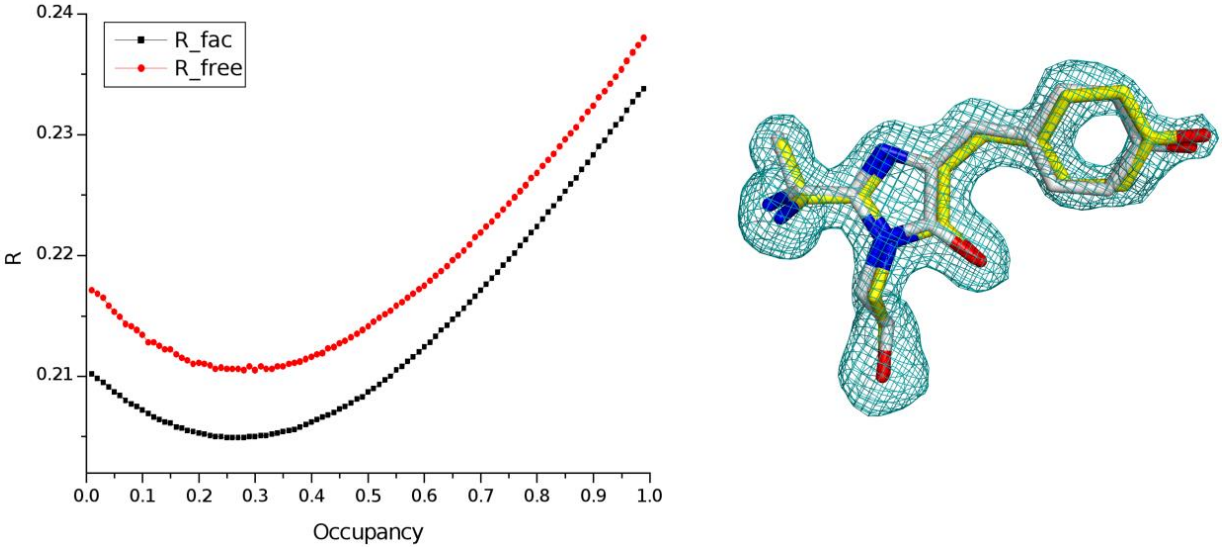

Supplementary Fig. 28 | LCLS LR23 PDP 400-515 nm 1100 fs. Left: R_{fac}/R_{free} calculation for varied occupancy of refined coordinates. Occupancy refers to the proportion of extrapolated coordinates (light) compared to ground state coordinates (dark). Both R_{fac} and R_{free} minimize at dark = 0.74 and light = 0.26. Right: Chromophore omitted F_o-F_c density contoured at +3σ level (teal) for 0.74:0.26 (ground:light) occupancy model. The coordinates refined to an extrapolated value of N_{EXT} = 5.6 are shown in grey (light) and ground state in yellow.

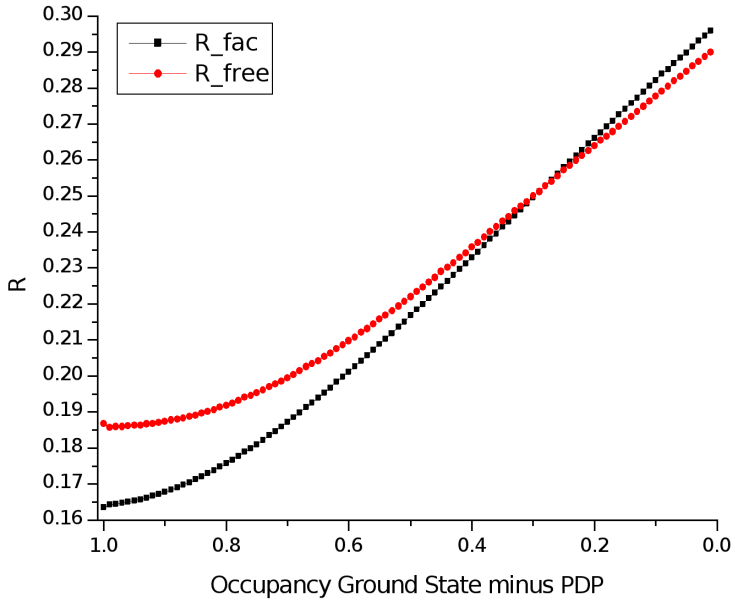

Supplementary Fig. 29 | LCLS LR23 Dark Occupancy Determination. Using Dark, Laser OFF data only (Extended Data Table 2). The R-factors were analysed with a resolution limit of 1.5 Å. The additional occupancy of PDP coordinates degrades the R-factor and R-free factor.

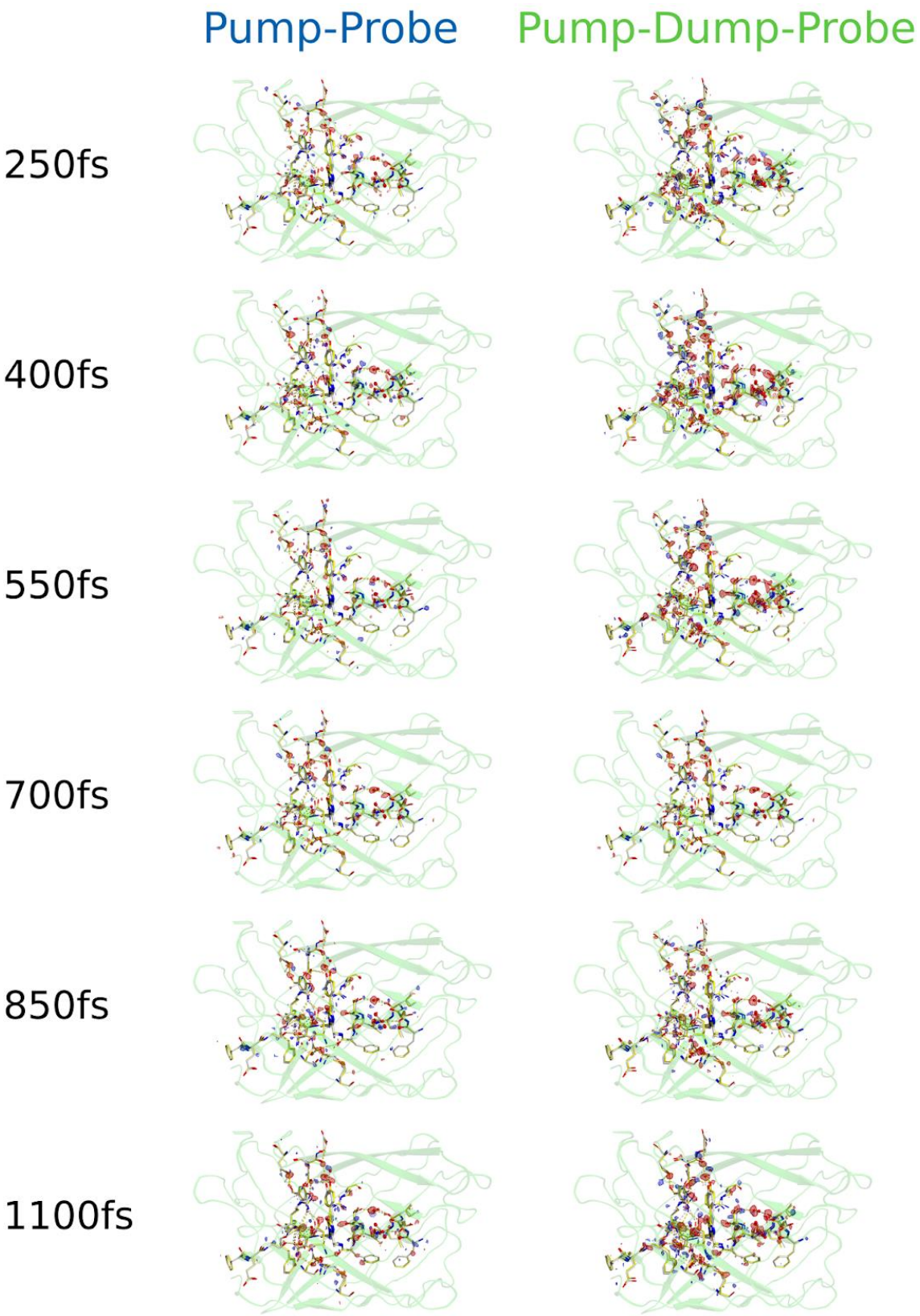

Supplementary Fig. 30 | LCLS LR23 TR-SFX PP vs PDP. Q-weighted difference electron density for each bin of the pump probe (400 nm) on the left and of the pump-dump probe (400-515 nm) on the right. The secondary structure (green) of the ground state coordinates (yellow) and PP (grey) and PDP (grey) coordinates are shown with electron density contoured at +3σ rms (blue) and -3σ rms (red).

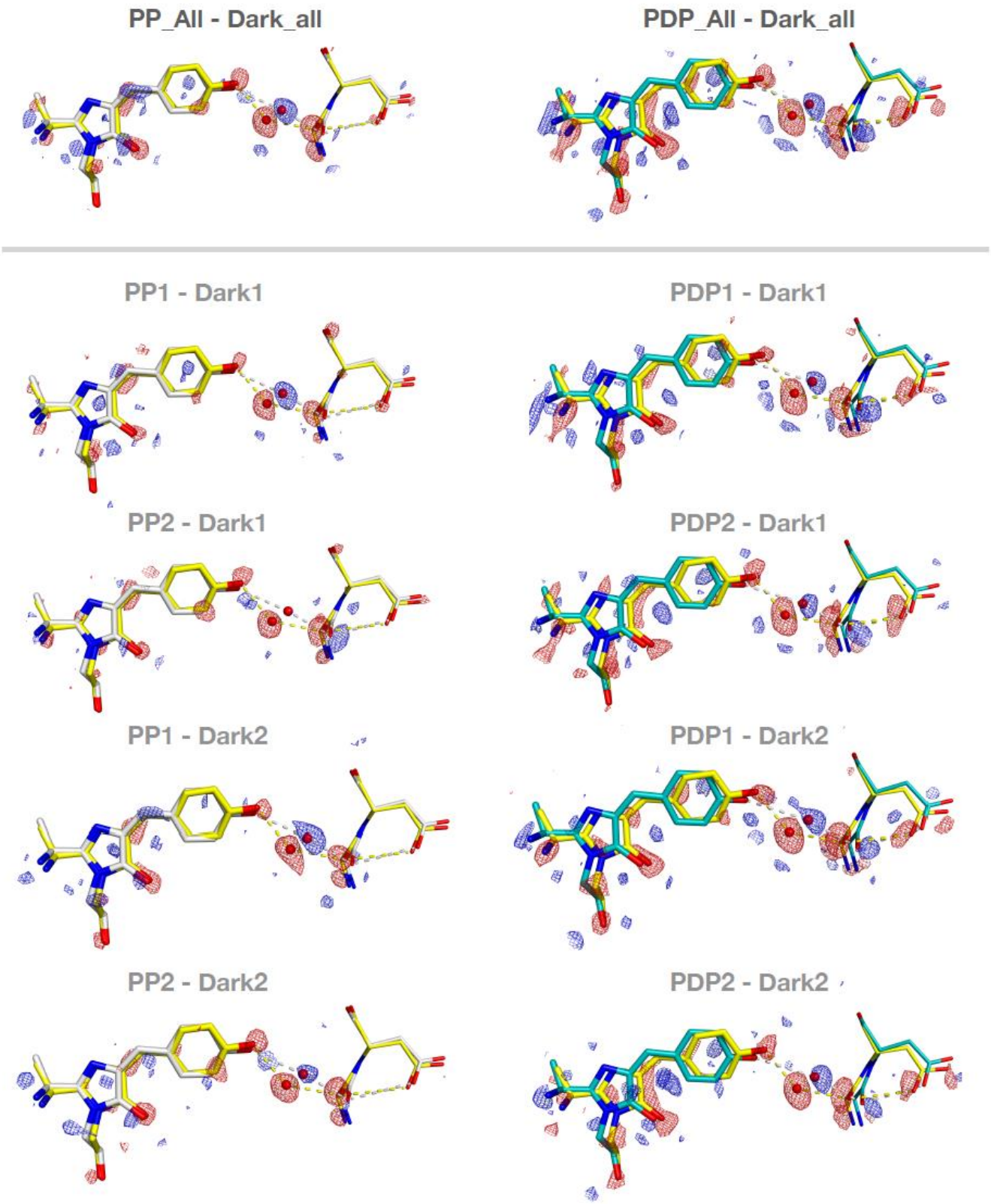

Supplementary Fig. 31 | LCLS LR23 PP vs PDP split data comparison. Femtosecond time resolved Pump-Probe (PP: left) and Pump-Dump-Probe (PDP: right) TR-SFX experiment of rsKiiro off state with a trans neutral chromophore. In the top row, Q-weighted Fo-Fo maps are shown for all of the collected PP, PDP, and dark data (as in Figure 2 of the main text). For the rows below, all datasets were split in two to demonstrate the reproducibility of the signals.

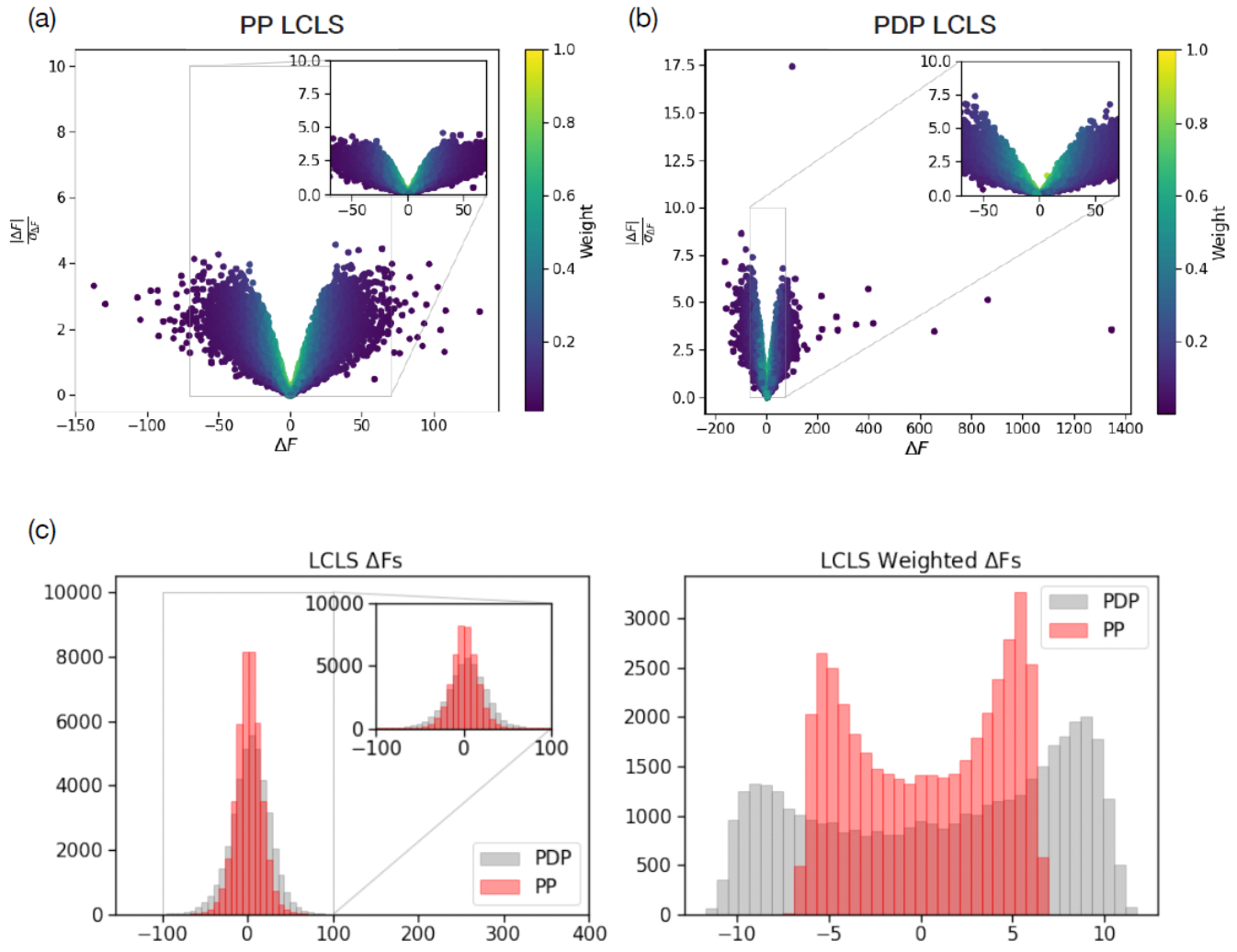

Supplementary Fig. 32 | LCLS LR23 Difference Structure Factors. Difference structure factor amplitudes for the femtosecond time resolved Pump-Probe (a) and Pump-Dump-Probe (b) LCLS TR-SFX experiment of rsKiiro are plotted, along with the weight assigned to each difference by the Q-weighting scheme. In (c), the distributions of difference structure factors amplitudes before and after Q-weighting are shown. Larger amplitudes are observable for the PDP dataset. Structure factors were plotted using the Reciprocal Spaceship package.

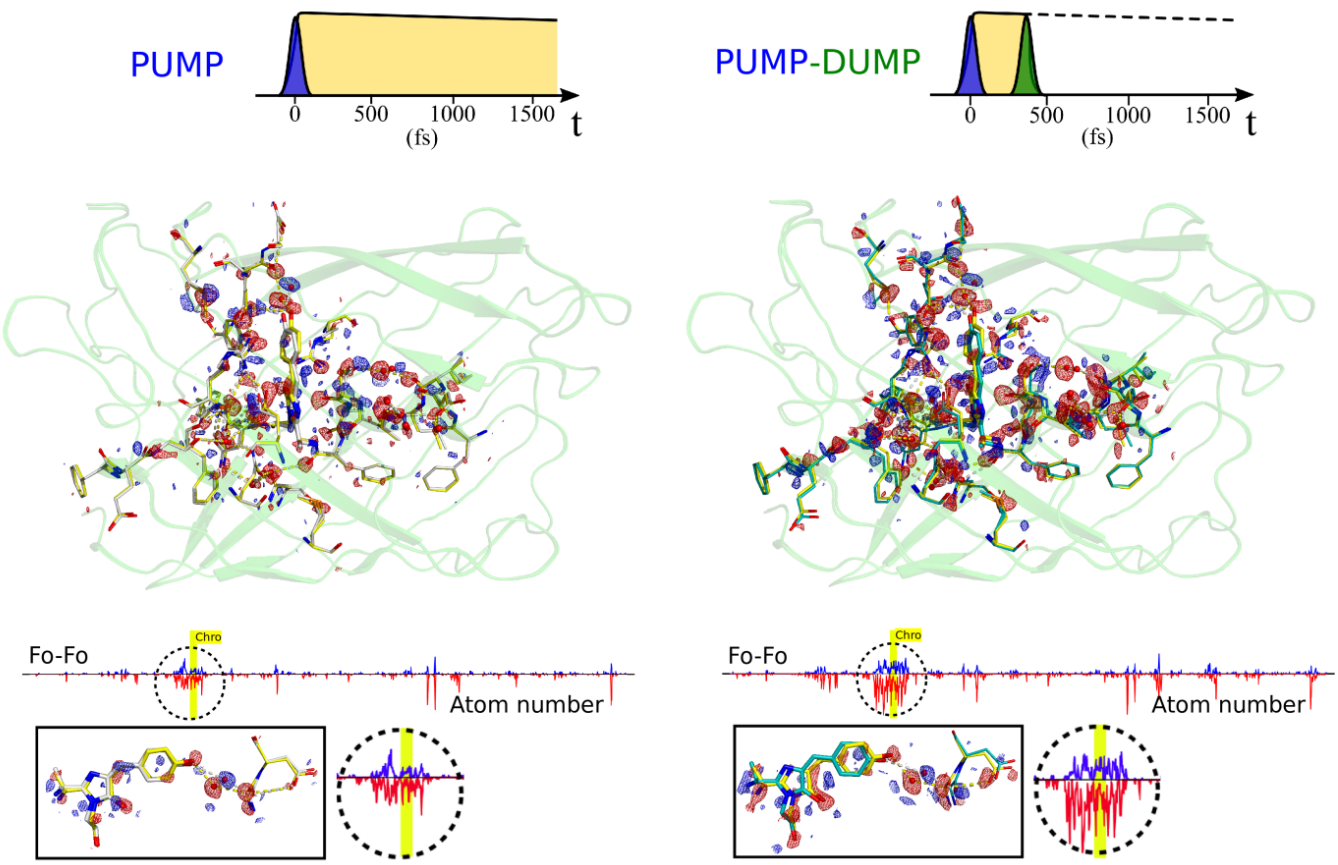

Supplementary Fig. 33 | LCLS LR23 Full protein overview of the PP and PDP electron density differences shown in Figure 2. The Fo-Fo difference maps are contoured at 3 sigma, as in Figure 2. The zoomed view of the integration of the electron density differences in the chromophore region emphasizes the amplification of the PDP data relative to the PP data.

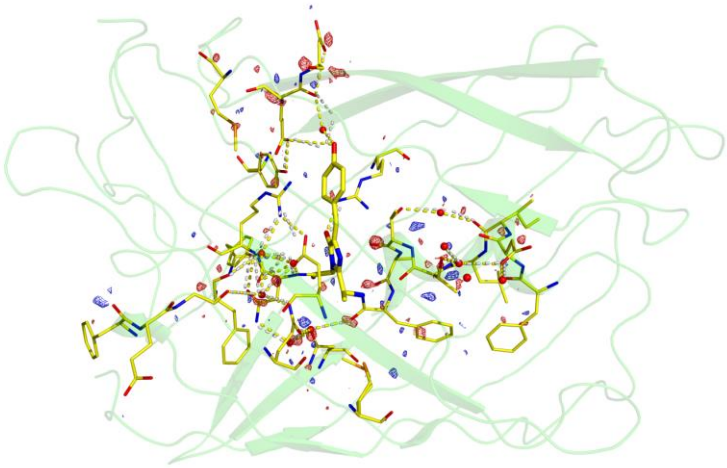

Supplementary Fig. 34 | LCLS LR23 Non-resonant pumping control. Fobs-Fobs Q weighted difference map for non-resonant 515nm pulse only, for LCLS experiment LR23. The data is for all positive sub-picosecond Dump-Probe delays. The map is contoured at 3 rms level. The difference data is calculated from merging 15,949 indexed Laser-ON diffraction images and 35,030 reference dark, indexed Laser-OFF diffraction images. Crystallographic statistics are shown in Supplementary Table. 3.

Supplementary Table. 3 | LCLS LR23 Dump only crystallographic table.

Dataset	Nonresonant-515nm-1ps
Wavelength (eV)	9,097.5
Resolution (Å)	31.94–1.8(1.90-1.80)[1] 31.94–1.5(1.58-1.53)[2] 31.94–1.32(1.38-1.33)[3]
Space group	$P2_12_12_1$
Unit cell (Å)	39.36 74.06 78.68 90 90 90
No. of patterns	23,216
No. of merged patterns	15,949
Total reflections	3,487,139[1] 4,113,940[2] 4,251,050[3]
Unique reflections	56,742[3]
Completeness	100.0[1]
Mean I/σ(I)	6.088(3.43)[1] 4.463(1.39)[2] 3.476(0.04)[3]
Wilson B-factor ($Å^{-2}$)(sigma)	13.390(0.466)
R-split	14.19(28.45)[1] 15.96(74.02)[2] 17.13(274.98)[3]
CC* correlation	0.9924(0.9620)[1] 0.9930(0.8398)[2] 0.9932(0.3243)[3]
$CC_{1/2}$ correlation	0.9701(0.8613)[1] 0.9725(0.5446)[2] 0.9732(0.0554)[3]

[1,2,3] Represent merged statistics for distinct resolution shells

5.2. SACLA 2017B8008

Additional experiments were aimed at evaluating the high peak power used in the TR-SFX experiments. Considering the high peak power of the Stokes field, TA spectroscopy measurements provide confidence on the resonant nature with stimulated emission that is highly selective, and also does not create detectable transient absorption in the absence of the pump interaction (Extended Data Fig.3h). However we addressed potential concern regarding non-resonant 3-photon ionization of water[11] that has been shown to occur already at an excitation of 100 GW cm^{-2} . Negative control experiments at LCLS already confirmed an absence of photoinduced signals for Stokes-only conditions at an average ~500 fs delay time (Supplementary Fig. 34) In addition, we collected 71,055 diffraction patterns with Stokes-only pumping (4 mJ/mm^2) and a 0-1 ps delay and 101,378 dark frames at 1.5 Å resolution at SACLA, which could be processed and scaled with excellent statistics (Supplementary Table. 4). Also for this data set, refinement did not reveal Q-weighted electron density differences due to the interaction with the Stokes field, in spite of its high intensity, the pressure differential, and possible 3-photon water ionization background reactions.

A non-resonant PP control experiment was conducted using only 515 nm illumination pulses on the preilluminated off state. Q-weight difference map between merged 0-1 ps laser on and merged laser off, dark data (Supplementary Fig. 35) shows no significant light induced differences consistent with TA results (Extended Data Fig. 3h). Crystallographic statistics are shown in Supplementary Table. 4.

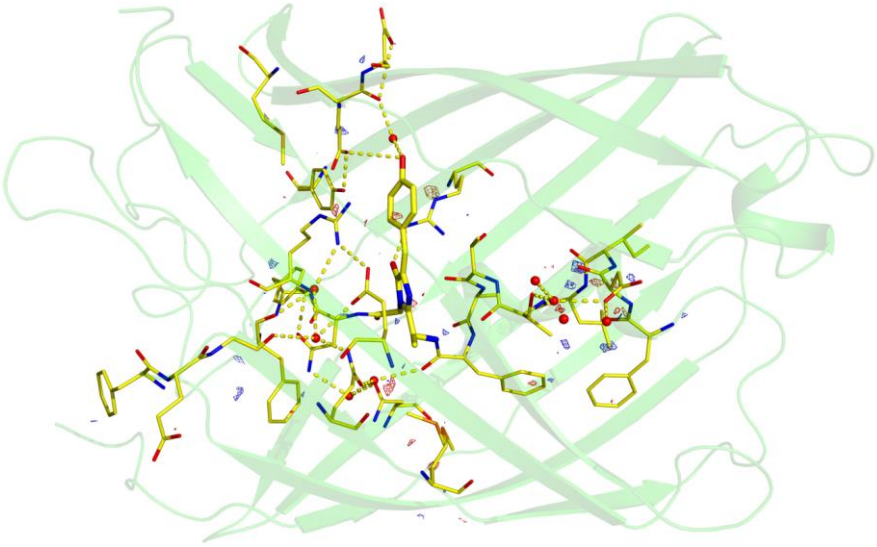

Supplementary Fig. 35 | SACLA 2017B8008 non-resonant pumping. Negative control map showing the Q-weighted difference electron density between the non-resonant, 515 nm 0-1 ps pumping of the off state and merged laser-off, dark data. The secondary structure (green) of the ground state coordinates (yellow) are shown with electron density contoured at +3σ rms (blue) and -3σ rms (red). The experiment used merging of 101,387 dark frames and 71,055 pumped frames with a resolution extending to 1.35Å and excellent statistics (Supplementary Table. 4).

Supplementary Table. 4 | SACLA 2017B8008 crystallographic statistics

	Dark	515nm 0-1ps
Indexed Patterns:	101378	71055
Resolution Limits (Å)	31.77-1.80 (1.864-1.800)[1]	31.77-1.80 (1.864-1.800)[1]
	31.77-1.50 (1.554-1.500)[2]	31.77-1.50 (1.554-1.500)[2]
	31.77-1.43 (1.398-1.350)[3]	31.77-1.43 (1.398-1.350)[3]
Number of Unique reflection indices:	21985[1]	21985[1]
	37586[2]	37586[2]
	51273[3]	51273[3]
No. Merged Reflections:	18598709 (1011010)[1]	13424238 (730782)[1]
	21443852 (114082)[2]	15442639 (77620)[2]
	21475550 (0)[3]	15462354 (0)[3]
Completeness (%):	100.00 (100.00)[1]	100.00 (100.00)[1]
	99.52 (95.32)[2]	98.92 (89.62)[2]
	79.11 (0.00)[3]	77.18 (0.00)[3]
Signal to noise:	15.995 (7.51)[1]	13.262 (5.91)[1]
	10.524 (1.02)[2]	8.709 (0.86)[2]
	9.768 (N/A)[3]	8.248 (N/A)[3]
Wilson b factor:	20.83[1]	21.11[1]
	24.54[2]	25.09[2]
	23.51[3]	24.66[3]
R_{Split} (%):	5.66 (13.62)[1]	6.64 (17.52)[1]
	6.75 (152.39)[2]	8.06 (250.45)[2]
	6.96 (N/A)[3]	8.28 (N/A)[3]
CC*:	1.00 (0.99)[1]	1.00 (0.99)[1]
	1.00 (0.56)[2]	1.00 (0.36)[2]
	1.00 (N/A)[3]	1.00 (N/A)[3]
$CC_{1/2}$:	0.99 (0.97)[1]	0.99 (0.96)[1]
	0.99 (0.19)[2]	0.99 (0.07)[2]
	0.99 (N/A)[3]	0.99(N/A)[3]

[1,2,3] Represent merged statistics for distinct resolution shells N/A is used for when statistical measures for the inner shell where unphysical.

5.3. SACLA 2019B8021

Figure 3 shows data from experiments collected during SACLA 2019B8021. This was a repeat of LR23 experiment as well as measuring longer PDP delay of 2 ps. PP and PDP datasets were collected. FSC and R-split for merged laser off and dark data are shown in Supplementary Fig. 36. All sub-ps data was merged in a single dataset with an average delay of 500fs for both PP and PDP. N_{EXT} determination is shown in Supplementary Fig. 37. The PP (Supplementary Fig. 38) signals show a decay of the light induced difference after 3ps. Sub-picosecond PP and PDP (Supplementary Fig. 39) show the same increase signals due to the presence of the dump pulse and in the same locations as those from LCLS (Supplementary Fig. 40). The PDP shows a moderate decay of the electron density signals after 3ps and 100ps (Supplementary Fig. 41). Negative time control maps are shown in Supplementary Fig. 42. Crystallographic statistics for the PP and PDP are shown in Supplementary Table. 5.

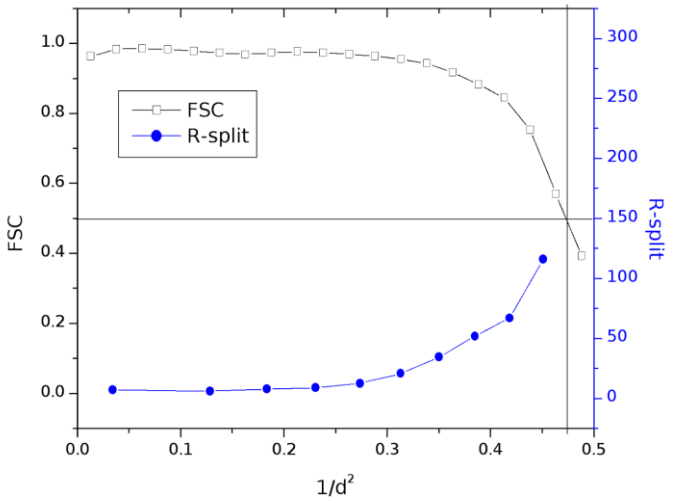

Supplementary Fig. 36 | SACLA 2019B8021 FSC and R-Split for the all merged laser off, dark data. An FSC of 0.5 is chosen for a limiting 1.44 Å.

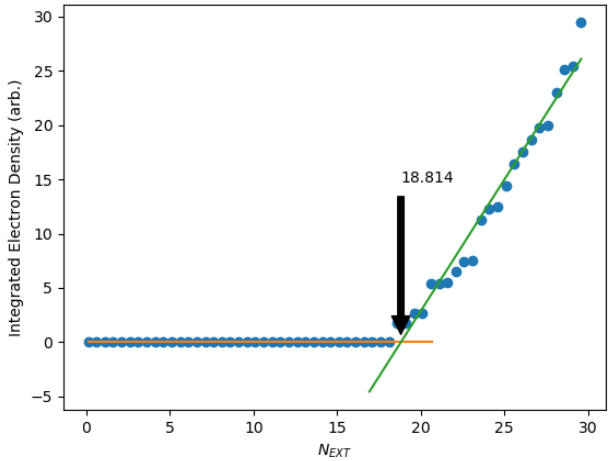

Supplementary Fig. 37 | SACLA 2019B8021 occupancy refinement. Pump Probe <1 ps (left) and Pump-Dump Probe <1 ps (right): Extrapolated factor, N_{EXT}, determination through the intersection point of two linear fits to the magnitude of integrated negative electron density, shown as blue circles.

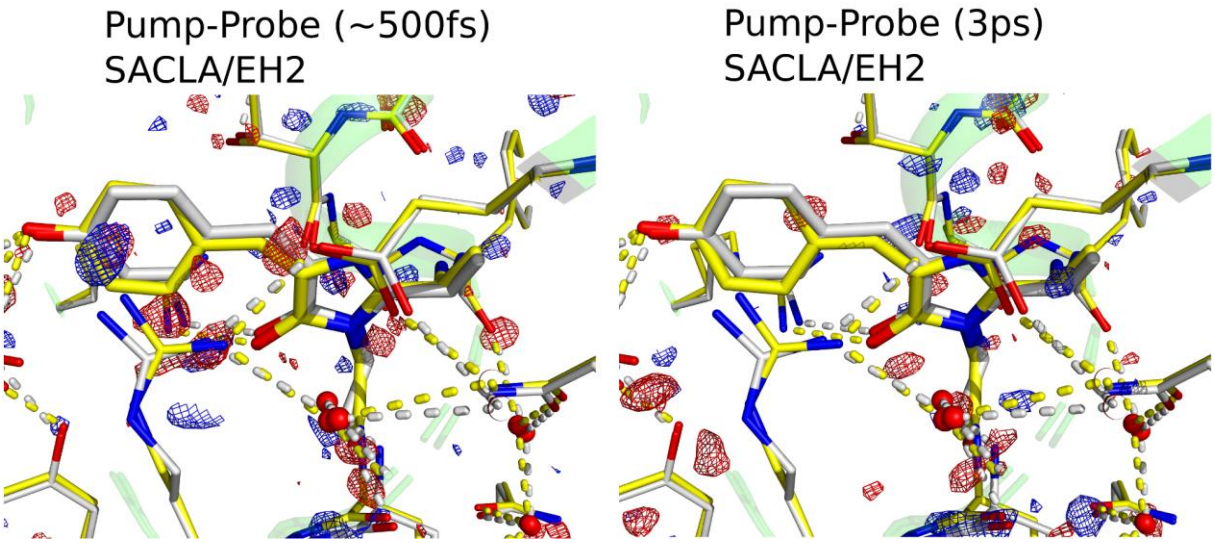

Supplementary Fig. 38 | SACLA 2019B8021 TR-SFX PP difference maps. A comparison of the average ~500 fs delay and 3 ps delay pump-probe data shows a clear decay of Q-weighted difference density features. The secondary structure (green) of the ground state coordinates (yellow) are shown with electron density contoured at +3σ rms (blue) and -3σ rms (red).

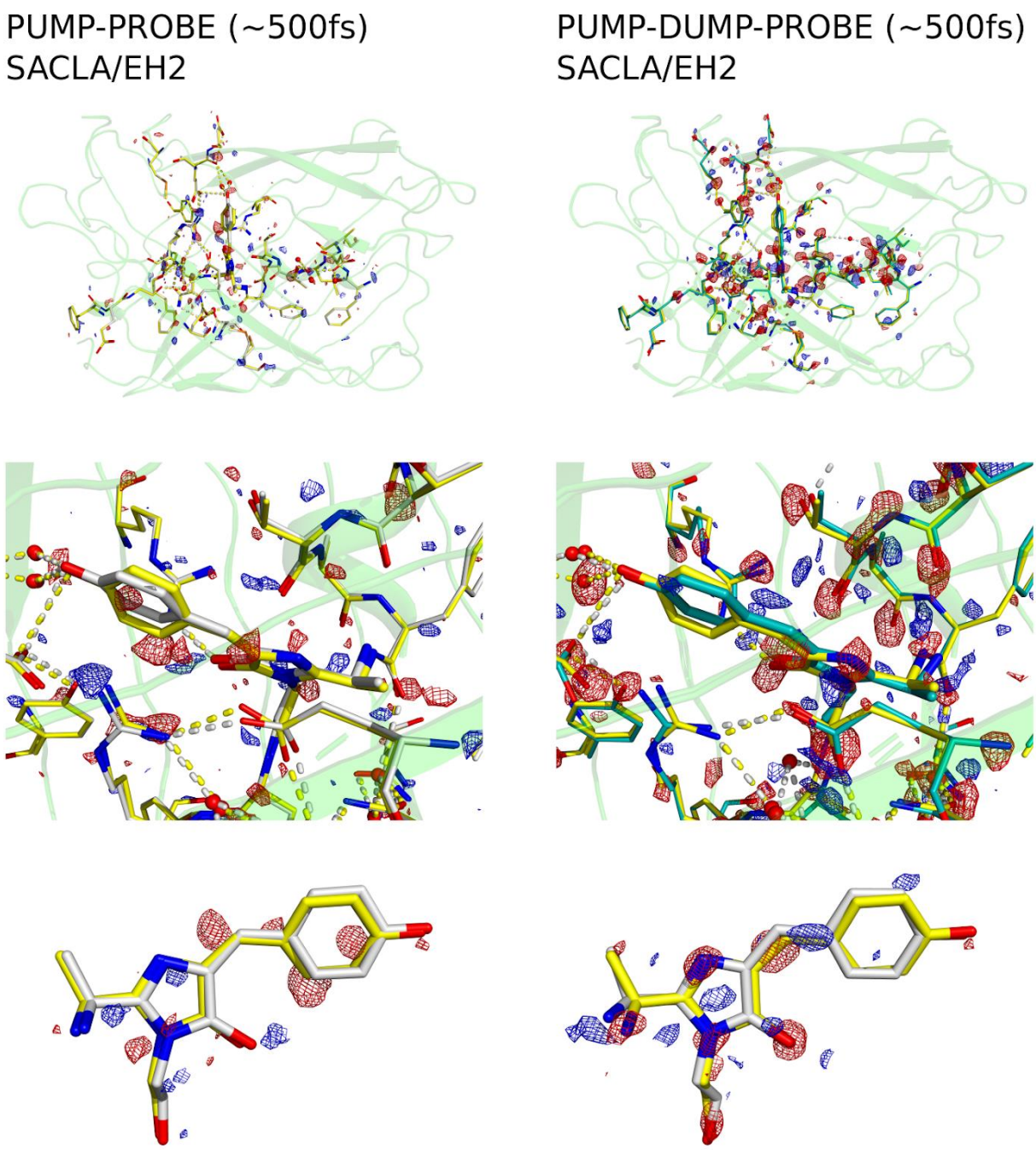

Supplementary Fig. 39 | SACLA 2019B8021 TR-SFX PP vs PDP difference maps. Q-weighted difference electron density, on the left: differences between the pump probe average delay 500 fs and dark (laser off). On the right: differences between the pump-dump probe average delay 500 fs and dark (laser off). The addition of the dump-pulse 350 fs after the pump, increases the electron density differences amplitudes, and larger shifts of the fitted coordinates to extrapolated structure factors (shown in grey and green), taken as N_{EXT} = 18.6 for the pump probe and N_{EXT} = 17.1 for pump-dump. The secondary structure (green) of the ground state coordinates (yellow) are shown with electron density contoured at +3σ rms (blue) and -3σ rms (red).

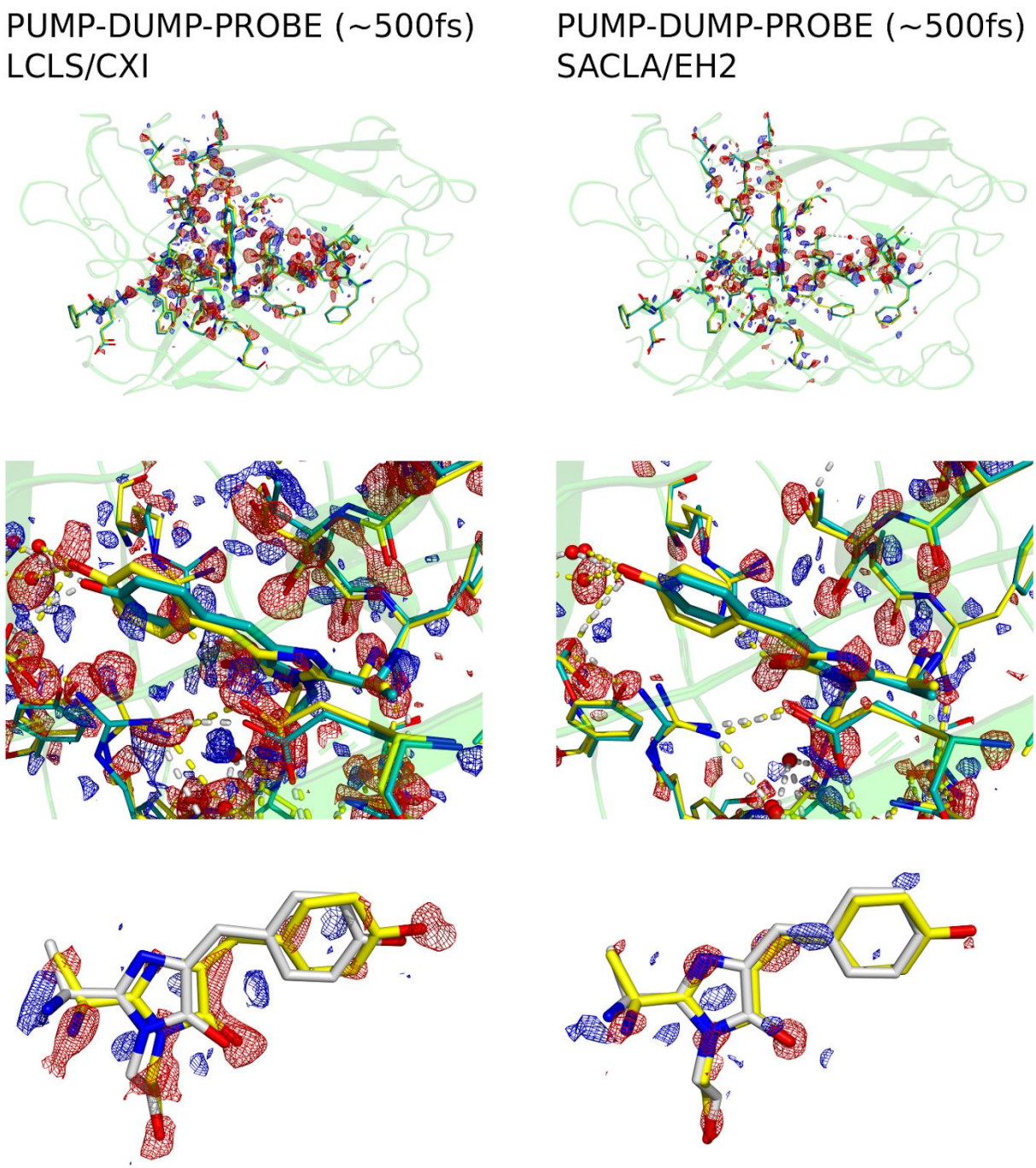

Supplementary Fig. 40 | LCLS LR23 PDP vs SACLA 2019B8021 PDP difference maps. Comparison of Q-weighted difference electron density differences of the pump-dump probe signals at LCLS/CXI and SACLA/EH2. Left: differences between the pump dump-probe 0-1 ps probe delay and dark (laser off). Right: differences between the pump-dump probe average probe delay 500 fs and dark (laser off). Extrapolated structures for each structure are shown in grey / teal, the secondary structure (green) of the ground state coordinates (yellow) are shown with electron density contoured at +3σ rms (blue) and -3σ rms (red).

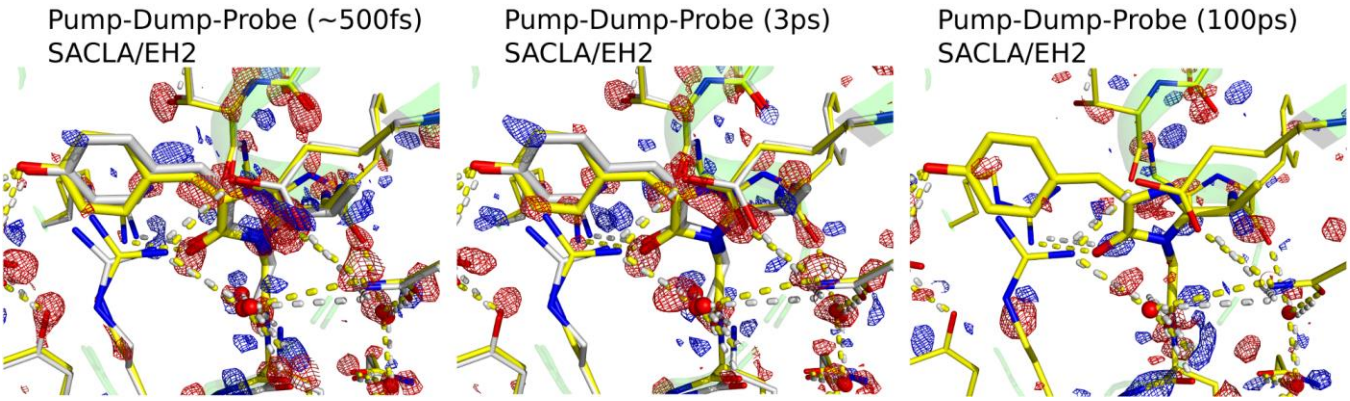

Supplementary Fig. 41 | SACLA 2019B8021 TR-SFX PDP difference maps. The comparison of the average ~500 fs delay, 3 ps and 100 ps delay pump-dump-probe data shows a moderate decay of the electron density signals from 500 fs to 3 ps, corresponding to the 4 ps decay time observed for the ground state intermediate induced absorption at 440 nm (Extended Data Fig. 3e). By 100 ps the signals are reduced to mostly noise. Extrapolated structures for each structure are shown in grey / teal, the secondary structure (green) of the ground state coordinates (yellow) are shown with electron density contoured at +3σ rms (blue) and -3σ rms (red).

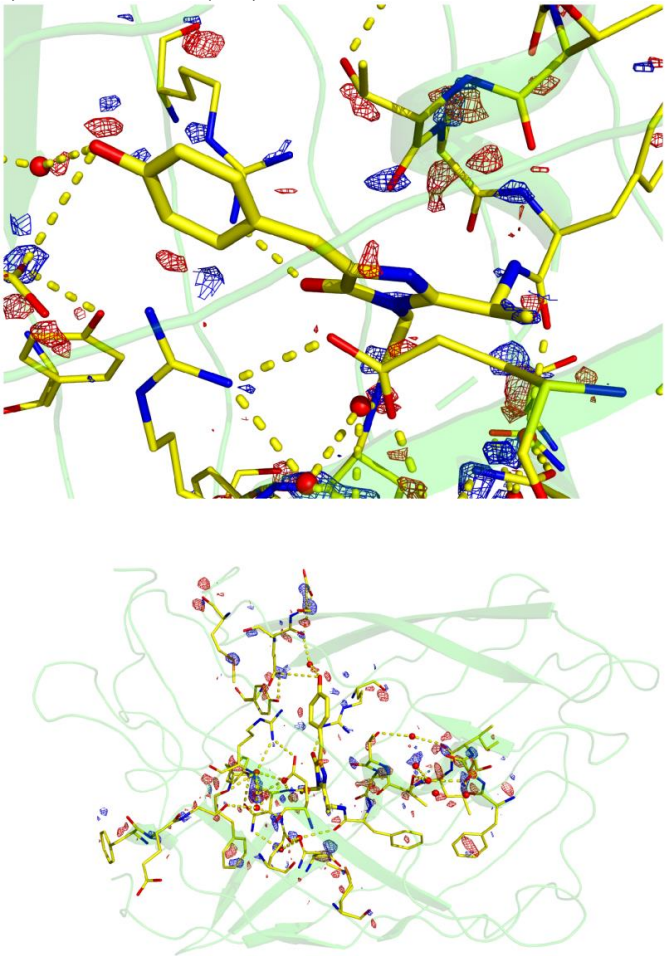

Supplementary Fig. 42 | SACLA2019B8021 TR-SFX PP Negative time control. Difference maps for minus 5 ps PP data with 400nm excitation. The X-ray probe arrives 5 ps before the 400nm laser pulse. Q-weighted electron density differences, contoured at +3σ rms (blue) and -3σ rms (red) are shown for the negative 5 ps laser on data, merging 17,627 frames, and the dark laser off data, merging 77,581 frames (Supplementary Table. 5). Coordinates are shown for the refined dark data.

Supplementary Table. 5 | SACLA 2019B8021 TR-SFX PP & PDP crystallographic statistics

	Dark	400nm 0 - 1 ps	400nm 3 ps	400nm 100 ps	400nm -5 ps	400nm-515nm 0 - 1 ps*	400nm-515nm 3 ps*	400nm-515nm 100 ps*	400nm-515nm 3 ps†
Indexed Patterns:	77581	18886	20472	18886	17627	54743	83187	25204	21796
Resolution Limits (Å)	18.84-1.70 (1.761-1.700)[1]	18.53-1.70 (1.761-1.700)[1]	18.53-1.70 (1.761-1.700)[1]	18.53-1.70 (1.761-1.700)[1]	18.53-1.70 (1.761-1.700)[1]	18.84-1.70 (1.761-1.700)[1]	18.84-1.70 (1.761-1.700)[1]	18.53-1.70 (1.761-1.700)[1]	18.53-1.70 (1.761-1.700)[1]
	18.84-1.65 (1.709-1.650)[2]	18.53-1.65 (1.709-1.650)[2]	18.53-1.65 (1.709-1.650)[2]	18.53-1.65 (1.709-1.650)[2]	18.53-1.65 (1.709-1.650)[2]	18.84-1.65 (1.709-1.650)[2]	18.84-1.65 (1.709-1.650)[2]	18.53-1.65 (1.709-1.650)[2]	18.53-1.65 (1.709-1.650)[2]
	18.84-1.46 1.491-1.440)[3]	18.53-1.50 (1.491-1.440)[3]	18.53-1.53 (1.491-1.440)[3]	18.53-1.53 (1.491-1.440)[3]	18.53-1.53 (1.491-1.440)[3]	18.84-1.46 (1.491-1.440)[3]	18.84-1.46 (1.491-1.440)[3]	18.53-1.55 (1.491-1.440)[3]	18.53-1.47 (1.491-1.440)[3]
Number of Unique reflection indices:	26206[1]	26206[1]	26205[1]	26205[1]	26206[1]	26206[1]	26209[1]	26206[1]	26205[1]
	28578[2]	28578[2]	28577[2]	28577[2]	28578[2]	28578[2]	28581[2]	28578[2]	28577[2]
	42704[3]	42704[3]	42703[3]	42703[3]	42704[3]	42704[3]	42707[3]	42704[3]	42703[3]
No. Merged Reflections:	9886523 (135932)[1]	4822444 (50790)[1]	2327708 (29358)[1]	2258197 (18609)[1]	1841923 (19475)[1]	7427749 (120500)[1]	10902871 (150894)[1]	3553008 (32192)[1]	2387057 (28810)[1]
	9957691 (88288)[2]	4847105 (30746)[2]	2342594 (18535)[2]	2266705 (10743)[2]	1850853 (11375)[2]	7492574 (80164)[2]	10982523 (98384)[2]	3567097 (17641)[2]	2401810 (18347)[2]
	10044009 (1397)[3]	4872185 (182)[3]	2356435 (47)[3]	2272675 (25)[3]	1857695 (18)[3]	7576103 (1587)[3]	11079889 (1945)[3]	3575821 (4)[3]	2416044 (37)[3]
Completeness (%):	100 (100)[1]	99.93 (99.42)[1]	99.86 (98.80)[1]	99.37 (94.80)[1]	99.41 (95.38)[1]	100 (100)[1]	99.99 (100)[1]	99.90 (99.07)[1]	99.75 (98.10)[1]
	99.99 (99.93)[2]	99.75 (97.92)[2]	99.33 (94.18)[2]	97.78 (81.99)[2]	97.90 (82.93)[2]	100 (100)[2]	99.99 (99.96)[2]	99.28 (93.24)[2]	99.20 (93.93)[2]
	88.38 (13.59)[3]	79.58 (2.09)[3]	75.54 (0.55)[3]	70.45 (0.29)[3]	71.09 (0.22)[3]	88.49 (14.60)[3]	89.46 (17.89)[3]	72.85 (0.05)[3]	75.53 (0.43)[3]
Signal to noise:	12.242 (4.19)[1]	8.796 (3.18)[1]	6.303 (2.59)[1]	6.574 (2.75)[1]	6.017 (3.88)[1]	10.637 (3.99)[1]	12.716 (4.26)[1]	7.900 (2.86)[1]	6.406 (2.96)[1]
	11.500 (3.37)[2]	8.295 (2.67)[2]	6.013 (2.57)[2]	6.547 (5.65)[2]	5.823 (4.10)[2]	10.016 (3.23)[2]	11.936 (3.38)[2]	7.486 (2.62)[2]	6.121 (3.11)[2]
	9.357 (4.59)[3]	7.482 (1.69)[3]	5.711 (2.14)[3]	6.453 (8.15)[3]	5.836 (0.74)[3]	8.305 (7.19)[3]	9.669 (4.27)[3]	7.648 (7.35)[3]	5.828 (2.64)[3]
Wilson b factor:	22.08[1]	22.28[1]	22.25[1]	21.80[1]	22.40[1]	22.07[1]	22.31[1]	21.95[1]	22.36[1]
	22.23[2]	22.42[2]	22.31[2]	21.93[2]	22.39[2]	22.21[2]	22.48[2]	22.08[2]	22.58[2]
	21.18[3]	21.50[3]	21.84[3]	16.17[3]	21.28[3]	21.73[3]	21.73[3]	22.54[3]	23.62[3]
R_{Split} (%):	7.45 (28.00)[1]	10.98 (39.35)[1]	15.12 (48.15)[1]	14.57 (50.17)[1]	16.92 (52.66)[1]	8.81 (28.97)[1]	7.09 (27.15)[1]	10.91 (43.80)[1]	13.78 (50.14)[1]
	7.61 (36.70)[2]	11.16 (51.44)[2]	15.26 (49.46)[2]	14.63 (49.95)[2]	16.98 (53.67)[2]	8.97 (37.75)[2]	7.25 (35.41)[2]	11.08 (56.75)[2]	13.95 (59.70)[2]
	8.06 (126.90)[3]	11.35 (N/A)[3]	15.32 (N/A)[3]	14.65 (N/A)[3]	16.99 (N/A)[3]	9.40 (90.12)[3]	7.71 (62.87)[3]	11.12 (N/A)[3]	14.07 (N/A)[3]
CC*:	1.00 (0.96)[1]	0.99 (0.92)[1]	0.98 (0.90)[1]	0.99 (0.89)[1]	0.98 (0.85)[1]	1.00 (0.96)[1]	1.00 (0.97)[1]	0.99 (0.90)[1]	0.99 (0.86)[1]
	1.00 (0.94)[2]	0.99 (0.88)[2]	0.98 (0.89)[2]	0.99 (0.88)[2]	0.98 (0.88)[2]	1.00 (0.93)[2]	1.00 (0.95)[2]	0.99 (0.84)[2]	0.99 (0.83)[2]
	1.00 (N/A)[3]	0.99 (N/A)[3]	0.98 (N/A)[3]	0.99 (N/A)[3]	0.98 (N/A)[3]	1.00 (0.79)[3]	1.00 (0.92)[3]	0.99 (N/A)[3]	0.99 (N/A)[3]
$CC_{1/2}$:	0.99 (0.87)[1]	0.97 (0.74)[1]	0.94 (0.68)[1]	0.95 (0.65)[1]	0.92 (0.56)[1]	0.98 (0.86)[1]	0.99 (0.88)[1]	0.98 (0.68)[1]	0.96 (0.59)[1]
	0.99 (0.80)[2]	0.97 (0.64)[2]	0.94 (0.67)[2]	0.95 (0.63)[2]	0.92 (0.63)[2]	0.98 (0.76)[2]	0.99 (0.81)[2]	0.98 (0.55)[2]	0.96 (0.52)[2]
	0.99 (0.05)[3]	0.97 (N/A)[3]	0.94 (N/A)[3]	0.95 (N/A)[3]	0.92 (N/A)[3]	0.98 (0.45)[3]	0.99 (0.74)[3]	0.98 (N/A)[3]	0.96 (N/A)[3]

*Pump-dump delay: 500 fs †Pump-dump delay: 2ps [1,2,3] Represent merged statistics for distinct resolution shells N/A is used for when statistical measures for the inner shell where unphysical.

5.4. PAL XFEL 2020-2nd-NCI-007

Figure 1 shows data from experiments collected at PAL XFEL 2020-2nd-NCI-007. This was a control experiment, collecting TR-SFX 100 µs pump-probe delay to confirm that photoisomerization was complete by this time. The FSC is shown in Supplementary Fig. 43. Q-weight difference maps of 100 µs and negative laser on data in Supplementary Fig. 44 clearly shows the emergence of cis photoproduct after 100 µs. Occupancy refinement for the 100 µs and negative data sets are shown in Supplementary Fig. 45 & Supplementary Fig. 46 respectively. Crystallographic statistics are shown in Supplementary Table. 6.

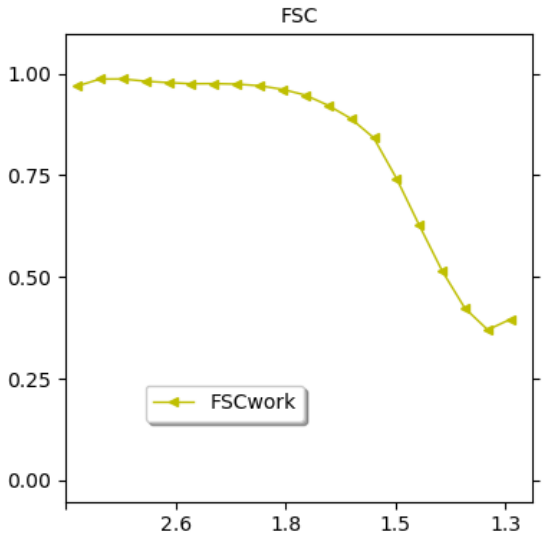

Supplementary Fig. 43 | PAL-XFEL 2020-2nd-NCI-007 The Fourier shell coefficient (FSC) and all merged laser off, dark data. An FSC of 0.5 is chosen for a limiting 1.42 Å.

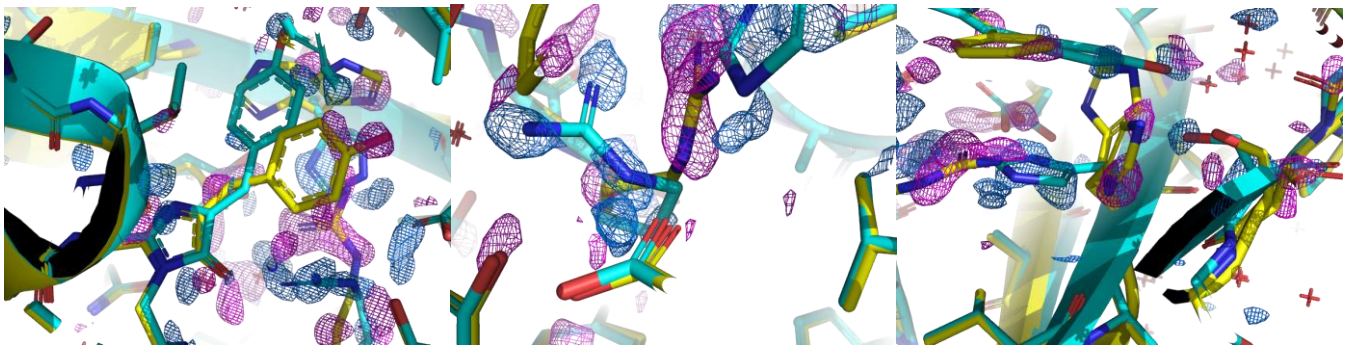

Supplementary Fig. 44 | PAL-XFEL TR-SFX PP 100 µs difference maps. Q-weighted difference electron density between the 400 nm 100 µs and negative 1 ps laser-on, dark data. The ground state coordinates are shown in yellow and cis, photproduct coordinates are shown in blue. Electron density contoured at +2 rms (blue) and -2 rms (magenta). Signals clearly show emergence of the photoproduct after 100 µs.

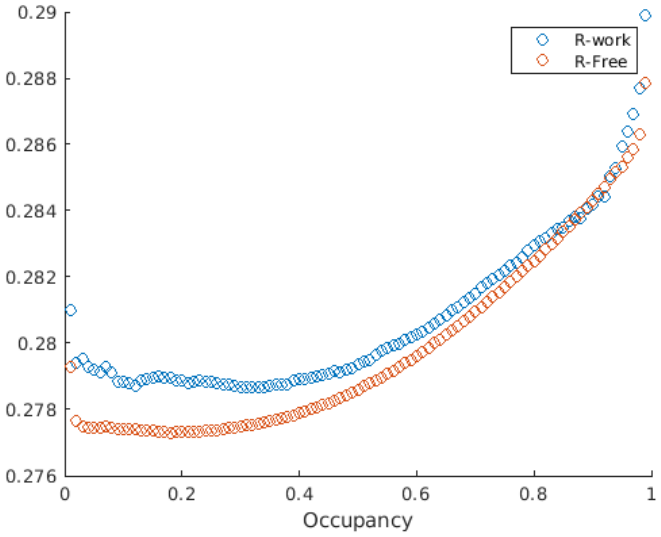

Supplementary Fig. 45 | PAL-XFEL TR-SFX PP 100 μs occupancy refinement. 100 μs-laser-on: R_{work}/R_{free} calculation for varied occupancy of refined coordinates. Occupancy refers to the proportion of ground state (trans) coordinates (dark) compared to the photoproduct (cis) coordinates. R_{fac} (and R_{free}) minimize at photoproduct = 0.18 (0.21) and dark = 0.82 (0.79).

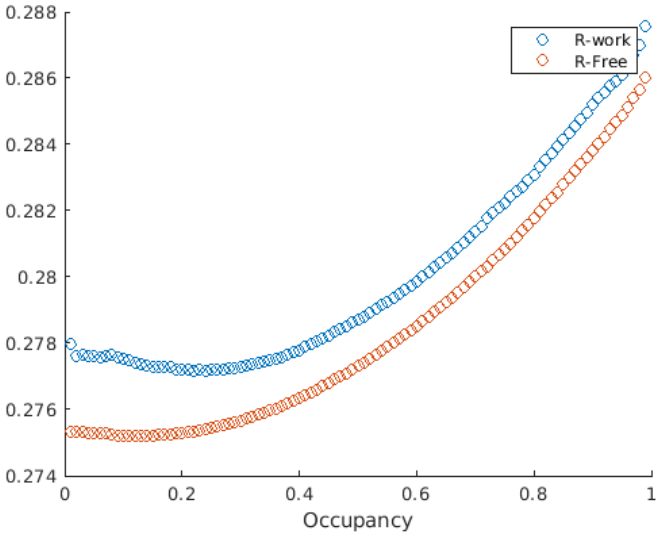

Supplementary Fig. 46 | PAL-XFEL TR-SFX PP negative delay occupancy refinement. Neg-1ps-laser-on: R_{work}/R_{free} calculation for varied occupancy of refined coordinates. Occupancy refers to the proportion of ground state (trans) coordinates (dark) compared to the photoproduct (cis) coordinates. R_{fac} (and R_{free}) minimize at photoproduct = 0.12 (0.16) and dark = 0.88 (0.84).

Supplementary Table. 6 | PAL-XFEL TR-SFX PP crystallographic statistics

	neg-1ps-laser-on	100us-laser-on
Indexed Patterns:	49465	60993
Resolution Limits (Å):	78.69-1.55 (1.605-1.550)[1]	78.69-1.55 (1.605-1.550)[1]
	78.69-1.45 (1.502-1.450)[2]	78.69-1.45 (1.502-1.450)[2]
	78.69-1.35 (1.398-1.350)[3]	78.69-1.35 (1.398-1.350)[3]
Number of Unique reflection indices:	34233[1]	34233[1]
	41638[2]	41638[2]
	51398[3]	51398[3]
No. Merged Reflections:	11752976 (247091)[1]	14106334 (252617)[1]
	12005396 (92501)[2]	14357015 (91162)[2]
	12060432 (14662)[3]	14403050 (10532)[3]
Completeness (%):	100.00 (100.00)[1]	100.00 (100.00)[1]
	99.96 (99.59)[2]	99.98 (99.78)[2]
	95.90 (64.79)[3]	95.02 (56.33)[3]
Signal to noise:	6.648 (1.95)[1]	7.601 (1.81)[1]
	5.685 (0.97)[2]	6.434 (0.76)[2]
	4.905 (0.56)[3]	5.537 (0.18)[3]
Wilson b factor:	23.39[1]	25.62[1]
	23.52[2]	26.28[2]
	22.87[3]	26.54[3]
R_{Split} (%):	10.18 (53.79)[1]	8.64 (56.11)[1]
	10.58 (114.57)[2]	8.96 (146.34)[2]
	10.85 (236.85)[3]	9.16 (419.81)[3]
CC*:	1.00 (0.90)[1]	1.00 (0.91)[1]
	1.00 (0.69)[2]	1.00 (0.63)[2]
	1.00 (0.55)[3]	1.00 (0.06)[3]
$CC_{1/2}$:	0.99 (0.68)[1]	0.99 (0.69)[1]
	0.99 (0.31)[2]	0.99 (0.25)[2]
	0.99 (0.18)[3]	0.99 (0.00)[3]

[1,2,3] Represent merged statistics for distinct resolution shells

6. Photo conversion quantum yield measurements

The photo conversion (photo-product) yields of both the off→on and on→off reaction were measured in both solution and in crystalline samples of rsKiiro. Solution sample was prepared in a Harrick cell with 25.6 μm spacer producing an OD of ~0.2 @ 488 nm, crystal "pancakes" were prepared in the method described[12] with final OD of ~0.3 @ 488 nm.

off → on: a 488 nm CW laser was tightly focused (41x47 μm FWHM) and directed onto an amplified photodiode (Thorlabs PDA36A2) and attenuated to be weakly actinic, (t_{conv} > 20 s). The sample was fully converted to the off state and then illuminated with a loosely focused 405 nm CW laser (177x178 μm FWHM) at a range of powers (8-22 μW) and the kinetic rate measured using a digital oscilloscope (Picoscope). The total switch rate from off→on:

$$off \xrightarrow{k_{FT},-k_{BT},k_{TH}} on$$

Where k_{FT}, k_{BT} & k_{Th} are the total forward and backwards rates and the thermal recovery rate. As the values of k_{BT} (>0.05 s^{-1}) & k_{Th} (4x10^{-4} s^{-1}at 293 K (Extended Data Fig. 1c) are significantly smaller than switching rates observed at the power densities used (1-5 s^{-1}) both can be disregarded and a single rate considered, therefore

$$k_{FT} = \phi_{off\rightarrow on} P_d \sigma_{405}$$

Where $\phi_{Off\rightarrow On}$, P_d and σ_{405} is the total off → on photoconversion quantum yield, photon density per second and single molecule cross section at 405 nm (1.38x10^{-16} cm^2) respectively. $\phi_{Off\rightarrow On}$ was found to be 15.9±1.2% in solution and 18.3±2.2% in the crystalline sample.

on → off: The measurement was repeated for other reaction, in this case the roles 488 nm and 405 nm. CW lasers were reversed and the focus sizes adjusted accordingly. $\phi_{On\rightarrow Off}$ was determined to be 0.63±0.03% in solution and 0.12±0.01% in the crystalline sample.

Interestingly this shows that the quantum yield in the on→off reaction is 5 times smaller in a crystalline sample, while the off→on is 1.15 times larger.

7. Time-correlated single photon counting (TCSPC)

Determination of the excited state barrier height using temperature-dependent fluorescence lifetime measurements was described previously in depth [13]. Briefly, fluorescence lifetime decays were measured on a Horiba Fluorolog-3 fluorescence spectrometer using time-correlated single photon counting (TCSPC). Sample temperature was controlled with a water bath (NESLAB RTE-7 circulating bath, Thermo Fisher Scientific) and measured with a thermocouple (870 Digital Thermometer, Keithley). Samples were diluted to 1.5 μM (A_{487} ~0.1) with buffer containing 10 mM Tris HCl (Fisher, CAS 1185-53-1) at pH 8.0, 50 mM NaCl (Fisher, CAS 7647-14-5), and 30% glycerol (Fisher, CAS 56-81-5) (v/v) in a 1.5 mL quartz cuvette (Hellma Analytics). The cuvette was equilibrated at the desired temperature for 5 minutes before data acquisition. The sample was excited with 487 nm light polarized at 0 degrees from a Fluorolog EXTREME supercontinuum laser (pulse width ~20-40 ps), and fluorescence emission polarized at the magic angle (55°) was detected at 504 nm. Three separate measurements were obtained at each temperature. The excitation and emission slit widths were set to 5 nm to keep the detection rate

below 2%. The instrument response function was measured at 487 nm by scattered light from a solution of LUDOX® HS-40 colloidal silica (Sigma, CAS 7631-86-9).

Representative fluorescence decays at each temperature from 278K to 298K are shown in Extended Data Fig. 1i. The decay data was analyzed using the DecayFit software in MATLAB[14]. In brief, the program performs an iterative reconvolution of the instrument response function (IRF) with a simulated decay model using a least squares analysis, allowing for a channel shift between the IRF and each decay. By analyzing the chi-squared values and the residuals plot, we determined that a triple exponential model best represents the data. Supplementary Table. 7 summarizes the average fluorescence lifetimes, relative populations, and standard deviations from the triplicate measurements at each temperature.

The excited state energy barrier was determined by fitting the temperature-dependent fluorescence lifetimes to Equation (S1), assuming an Arrhenius behaviour of barrier crossing:

$$\frac{1}{\tau} = \mathcal{A}_1 + \mathcal{A}_2 e^{-\frac{E_\alpha}{RT}} \quad \text{(S1)}$$

Where $\boldsymbol{\mathcal{A}}_1$ and $\boldsymbol{\mathcal{A}}_2$ are temperature independent constants and E_α is the excited state energy barrier height. See Supplementary Text S6 in Romei et al.[13] for a derivation of this Arrhenius equation and validation of the Arrhenius behaviour of barrier crossing. As shown in Supplementary Table. 7, the population of the slow lifetime component is less than 3%. Lifetime components with minimal populations are broad and carry large uncertainties (see Supplementary Texts S6 and S7 in Romei et al.[13]), which prevents accurate extraction of any temperature dependence. The fast and middle lifetime components from the triple exponential decay, which comprise >97% of the population, were each fit to the Arrhenius equation. To accurately calculate the energy barrier and its corresponding confidence interval, a parametric bootstrap analysis was performed (see Materials and Methods in Romei et al.[13] for MATLAB code and further details). The fitting parameters from the bootstrap analysis are listed in along with confidence intervals that report one standard deviation from the median, and the fit from the bootstrap are shown in Supplementary Table. 8 and plotted in Extended Data Fig. 1j with the temperature-dependent fluorescence lifetimes for the fast and middle lifetime components.

	1st comp.			2nd comp.			3rd comp.		
Temp (K)	Avg. Pop	k*	SD*	Avg. Pop	k*	SD	Avg. Pop	k*	SD*
278.45	0.03	0.54	0.03	0.35	1.4	0.07	0.61	4.14	0.2
280.15	0.027	0.54	0.02	0.34	1.42	0.07	0.64	4.15	0.3
282.15	0.026	0.55	0.01	0.35	1.5	0.01	0.63	4.57	0.02
284.15	0.023	0.54	0.03	0.33	1.53	0.08	0.64	4.58	0.3
286.05	0.02	0.53	0.005	0.34	1.57	0.01	0.64	4.7	0.06
287.95	0.021	0.54	0.007	0.34	1.67	0.007	0.64	5.14	0.05
289.85	0.019	0.54	0.01	0.33	1.71	0.06	0.65	5.3	0.3
291.75	0.017	0.52	0.02	0.3	1.68	0.08	0.69	5.11	0.3
293.75	0.017	0.53	0.01	0.33	1.84	0.04	0.65	5.87	0.2
295.75	0.017	0.54	0.008	0.3	1.84	0.01	0.68	5.7	0.1
297.55	0.015	0.53	0.002	0.31	1.93	0.02	0.68	6.08	0.2

*Rate components k, and standard deviation SD, all in units of (ns^{-1})

Supplementary Table. 7 TCSPC rates. Temperatures, average populations, lifetime rates (k), and standard deviations (SD) are shown for the three components fitted to the traces in Extended Data Fig. 1i

The fast and middle fluorescence lifetimes as a function of temperature yielded excited state energy barriers of 3.6 and 4.0 kcal mol^{-1}(or 15.0 and 16.73 kJ mol^{-1}), respectively, which are similar within error. The observation of multiple lifetimes in fluorescent proteins is not unusual[15–17] may suggest the

presence of multiple ground state conformations or increased flexibility within the chromophore pocket[18,19](Supplementary Fig. 48 - Supplementary Fig. 50). Interestingly, regardless of the origin of this heterogeneity, the excited state energy barrier height is largely conserved.

Component	$\mathcal{A}_1$ (ns^{-1})	$\mathcal{A}_1$ CI* (1σ, ns^{-1})		$\mathcal{A}_2$ (ns^{-1})	$\mathcal{A}_2$ CI* (1σ, ns^{-1})		ESB† (kcal/mol)	ESB† CI* (1σ, kcal/mol)	
Fast	0.241	3E-14	1.417	2.40E+03	1.84E+03	8.83E+03	3.576	3.392	4.439
Middle	0.513	0.312	0.684	1.24E+03	8.79E+02	1.70E+03	4.008	3.749	4.252
Slow					N/A				

*CI: confidence interval upper and lower bounds, † ESB: Excited state barrier (kcal/mol)

Supplementary Table. 8 Fitting parameter from bootstrap Arrhenius plots of the TCSPC recovered rates.

This data further supports the efficient photoswitching behaviour of rsKiiro. Since fluorescence and energy barrier crossing are competing processes in the excited state, the observed low excited state energy barrier height explains the low fluorescence quantum yield compared to other fluorescent proteins. Instead of emitting a photon through fluorescence, the chromophore crosses the energy barrier along the bond rotation reaction coordinate. The magnitudes of the fluorescence lifetimes also support this conclusion. Typical fluorescence lifetimes in fluorescent proteins are on the order of ns and show strong positive correlations with fluorescence quantum yield[20]. The fast and middle components of rsKiiro are <300 ps and <750 ps, respectively, meaning that most of the chromophore population crosses over the excited state en

8. Fluorescence spectra and fluorescence quantum yield

The absolute fluorescence quantum yield (FQY) for the cis on state was determined as previously described [13,21]. Briefly, fluorescence spectra were measured on a PerkinElmer LS 55 fluorescence spectrometer. Excitation and emission slit widths were set to 1.0 nm. The sample was excited at 487 nm, and the emission spectrum was obtained every 0.5 nm at 120 nm/min. Sample absorption was determined using a PerkinElmer Lambda 365 UV-vis spectrophotometer and then converted into absorption factor according to the following equation: $f = 1 - 10^{-A_{488}}$, where is the absorption factor and is the absorbance at 488 nm. The absorption factor was plotted against the integrated emission spectrum for different protein concentrations, and the slope of the linear fit was compared against that of fluorescein (Aldrich, CAS 2321-07-5) in 0.1 M NaOH, a known standard with a reported absolute FQY of 0.90 at 488 nm [22]. The equation used to calculate FQY is as follows:

$$FQY_X = FQY_{ST}\left(\frac{Slope_X}{Slope_{ST}}\right)\left(\frac{\eta_X^2}{\eta_{ST}^2}\right) \qquad \text{(S2)}$$

where X and ST reference the sample of interest and the fluorescein standard, respectively, slope refers to the slope of the linear fit mentioned above, and η is the refractive index of the solution.

To measure the FQY of the trans off state, a similar protocol as described above was used, although samples were illuminated for one minute with a 30 mW 488 nm diode laser (85-BCD-030-115, Melles Griot) immediately prior to all absorption and fluorescence measurements. Emission spectra were measured by exciting at 387 nm. Coumarin 153 (Sigma, CAS 53518-18-6), which has a reported absolute FQY of 0.53 in ethanol [21], was used as the FQY standard to properly match the excitation wavelength with the protonated trans rsKiiro chromophore.

The fluorescence quantum yield (FQY) of rsKiiro in the native cis on state is 6.8 ± 0.1%. FQYs of traditional GFPs are an order of magnitude greater, roughly spanning a range between 50 and 90%[20].

Such a low FQY of rsKiiro suggests that nonradiative decay processes such as chromophore photoisomerization mostly outcompete fluorescence in the excited state, and the determination of fast fluorescence lifetime decays and a low excited state energy barrier height further supports this conclusion. The FQY of the trans off state is 0.49 ± 0.03%, an order of magnitude lower than that of the cis on state. The decreased FQY for the trans state could be attributed to increased flexibility of the protein and the chromophore and indicates that excited state proton transfer does not likely occur.

8.1. Fluorescence lifetime estimate from Strickler Berg relation

In order to evaluate the rate corresponding to fluorescence decay we use the Strickler-Berg relation[23]

$$Fk_{fl} = 3 \times 10^{-9} n^2 \langle \bar{\nu}^{-3} \rangle_{em}^{-1} \int \frac{\varepsilon(\bar{\nu})}{\bar{\nu}} d\bar{\nu} \, (s^{-1}) \qquad \text{(S3)}$$

Using an extinction coefficient for the neutral trans chromophore ε = 32,909 $M^{-1}cm^{-1}$. Calculation using the absorption (390 nm maximum) and fluorescence (490 nm maximum, Extended Data Fig. 1b) spectra and approximately 60 nm FWHM spectral parameters, the Strickler-Berg relationship calculates a pure radiative lifetime of 5.34 ns when using a value of n=1.33 for water. Taking the experimental value for the fluorescence quantum yield of the off state φ(off) = 0.49 ± 0.03%, the resulting fluorescence lifetime is τ_{fl} = 30 ps. This value is very close to the experimental value of excited state decay measured by TA spectroscopy to be 50 ps (see above and Extended Data Fig. 1d). The rate k_{fl} = 2x10^{10} s^{-1} for the off state. Similarly, for the on-state cis anioic chromophore using a value of 98,727 $M^{-1}cm^{-1}$ and values for the absorption and emission of 485 nm and 515 nm, the pure radiative lifetime is calculated as 2.28 ns. Using the experimentally determined fluorescence quantum yield of φ(off) = 6.8 ± 0.1%, the calculated fluorescence lifetime is τ_{fl}=150 ps.

9. Cyro-trapping of rsKiiro intermediates

To gain insight into the reaction pathways of rsKiiro and attempt to isolate a reaction intermediate, Arrhenius measurements of both the on→off and off→on reactions were performed over a range of cryogenic temperatures (190-293 K). A small volume of rsKiiro solution was mixed with glycerol (to avoid icing, 1:4 ratio) and loaded onto a CryoLoop (Hampton Research) suspended inside an inverted microscope to monitor change in absorption. The sample was cooled using a cryo stream (Oxford Instruments). The on→off and off→on were driven using a 480 nm and 400 nm LED's respectively, focused onto the loop using f=100 mm lenses. The off→on reaction was performed both when the pre-conversion was performed at the same cryo temperature and at room temperature. The results are shown in Fig 2 (right). A full description of the methodology and fitting is described in the supplementary discussion.

9.1. Steady state MX Cryo-structures

Following the observation of Arrhenius break in rsKiiro photo-switching reaction in both the forward and reverse reaction (Extended Data Fig. 1e & k), crystals were prepared in attempt to cryo-trap structural intermediates at cool temperatures. Supplementary Fig. 47 shows the preparation of each state.

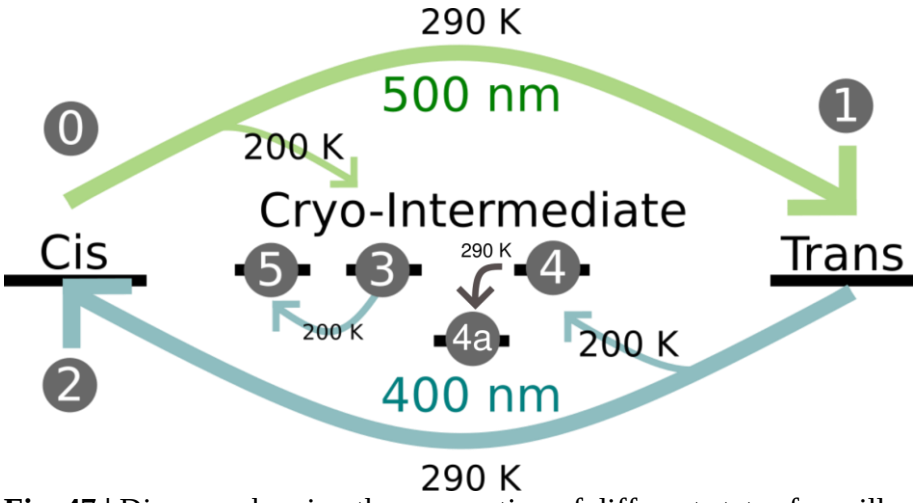

Supplementary Fig. 47 | Diagram showing the preparation of different states from illumination schemes at temperatures 290 K and 200 K using 500 nm and 400 nm light and existence of possible cryo-trapped-intermediate structures as indicated by the Arrhenius behaviour.

The intermediate structures 3 and 4 should be thermally unstable at room temperature. This means annealing a crystal should relax the structure from the intermediate to a normal cis or trans state. If the crystal is oriented correctly (orthogonal to the X-ray beam) then multiple data collections from the same crystal can be performed and the crystal annealed in between. Comparison of the annealed and un-annealed structures should then provide strong evidence for the presence of any cryo-trapped intermediates.

Batch grown crystals around 10x10x100 μm in size were grown in conditions of 25% Poly-ethylene glycol 3350 in 0.2 M lithium sulphate, 0.1 M Tris-HCl pH 8.5 with a final protein concentrating of 10 mg/ml (similar to Hutchison et al.[24]). A single crystal was fished onto an appropriately sized loop and illuminated. To ensure that the heating effects of illumination were accounted for the same power densities used in the spectroscopy were used in the crystal preparation. A crystal was assumed to have an optical density of 1. Using the measured rate constants at 200 K it was calculated 95% conversion would occur after 30 minutes of 400 nm and 69 minutes of 500 nm illumination respectively. As soon as illumination time was complete the crystals were flash frozen into liquid nitrogen. Data collection occurred at Diamond Light Source, Oxfordshire during beamtimes MX22819-1 and MX17221-42 at beamline i03 using an exposure time of 10 ms for 3600 images at 100% transmission for wavelengths 0.97 Å or 0.73 Å. Structure 3 and 4 were annealed by blocking the 100 K cryo-stream for a time of 1 s. After measurement of the cryo trapped structure, the crystal was annealed and another structure collected at a shifted point on the crystal. X-ray diffraction data was merged using the STARANISO[10] package.

Difference map were then calculated as described above. Q-weighted difference maps of 0 – 1 and 0 – 4 and 0 – 4a are shown in Supplementary Fig. 48, Supplementary Fig. 49 and Supplementary Fig. 50 respectively. An intermediate state was found in structure 4 (Supplementary Fig. 50). Crystallographic data and refinement statistics are shown in Supplementary Table. 9.

Supplementary Table. 9 | MX-Crystallography statistics for cryo-trapping processed with STARANISO[10].

Condition	**0** **On state:** **Cis Structure (unilluminated)**			**1** Off state **Trans Structure (illuminated at 290 K)**			**4** **Cis structure intermediate (illuminated at 290 K then 200 K)**			**4a** **Thermal annealing at 290 K of the cis intermediate structure**		
PDB ID	7QLI			7QLJ			7QLK			7QLL		
Spacegroup name	$P2_12_12_1$			$P2_12_12_1$			$P2_12_12_1$			$P2_12_12_1$		
Unit cell parameters	38.560 73.467 78.038 90.0 90.0 90.0			38.7470 73.5243 78.1062 90.0 90.0 90.0			38.648 73.746 78.142 90.0 90.0 90.0			38.671 73.803 78.111 90.0 90.0 90.0		
Wavelength (Å)	0.72932			0.91587			0.72931			0.72932		
	Overall	Inner Shell	Outer Shell	Overall	Inner Shell	Outer Shell	Overall	Inner Shell	Outer Shell	Overall	Inner Shell	Outer Shell
Low resolution limit	53.549	53.549	1.261	39.053	39.053	1.039	53.633	53.633	1.546	53.645	53.645	1.4
High resolution limit	1.155	3.526	1.159	1.02	2.838	1.02	1.459	4.277	1.459	1.336	3.917	1.336
Rmerge (all I+ & I-)	0.122	0.044	2.088	0.063	0.035	0.777	0.135	0.053	1.914	0.087	0.062	1.404
Rmerge (within I+/I-)	0.123	0.044	2.028	0.061	0.034	0.705	0.136	0.052	1.819	0.086	0.061	1.287
Rmeas (all I+ & I-)	0.127	0.046	2.171	0.069	0.038	0.873	0.14	0.056	1.988	0.091	0.064	1.534
Rmeas (within I+/I-)	0.133	0.047	2.194	0.073	0.04	0.889	0.147	0.056	1.964	0.094	0.066	1.53
Rpim (all I+ & I-)	0.035	0.013	0.593	0.027	0.015	0.392	0.039	0.016	0.534	0.026	0.018	0.597
Rpim (within I+/I-)	0.05	0.018	0.836	0.039	0.021	0.533	0.055	0.021	0.739	0.036	0.025	0.808
Total number of observations	791089	37596	39592	688584	35224	27383	452492	20581	23068	496420	27160	13721
Total number unique	59836	2990	2992	112855	5642	5645	34513	1725	1725	44451	2222	2224
Mean(I)/sd(I)	12.1	46.4	1.4	12.8	38.1	2.2	10.7	32.1	1.4	15.7	38.7	1.2
Completeness (spherical)	77	100	17.5	98.9	100	94.3	87	99.9	27.6	86.3	100	33.5
Completeness (ellipsoidal)	94.8	100	63.7	98.9	100	94.3	94.1	99.9	49.6	90.6	100	47.1
Multiplicity	13.2	12.6	13.2	6.1	6.2	4.9	13.1	11.9	13.4	11.2	12.2	6.2
CC(1/2)	0.999	0.999	0.5	0.999	0.999	0.593	0.999	0.999	0.643	0.999	0.999	0.455
Refinement:												
Resolution	53.55 - 1.16			39.05 - 1.02			53.69 - 1.46			53.70-1.32		
No. reflections all/free	59836 / 2888			112852 / 5501			34516 / 1672			44562 / 2261		
R-factor/R-free	0.161 / 0.179			0.122 / 0.140			0.172 / 0.197			0.169 / 0.198		
RMS Deviations:												
Bonds	0.0134			0.0226			0.0126			0.0133		
Angles	1.811			1.542			1.834			1.844		

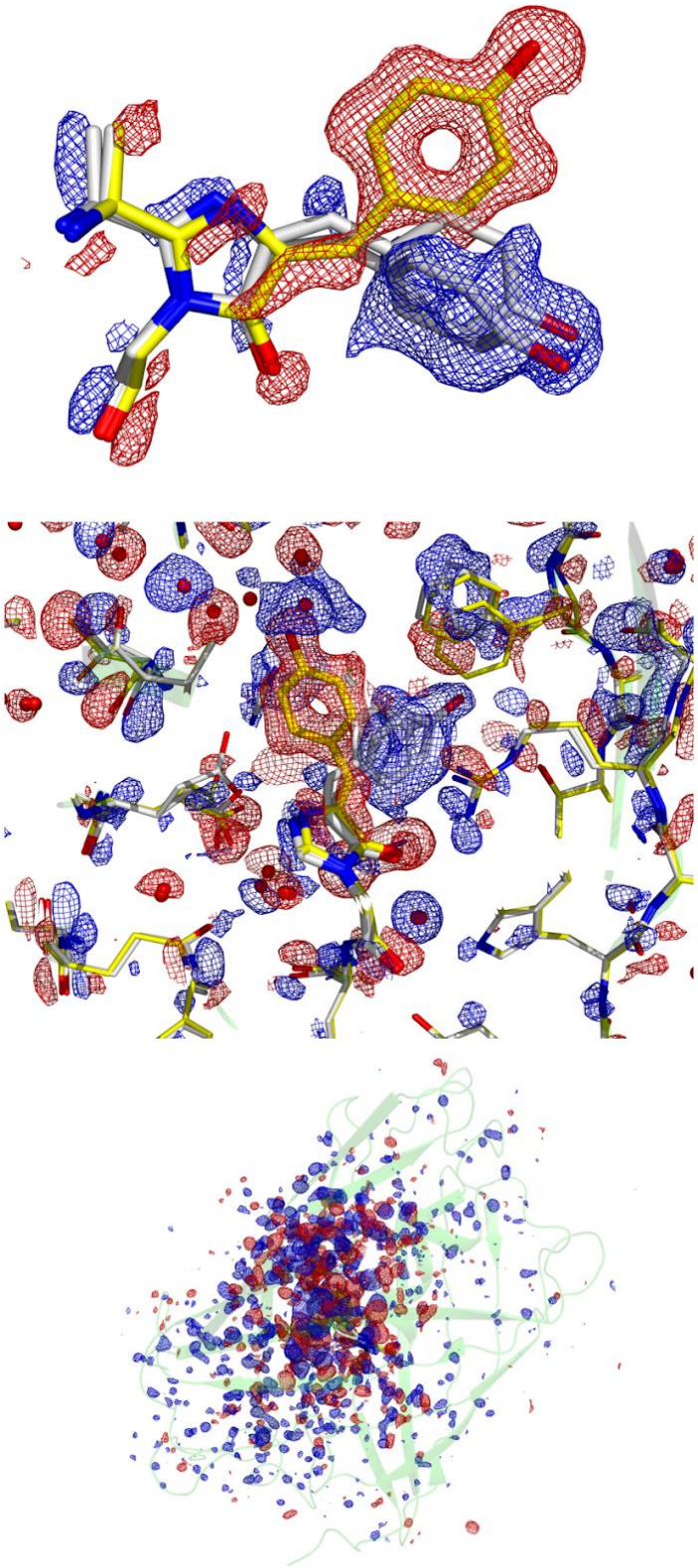

Supplementary Fig. 48 | MX Crystallography trans-cis photoisomerization. Q-weighted difference electron density of cryo-MX structures **0** (on state) (PDB ID 7QLI) and **1** (off state by 500nm illumination at 290K) (PDB ID 7QLJ) (Supplementary Fig. 47). The secondary structure (green) of the cis-ground state coordinates (yellow) and trans-state model (grey) are shown with electron density contoured at +3 rms (blue) and -3 rms (red). Note the additional chromophore conformation in the trans state with partial occupancy that is not observed at room temperature SFX data.

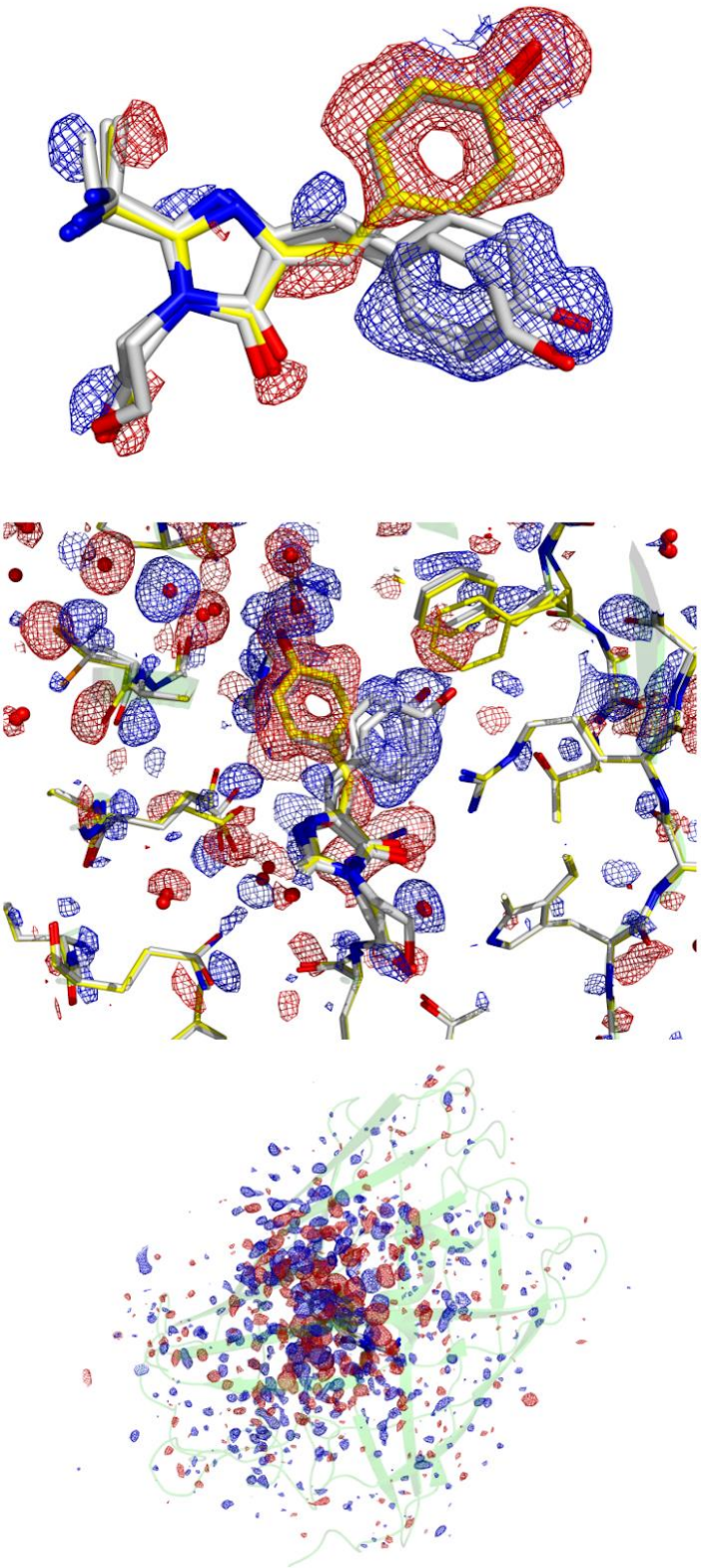

Supplementary Fig. 49 | MX Crystallography 200 K photoisomerization. Q-weighted difference electron density of cryo-MX structures **0** (on state) (PDB ID 7QLI) and **4** (off state by 500nm illumination at 200K) (PDB ID 7QLK). Showing that cis-trans photoisomerization proceeds at 200 K. The cis ground state (yellow carbon chromophore structure) was illuminated with 500 nm light at 200 K temperature. The photoproduct shows the same two trans chromophore structures (grey carbon chromophore structures), and associated amino acid changes as seen at 293 K temperature (Supplementary Fig. 48). Electron density contoured at +3 rms (blue) and -3 rms (red).

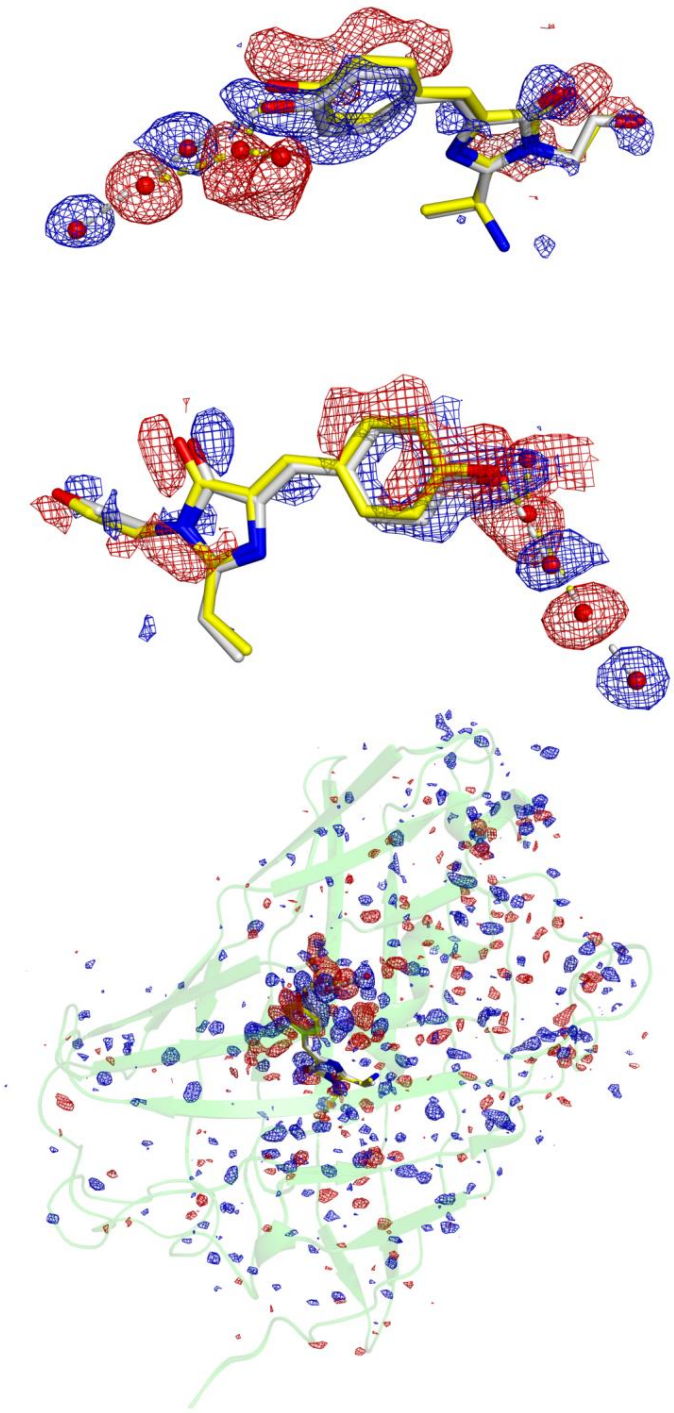

Supplementary Fig. 50 | MX Crystallography Thermal annealing of cryo-trapped intermediate. Thermal annealing of a photoproduct in the trans-cis direction: Q-weighted difference electron density of cryo-MX structures between **4** and the annealed crystal (**4a**). A trans structure was accumulated at 293 K to full occupancy. The relaxed trans structure was cooled to 200 K and subsequently illuminated with 400 nm light. The resulting photoproduct (Structure '**4**' in Supplementary Fig. 47) had fully occupied cis- chromophore conformation (yellow carbon coordinates).The photoproduct was heated to 293 K for 1 second then cryo-cooled for MX data collection (Structure '**4a**') (grey carbon coordinates). Isomorphous difference maps are shown (red, -3 rms; blue, 3 rms).

Supplementary Discussion

10. rsKiiro development

The target sample for these studies is a photoswitching fluorescent protein named “rsKiiro”. Part of the EosFP family of fluorescent proteins it is a mutant of “Skylan-NS”[25]. It was the culmination of >80 iterations selected for 3 factors: increased photoproduct quantum yield, improved diffraction quality and resolution following photoconversion and expression yield. Potential mutants were developed using site-directed mutagenesis of high performing photoswitching fluorescent proteins reported in the literature which, in addition to Skylan-NS, included TGP[26], rsTagRFP[27] and rsEGFP2[28]. Mutations targeted key side chains in and around the chromophore region that have been reported to influence photo-switching behaviour in similar systems. rsKiiro is a L62A / M159T mutant of Skylan-NS, A rsFP originally derived from a species of coral known as *Lobophyllia Hemprichii*[25]. Structurally, rsKiiro is similar to Green Fluorescent Protein (GFP) with an 11-stranded beta-barrel surrounding an alpha helix. The chromophore of rsKiiro is formed from the Ala-Tyr-Gly tripeptide at residue numbers 62-64 in the alpha helix. During folding an autocatalytic condensation reaction produces the 4-(p-hydroxybenzylidene)-5-imidazolinone (p-HBI) chromophore. The optimized sequence included the ‘fast-switching’ M159T mutation that also yields similar phototransformation improvements also seen in the Dronpa FP[29]. The mutation retained the excellent crystallographic statistics, resolution and quality after photoconversion as also seen in the ‘Skylan-NS’ crystals[24].

```
CLUSTAL O(1.2.4) multiple sequence alignment


EosFP           MSAIKPDMKINLRMEGNVNGHHFVIDGDGTGKPFEGKQSMDLEVKEGGPLPFAFDILTTA     60
rsKiiro         MSAIKPDMKIKLRMEGNVNGHHFVIDGDGTGKPFEGKQSMDLEVKEGGPLPFAFDILTTA     60
skylan-NS       MSAIKPDMKIKLRMEGNVNGHHFVIDGDGTGKPFEGKQSMDLEVKEGGPLPFAFDILTTA     60
                **********:**************************************************

EosFP           FHYGNRVFAEYPDHIQDYFKQSFPKGYSWERSLTFEDGGICIARNDITMEGDTFYNKVRF     120
rsKiiro         FAYGNRVFAKYPDNIQDYFKQSFPKGYSWERSLTFEDGGICNARNDITMEGDTFYNKVRF     120
skylan-NS       FLYGNRVFAKYPDNIQDYFKQSFPKGYSWERSLTFEDGGICNARNDITMEGDTFYNKVRF     120
                * ********:***:***************************** ******************

EosFP           HGVNFPANGPVMQKKTLKWEPSTEKMYVRDGVLTGDITMALLLEGNAHYRCDFRTTYKAK     180
rsKiiro         YGTNFPANGPVMQKKTLKWEPSTEKMYVRDGVLTGDVETALLLEGNAHYRCDFRTTYKAK     180
skylan-NS       YGTNFPANGPVMQKKTLKWEPSTEKMYVRDGVLTGDVEMALLLEGNAHYRCDFRTTYKAK     180
                :*.**********************************:  **********************

EosFP           EKGVKLPGYHFVDHCIEILSHDKDYNKVKLYEHAVAHSGLPDNARR   226
rsKiiro         EKGVKLPGAHFVDHCIEILSHDKDYNKVKLYEHAVAHSGLPDNARR   226
skylan-NS       EKGVKLPGAHFVDHCIEILSHDKDYNKVKLYEHAVAHSGLPDNARR   226
                ******** ************************************
```

Supplementary Fig. 51. Multiple sequence alignment for the rsKiiro, skylan-NS and EosFP sequences.

Improved photoproduct quantum yield is critical for femtosecond TR-SFX studies due to the temporal scales of the experiment being shorter the excited state life of these systems (~50 ps, see below). Excitation events that follow non-photoreaction electronic pathways which return to the ground state of

the system have no opportunity to be re-excited and contribute to the total photoactive population. Therefore the theoretical maximum population that could be obtained by femtosecond excitation is capped at the photoproduct quantum yield (see below). This is not usually achievable as other excitation pathways such as excited state absorption leading to double excitation and stimulated emission will occur with strong optical pumping preventing a 100% occupancy of the S_1 electronic state. Despite improvements in TR-SFX data processing it is still not possible to reliably detect photoinduced differences of populations below ~10% level and the feasibility of a femtosecond TR-SFX experiment can hinge on the quantum yields of the sample. The situation is more relaxed with longer nanosecond timescale excitation where multiple re-excitations events can occur within the duration the pulse enabling final populations in excess of photoproduct quantum yield.

As previously mentioned the population differences are small and light induced difference on such short timescales can be incredibly subtle therefore maximizing crystallographic resolution is very important, the improvements made in rsKiiro meant that at room temperature microcrystal SFX structures collected at SACLA and LCLS XFELs routinely reach resolutions below <1.5 Å. This was an improvement from the 1.8 Å previously measured on Skylan-NS microcrystals. Depending on sample delivery method XFEL beamtimes have very demanding sample consumption particularly with optically driven reactions where the use of a grease injector is not desirable due to the potential for light-piping up the jet coupled with high quantum yield causing accumulated photo conversion in upstream crystals reducing the potential signal to noise obtainable in PP measurements. The GDVN consumed >5g of protein during LR23.

Screening for expression yield was quickly determined during initial grow ups. Due to the mutations being mostly limited to the chromophore region and crystallization conditions of the parent molecules being readily available in the literature obtaining initial crystals for testing was usually straight forward. These batch grown microcrystals used for the screening photoproduct quantum yield by performing femtosecond flash photolysis measurements on crystalline “pancakes” as described in the main text, both yield and non-recoverable bleaching were screening factors. Finally cryo-MX structures were collected in both the ground state and pre-illuminated crystals to confirm that crystal order was not disrupted through photo-activation.

rsKiiro has been selected for the specific photochemical characteristics described in the manuscript, that include the action of the double well potentials for both the off and the on states and the complete 100% photoswitching between on and off states. Additional characteristics considered for its selection included the photochemical quantum yield of photoisomerisation, the excited state lifetime which exceeds the vibrational dephasing time, and the activated barrier crossing and incoherent reaction pathway for photoisomerisation. The sequence is based on the EosFP gene from *Lobophyllia hemprichii* and the orthorhombic crystal form was found to diffract to high resolution in both the dark and the illuminated states. The expression and crystallisation characteristics were additionally excellent. These characteristics of rsKiiro allowed the investigation of the coherence contributions on ultrafast timescale as described. These are also fully distinct and different from other photoswitching FPs described in the literature. These include rsEGFP2[30,31], which is based on the *Aequorea Victoria gfp* sequence, and irisFP[32], that both have very different photochemical properties and structures.

11. Thermodynamic modelling of rsKiiro photo-switching

11.1. Analytical solution to the overall off → on conversion process using the Master Rate Equation method.

The temperature dependence of the off → on photoisomerization reaction takes the primary evidence from the femtosecond time resolved SFX crystal structure that identifies the short lived A_2 structure that is not populated at room temperature in equilibrium conditions. The proposed model for the off → on reaction is shown in Extended Data Fig. 1g & Supplementary Fig. 52 .

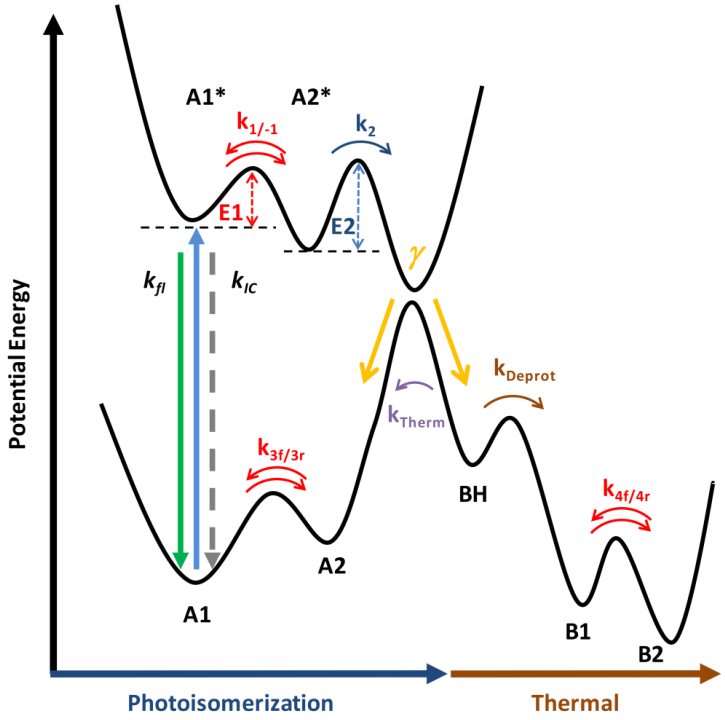

Supplementary Fig. 52 | Proposed electronic structure model for rsKiiro off→on photoreaction.

In the Born-Oppenheimer approximation there will exist both A_1^* and A_2^* coordinates with a singlet excited state electronic structure. We thus consider two separate barriers E_1 and E_2

$$
\begin{aligned}
A_1 &\xrightarrow{k_{exc}} A_1^* \\
A_1^* &\underset{k_{1r}}{\overset{k_{1f}}{\rightleftarrows}} A_2^* \\
A_2^* &\xrightarrow{\gamma k_2} BH \\
A_2^* &\xrightarrow{(1-\gamma)k_2} A_2 \\
A_2 &\underset{k_{3r}}{\overset{k_{3f}}{\rightleftarrows}} A_1 \\
BH &\xrightarrow{k_{Deprot}} B_1 \\
BH &\xrightarrow{k_{Therm}} A_2 \\
B_1 &\underset{k_{4r}}{\overset{k_{4f}}{\rightleftarrows}} B_2
\end{aligned}
\qquad \text{(S4)}
$$

$$A_2^* \xrightarrow{k_{fl}} A_2$$
$$A_1 \xrightarrow{k_{relax(A-B)}} B_2$$

Using the master equation method[33,34] the time dependence is given by

$$\frac{dx}{dt} = K_c x \tag{S5}$$

Or

$$\frac{dx}{dt} = -\sum_{j=1}^{m} K_{ij} x_i + \sum_{j=1}^{m} K_{ji} a_j (i = 1,2,..,m, i \neq j) \tag{S6}$$

There x is a vector of concentrations of species, and $K_c x$ is given as:

$$\begin{bmatrix} -k_{exc} - k_{relax} - k_{3r} & 0 & 0 & k_{3f} & 0 & 0 & 0 \\ \mathrm{k_{exc}} & -k_{1f} & k_{1r} & 0 & 0 & 0 & 0 \\ 0 & k_{1f} & -k_{1r} - \gamma k_2 - (1-\gamma)k_2 - k_{fl} & 0 & 0 & 0 & 0 \\ k_{3r} & 0 & k_{fl} + (1-\gamma)k_2 & -k_{3f} & k_{Therm} & 0 & 0 \\ 0 & 0 & \gamma k_2 & 0 & -k_{Therm} - k_{Deprot} & 0 & 0 \\ 0 & 0 & 0 & 0 & k_{Deprot} & -k_{4f} & k_{4r} \\ k_{relax} & 0 & 0 & 0 & 0 & k_{4f} & -k_{4r} \end{bmatrix} \times \begin{bmatrix} A_1 \\ A_1^* \\ A_2^* \\ A_2 \\ BH \\ B_1 \\ B_2 \end{bmatrix} \tag{S7}$$

Diagonalization of Kc

$$K_c \xi = \lambda \xi$$

solves the master equation analytically to provide the eigenvalues λ(n) alternatively these may be solved using MATLAB's symbolic methods.

```
syms kexc krelax k3f k1f k1r gamma k2 kfl k3r ktherm kdeprot k4f k4r

A = sym([(-kexc-krelax-k3r) 0 0 k3f 0 0 0; kexc -k1f k1r 0 0 0 0; 0 k1f (-k1r-(gamma*k2)-(1-gamma)*k2-kfl) 0 0 0 0; k3r 0 (kfl+(1-gamma)*k2) -k3f ktherm 0 0; 0 0 (gamma*k2) 0 (-ktherm-kdeprot) 0 0; 0 0 0 0 kdeprot -k4f k4r;krelax 0 0 0 0 k4f -k4r])

[V]=eig(A)
```

Box: matlab code to compute eigenvalues using symbolic function

The dimensions of the computed eigenvalue functions, which are not printed here, are 429 terms.

This in principle provides solutions to the master equation

$$x = PLP^{-1}x_0 \tag{S8}$$

Where $P = [\xi_1, .., .., \xi_n]$is the matrix whose i[th] column is the eigenvector ξ_i and

$$L = \begin{bmatrix} \exp(\lambda_1 t) & 0 & 0 & 0 \\ 0 & \exp(\lambda_1 t) & 0 & 0 \\ 0 & 0 & \ddots & \vdots \\ 0 & 0 & \cdots & \exp(\lambda_n t) \end{bmatrix} \tag{S9}$$

Alternatively solutions may be found from 'Sylvester's formula'[34] which depend on the eigenvalues only and do not need the eigenvectors

$$x = \exp(Kt)\, x_0 \tag{S10}$$

$$\exp(Kt) = \sum_{i=1}^{n} M_i \exp(\lambda_i t) \tag{S11}$$

$$M_i = \prod_{\substack{j=1 \\ j \neq i}}^{n} (K - \lambda_j I) / \prod_{\substack{j=1 \\ j \neq i}}^{n} (\lambda_i - \lambda_j) \tag{S12}$$

This provides analytical solutions to the coupled differential equation. In practice the system could be solved in more straightforward manner using numerical approach, which however requires that all parameters are known. Therefore, the steady state approximation reduces the complexity of an analytical approach.

Similarly, the photoisomerization of the B_1 state to produce the relaxed A_1 photoproduct is directly equivalent but lacks the final relaxation as the B_1 state is the dark resting species. Furthermore, the thermal protonation follows the cis-trans photoisomerization (Supplementary Fig. 52). However this manuscript does not include experimental observation of these processes directly and also does not contain measurement of the explicit rates.

11.2. Summary of theoretical considerations for temperature dependence of the trans-cis photoisomerization

It has previously been shown that the temperature dependence of fluorescence and internal conversion is expected to be small[35], summarized below. The fluorescence rate can be considered to relatively independent of temperature because the absorption and fluorescence spectra do not change significantly over the temperature range that is studied. Therefore the Strickler-Berg relation predicts the rate not to change significantly. The temperature dependence of internal conversion is known from theory and is argued to be weak for fluorescent proteins on the basis of the following arguments previously put forward[35]:

The internal conversion rate constant has a temperature dependent and a temperature independent part

$$k_{IC} = k_{IC}^{0}\left(T_{independent}\right) + k_{IC}\left(T_{dependent}\right) = k_{IC}^{0} + k_{IC}^{T} \exp\left(-\frac{E_A}{RT}\right) \tag{S13}$$

Fluorescence and internal conversion can be described by the "spin-boson Hamiltonian", in which "spin" is a two-level system (e.g. electronic ground and excited states), and "boson" is a bath of harmonic oscillators that couple to the two-level system to various degrees [36,37]

$$H = \Sigma_{n=g,e}(E_n + \Sigma_\alpha g_{n\alpha} x_\alpha)|n\rangle\langle n| + V_{g,e}|g\rangle\langle e| + V_{e,g}|e\rangle\langle g| + \Sigma_\alpha \left(\frac{p_\alpha^2}{2m_\alpha} + \frac{1}{2} m_\alpha \omega_\alpha^2 x_\alpha^2\right) \tag{S14}$$

where $|g\rangle$ and $|e\rangle$ are the electronic ground and excited states, E_n are the corresponding electronic energies without any couplings, α are the harmonic bath normal modes, x_α and p_α are their displacements and momenta, m_α and ω_α are their masses and frequencies, $V_{g,e}$ and $V_{e,g}$ are the electronic couplings between two electronic states, and $g_{n\alpha}$ are the couplings between the bath modes and the electronic states. The interpretation is that fluorescence and internal conversion between two electronic energy levels are a competition between photons and phonons governed by their relative coupling strengths.

Fermi's golden rule expresses the internal conversion rate

$$k_{IC} = \frac{|V_{eg}|^2}{\hbar^2} e^{-\Sigma_\alpha S_\alpha (2n_\alpha + 1)} \int_{-\infty}^{\infty} dt\, e^{i\omega_{eg}t + \Sigma_\alpha S_\alpha \left(n_\alpha e^{i\omega_\alpha t} + (n_\alpha + 1) e^{-i\omega_\alpha t}\right)} \quad \text{(S15)}$$

where S_α are dimensionless quantities, the Huang-Rhys factors, which are directly related to the vibronic coupling strengths. Further detail is found in references[35–37] that discuss two possible regimes that differ in the coupling strengths. If the vibronic couplings are weak it is shown that $k_{IC} \sim e^{-\omega_{eg}}$ and is thus dominated by the energy gap, which is known as the Englman-Jortner energy-gap law. In the opposite regime of strong coupling

$$k_{IC} = \frac{|v_{e,g}|^2}{\hbar} \sqrt{\frac{\pi}{k_B T E_r}}\, e^{-\frac{E_A}{k_B T}} \quad \text{(S16)}$$

With

$$E_A \equiv \frac{(E_{eg} - E_r)}{4E_r} \quad \text{(S17)}$$

The temperature dependence of k_{IC} therefore depends on the magnitude of the Huang-Rhys factors. Lin et al.[35] previously argued that for fluorescent proteins computational results from Bochenkova et al. could be used[38]. From that data Lin et al estimated the summation. $\Sigma_\alpha S_\alpha n_\alpha$ to be approximately 0.5 which would be well below the expected value where temperature dependence would be significant. The same authors Lin et al.[35] carried on to evaluate theoretical arguments that show weak temperature of the branching ratio γ. Using the Launau-Zener theory[36,39,40]

$$\gamma = \exp\left(-\frac{2\pi |V_{12}|^2}{\hbar v |F_1 - F_2|}\right) \quad \text{(S18)}$$

Where V_{12} is the coupling between two surfaces, V is the nuclear velocity approaching the intersection, and F_1 and F_2 are the slopes (R is the nuclear position along the reaction coordinate) of the corresponding surfaces at the intersection. Lin et al argued that the Franck-Condon excitation is weakly temperature dependent, such that the nuclear velocity is proportional to $v \sim \sqrt{T}$ which is weaker than Arrhenius behaviour.

11.3. Modelling of the temperature dependence of cis-trans and trans-cis photoisomerization

The following considerations inform a model for the analysis of the temperature dependence of photoisomerization of the rsKiiro fluorescent protein. Firstly we analyse the cis-trans photoisomerization, as we have available measurements of the temperature dependence of both the fluorescence decay (Extended Data Fig. 1i) as well as the photoisomerization rate (Extended Data Fig. 1e & k).

The overall fraction of the fraction of B_1* converted to the A state is

$$\varphi_{overall} = \frac{\frac{k_{1f}}{k_{1r}} k_2}{k_f + k_{IC} + \frac{k_{1f}}{k_{1r}} k_2} \times \gamma \quad \text{(S19)}$$

The overall temperature dependence of photoisomerization from the conventional Arrhenius equation is

$$\varphi_{overall}(T) = \frac{\frac{A_{1f}}{A_{1r}} A_2 \exp\left(-\frac{E_{1f} - E_{1r} + E_2}{RT}\right)}{k_f + k_{IC} + \frac{k_{1f}}{k_{1r}} k_2} \times \gamma \quad \text{(S20)}$$

For both the on→off and off→on photoisomerization the fluorescence contributes only very little to the excited state decay (6% and 0.5 % respectively). In both cases the internal conversion will dominate the excited state decay. As previously discussed, the temperature dependence of the internal conversion rate depends on the magnitude of the Huang-Rhys factors. We are therefore able to compare the temperature dependence of the fluorescence, which measures all the contributions to the excited state decay, with the temperature dependence of the photoisomerization rate (k_{PI}). The total rate (k_T) from all contributions can be decomposed as:

$$k_T = k_{PI} + k_{IC} + k_R \quad \text{(S21)}$$

And further expressed as

$$k_T = \gamma_{PI} k_T Q_{PI} + \gamma_{IC} k_T Q_{IC} + \gamma_R k_{T(300k)} \quad \text{(S22)}$$

Where γ_n and Q_n are the quantum yields and temperature scalings of each process respectively.

For the on→off reaction γ_{PI} was found to be 0.63% from CW illumination of solution samples (see below) and Q_{Ph} can be determined using the E_{PI} = 2.0±0.4 kJ mol^{-1} from Arrhenius measurements (Extended Data Fig. 1k) and normalizing to the 300 K rate. By subtracting the scaled temperature dependent contributions due to the photoisomerization rate, it is possible to fit the Arrhenius equation to the remaining temperature dependent rate and obtain and effective barrier for the internal conversion processes (Extended Data Fig. 1l) of E_{IC} =16.5 ± 0.6 kJ mol^{-1}.The third term in (S22), the radiative rate, is assumed to be temperature independent and therefore will not contribute to the gradient in the Arrhenius plots.

We can perform the same calculation for the off→on reaction using the temperature dependence of the excited state decay obtained from transient absorption spectra (Extended Data Fig. 1d). E_{PI}= 3.5 ±1.2 kJ mol^{-1} (Extended Data Fig. 1e) & γ_{PI}= 15.9±1.2% (Supplementary section 6). The final recovered E_{IC} = 16.51 ± 0.53 kJ mol^{-1} (Extended Data Fig. 1f)

All the barriers recovered from these fittings are shown in Extended Data Fig. 1h. It can be seen that there very similar barriers obtained for E_{IC} in both the on→off and off→on reactions while the E_{PI} barrier is approximately twice as large for the off→on reaction.

Nevertheless, the temperature dependence of photoisomerization is dominated by the excited state pre-equilibrium between A_1* and A_2* states in combination with an excited state barrier.

$$A_1^* \underset{k_{1r}}{\overset{k_{1f}}{\rightleftarrows}} A_2^* \overset{k_2}{\rightarrow} BH \quad \text{(S23)}$$

For this process the overall rate becomes

$$k_{overall} \sim \frac{A_{1f}}{A_{1r}} A_2 \exp\left(-\frac{E_{1f} - E_{1r} + E_2}{RT}\right) \quad \text{(S24)}$$

Therefore the Arrhenius pre-factor for the high-temperature regime measured for both on→off and off→on directions is $\frac{A_{1f}}{A_{1r}} A_2$ while the effective activation energy is $E_{1f} - E_{1r} + E_2$. It is worth noting

that such re-equilibrium can lead to a effective negative activation energy which[41–43] has also been reported for the analysis of fluorescence decay of the Green Fluorescent Protein (GFP)[44].

11.4. Ground state evolution in the off → on direction

With excitation of the A_1 ground state, with neutral trans chromophore in relaxed geometry, the macroscopic absorption differences at room temperature shows an isosbestic point and are assigned to the conversion of A_1 to produce the final B_2 state with anionic cis chromophore structure. The ground state species evolution for the trans-neutral off state to the cis anionic on state chromophore

$$A_1 \underset{k_r}{\overset{k_f, k_{therm}}{\rightleftarrows}} BH \xrightarrow[k_{Deprot}]{} B_1 \xrightarrow[k_{relax}]{} B_2 \tag{S25}$$

The forward rate constant k_f is proportional to the optical excitation rate and the primary quantum yield, and at room temperature exceeds the thermal rate constant k_{therm}=1.7x10^{-3} s^{-1} by several orders of magnitude which can be neglected. The reverse rate constant k_r is similarly proportional to the optical excitation rate and the primary quantum yield and can be neglected since the deprotonation rate k_{Deprot}= 1/40 μs = 1.5x10^4 s^{-1} far exceeds the optical excitation rate. Subsequent to deprotonation of the cis neutral chromophore photoproduct, a relaxation of the B_1 product to form the folly relaxed B_2 product with rate k_{Relax} is assumed from the crystallographic observation that traps the B_1 state at low temperature. Since the B_2 state was observed at room temperature at the 100 μs time point following femtosecond excitation of A_1, the value of k_{Relax} at room temperature is higher than ~2x10^4 s^{-1}. Therefore the overall ground state process at room temperature is well described with the two-state forward phototransfer.

$$A_1 \xrightarrow{\varphi, k_f} B_2 \tag{S26}$$

With

$$\frac{d[A_1]}{dt} = \frac{P_0}{V}(1 - 10^{-A_t})\left(-\frac{\epsilon_{A_1} l[A_1]}{A_t}\varphi\right) \tag{S27}$$

With P_0 the incident light power, l the path length, V the volume and A_t the total absorbance. For the dilute limit taking the first term in the Taylor expansion allows the approximation

$$k_{overall} = \frac{d[A_1]}{dt} = \frac{P_0}{V}\ln 10\ \left(\epsilon_{A_1} l[A_1]\right)\varphi_{off\rightarrow on} \tag{S28}$$

Similarly, for the photoconversion of the on state with cis anion chromophore to the relaxed off state, the overall process for ground state evolution is (not showing thermal relaxation)

$$B_2 \underset{k_r}{\overset{k_f}{\rightleftarrows}} A^- \xrightarrow[k_{Prot}]{} A \xrightarrow[k_{relax}]{?} A_1 \tag{S29}$$

The possible intermediate and relaxation in this direction of conversion is implied from cryotrapping (Supplementary Fig. 48 - Supplementary Fig. 50). With the observation of isosbestic point the overall process is described as

$$B_2 \underset{k_{therm}}{\overset{\varphi k_f}{\rightleftarrows}} A_1 \tag{S30}$$

Neglecting the contribution of k_{therm} the overall rate for the on-to-off conversion is

$$k_{overall} = \frac{d[B_2]}{dt} = \frac{P_0}{V}\, ln10\, \left(\epsilon_{B_2} l[B_2]\right)\varphi_{on\rightarrow off} \qquad \text{(S31)}$$

11.5. Modelling of the convex Arrhenius behaviour of the on→off and off→on photoconversion

In contrast to recently reported temperature dependence of fluorescence of fluorescent proteins that scanned a relatively small range of temperatures near ambient values (279 - 315 K), here we show that the kinetics of photo-conversion measured for lower temperatures significantly deviate from the high temperature regime. A few µL of rsKiiro (60mg/mL) solution mixed with 100% glycerol cryoprotectant in a 30:70 ratio was loaded onto a 20 µm CryoLoop™ (Hampton) to give a final OD @ 490 nm of 0.2-0.3. The absorption was monitored using a fiber based spectrometer linked to a microscope and the temperature was controlled using a cryo stream (Oxford instruments) positioned ~1 cm from the loop. The forward on→off reaction was driven by an unfocused 15 mW 473 nm CW laser, while the reverse reaction was driven by an unfocused 5 mW 400 nm CW laser. For both directions a convex Arrhenius behaviour is observed (Extended Data Fig. 1e & k), separate analysis of the linear regions therefore retrieves larger activation energies as well as larger pre-factors for the low temperature regime.

We note that the transition temperature of the kinetic series in Extended Data Fig. 1e & k are 229±2 K, 208±4 K, 236±10 K for the on→off, off→on with low temp and room temp preconversion conditions respectively. The usual interpretation of kinetic transitions in this temperature range is the glass transition in proteins[45]. An empirical approach to model a transition temperature writes the rate coefficient approximated by the Vogel-Tammann-Fulcher (VTF) relation

$$k_\alpha(T) = A_\alpha \exp\left(-\frac{DT_0}{T - T_0}\right) \qquad \text{(S32)}$$

Where T_0 is an experimentally determined transition temperature and the amplitudes A_α and D are empirical from experiment. The rate is taken to depend inversely proportional to the viscosity in the mechanical Maxwell relation[45].

While the viscosity changes at the glass transition cannot be excluded we consider as primary evidence that thermal relaxation of the metastable off state significantly increases the value of the transition temperature for the convex Arrhenius plot for the off-on transition (Extended Data Fig. 1e & k). Therefore, we model this dominating relaxation behaviour as a Gibbs Free Energy difference ΔG between relaxed and strained conformations of the excited state intermediate E_2*. This model directly connects the ultrafast SFX measurements and structural determination of the chromophore and hydrogen bonding dynamics with the thermodynamics that describe the temperature dependence of photoisomerization.

For an equilibrium that models a temperature dependence of an intermediate A_1^* / A_2^* with a $K_{eq} = k_f/k_r$, the Gibbs Free energy is $\Delta G = -RT \ln K_{eq}$

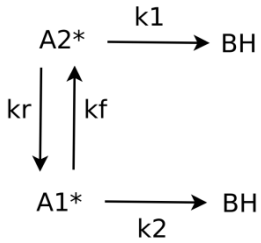

Here we treat the observed behaviour as a switching between two distinct confirmations each with their own reaction pathways that undergo a transition between the active and inactive at the point of the break. The rate constants k_1 and k_2 dominate in the high and low temperature region so that the overall rate k_{all} is

$$k_{all} = \frac{k_1}{1 + \exp\left(+\frac{\Delta G}{RT}\right)} + \frac{k_2}{1 + \exp\left(-\frac{\Delta G}{RT}\right)} \quad \text{(S33)}$$

Where

$$k_1 = \mathcal{A}_1 \exp\left(-\frac{E_{T1}}{RT}\right)$$

$$k_2 = \mathcal{A}_2 \exp\left(-\frac{E_{T2}}{RT}\right)$$

And

$$\Delta G = \Delta H - T\Delta S$$

$\mathcal{A}_n$ and E_{Tn} are the Arrhenius prefactors and total activation energy for each of the reactions, ΔH is the change in entropy and ΔS the enthalpy. By fixing the values for E_{T1} and E_{T2} to the same as the local (linear) fits to the Arrhenius equation, allows the values ΔH and ΔS to be determined from the steepness and location of the Arrhenius break. In order to produce the convex behaviour it is necessary to incorporate an Enthalpy-Entropy compensation such that the sign of ΔG changes across the transition temperature. The break position (T_k) the point at which $\Delta G = 0$. This uses a modified expressions previously developed by Klinman et. al to model convex Arrhenius behaviour in enzymology [46].

Supplementary Table. 10. Arrhenius fitting of rsKiiro photoswitching reactions

Reaction	E_{T1} (kJ/mol)	E_{T2} (kJ/mol)	$\mathcal{A}_1$ (s^{-1})	$\mathcal{A}_2$ (s^{-1})	ΔH (kJ mol^{-1})	ΔS (kJ mol^{-1} K^{-1})	T_t (K)
on – off	2±0.4	32±3	1.5±0.7	32±5	66±4	0.29±0.02	229±2
off- on (Low temp precon.)	3.5±1.2	40±4	0.9±1.2	22±3	51±20	0.24±0.1	208±4
off – on (room temp precon.)	-	55±20	-	26±10	58±25	0.25±0.13	236±10

Practically for the purposes of fitting the modification to k_1 and k_2 produces a sigmoid-like switching behaviour such that k_1 dominates at high temperature and k_2 low temperature. The temperature at which the transition occurs depends on the ratio of H to S while curvature of the break is inversely proportional

to H, we therefore substitute S for H/T_k. The sections above and below the Arrhenius break were independently linearly fit (Extended Data Fig. 1e & k, dashed lines) using a similar bootstrap method to that described in supplementary of Romei et al.[13] to obtain values of A_n and E_n (Supplementary Table. 10) for the high and low temperature regions. For fitting the full range of temperatures the activation energies and prefactors obtained from the linear fits were used in Eqn. (S33) and the only free parameters were H and T_k . It was necessary to relax constraints on the value of the A_2 to secure a good fit, we justify this by noting that due to the limited number of data points available the linear fits there will still be contributions from the other confirmer. Due to the similarity between the high temperature behaviour of the two off→on conditions and the limited number of data points for the room temperature preconversion the linear fit of the cryo preconversion was used to fit both datasets, we justify this as the difference between them is attributed to cryo temperatures modifying the reaction pathway therefore these data sets must converge at room temperature. We observe very similar values for the H for all three conditions, due to the larger error in the cryo on→off dataset at the transition temperature it is possible force the fit to a very large value (i.e H >500 kJ/mol) we disregard this as aphysical.

11.6. Explicit thermodynamics treatment of barriers in the reactive coordinate and non-radiative transitions

In order to derive the functional significance of the double-well adiabatic potential discovered in our ultrafast crystallography experiments we combined the structural information with kinetics measurements and thermodynamics modelling. The double-well adiabatic nature of both the off and on states was additionally shown from the thermodynamic analysis of reversible photoisomerisation as well as the excited state decay. We thus analyses and quantitatively modelled the temperature dependence of the radiative and non-radiative transitions of both the on and off states (Extended Data Figure 9) (Section 11 of the Supplementary materials).

The temperature dependence of both the *trans-cis* and *cis-trans* photoisomerization shows convex non-Arrhenius kinetics in which the transition temperature is additionally sensitive to structural annealing which lowers the 'A*2' potential level (Fig. 5). Convex Arrhenius kinetics are conventionally analysed using parameters for double-well potentials. Modelling of the non-Arrhenius kinetics invoked an Entropy-Enthalpy compensation scheme and retrieved the relaxation parameters of the second energy level of the double-well potential (Fig. 2, 5, A1*, A2*, Extended Data Fig. 1e & k and section 11.5 of supplementary materials). A full thermodynamics treatment of photoisomerization employs the knowledge of the double-well potential (Extended Data Fig. 1g) and uses the experimental separation of the radiative and non-radiative transitions that showed different barrier values (Extended Data Fig. 1f & l). We determined the temperature dependence of the excited state decay of the off state from stimulated emission decay kinetics (Extended Data Fig. 1d), and on state from fluorescence measurements (Extended Data Fig. 1i &-j) for samples in solution. We find that the internal conversion of the *trans* off state encounters a larger barrier at 17.0±0.6 kJ mol^{-1} than that found for the effective barrier $E_{total} = E_{1forward} - E_{1reverse} + E_2 = 14.1\pm0.7$ kJ mol^{-1} for photoisomerization. Similarly, the internal conversion of the *cis* state encounters a larger barrier at 16.5±0.6 kJ mol^{-1} than that found for the effective barrier $E_{total} = E_{1forward} - E_{1reverse} + E_2 = 12.7\pm1.1$ kJ mol^{-1} for photoisomerization.

Our treatment addresses the thermodynamics of the total excited state decay, $k_{total} = k_{pc} + k_{IC} + k_{fl}$ and evaluates the magnitude of the barriers in light of theoretical considerations, known as Landau-Zener theory [40] and Engleman-Jortner's approach[47] to internal conversion (see section 11.2 of

supplementary materials for details). We conclude from the apparent barriers in the reactive and non-radiative pathways that internal conversion is dominated by a free rotor motion in combination with low frequency motion, which includes a combination of torsional and coupling coordinates. This model adheres to what is known as the Seidner-Domcke formalism[48]

The involvement of the double-well potential (Fig. 2) in the photoisomerization pathway was investigated from the details of the temperature dependence of kinetics (Fig 5 & Extended Data Fig. 1). In order to derive the functional significance of the double-well potential discovered from our ultrafast crystallography experiments we take advantage of the structural knowledge together with thermodynamics and kinetics information that is otherwise not accessible for explicit modelling. Both the cis(A)-trans(B) and trans-cis photoconversion showed relatively small temperature sensitivity near ambient temperatures (Fig. 5) An Arrhenius fit of the high temperature (293 K – 250 K) region retrieved values for the activation energies of 2±0.4 and 3.5±1.2 kJ/mol respectively (Fig. 5). A further lowering of the temperature dramatically reduced the kinetics in both directions resulting in convex Arrhenius behaviour (Fig 5 & Extended Data Fig. 1e,k). The modelling of temperature dependence of double-well potentials, notably involving hydrogen bonding modification, is well established and is known to result in reduced or negative activation energy since the effective barrier $E_{Total} = E_{1forward} - E_{1reverse} + E_2$ determines the overall temperature dependence and the pre-factors become the resulting combination[41,42,44,49] and will show an apparent underestimation of the apparent attempt frequency (see above). Interestingly a negative activation barrier of -5 kJ mol^{-1} was observed for the proton transfer in the Green Fluorescent Protein and modelled with a double well potential[44]. Significantly larger activation energy and pre-factors are shown for both cis-trans and trans-cis reactions (Extended Data Fig. 1h). Cryo-trapping of photoproducts after illumination at temperatures that are in low and high temperature regimes of the convex Arrhenius behaviour confirmed that cis-trans- and trans-cis photoisomerization is maintained in all cases (see above). The transition temperatures were 229 K and 208 K for cis-trans and trans-cis directions (Fig. 5). The conventional interpretation invokes the glass transition proposed by Marcus[50]. However we found that pre-converting to the trans (Extended Data Fig. 1e) state at room temperature both significantly reduced the subsequent conversion rate as well as shifting the transition temperature to higher value (236 K, Fig. 5, Right, blue series) as compared to pre-conversion at cryo temperatures. This key observation argues against the conventional glass transition models proposed for similar transition temperatures of kinetics. We therefore developed a model that involves the relaxation of the secondary, intermediate, well for both directions using a single Gibbs free energy difference. To arrive at the convex Arrhenius behaviour the fractional occupancies of intermediate states follow the enthalpy-entropy compensation such that $\Delta H = T_T \Delta S$ where T_T is the transition temperature (see above). The thermodynamics therefore connect the chemical structures with the double-well behaviour. The PDP experiment resolved the A_2 structure, whereas cryo-trapping resolved the unrelaxed B_1 for the cis state, as shown by hydrogen bonding rearrangements and a positional change of the chromophore (F_o-F_o difference map shown in Fig. 5, and see below).

Finally, we show the functional importance and physical significance of the ultrafast crystal structures and the wavepacket dynamics in the double well description for the photoisomerization reaction pathway. Specifically we connect the double well potential behaviour with the thermodynamics and observed non-Arrhenius behaviour of the photoswitching kinetics. This analysis requires precise knowledge of non-radiative transitions and the full temperature dependence of competing channels of

photochemical dynamics. The cis-trans and trans-cis photoisomerization of the fluorescent protein chromophore includes ultrafast barrier crossing and avoidance of internal conversion processes with barriers 16.5 ±0.6 & 17.0 ±0.6 kJ mol^{-1}respectively (Extended Data Fig. 1h)

We measured the temperature dependence of the fluorescence of the cis chromophore in the ON state in the high temperature region using TCSPC (7). The fluorescence was biphasic with lifetimes of 170 ps and 600 ps (@ 294 K), for which similar activation energies of 3.5 ± 0.9 and 4.0 ± 0.2 kcal mol^{-1} were determined. The statistical analysis showed these activation energies exceeded that determined for photoconversion. For analysis of the contributions to the total rate of excited state decay, $k_{total} = k_{pc} + k_{IC} + k_{ISC} + k_{fl}$ the fluorescence can be neglected at a quantum yield of 6.8 ± 0.1% and 0.49 ± 0.03% (8) for the cis and trans chromophores respectively and ISC is similarly neglected. The dominant contributions to decay are photoisomerization (k_{pc}) and internal conversion (k_{IC}). Using the Landau-Zener formulism the branching ratio at the conical intersection is found to be proportional to $\propto e^{-1/2\sqrt{T}}$ via the temperature dependence of the nuclear velocity neglecting non-equilibrium effects on the Franck-Condon excitation[35,36,40]. The Landau-Zener equation therefore predicts that the temperature dependence of a small range can be neglected. The theoretical considerations for the temperature dependence of internal conversion are previously considered specific for fluorescent proteins and assumed to be weakly temperature dependent[35]. Neglecting a temperature independent zero-point motion tunnelling contribution due to the large mass involved in transfer, the Englman-Jortner approach[36,47,51] in the weak coupling regime predicts from the energy gap law that temperature dependence is weak. Also in the strong coupling limit an activated barrier crossing behaviour is retrieved that predicts weak temperature dependence and is proportional to $\propto e^{\frac{(Ege-Er)^2}{4Er}}$ where E_{ge} and E_r are the electronic and relaxation energies. The experimental temperature dependence of fluorescence was analysed by applying the measured quantum yields of photoconversion and internal conversion, and in this manner retrieved the activation energy for E_{IC} = 16.5 ± 0.6 kJ mol^{-1} (11.3). The lowest energy solution to strong coupling term for the observed 16.5 kJ mol^{-1} barrier to internal conversion for the cis state would therefore need a 11,683 cm^{-1} relaxation energy which disfavours a strong vibronic coupling mechanism for internal conversion, following Englman-Jortner. Internal conversion is therefore considered to be dominated by a free rotor motion in combination with low frequency motion, which includes a combination of torsional and coupling coordinates in Seidner-Domcke formalism[48]. This differs from the behaviour of the isolated p-hydroxybenzylidene imidazolidinone (HBDI) chromophore in solution, for which near-barrierless internal conversion was seen at high temperatures[52]. Here we have shown that the internal conversion of the cis state encounters a larger barrier at 16.5 kJ mol^{-1} than that found for the effective barrier $E_{total} = E_{1forward} - E_{1reverse} + E_2$ = 2 kJ mol^{-1} for photoisomerization. Since spectroscopy did not find a separation of time scales within the excited state decay for the trans chromophore, a further branching in Seidner-Domcke potential separates the paths in additional coordinates beyond the model shown (Extended Data Fig. 1g & Supplementary Fig. 52). Therefore, our full analysis finds the thermodynamics and barriers of non-radiative transitions separate from photoisomerization and extends the detailed and complete thermodynamics modelling of structural dynamics of all origins on ultrafast time scales of the rsKiiro fluorescent protein.

In conclusion, we find for both the trans off state and the cis on state that the internal conversion encounters a larger barrier than that found for the effective barrier for photoisomerization. In addition,

we find a relaxation mechanism within the double well potential that results in convex Arrhenius plots for the photoisomerization reaction of both the on and off states. We also determined crystal structures for cryo-trapped intermediates in the double well potential of the on state, shown in Extended Data Figure 9. We present an unprecedented opportunity to use knowledge of ultrafast crystallography to explain and quantitatively model the thermodynamics of functional reactions, in this case the photoisomerization coordinates in both forward and reverse directions.

12. Hybrid Quantum Mechanics / Molecular Mechanics Computations

The main aim of the computations is to test the conjecture that there are two configurations, corresponding the A_1 and A_2 minima (Fig. 2), separated by a small barrier on both the electronic ground state (S_0) and excited state (S_1) potential energy surfaces. We therefore constructed initial models for A_1 and A_2 based on the differences between the resting state structure and the pump-probe structure. In the A_1 configuration (Extended Data Fig. 8a), the hydroxyl group of the chromophore donates a hydrogen bond to a water molecule, which donates hydrogen bonds to the carboxylate side chain of Glu144 and the backbone carbonyl of Gly155. In the A_2 configuration (Extended Data Fig. 8a), the hydroxyl group of the chromophore forms a direct hydrogen bond with the side chain of Glu144, while the water molecule donates a hydrogen bond to the chromophore hydroxyl.

The initial structure for these two models was the resting state X-ray structure of rsKiiro. For amino acids resolved in multiple conformations, we selected A-conformation, with the exception of His194, for which the B conformer was selected that can form additional hydrogen bonds to stabilize the chromophore pocket. In addition, the B-conformation of His194 also has a higher population in the crystal. All other missing hydrogens atoms were added with the GROMACS pdb2gmx tool. To model the interactions, we used the Amber03 Molecular Mechanics (MM) forcefield[53]. The missing chromophore parameters were obtained using the AnteChamber protocol [54].

Geometry optimizations were performed at both the MM level and the hybrid quantum mechanics / molecular mechanics (QM/MM) level with Gromacs version 4.5.5[55], in combination with the TeraChem quantum chemistry program[56]. This Gromacs/TeraChem QM/MM interface is available for download from Github (https://github.com/dmmorozo/GromacsTc).

Geometry optimization of the initial structure was performed in two steps. First, we carried out 1000 energy minimization steps at the AMBER03 force field level with L-BFGS algorithm. This MM optimization was followed by a second geometry optimization at the QM/MM level until the maximum force on any atom was below a threshold of 4 kJ/mol/nm. The QM region in these calculations consisted of the chromophore, three water molecules that are in direct hydrogen bonding contact with the chromophore, and the side chains of amino acids Arg66, Arg91, Glu144, Tyr177, His194, and Glu212. In addition, eight hydrogen link atoms were added on the chemical bonds connecting the QM and MM subsystems. The QM region thus contained 120 atoms, which are shown in ball-and-stick representation in Extended Data Fig. 8b. The QM region was modelled with Density Functional Theory (DFT), using the PBE0 functional[57] in combination with the cc-pVDZ basis set[58] and the DFT-D3 Grimme's empirical dispersion corrections[59]. To perform energy minimization in the electronic excited state, we used the Time-Dependent DFT within the Tamm-Dancoff approximation[60].

To locate the transition state between the A_1 and A_2 conformations on both ground (S_0) and excited (S_1) states an interpolation procedure was used. First, we interpolated the geometry from A_1 to A_2. Then, for each interpolation point, the geometry was optimized using constraints on the distances (i) between the chromophore phenol oxygen and the carboxylate of Glu144, (ii) between the chromophore phenol oxygen atoms and the water molecule, and (iii) between the carboxylate of Glu144 and the water molecules. The constrained distances are indicated by the dashed red lines in Extended Data Fig. 8b. Even if this setup does not guarantee that the lowest energy transitions state is found, the geometry with the lowest potential energy can be considered an upper bound to the actual transitions state.

An energy diagram based on the energies of the optimized (local) minima and transition states in both the S_0 and S_1 electronic states, is shown in Extended Data Fig. 8c. The results of the QM/MM optimizations suggest that there are indeed two energy minima, which we assign to the A_1 and A_2 conformations. In S_0 the A_1 conformation is more stable than the A_2 conformation by 8.97 kJ/mol. In S_1 the order reverses and the energy of the A_2 conformation is 7.98 kJ/mol below that of the A_1 conformation. The barriers connecting these minima are 38.11 and 21.16 kJ/mol in the ground and excited state, respectively. While the calculated barriers would be too high to account for ultrafast transitions between A_1 and A_2, we emphasize that the barriers are upper bound estimates.

To compare with spectroscopic data, we also computed the absorption and emission wavelengths at the XMCQDPT2[61] multiconfigurational correlated level of theory. These calculations were performed with the Firefly[62] package. The CASSCF reference wavefunction for the XMCQDPT2 calculations was based on an active space with 12 electrons distributed over 11 π-orbitals on the chromophore and was averaged over the five lowest singlet states. In these calculations, the rest of the protein was included as MM point charges that can polarize the QM wave function. The results of these XMCQDPT2/SA5-CASSCF(12,11)/cc-pVDZ//Amber03 QM/MM computations suggest a Stokes shift of 0.67 eV in the A_1 conformation and 0.77 eV in the A_2 conformation. These values are in line with the energy differences between the pump and probe pulses.

13. Density Matrix Simulations & Wigner Phase Space Analysis

To compliment the experimental findings non-perturbative density matrix simulations were performed. This simulation demonstrates a proof of principle, that vibrational coherence in an excited electronic state can be transferred to a lower energy electronic state via a dump interaction. A Wigner phase space analysis of the density matrix for the model system was used to elucidate the coherence and population dynamics of the system.

The density matrix formalization is useful for describing the statistical state at which a quantum mechanical system is in. The density matrix encodes information on the populated states through the diagonal elements of the matrix. The interaction of a system with an electric field on the coherent timescale will excite multiple states coherently and is experimentally visible in oscillations in the transient signal. These coherences between states are encoded in the off-diagonal elements of the density matrix. Off-diagonal elements between states in the same electronic level represent vibrational coherence whereas those that occur between electronic states characterize electronic coherence. As such the density matrix formalization allows for the observation of population and coherence.

A four-level system was used as a simple model of the rsKiiro fluorescent protein. Containing two vibrational states in both a ground and excited electronic state with the vibrational frequency set to 170 cm^{-1} for both levels. The excited state levels were set such that the 400 nm experimental pump could populate both vibrational levels of the excited state ($|2\rangle$ & $|3\rangle$) from, predominately, the vibrationally cold ground electronic state ($|0\rangle$) (Supplementary Fig. 53). The dump pulse carrier frequency was selected to maximize the dump population efficiency and is red shifted from the pump pulse.

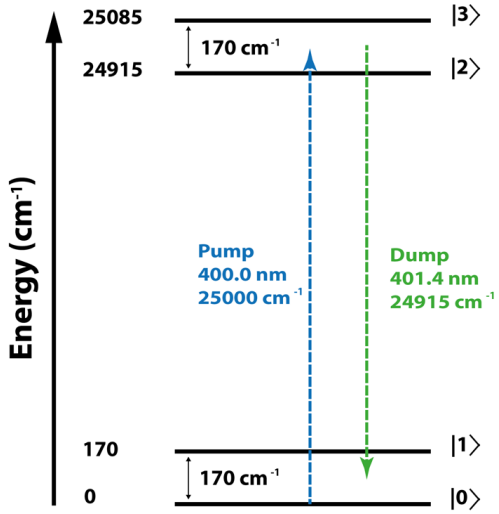

Supplementary Fig. 53 | Energy level diagram of four level system used to simulate coherence and population dynamics in rs-Kiiro protein.

The four-level (16 element) density matrix simulation evolves under the Liouville von Neumann equation, with a Hamiltonian that can be deconstructed into three separate contributions: An unperturbed term which describes the energy of the system, a perturbed term which contains the perturbation due to the laser(s) electric field(s) and a final relaxation term which describes the population dynamics of the system. A full derivation of the density matrix formulation is shown later. The time dependent density matrix elements evolve via the following rate equations where the off-diagonal elements ρ_{ij} are the coherence between states and diagonal elements ρ_{ii} are the population in that respective state, where

$\sum \rho_{ii} = 1$. $\omega_{ij} = \frac{|\varepsilon_i - \varepsilon_i|}{\hbar}$ are the transition frequencies between states i and j with energies $\varepsilon_{i,j}$. E is the time dependent electric field of the laser pulse(s) and μ_{ij} is the transitional dipole moment between states i and j. $\bar{\Gamma}_{ij}$ is the off-diagonal decay rate, defined as $\bar{\Gamma}_{ij} = \frac{(\gamma_{ii} + \gamma_{jj})}{2} + \Gamma_{ij}$, where γ_{ii} is the decay rate of state i and Γ_{ij} is the pure dephasing rate of the coherence between i and j. All rates are defined as the inverse of the decay/dephasing time e.g. $\Gamma_{ij} = T_{ij}^{-1}$, where T_{ij} is the dephasing time between states i and j.

Off-diagonal elements rate equations:

$$\dot{\rho}_{01} = -\bar{\Gamma}_{01}\rho_{01} + i\omega_{10}\rho_{01} + \frac{iE}{\hbar}(\mu_{02}\rho_{21} + \mu_{03}\rho_{31} - \mu_{12}\rho_{20} - \mu_{13}\rho_{30}) \quad \text{(S34)}$$

$$\dot{\rho}_{02} = -\bar{\Gamma}_{02}\rho_{02} + i\omega_{20}\rho_{02} + \frac{iE}{\hbar}(\mu_{02}(\rho_{22} - \rho_{00}) + \mu_{03}\rho_{32} - \mu_{12}\rho_{01}) \quad \text{(S35)}$$

$$\dot{\rho}_{03} = -\bar{\Gamma}_{03}\rho_{03} + i\omega_{30}\rho_{03} + \frac{iE}{\hbar}(\mu_{03}(\rho_{33} - \rho_{00}) + \mu_{02}\rho_{23} - \mu_{13}\rho_{01}) \quad \text{(S36)}$$

$$\dot{\rho}_{12} = -\bar{\Gamma}_{12}\rho_{12} + i\omega_{21}\rho_{12} + \frac{iE}{\hbar}(\mu_{12}(\rho_{22} - \rho_{11}) + \mu_{13}\rho_{32} - \mu_{02}\rho_{10}) \quad \text{(S37)}$$

$$\dot{\rho}_{13} = -\bar{\Gamma}_{13}\rho_{13} + i\omega_{31}\rho_{13} + \frac{iE}{\hbar}(\mu_{13}(\rho_{33} - \rho_{11}) + \mu_{12}\rho_{23} - \mu_{03}\rho_{10}) \quad \text{(S38)}$$

$$\dot{\rho}_{23} = -\bar{\Gamma}_{23}\rho_{23} + i\omega_{32}\rho_{23} + \frac{iE}{\hbar}(\mu_{02}\rho_{03} + \mu_{12}\rho_{13} - \mu_{03}\rho_{20} - \mu_{13}\rho_{21}) \quad \text{(S39)}$$

$$\bar{\Gamma}_{ij} = \frac{(\gamma_{ii} + \gamma_{jj})}{2} + \Gamma_{ij} \quad \text{(S40)}$$

Diagonal elements rate equations:

$$\dot{\rho}_{11} = -\gamma_{11}\rho_{11} + \gamma_{12}\rho_{22} + \gamma_{13}\rho_{33} + \frac{iE}{\hbar}\big(\mu_{12}(\rho_{21} + \rho_{12}) + \mu_{13}(\rho_{31} - \rho_{13})\big) \quad \text{(S41)}$$

$$\dot{\rho}_{22} = -\gamma_{22}\rho_{22} + \gamma_{23}\rho_{33} + \frac{iE}{\hbar}\big(\mu_{02}(\rho_{02} + \rho_{20}) + \mu_{12}(\rho_{12} - \rho_{21})\big) \quad \text{(S42)}$$

$$\dot{\rho}_{33} = -\gamma_{33}\rho_{33} + \frac{iE}{\hbar}\big(\mu_{03}(\rho_{03} - \rho_{30}) + \mu_{13}(\rho_{13} - \rho_{31})\big) \quad \text{(S43)}$$

$$\dot{\rho}_{00} = -\dot{\rho}_{11} - \dot{\rho}_{22} - \dot{\rho}_{33} \quad \text{(S44)}$$

The electric field was simulated as transform limited Gaussian pulse $\tilde{E}_0(\omega)$ which is spectrally shaped via a spectral phase transfer function $\varphi(\omega)$.

$$\tilde{E}(\omega) = \tilde{E}_0(\omega)\exp\big(i\varphi(\omega)\big) \quad \text{(S45)}$$

The spectral phase transfer function is a Taylor polynomial where the first order constant b determines the temporal position of the pulse and the second order constant c is the spectral chirp of the pulse.

$$\varphi(\omega) = a(\omega_0) + b\big(\omega_0(\omega - \omega_0)\big) + \frac{c}{2}(\omega_0(\omega - \omega_0)^2) + \frac{d}{6}(\omega_0(\omega - \omega_0)^3) \ldots \quad \text{(S46)}$$

The simulated time-dependent density matrix was then analyzed by a Wigner transform, to give the probability distribution in phase space. The Wigner function yields a classical like distribution, quantifying the probability of finding the system with momentum q and position p. This classical representation of a quantum mechanical system is an approximation, as Heisenberg's uncertainty

principle forbids simultaneous measurement of momentum and position. Such the function is a quasiprobability distribution and can be negative.

Computing the Wigner function allows a topographical representation to be constructed. These 3-dimensional representations of position, momentum and the Wigner quasi-probability distributions allow a visual representation of the population and coherence dynamics of the system constructed from the density matrix. The plots materialize as a superposition of individual Fock states, if coherence (off-diagonal) elements are absent the plots are spherically symmetric. In this case the Wigner distribution of that system, is a linear combination of the individual Fock states. The coherence between states is observed as spherical asymmetries in the plots, where the number of lines of symmetry is equal to the number difference between the Fock states which that coherence is observed. Such a coherence between state $|3\rangle$ and $|1\rangle$ the Wigner distribution would have two (3-1) lines of symmetry. The coherence amplitude is proportional to the relative spherical difference in the plot. These properties of the Wigner function allow the separation of plots for different electronic states if electronic coherence is ignored. A full derivation of the computational Wigner function follows.

13.1. Density Matrix Simulations

The following is a full derivation of the formulization of the non-perturbative, time-dependent density simulations. This code was written by the Buckup Group in Heidelberg University[63,64].

Schrödinger Equation for evolution of wavefunction $|\psi(t)\rangle$:

$$i\hbar\frac{d}{dt}|\psi(t)\rangle = H(t)|\psi(t)\rangle \tag{S47}$$

Deriving the Louisville-Von Neumann Equation by product rule:

$$\frac{d}{dt}\underbrace{\rho(t)}_{|\psi(t)\rangle\langle\psi(t)|} = \underbrace{\left(\frac{d}{dt}|\psi(t)\rangle\right)}_{\frac{-i}{\hbar}H|\psi(t)\rangle}\langle\psi(t)| + |\psi(t)\rangle\underbrace{\left(\frac{d}{dt}\langle\psi(t)|\right)}_{\frac{i}{\hbar}\langle\psi(t)|H}$$

$$\frac{d}{dt}\rho(t) = \frac{-i}{\hbar}H\underbrace{|\psi(t)\rangle\langle\psi(t)|}_{\rho(t)} + \frac{i}{\hbar}\underbrace{|\psi(t)\rangle\langle\psi(t)|}_{\rho(t)}H = \frac{-i}{\hbar}[H,\rho(t)]$$

$$i\hbar\frac{d}{dt}\rho(t) = [H(t),\rho(t)] \tag{S48}$$

The total Hamiltonian is expressed in the three terms: an unperturbed term, the perturbed term which contains the perturbation due to the laser and a final term which describes the relaxation of the system:

$$i\hbar\frac{d}{dt}\rho(t) = [H_0(t),\rho(t)] + [H_I(t),\rho(t)] + [H_R(t),\rho(t)] \tag{S49}$$

The unperturbed term contains the energy of the system without any interaction and is a diagonal matrix:

$$H_0(t) = \hbar\begin{bmatrix}\omega_0 & 0 & \cdots & 0\\ 0 & \omega_1 & \cdots & 0\\ \vdots & \vdots & \ddots & \vdots\\ 0 & 0 & \cdots & \omega_n\end{bmatrix} \tag{S50}$$

$$[H_0(t),\rho(t)] = -\hbar\begin{bmatrix}0 & \omega_{0,1}\cdot\rho_{0,1}(t) & \cdots & \omega_{0,n}\cdot\rho_{0,n}(t)\\ \omega_{1,0}\cdot\rho_{1,0}(t) & 0 & \cdots & \omega_{1,n}\cdot\rho_{1,n}(t)\\ \vdots & \vdots & \ddots & \vdots\\ \omega_{n,0}\cdot\rho_{n,0}(t) & \omega_{n,1}\cdot\rho_{n,1}(t) & \cdots & 0\end{bmatrix} \tag{S51}$$

The interaction term describes the coupling of the laser field with electronic coherence via the transition dipole moments:

$$H_I(t) = \begin{bmatrix} 0 & \vec{\mu}_{0,1} \cdot \vec{E}(t) & \cdots & \vec{\mu}_{0,n} \cdot \vec{E}(t) \\ \vec{\mu}_{1,0} \cdot \vec{E}(t) & 0 & \cdots & \vec{\mu}_{1,n} \cdot \vec{E}(t) \\ \vdots & \vdots & \ddots & \vdots \\ \vec{\mu}_{n,0} \cdot \vec{E}(t) & \vec{\mu}_{n,1} \cdot \vec{E}(t) & \cdots & 0 \end{bmatrix} \quad \text{(S52)}$$

Noting $\vec{\mu}_{i,j} = \vec{\mu}_{j,i}$

$$[H_I(t), \rho(t)] = -\vec{E}(t) \begin{bmatrix} \sum_{i\neq 0}^{n} \vec{\mu}_{0,i}(\rho_{0,i}(t) - \rho_{i,0}(t)) & \vec{\mu}_{0,1}(\rho_{0,0}(t) - \rho_{1,1}(t)) + \sum_{i\neq 0,1}^{n} (\vec{\mu}_{i,1} \cdot \rho_{0,i}(t) - \vec{\mu}_{0,i} \cdot \rho_{i,1}(t)) & \cdots & \vec{\mu}_{0,n}(\rho_{0,0}(t) - \rho_{n,n}(t)) + \sum_{i\neq 0,n}^{n} (\vec{\mu}_{i,n} \cdot \rho_{0,n}(t) - \vec{\mu}_{0,n} \cdot \rho_{i,n}(t)) \\ \vec{\mu}_{1,0}(\rho_{1,1}(t) - \rho_{0,0}(t)) + \sum_{i\neq 1,0}^{n} (\vec{\mu}_{i,0} \cdot \rho_{1,i}(t) - \vec{\mu}_{1,i} \cdot \rho_{i,0}(t)) & \sum_{i\neq 1}^{n} \vec{\mu}_{1,i}(\rho_{1,i}(t) - \rho_{i,1}(t)) & \cdots & \vec{\mu}_{1,n}(\rho_{1,1}(t) - \rho_{n,n}(t)) + \sum_{i\neq 1,n}^{n} (\vec{\mu}_{i,n} \cdot \rho_{1,i}(t) - \vec{\mu}_{1,i} \cdot \rho_{i,n}(t)) \\ \vdots & \vdots & \ddots & \vdots \\ \vec{\mu}_{n,0}(\rho_{n,n}(t) - \rho_{0,0}(t)) + \sum_{i\neq n,0}^{n} (\vec{\mu}_{i,0} \cdot \rho_{n,i}(t) - \vec{\mu}_{n,i} \cdot \rho_{i,0}(t)) & \vec{\mu}_{n,1}(\rho_{n,n}(t) - \rho_{1,1}(t)) + \sum_{i\neq n,1}^{n} (\vec{\mu}_{i,1} \cdot \rho_{n,i}(t) - \vec{\mu}_{n,i} \cdot \rho_{i,1}(t)) & \cdots & \sum_{i\neq n}^{n} \vec{\mu}_{n,i}(\rho_{n,i}(t) - \rho_{i,n}(t)) \end{bmatrix}$$

The relaxation term is described phenomenologically as populations decay times ($1/T_{ii}$) for the diagonal terms and coherence times ($1/T_{ij}$) for the off-diagonal terms:

$$[H_R(t), \rho(t)] = i\hbar \begin{bmatrix} 1/T_{0,0} \cdot \rho_{0,0}(t) & -1/T_{0,1} \cdot \rho_{0,1}(t) & \cdots & -1/T_{0,n} \cdot \rho_{0,n}(t) \\ -1/T_{1,0} \cdot \rho_{1,0}(t) & -1/T_{1,1} \cdot \rho_{1,1}(t) & \cdots & -1/T_{1,n} \cdot \rho_{1,n}(t) \\ \vdots & \vdots & \ddots & \vdots \\ -1/T_{n,0} \cdot \rho_{n,0}(t) & -1/T_{n,1} \cdot \rho_{n,1}(t) & \cdots & -1/T_{n,n} \cdot \rho_{n,n}(t) \end{bmatrix} \quad \text{(S53)}$$

13.2. Wigner Phase Space Analysis

The following is a full derivation of how a numerical algorithm that can calculate the Wigner quasi-probability distribution of a system from the time dependent density matrix. The Laguerre polynomial method for calculating the Wigner function was used, courtesy of the open source Quantum Toolbox in Python (QUTIP) package[65]. Derivation is adapted from "Measuring the Quantum State of Light" Ulf Leonhardt[66]. Expressing the density matrix in the Fock basis, where M is the number of states (energy levels) in the system:

$$\hat{\rho} = \sum_{m,n=0}^{M} \rho_{mn} |m\rangle\langle n| \quad \text{(S54)}$$

Inserting into the Fock basis expansion of the density matrix into Wigner's formula yields:

$$W(q,p) = \sum_{m,n=0}^{M} \rho_{mn} W_{mn}(q,p) \quad \text{(S55)}$$

With:

$$W_{mn}(q,p) = \frac{1}{\pi} \int_{-\infty}^{+\infty} \exp(2ipx) \langle q - x \mid m \rangle \langle n \mid q + x \rangle dx \quad \text{(S56)}$$

Schrodinger's wave functions are off for odd states and even for even states such we obtain an expression for $W_{mn}(q,p)$:

$$W_{mn}(q,p) = \frac{(-1)^m}{\pi}\int_{-\infty}^{+\infty} \exp(2ipx)\langle x-q \mid m\rangle\langle n \mid x+q\rangle dx \tag{S57}$$

This function for $W_{mn}(q,p)$ is equivalent to the Fourier-transformed distribution, $\tilde{W}_{mn}$, known as the characteristic function:

$$W_{mn}(q,p) = \frac{(-1)^m}{\pi}\tilde{W}_{mn}(-2p,2q) \tag{S58}$$

The characteristic function can be expressed in polar coordinates $\exp(-ip\hat{q} - iq\hat{p})$:

$$\begin{aligned} W_{mn}(q,p) &= \frac{(-1)^m}{\pi}\mathrm{tr}\{|m\rangle\langle n|\exp(2ip\hat{q} - 2iq\hat{p})\} \\ &= \frac{(-1)^m}{\pi}\langle n|\exp(2ip\hat{q} - 2iq\hat{p})|m\rangle \\ &= \frac{(-1)^m}{\pi}\langle n|\hat{D}(2\alpha)|m\rangle \end{aligned} \tag{S59}$$

Where the complex amplitude (α) can be decomposed into a real an imaginary component $\alpha = 2^{-1/2}(q + ip)$ and $\hat{D}$ is the Hermitian displacement operator. Expressing the displacement operator in the form of the Baker-Hausdorff formula and expanding using the following property for the creation and annihilation operator of Fock States:

$$\hat{a}^v|n\rangle = \left[\frac{n!}{(n-v)!}\right]|n-v\rangle \tag{S60}$$

$$\begin{aligned} \langle n|\hat{D}(2\alpha)|m\rangle = \quad & \exp(-2|\alpha|^2)\sum_{v=0}^{n}\sum_{\mu=0}^{m}(2\alpha)^v(-2\alpha^*)^\mu \\ & \times\frac{1}{v!\,\mu!}\left[\frac{n!\,m!}{(n-v)!\,(m-\mu)!}\right]^{1/2} \\ & \times\langle n-v \mid m-\mu\rangle \end{aligned} \tag{S61}$$

Using the orthonormal properties of Fock states, the double sum is reduced to a single sum with a polynomial of $|\alpha|^2$. Employing Laguerre polynomials L_m^k, the displacement operator reduces to:

For $m \geq n$

$$\langle n|\hat{D}(2\alpha)|m\rangle = \left(\frac{n!}{m!}\right)^{1/2}\exp(-2|\alpha|^2)(-2\alpha^*)^{m-n}L_n^{m-n}(4|\alpha|^2) \tag{S62}$$

And for $m < n$

$$\langle n|\hat{D}(2\alpha)|m\rangle = \langle m|\hat{D}(-2\alpha)|n\rangle^* \tag{S63}$$

Recasting q and p in phase space polar coordinates r and φ:

$$q = r\cos\varphi, p = r\sin\varphi$$

Such $\alpha = 2^{-1/2}\, r\exp(-i\varphi)$ and expanding Equation (S55), where $k = m - n$:

$$W(q,p) = \sum_{k=-M}^{M} w(r,k)\exp(-ik\varphi) \tag{S64}$$

With

$$w(r,k) = \begin{cases} \sum_{n=0}^{M-k} w_n(r,k)\rho_{n+k,n} & \text{for } k \geq 0 \\ w(r,-k)^* & \text{for } k < 0 \end{cases} \quad \text{(S65)}$$

And

$$w_n(r,k) = \frac{1}{\pi}(-1)^n \left[\frac{n!}{(n+k)!}\right]^{1/2} \exp(-r^2)(r\sqrt{2})^k L_n^k(2r^2) \quad \text{(S66)}$$

The above can be calculated numerically as the recurrence relation of Laguerre polynomials allows $w_n(r,k)$ to be expressed as:

$$w_n(r,k) = \frac{1}{\sqrt{n(n+k)}}[(2r^2+1-k-2n)w_{n-1}(r,k) - \sqrt{(n-1)(n-1+k)}w_{n-2}(r,k)] \quad \text{(S67)}$$

With the initial value of recurrence:

$$w_0(r,k) = \frac{1}{\pi}(k!)^{-1/2}(r\sqrt{2})^k \exp(-r^2) \quad \text{(S68)}$$

$$w_0(0,0) = \frac{1}{\pi} \quad \text{(S69)}$$

and

$$w_{-1}(r,k) = 0 \quad \text{(S70)}$$

Such the $w_n(r,k)$ function in summation of Equation (S65) is efficiently calculated *en passant*. Defining a phase space projection over which the algorithm can compute the Wigner function allow a topographical representation to be constructed. These 3-dimensional representations of position, momentum and the Wigner quasi-probability distributions allows a visual representation of the population and coherence dynamics of the system constructed from the density matrix.

13.3. Simulation Parameters

Simulation parameters chosen to best replicate the experimental values, such that the population and moreover the coherence dynamics were representative of rsKiiro's are shown in Supplementary Table. 11. The electronic and vibrational coherence was presumed to have a dephasing time of 100 fs (Supplementary Table. 1) and 1 ps[67]. The excited state lifetime was set to the experimentally measured 50 ps and a vibrational relaxation time of 1 ps for both ground and excited states[67]. The initial state populations were thermally populated with a Boltzmann distribution at 298 K. The full width half maximum of the Gaussian laser electric fields matched the experimentally used 100 fs for both the pump and dump pulses. The peak amplitude of the laser pulse was arbitrarily set at 5 x 10^7 V m^{-1} and the transition dipole moments to 4.2 x 10^{-29} C m for a maximum excitation efficiency in pumping.

Supplementary Table. 11 | Density matrix simulation parameters.

Parameter		Value
Dephasing of coherence	Electronic $(\Gamma_{el})^{-1}$	100 fs
	Vibrational $(\Gamma_{el})^{-1}$	1 ps
Decay rates	$\|0,1\rangle \rightarrow \|0,0\rangle$ $(\gamma_{01})^{-1}$	1 ps
	$\|1,0\rangle \rightarrow \|0,1\rangle$ $(\gamma_{21})^{-1}$	20 ps
	$\|1,1\rangle \rightarrow \|1,0\rangle$ $(\gamma_{32})^{-1}$	1 ps
Starting populations in states at 298 k, thermally populated	$\|0\rangle$	0.69
	$\|1\rangle$	0.31
	$\|2\rangle$	4.0×10^{-53}
	$\|3\rangle$	1.7×10^{-53}
Transition dipole moment	μ	4.20×10^{-29} C m
Peak amplitude of laser electric field	Pump	5×10^{7} V m^{-1}
	Dump	5×10^{7} V m^{-1}
Duration of Gaussian laser pulse		
	Pump	100 fs
	Dump	100 fs
Dump delay time		350 fs

Transition dipole moment coupling coefficient matrix, for dipole allowed transitions:

$$\begin{array}{c} \\ |0\rangle \\ |1\rangle \\ |2\rangle \\ |3\rangle \\ \\ \end{array} \begin{array}{c} \begin{array}{cccc} |0\rangle & |1\rangle & |2\rangle & |3\rangle \end{array} \\ \begin{bmatrix} 0 & 0 & \mu & \mu \\ 0 & 0 & \mu & \mu \\ \mu & \mu & 0 & 0 \\ \mu & \mu & 0 & 0 \end{bmatrix} \end{array}$$

Coherence dephasing matrix:

$$\begin{array}{c} \\ |0\rangle \\ |1\rangle \\ |2\rangle \\ |3\rangle \\ \\ \end{array} \begin{array}{c} \begin{array}{cccc} |0\rangle & |1\rangle & |2\rangle & |3\rangle \end{array} \\ \begin{bmatrix} 0 & \Gamma_{vib} & \Gamma_{el} & \Gamma_{el} \\ \Gamma_{vib} & 0 & \Gamma_{el} & \Gamma_{el} \\ \Gamma_{el} & \Gamma_{el} & 0 & \Gamma_{vib} \\ \Gamma_{el} & \Gamma_{el} & \Gamma_{vib} & 0 \end{bmatrix} \end{array}$$

Decay rates between states:

$$\begin{array}{c} \\ |0\rangle \\ |1\rangle \\ |2\rangle \\ |3\rangle \\ \\ \end{array} \begin{array}{c} \begin{array}{cccc} |0\rangle & |1\rangle & |2\rangle & |3\rangle \end{array} \\ \begin{bmatrix} 0 & \gamma_{01} & 0 & 0 \\ 0 & \gamma_{11} & \gamma_{21} & 0 \\ 0 & 0 & \gamma_{22} & \gamma_{32} \\ 0 & 0 & 0 & \gamma_{33} \end{bmatrix} \end{array}$$

Where $\gamma_{01} = \gamma_{11}, \gamma_{21} = \gamma_{22}$ and $\gamma_{32} = \gamma_{33}$

13.4. Pump vs Pump-Dump scheme

Time evolution of diagonal elements of the density matrix are plotted in Supplementary Fig. 54. Time evolution of diagonal elements of the density matrix are plotted in Supplementary Fig. 55. Initially both $|0\rangle$ and $|1\rangle$ are thermally populated, some small population relaxation to the vibrational cold state occurs pre pump pulse due to rate equations. Upon excitation with pump laser pulse both electronic excited states $|2\rangle$ and $|3\rangle$ are populated. In the pump only scheme a gradual decay of 1 ps for both electronic states back to the vibrationally cold states is observed. The long-lived excited state (~20 ps) shows no substantial decay back to ground state over the duration of the simulation. The dump pulse predominately transfers from $|3\rangle \rightarrow |1\rangle$ and $|2\rangle \rightarrow |1\rangle$, in line with schematic level diagram of the simulation Supplementary Fig. 53. Summation of the diagonal elements of states in the same electronic level are shown in Supplementary Fig. 55. The dump efficiency differs from the experimentally observed complete dumping, due to the limited vibrational levels used in the simulation.

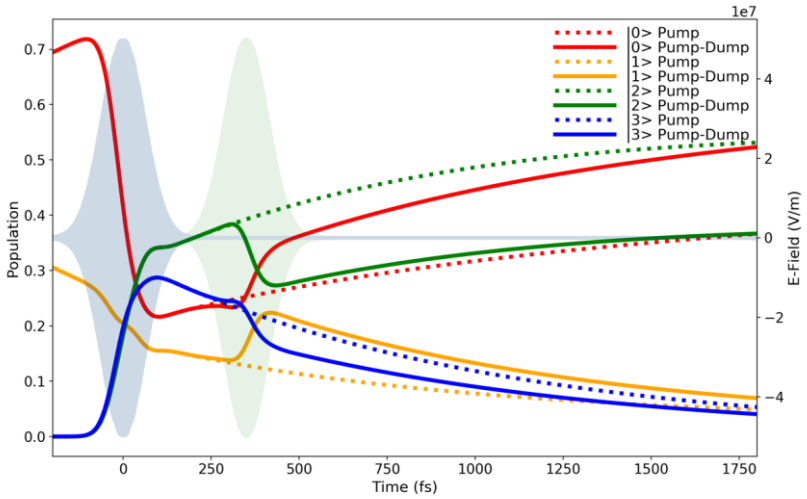

Supplementary Fig. 54 | Time evolution of diagonal elements of the density matrix calculation. Diagonal elements of the four states show the population dynamics in the pump (dotted) and pump-dump (solid) scheme. The pale blue and green Gaussians show the real part of the laser electric field with a pump-dump delay of 350 fs. Population is initially in a thermal distribution in states |0> and |1> before being excited to both the |2> and |3> states by the pump pulse. The dump pulse facilitates a population transfer back down to ground electronic state.

The vibrational coherence between states in the same electronic level is shown in Supplementary Fig. 56. The modulus of the complex off-diagonal elements is depicted for both ground state in yellow ($|0,1\rangle$) and excited state in red. Coherence is initially generated in both ground and excited states by the pump pulse. The creation of ground state impulsive coherence in the (near-)resonant case is in the direction of the nuclear binding force. The excited state coherence is displacement driven.

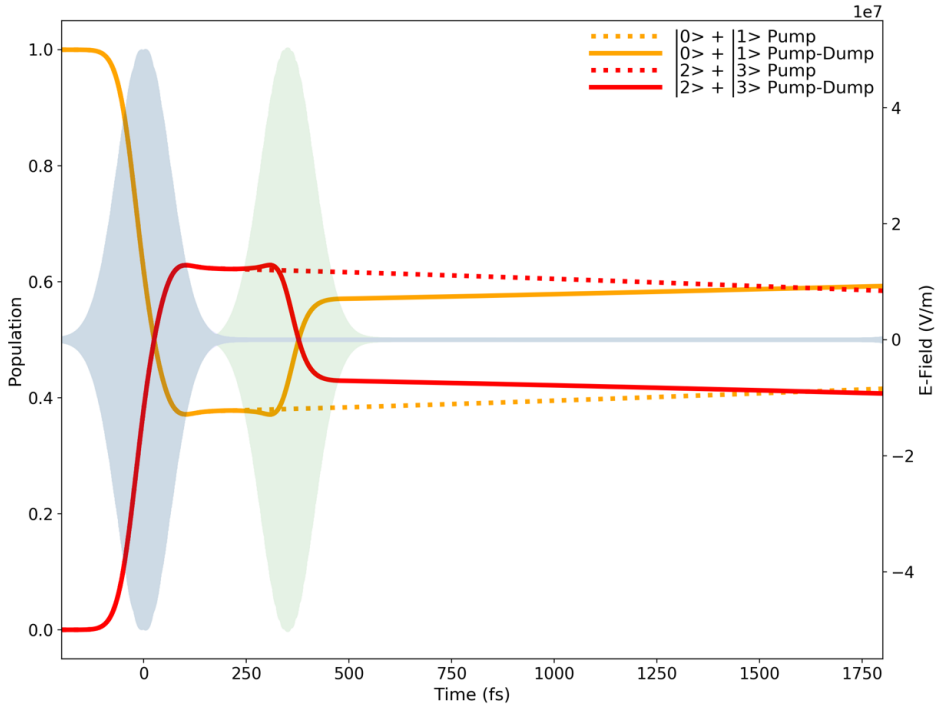

Supplementary Fig. 55 | Summation of the diagonal elements of states in the same electronic level. Ground state (yellow) |0> + |1> and excited state (red) |2> + |3>, shown for both pump (dotted) and pump-dump (solid) schemes. The pale blue and green Gaussians show the real part of the laser electric field with a pump-dump delay of 350 fs.

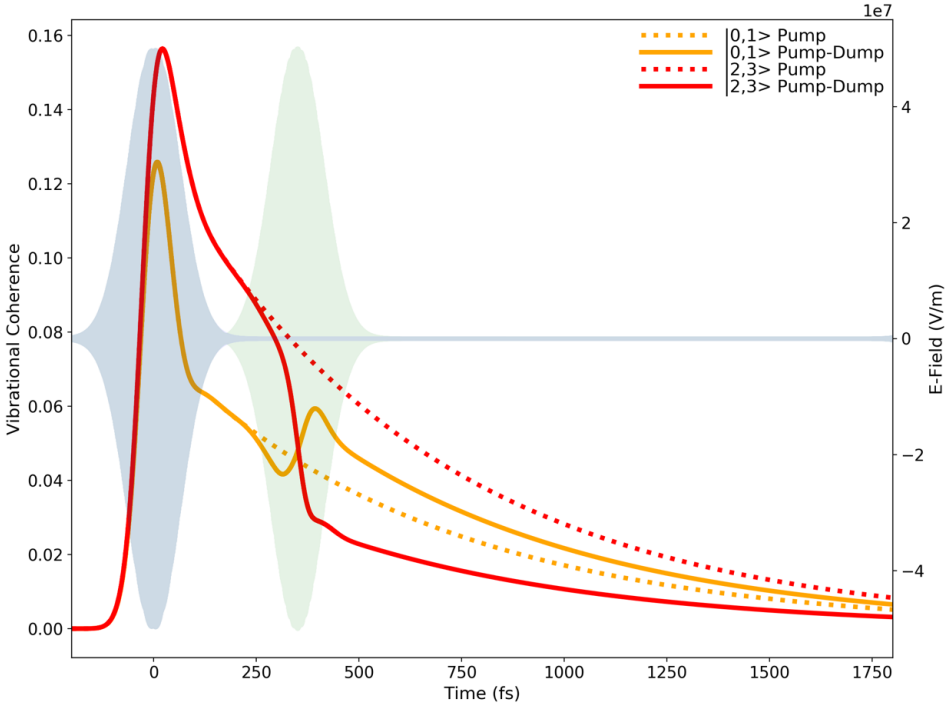

Supplementary Fig. 56 | Modulus of the off-diagonal elements show coherence between states in the same electronic level. Ground state vibrational coherence (|0,1>) shown in yellow and excited state vibrational coherence (|2,3>) shown in red for both pump (dotted) and pump-dump schemes (solid). The pale blue and green Gaussians show the real part of the laser electric field with a dump delay of 350 fs.

The dump pulse within the vibrational dephasing time facilitates a transfer of the coherent momentum in the excited state to the ground state. A sharp decline in the excited state coherence is observed within the timescale of the dump pulse and an increase in ground state coherence, compared with the no dump interaction. The remaining coherence in the excited state is due to the sub-optimal population transfer. It is noted that shorter pulses, imparting more vibrational coherence momentum in the pump case and produced a more effective coherence transfer.

A transfer of vibrational coherence from the excited electronic state to the ground electronic state is observed facilitated by the dump laser pulse.

The Wigner transforms for both experimental laser schemes are shown in Supplementary Fig. 57. The electronic coherence for ground and excited state Wigner plots have been neglected. The system can be deconstructed into components from the excited and ground states, these Wigner plots are shown. The full system can be seen to be a linear combination of the two electronic states minus the electronic coherent interactions, which have been ignored in the individual state plots. The effect of the electronic coherence can be observed in the full system plots centred on the two laser pulses. Fine structure can be observed in these plots as a superposition of many asymmetric coherence nodes, this fine structure quickly dissipates over the electronic dephasing time (~ 100 fs).

Population of the states can be observed by the amplitude of the Wigner plots. The dump population transfer is distinguished by the increase in the ground state amplitude and a decrease in the excited state, compared to the pump scheme.

The coherence in the states is displayed in the spherical asymmetry of the plots. The rotation of these nodes matches that of the vibrational frequency. In the pump scheme we see an initial large asymmetric node generated in both the ground and excited state. At longer times we see a gradual decay of the asymmetry until a spherically symmetric representation is formed, characteristic of a coherently cold state. The rate of the asymmetric node dissipating to a symmetric plot is characteristic of the vibrational dephasing rate.

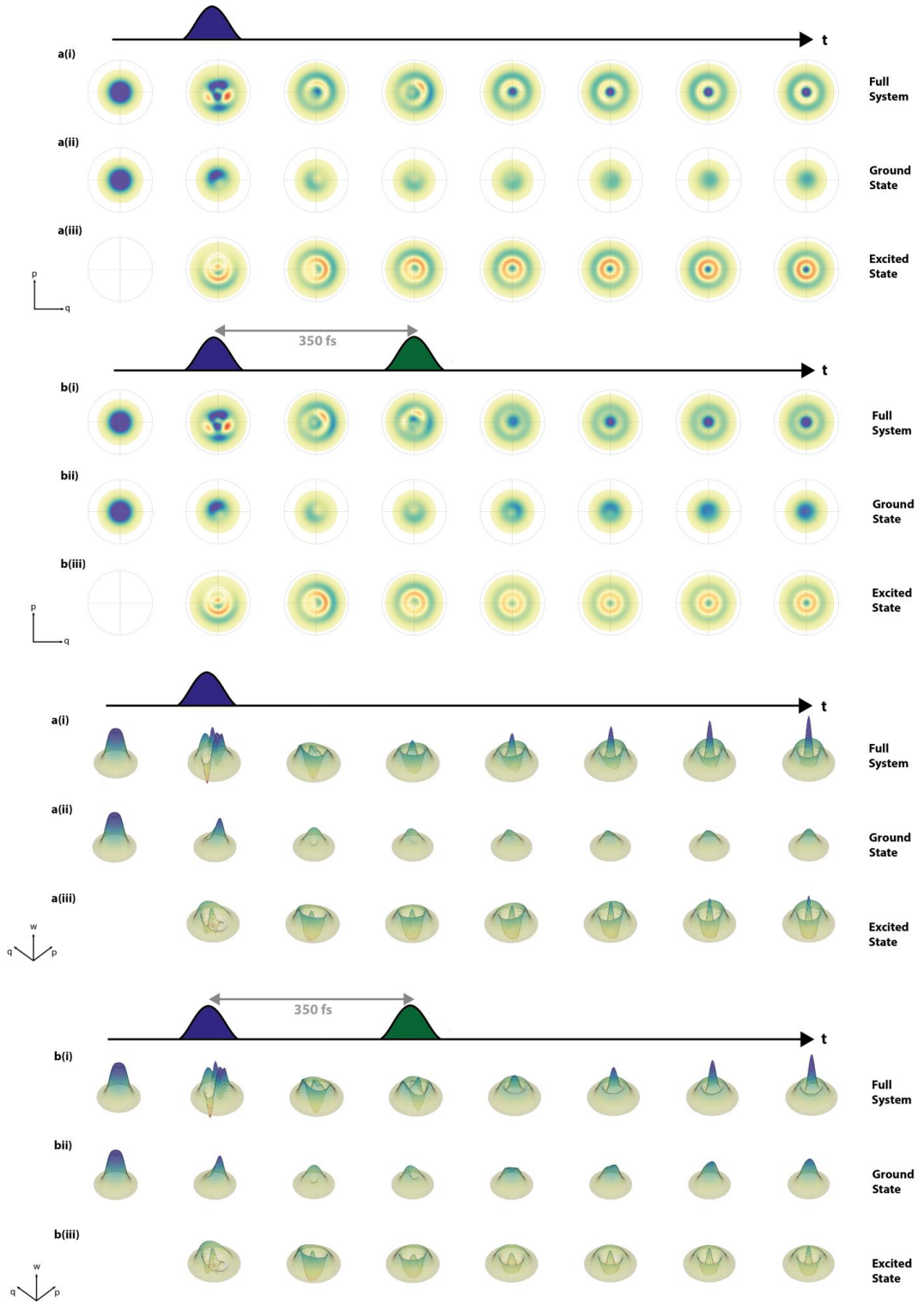

Supplementary Fig. 57 | Pump-probe and pump-dump-probe Wigner plots. Contour (top) and surface (bottom) plots of Wigner functions of the full system (i), ground electronic states (ii) and excited electronic states (iii), for both pump (a) and pump-dump (b) schemes at various time delays. The separated ground and excited state plots neglect electronic coherence, such structure can be observed beyond that of a superposition of the GS and ES plots. The electronic coherence decays with a time of 100 fs such beyond this after the pulse the remaining coherence in purely vibrational. The Wigner plots are shown at 175 fs intervals. Absolute scale has been used throughout all plots for the colour maps.

The coherent transfer of the dump is observed as a reduction in the asymmetry of the excited state Wigner plot and increase in asymmetry of the ground state. Such the ground state has a more pronounced node in the dump scheme and the opposite is true for the excited state.

The coherent dynamics around the dump pulse are examined in Supplementary Fig. 58. The ground state coherence transfer is observed after the peak of the laser pulse. In the first half the laser pulse a decrease in coherence is observed in the 300 fs Wigner plot. This coincides with a slight increase in excited state population observed in 300 fs, see Supplementary Fig. 55. Beyond this time, a large increase in coherence is observed over the cycle of the laser pulse. The prevalence is shown in the enhancement of the asymmetry observed between a(i) and a(ii) after the centre of the dump pulse.

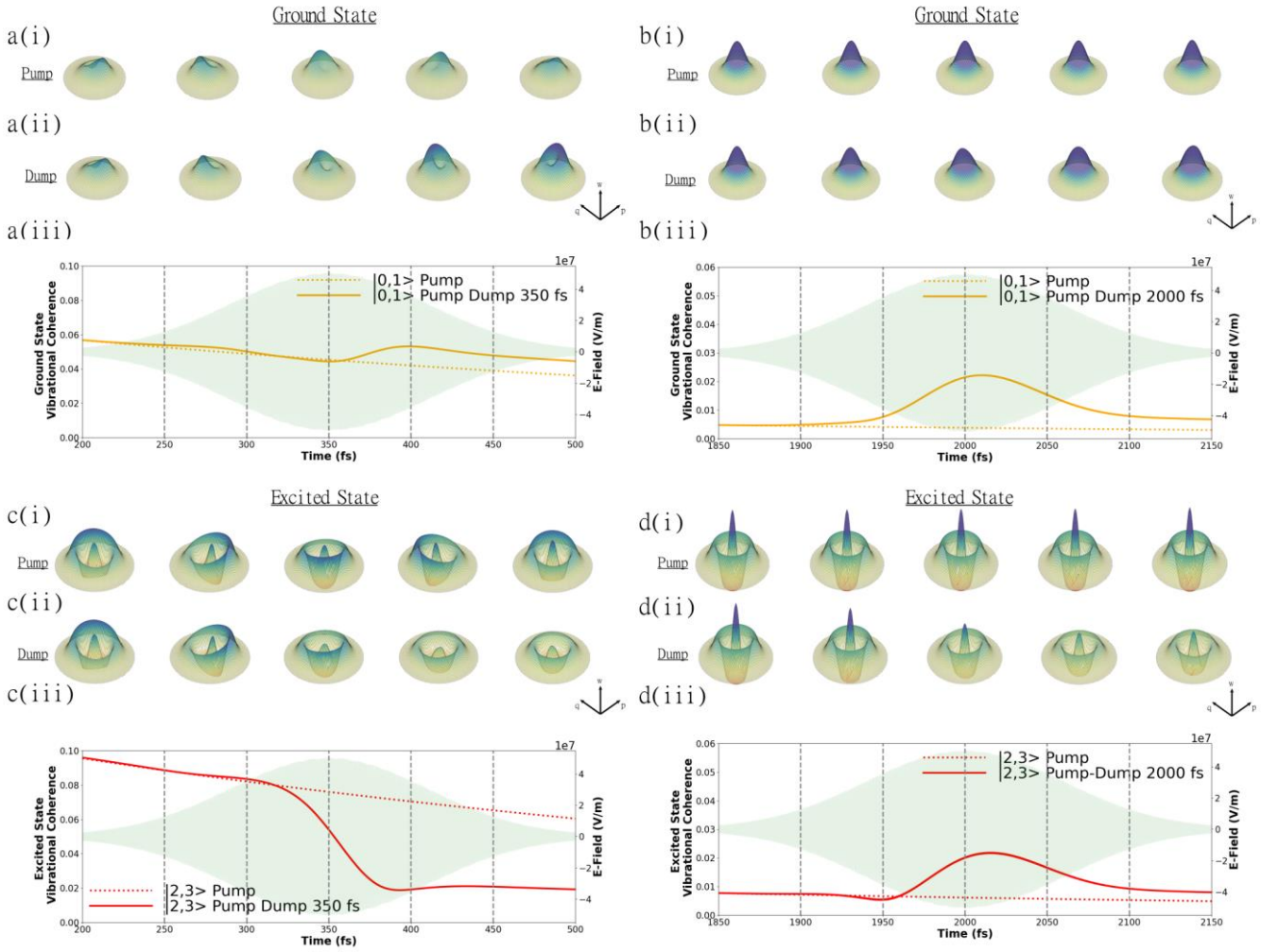

Supplementary Fig. 58 | Summary figure for density matrix calculations and Wigner transformations for ground and excited states. Results for a representative four-level system density matrix & Wigner transforms calculations on rsKiiro. Ground (a & b) and excited state (c & d) coherences for 350 fs (a & c) and 2 ps (b & d) pump-dump delay. In each case surface plots of Wigner functions are shown for the PP (i) and PDP (ii) cases, absolute scale is used for each colour map. Plots show the vibrational coherence (iii) (off-diagonal elements) of the ground electronic state, |0,1> (orange) and excited electronic state, |2,3> (red) in the pump (dashed) and pump-dump (solid) centred around the dump pulse.

Contrastingly the excited state coherence decreases from the beginning of the dump pulse. An almost 4-fold decrease in coherence in the excited state is observed. The large asymmetry in excited state Wigner plots at the start of the dump pulse is virtually symmetric by the end of the laser cycle. These simulations demonstrate a proof of principle that excited state vibrational coherence can be transferred to a lower electronic state by the simulated emission of a dump pulse.

13.5. Pump-Dump delay comparison

To compliment the SACLA experiment the effect of pump-dump delay time on the population and coherence dynamics of the toy system was investigated. A 350 fs and a 2 ps delay time was selected, replicating the TR-SFX experiment, the first being within the toy systems vibrational dephasing time (1 ps) and both delay times within the excited state lifetime (20 ps). The excited population dynamics for both dump delay schemes are shown in Supplementary Fig. 59. The dump efficiency decreases further in the 2 ps scheme (dashed) due to the pulse repopulating the largely vacant |3> state as vibrational cooling has occurred beyond 1 ps.

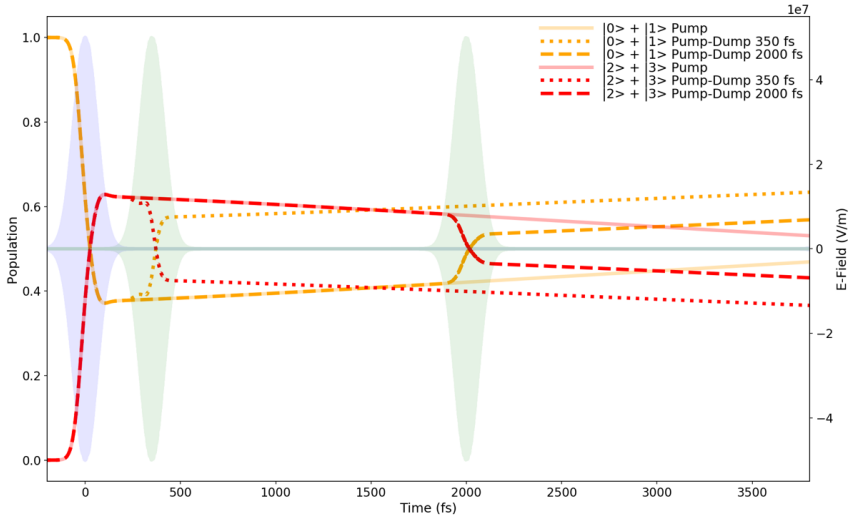

Supplementary Fig. 59| Summation of the diagonal elements of states in the same electronic level. Ground state (yellow) |0> + |1> and excited state (red) |2> + |3>, shown for both pump (solid), pump-dump 350 fs delay (dotted) and pump-dump 2 ps delay (dashed) schemes. The pale blue (pump) and green (dump) Gaussians show the real part of the laser electric field with either a dump delay of 350 fs or 2 ps.

The vibrational coherence of both pump-dump schemes is compared in Supplementary Fig. 60. As aforementioned in the Tannor-Rice optical control scheme, impulse momentum is imparted with the simulated emission dump pulse within the vibrational dephasing time of the system. Such in the 350 fs pump-dump delay, a transfer of vibrational coherence from the S_1 (|2,3>) to the S_0 (|0,1>) is observed (dotted line). Conversely the 2 ps delay creates vibrational coherence in both states (dashed line). Creation of vibrational coherence in the excited state is due to impulsive coherence in the direction of the nuclear binding force. Ground state coherence is displacement driven, the reversal of the pump coherence generated by the pump. The lack of a coherence transfer from excited to ground state in the 2 ps scheme due to the quenching of wave packet momentum beyond the 1 ps dephasing time validating the Tannor-Rice coherent dynamics.

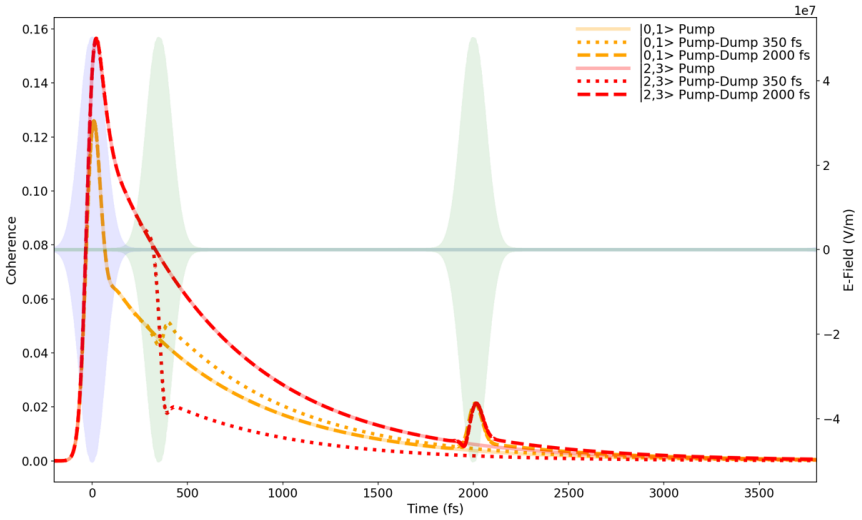

Supplementary Fig. 60| Modulus of the off-diagonal elements show coherence between states in the same electronic level. Ground state vibrational coherence (|0,1>) shown in yellow and excited state vibrational coherence (|2,3>) shown in red for both pump (solid), pump-dump 350 fs delay (dotted) and pump-dump 2 ps delay (dashed) schemes. The pale blue (pump) and green (dump) Gaussians show the real part of the laser electric field with either a dump delay of 350 fs or 2 ps.

Further elucidation of the dynamics can be garnered from a comparison of the Wigner distributions of the system over the laser cycle in both pump-dump schemes. Supplementary Fig. 61 shows the ground electronic state dynamics with the Wigner distributions plotted at 25 fs intervals over the central 100 fs of the dump pulse. In the early time of the 350 fs dump pulse, a continuing rotation of an asymmetric node (shown in Supplementary Fig. 61a(ii)) matches the vibrational frequency (170 cm^{-1}). The rotation of node is halted over the central portion of the laser pulse and growth of population is visible in both the positional and momentum axis. This is facilitated by both impulsive momentum and positional displacement being transferred from S_1 to the S_0 by stimulated emission, analogous to a Tannor-Rice scheme. In the 2 ps scheme the ground state distribution has no asymmetric nodes and is centralized. Upon interaction with central portion of the dump pulse the distribution is perturbed in both the position (q) and momentum (p) dimension. The positional perturbation of the maximum of the distribution is comparable in both dump schemes, however a far larger perturbation in the momentum axis is observed in the 350 fs scheme within the vibrational dephasing of the system.
The excited state Wigner distributions are shown in Supplementary Fig. 62, the 350 fs pump-dump scheme exhibits a loss of vibrational coherence in the excited state whereas a generation of coherence is observed in the 2 ps. The loss of coherence in the S_1 in the shorter delay attributed to removal of population in the coherently excited state. The generation in the longer scheme attributed to a combination of detuning of the dump pulse, causing a small positional displacement in lower vibrational state and repopulation of the higher vibrational level which population has relaxed out of at longer times. Reference Wigner plots in both surface and contour are shown in Supplementary Fig. 63 for reference.

13.6. Wavepacket assignment and discussion of coherence parameters and simulation

We discuss the wavepacket assignment in the framework of the existing Raman spectroscopy literature[68–71] and furthermore provide a coherence simulation with parameters relevant to the experimental conditions and observations. Pulsed resonant excitation of the molecular system prepares vibrational coherences in both the ground and excited states. The magnitude, phase and frequency limits

are determined by the electronic and vibrational dephasing, the detuning, pulse duration, intensity, carrier frequency and spectral phase. It is important to note that for a laser spectrum that is narrower than the absorption spectrum, the coherence magnitude of the ground state wavepacket is population driven and further enhanced by moderate detuning as are conditions typically used for TR-SFX and a representative of our PP data. The imparted impulse momentum in the ground state is in the direction of the nuclear binding force, while the excited state wavepacket is purely displacement driven and receives initial position and phase. For the ground state with small detuning the displacement is minimal in the lowest well that corresponds to the dark structure with the impulse momentum as shown in Fig. 2. Having shown the picoseconds time scale transfer of the PDP product back to the dark structure, coherence transfer between wells is described as adiabatic transfer on a double well potential energy surface. The transition energies for a four-state adiabatic model are taken from the electronic difference spectrum resolved by pump-dump-probe transient absorption spectroscopy (see above & Fig. 5). For the hydrogen-bonding changes and structural motions that characterize the A_1 and A_2 states, the adiabatic criterion is assumed for picoseconds transfer processes between these states. In this model the A_1 resting state is refilled in the adiabatic limit as shown in Fig. 2. A double-well potential in the excited state lowers the potential energy of the additional well relative to the dark state geometry and is populated within ~200 fs after the pump interaction.

We performed a non-perturbative density matrix simulation that fully demonstrates the coherence dynamics using the essential experimental parameters. Using Wigner transforms[72] of the density matrix that evolves under the Liouville von Neumann equation the phase space distributions demonstrate the coherence progression and transfer in the respective pump and dump interactions. We demonstrate the measured dynamics by modelling a simplified 4-level density matrix simulation that uses a 170 cm^{-1} vibrational frequency and matches the electronic transition energy of the neutral trans chromophore. The first pump interaction prepares population transfer from the vibrational ground state of S_0 into the two lowest vibrational states of S_1 (i.e. $\rho_{00} \rightarrow \rho_{22} + \rho_{33}$) and creates ground state coherence between the vibrational states in S_0, i.e. ρ_{01} from interaction with the Boltzmann distributions of ρ_{00} and ρ_{11} as well as excited state coherence ρ_{23} using the experimental laser spectrum and duration. We introduce the Stokes field with a 350 fs pump-dump delay according to the experimental value and using the criterion $\Gamma_{electronic} > \frac{1}{\Delta t_{pump-dump}} > \Gamma_{vibrational}$ (see above). The carrier frequency couples the population transfers and efficiently transfers the vibrational coherence $\rho_{23} \rightarrow \rho_{01}$. The simulation fully demonstrates Tannor-Rice dynamics[73–75] in the pump-dump scheme by transfer of coherence. The experimental results follow the Tannor-Rice time domain approach where the initial ultrafast pulse creates an intermediate state that is subsequently transferred into the final state by the dump pulse. The time delay between the pulses is used to control the reaction[73–75]. In the Wigner phase space, the transforms that are separated for the ground and excited state elements show the momentum and position transfer to the ground state that is stimulated by the Stokes field. In the wavepacket picture, the transfer of position and momentum of excited to ground state will cause the wavepacket to continue motion towards the dissociative state following the dump pulse (Fig. 2). Strikingly the density matrix simulation for the PDP condition doubles the magnitude of the ground state coherence and adds strong support to the assignments for the PP and PDP crystallographic data. The ~5000 cm^{-1} relaxation term between absorption (λ_{max}=390 nm) and fluorescence (λ_{max}=490 nm) energies formally requires a 4-level electronic system. The number of Fock states included in an extended model determine the high order

structure of the Wigner transforms and therefore take assumptions in the number of vibrationally excited levels. The transfer of electronic state $|2\rangle$ to the redshifted radiative state $|1\rangle$ proceeds under a Landau-Zener reaction driven Hamiltonian. A pump-dump simulation in a complete system however does not alter the physics of the coherence transfer dynamics demonstrated already in the 4-level system which is fully sufficient to demonstrate the structural dynamics observed in the time resolved experiments together with optical control and are additionally generally applicable to other systems.

These simulations are appropriate demonstration for the dynamics observed in rsKiiro. There are unlikely to exist general conclusions with regard to assignment of ultrafast crystallographic differences. The ultrafast motion is determined by quantum dynamics of electronic ground and excited states, optical parameters, electronic and vibrational coherence and dephasing, mode displacements, multimode character and coupling, concentrations and heterogeneity. In addition the crystallographic differences are determined by ordering parameters, resolution and signal to noise statistics. The outcome of the experiment cannot be predicted because of the complex characteristics of the structural dynamics and the measurements. The optical control experiment ensures that the observations after the dump interaction are exclusively showing the electronic ground state motions.

This work shows that for the off state of rsKiiro the ultrafast motions of PP and PDP experiments belong to coherent dynamics in the electronic ground state. It should be emphasized that this conclusion is unrelated to other proteins that have been studied by TR-SFX. These include the Photoactive Yellow protein[76] (PYP), bacteriorhodopsin[77,78], rsEGFP2[31] and myoglobin[79], which all have very different photochemical, structural and quantum dynamics characteristics. This work however provides experimental methods and coherence modelling in order to aid the assignment and evaluation of functional significance of the motions observed on the ultrafast time scale

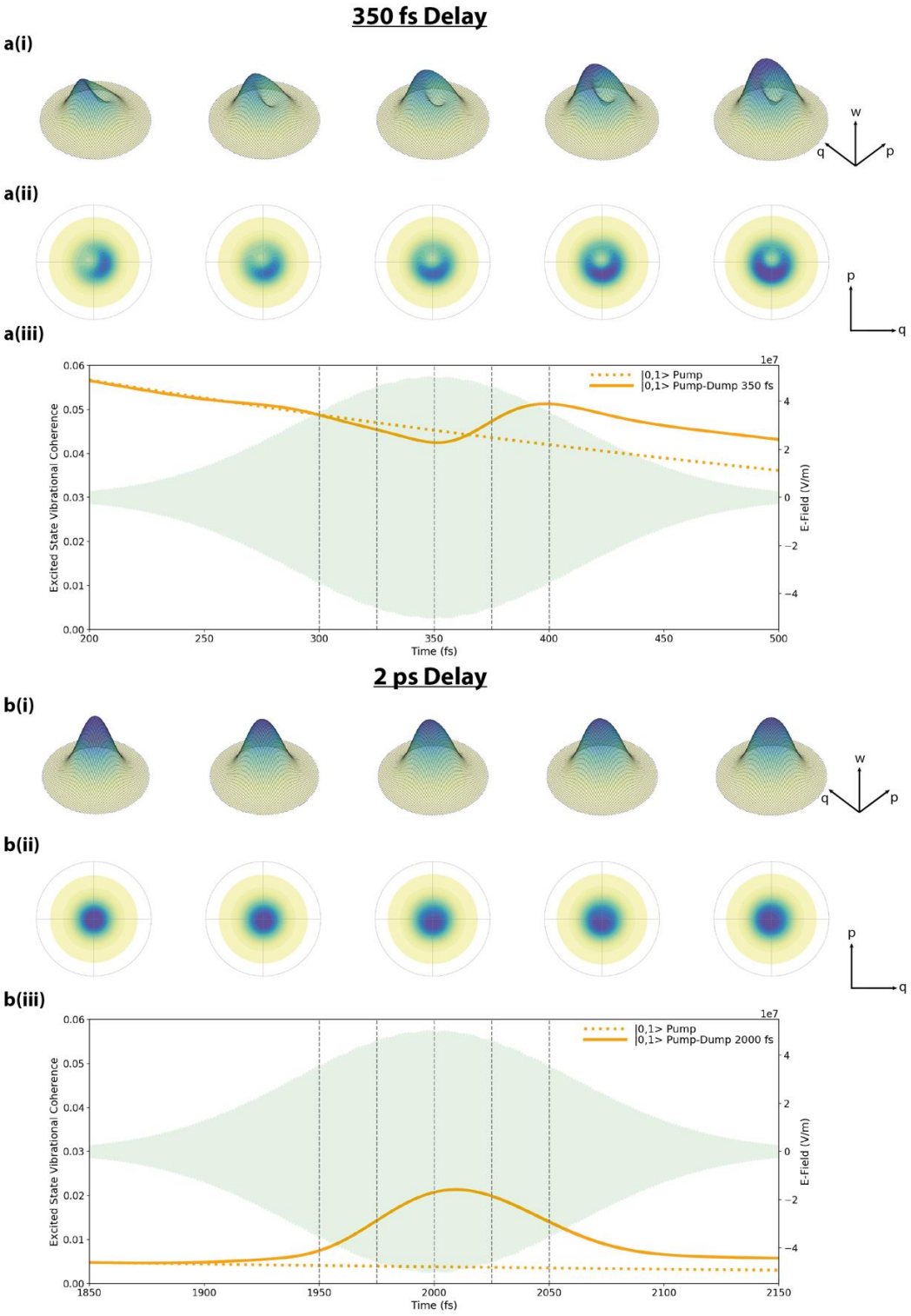

Supplementary Fig. 61| Ground state Wigner plots. Surface (i) and contour (ii) plots of Wigner functions of the ground electronic states for pump-dump delays of 350 fs (a) 2 ps (b). Vibrational coherence (off-diagonal elements) of the ground electronic state (|0,1>) (iii) for pump-dump delays of 350 fs (a) and 2 ps (b) , shown for pump (dotted) and pump-dump (solid) around the centre of the dump pulse, grey lines at 25 fs intervals depict time stamps of Wigner plots. Surface plot (i) colour schemes are normalized for each scheme to highlight asymmetric features.

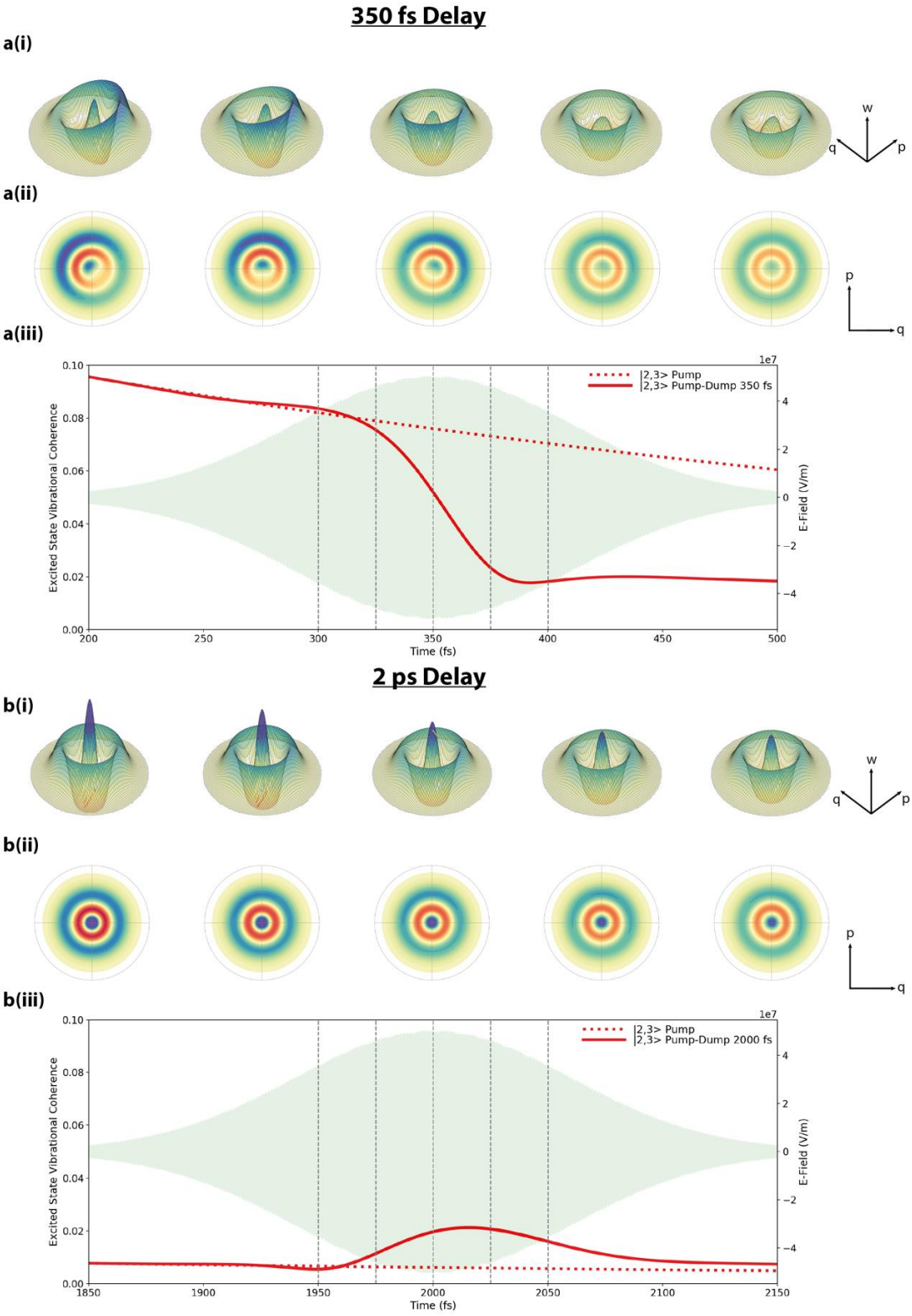

Supplementary Fig. 62| Excited state Wigner plots. Surface (i) and contour (ii) plots of Wigner functions of the excited electronic states for pump-dump delays of 350 fs (a) 2 ps (b). Vibrational coherence (off-diagonal elements) of the excited electronic state (|2,3>) (iii) for pump-dump delays of 350 fs (a) and 2 ps (b) , shown for pump (dotted) and pump-dump (solid) around the centre of the dump pulse, grey lines at 50 fs intervals depict time stamps of Wigner plots. Surface plot (i) colour schemes are normalized for each individual plot to highlight asymmetric features.

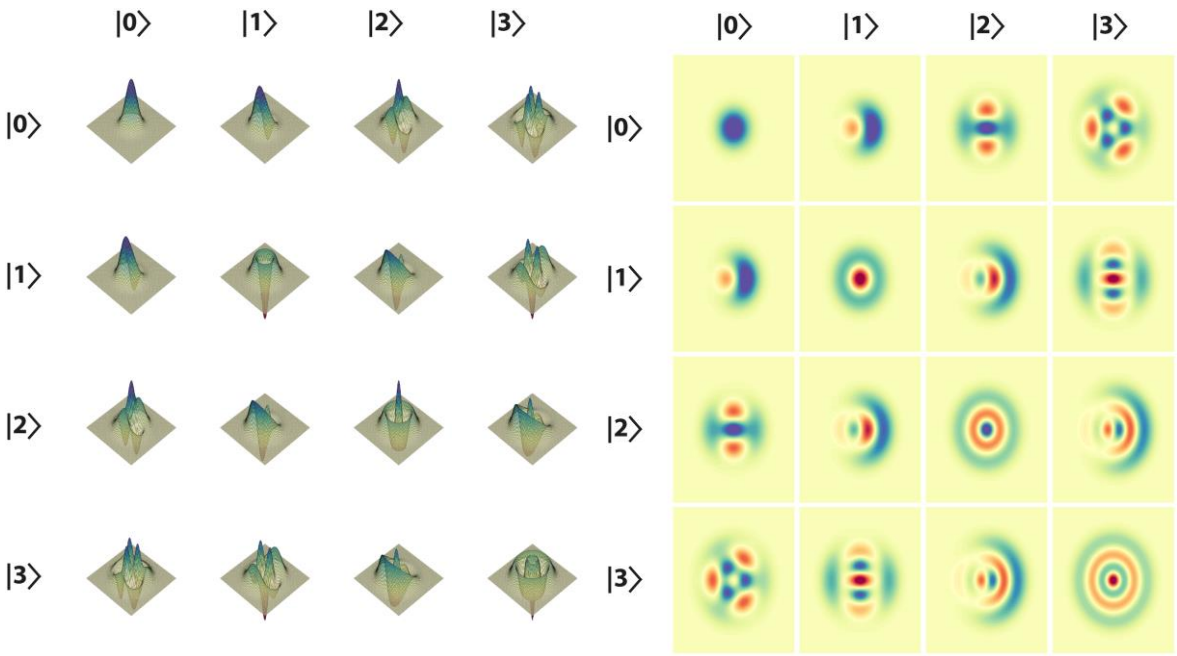

Supplementary Fig. 63 | Reference Wigner Plots. Surface (left) and contour plots (right) of normalized Wigner functions of various combinations of Fock states. Diagonal plots are pure states while off diagonal are mixed states with coherences present. The number of lines of symmetry in a Wigner plot is equal to the number difference between those Fock states. In the contour plots blue denotes a positive Wigner probability and red negative.

14. Supplementary references

1. Gahl, C. *et al.* A femtosecond X-ray/optical cross-correlator. *Nat. Photonics* **2**, 165–169 (2008).
2. Sanchez-gonzalez, A. *et al.* Coincidence timing of femtosecond optical pulses in an X-ray free electron laser. *J. Appl. Phys.* 203105 (2017) doi:10.1063/1.5012749.
3. Trebino, R. *et al.* Measuring ultrashort laser pulses in the time-frequency domain using frequency-resolved optical gating. *Rev. Sci. Instrum.* **68**, 3277–3295 (1997).
4. Linden, S., Giessen, H. & Kuhl, J. XFROG - A new method for amplitude and phase characterization of weak ultrashort pulses. *Phys. Status Solidi Basic Res.* **206**, 119–124 (1998).
5. Lincoln, C. N., Fitzpatrick, A. E. & Thor, J. J. V. Photoisomerisation quantum yield and non-linear cross-sections with femtosecond excitation of the photoactive yellow protein. *Phys. Chem. Chem. Phys.* **14**, 15752–15764 (2012).
6. Šrajer, V. *et al.* Protein Conformational Relaxation and Ligand Migration in Myoglobin: A Nanosecond to Millisecond Molecular Movie from Time-Resolved Laue X-ray Diffraction. *Biochemistry* **40**, 13802–13815 (2001).
7. Ursby, T. & Bourgeois, D. Improved Estimation of Structure-Factor Difference Amplitudesfrom Poorly Accurate Data. *Acta Crystallogr. Sect. A Found. Crystallogr.* **53**, 564–575 (1997).
8. Pandey, S. *et al.* Time-resolved serial femtosecond crystallography at the European XFEL. *Nat. Methods* **17**, 73–78 (2020).
9. Gorel, A., Schlichting, I. & Barends, T. R. M. Discerning best practices in XFEL-based biological crystallography – standards for nonstandard experiments. *IUCrJ* **8**, 532–543 (2021).
10. Tickle, I. *et al.* STARANISO. at http://staraniso.globalphasing.org/cgi-bin/staraniso.cgi (2018).
11. Prokhorenko, V. I., Halpin, A., Johnson, P. J. M., Miller, R. J. D. & Brown, L. S. Coherent control of the isomerization of retinal in bacteriorhodopsin in the high intensity regime. *J. Chem. Phys.* **134**, 085105 (2011).
12. Hutchison, C. D. M. *et al.* Photocycle populations with femtosecond excitation of crystalline photoactive yellow protein. *Chem. Phys. Lett.* **654**, 63–71 (2016).
13. Romei, M. G., Lin, C. Y., Mathews, I. I. & Boxer, S. G. Electrostatic control of photoisomerization pathways in proteins. *Science (80-.).* **367**, 76–79 (2020).
14. Fluorescence Decay Analysis Software 1.4, FlourTools. at www.fluortools.com/software/decayfit (2014).
15. Cotlet, M. *et al.* Excited-State Dynamics in the Enhanced Green Fluorescent Protein Mutant Probed by Picosecond Time-Resolved Single Photon Counting Spectroscopy. *J. Phys. Chem. B* **105**, 4999–5006 (2001).
16. Jung, G., Wiehler, J. & Zumbusch, A. The Photophysics of Green Fluorescent Protein: Influence of the Key Amino Acids at Positions 65, 203, and 222. *Biophys. J.* **88**, 1932–1947 (2005).
17. Ghosh, A. *et al.* Quantifying Microsecond Transition Times Using Fluorescence Lifetime Correlation Spectroscopy. *J. Phys. Chem. Lett.* **8**, 6022–6028 (2017).
18. Flors, C. *et al.* A stroboscopic approach for fast photoactivation-localization microscopy with Dronpa mutants. *J. Am. Chem. Soc.* **129**, 13970–13977 (2007).

19. Morozov, D. & Groenhof, G. Hydrogen Bond Fluctuations Control Photochromism in a Reversibly Photo-Switchable Fluorescent Protein. *Angew. Chemie Int. Ed.* **55**, 576–578 (2016).

20. Interactive chart of FP properties. http://www.fpbase.org/chart/.

21. Würth, C., Grabolle, M., Pauli, J., Spieles, M. & Resch-Genger, U. Relative and absolute determination of fluorescence quantum yields of transparent samples. *Nat. Protoc.* **8**, 1535–1550 (2013).

22. Gaigalas, A. K. & Wang, L. Measurement of the fluorescence quantum yield using a spectrometer with an integrating sphere detector. *J. Res. Natl. Inst. Stand. Technol.* **113**, 17 (2008).

23. Strickler, S. J. & Berg, R. A. Relationship between Absorption Intensity and Fluorescence Lifetime of Molecules. *J. Chem. Phys.* **37**, 814–822 (1962).

24. Hutchison, C. *et al.* X-ray Free Electron Laser Determination of Crystal Structures of Dark and Light States of a Reversibly Photoswitching Fluorescent Protein at Room Temperature. *Int. J. Mol. Sci.* **18**, 1918 (2017).

25. Zhang, X. *et al.* Highly photostable, reversibly photoswitchable fluorescent protein with high contrast ratio for live-cell superresolution microscopy. *Proc. Natl. Acad. Sci.* 201611038 (2016) doi:10.1073/pnas.1611038113.

26. Close, D. W. *et al.* Thermal green protein, an extremely stable, nonaggregating fluorescent protein created by structure-guided surface engineering. *Proteins Struct. Funct. Bioinforma.* **83**, 1225–1237 (2015).

27. Pletnev, S., Subach, F. V., Dauter, Z., Wlodawer, A. & Verkhusha, V. V. A Structural Basis for Reversible Photoswitching of Absorbance Spectra in Red Fluorescent Protein rsTagRFP. *J. Mol. Biol.* **417**, 144–151 (2012).

28. Grotjohann, T. *et al.* rsEGFP2 enables fast RESOLFT nanoscopy of living cells. *Elife* **1**, (2012).

29. Kaucikas, M. *et al.* Room temperature crystal structure of the fast switching M159T mutant of the fluorescent protein dronpa. *Proteins Struct. Funct. Bioinforma.* **83**, 397–402 (2015).

30. Woodhouse, J. *et al.* Photoswitching mechanism of a fluorescent protein revealed by time-resolved crystallography and transient absorption spectroscopy. *Nat. Commun.* **11**, 1–11 (2020).

31. Coquelle, N. *et al.* Chromophore twisting in the excited state of a photoswitchable fluorescent protein captured by time-resolved serial femtosecond crystallography. *Nat. Chem.* **10**, 31–37 (2018).

32. Colletier, J. P. *et al.* Serial Femtosecond Crystallography and Ultrafast Absorption Spectroscopy of the Photoswitchable Fluorescent Protein IrisFP. *J. Phys. Chem. Lett.* **7**, 882–887 (2016).

33. Pilling, M. J. & Robertson, S. H. Master Equation Models For Chemical Reactions Of Importance In Combustion. *Annu. Rev. Phys. Chem.* **54**, 245–275 (2003).

34. Summers, D. & Scott, J. M. W. Systems of first-order chemical reactions. *Math. Comput. Model.* **10**, 901–909 (1988).

35. Lin, C.-Y., Both, J., Do, K. & Boxer, S. G. Mechanism and bottlenecks in strand photodissociation of split green fluorescent proteins (GFPs). *Proc. Natl. Acad. Sci.* **114**, E2146–E2155 (2017).

36. Nitzan, A. *Chemical Dynamics in Condensed Phases Relaxation, Transfer and Reactions in*

Condensed Molecular Systems. (Oxford University Press, 2006).

37. Breuer, H.-P. & Petruccione, F. *The Theory of Open Quantum Systems*. (Oxford University Press, 2002).

38. Bochenkova, A. V. & Andersen, L. H. Ultrafast dual photoresponse of isolated biological chromophores: link to the photoinduced mode-specific non-adiabatic dynamics in proteins. *Faraday Discuss.* **163**, 297 (2013).

39. Kim, J. E., Tauber, M. J. & Mathies, R. A. Analysis of the Mode-Specific Excited-State Energy Distribution and Wavelength-Dependent Photoreaction Quantum Yield in Rhodopsin. *Biophys. J.* **84**, 2492–2501 (2003).

40. Wittig, C. The Landau−Zener Formula †. *J. Phys. Chem. B* **109**, 8428–8430 (2005).

41. Alvarez-Idaboy, J. R., Mora-Diez, N. & Vivier-Bunge, A. A Quantum Chemical and Classical Transition State Theory Explanation of Negative Activation Energies in OH Addition To Substituted Ethenes. *J. Am. Chem. Soc.* **122**, 3715–3720 (2000).

42. Krasnoperov, L. N., Peng, J. & Marshall, P. Modified Transition State Theory and Negative Apparent Activation Energies of Simple Metathesis Reactions: Application to the Reaction CH 3 + HBr → CH 4 + Br †. *J. Phys. Chem. A* **110**, 3110–3120 (2006).

43. Mozurkewich, M. & Benson, S. W. Negative activation energies and curved Arrhenius plots. 1. Theory of reactions over potential wells. *J. Phys. Chem.* **88**, 6429–6435 (1984).

44. Agmon, N. Kinetics of Switchable Proton Escape from a Proton-Wire within Green Fluorescence Protein. *J. Phys. Chem. B* **111**, 7870–7878 (2007).

45. Frauenfelder, H. *et al.* A unified model of protein dynamics. *Proc. Natl. Acad. Sci.* **106**, 5129–5134 (2009).

46. Nagel, Z. D., Dong, M., Bahnson, B. J. & Klinman, J. P. (Suppl. Mat.) Impaired protein conformational landscapes as revealed in anomalous Arrhenius prefactors. *Proc. Natl. Acad. Sci.* **108**, 10520–10525 (2011).

47. Englman, R. & Jortner, J. The energy gap law for radiationless transitions in large molecules. *Mol. Phys.* **18**, 145–164 (1970).

48. Seidner, L. & Domcke, W. Microscopic modelling of photoisomerization and internal-conversion dynamics. *Chem. Phys.* **186**, 27–40 (1994).

49. Donahue, N. M. Reaction Barriers: Origin and Evolution. *Chem. Rev.* **103**, 4593–4604 (2003).

50. Marcus, R. A. Foreword: Beyond the Historical Perspective on Hydrogen and Electron Transfers. in *Quantum Tunnelling in Enzyme-Catalysed Reactions* (eds. Allemann, R. K. & Scrutton, N. S.) (RSC Publishing, 2009).

51. Nitzan, A. & Jortner, J. Non radiative transition probabilities in the statistical limit. *Theor. Chim. Acta* **30**, 217–229 (1973).

52. Litvinenko, K. L., Webber, N. M. & Meech, S. R. Internal Conversion in the Chromophore of the Green Fluorescent Protein: Temperature Dependence and Isoviscosity Analysis. *J. Phys. Chem. A* **107**, 2616–2623 (2003).

53. Duan, Y. *et al.* A point-charge force field for molecular mechanics simulations of proteins based on condensed-phase quantum mechanical calculations. *J. Comput. Chem.* **24**, 1999–2012 (2003).

54. Sousa da Silva, A. W. & Vranken, W. F. ACPYPE - AnteChamber PYthon Parser interfacE. *BMC Res. Notes* **5**, 367 (2012).

55. Pronk, S. *et al.* GROMACS 4.5: a high-throughput and highly parallel open source molecular simulation toolkit. *Bioinformatics* **29**, 845–854 (2013).

56. Titov, A. V., Ufimtsev, I. S., Luehr, N. & Martinez, T. J. Generating Efficient Quantum Chemistry Codes for Novel Architectures. *J. Chem. Theory Comput.* **9**, 213–221 (2013).

57. Adamo, C. & Barone, V. Toward reliable density functional methods without adjustable parameters: The PBE0 model. *J. Chem. Phys.* **110**, 6158–6170 (1999).

58. Dunning, T. H. Gaussian basis sets for use in correlated molecular calculations. I. The atoms boron through neon and hydrogen. *J. Chem. Phys.* **90**, 1007–1023 (1989).

59. Grimme, S., Antony, J., Ehrlich, S. & Krieg, H. A consistent and accurate ab initio parametrization of density functional dispersion correction (DFT-D) for the 94 elements H-Pu. *J. Chem. Phys.* **132**, 154104 (2010).

60. Hirata, S. & Head-Gordon, M. Time-dependent density functional theory within the Tamm–Dancoff approximation. *Chem. Phys. Lett.* **314**, 291–299 (1999).

61. Granovsky, A. A. Extended multi-configuration quasi-degenerate perturbation theory: The new approach to multi-state multi-reference perturbation theory. *J. Chem. Phys.* **134**, 214113 (2011).

62. Granovsky, A. A. Firefly version 8. at http://classic.chem.msu.su/gran/firefly/index.html.

63. Brühl, E., Buckup, T. & Motzkus, M. Experimental and numerical investigation of a phase-only control mechanism in the linear intensity regime. *J. Chem. Phys.* **148**, 214310 (2018).

64. Wohlleben, W., Buckup, T., Herek, J. L. & Motzkus, M. Coherent Control for Spectroscopy and Manipulation of Biological Dynamics. *ChemPhysChem* **6**, 850–857 (2005).

65. Johansson, J. R., Nation, P. D. & Nori, F. QuTiP: An open-source Python framework for the dynamics of open quantum systems. *Comput. Phys. Commun.* **183**, 1760–1772 (2012).

66. Leonhardt, U. & Paul, H. Measuring the quantum state of light. *Prog. Quantum Electron.* **19**, 89–130 (1995).

67. Fujisawa, T., Kuramochi, H., Hosoi, H., Takeuchi, S. & Tahara, T. Role of Coherent Low-Frequency Motion in Excited-State Proton Transfer of Green Fluorescent Protein Studied by Time-Resolved Impulsive Stimulated Raman Spectroscopy. *J. Am. Chem. Soc.* **138**, 3942–3945 (2016).

68. Kumar, A. T. N., Rosca, F., Widom, A. & Champion, P. M. Investigations of amplitude and phase excitation profiles in femtosecond coherence spectroscopy. *J. Chem. Phys.* **114**, 701 (2001).

69. Kumar, A. T. N., Rosca, F., Widom, A. & Champion, P. M. Investigations of ultrafast nuclear response induced by resonant and nonresonant laser pulses. *J. Chem. Phys.* **114**, 6795–6815 (2001).

70. Hutchison, C. D. M. & van Thor, J. J. Populations and coherence in femtosecond time resolved X-ray crystallography of the photoactive yellow protein. *Int. Rev. Phys. Chem.* **36**, 117–143 (2017).

71. Mukamel, S. *Principles of Nonlinear Optical Spectroscopy*. (Oxford University Press, 1995).

72. Wigner, E. On the Quantum Correction For Thermodynamic Equilibrium. *Phys. Rev.* **40**, 749–759

(1932).

73. Tannor, D. J. & Rice, S. A. Control of selectivity of chemical reaction via control of wave packet evolution. *J. Chem. Phys.* **83**, 5013–5018 (1985).

74. Tannor, D. J., Kosloff, R. & Rice, S. A. Coherent pulse sequence induced control of selectivity of reactions: Exact quantum mechanical calculations. *J. Chem. Phys.* **85**, 5805–5820 (1986).

75. Kosloff, R., Rice, S. A., Gaspard, P., Tersigni, S. & Tannor, D. J. Wavepacket dancing: Achieving chemical selectivity by shaping light pulses. *Chem. Phys.* **139**, 201–220 (1989).

76. Pande, K. *et al.* Femtosecond structural dynamics drives the trans/cis isomerization in photoactive yellow protein. *Science (80-.).* **352**, 725–729 (2016).

77. Nogly, P. *et al.* Retinal isomerization in bacteriorhodopsin captured by a femtosecond x-ray laser. *Science (80-.).* **361**, eaat0094 (2018).

78. Nass Kovacs, G. *et al.* Three-dimensional view of ultrafast dynamics in photoexcited bacteriorhodopsin. *Nat. Commun.* **10**, 3177 (2019).

79. Barends, T. R. M. *et al.* Direct observation of ultrafast collective motions in CO myoglobin upon ligand dissociation. *Science (80-.).* **350**, 445–450 (2015).